Towards the Description of Core-Excited States within the Framework of Many-Body Perturbation Theory

Zur Erlangung des akademischen Grades eines

DOKTORS DER NATURWISSENSCHAFTEN

(Dr. rer. nat.)

von der KIT-Fakultät für Chemie und Biowissenschaften
des Karlsruher Instituts für Technologie (KIT)

genehmigte

DISSERTATION

von

M.Sc. Max Karl Kehry

1. Referent:	Prof. Dr. Willem M. Klopper
2. Referent:	apl. Prof. Dr. Florian Weigend
Tag der mündlichen Prüfung:	19.07.2022

Kurzfassung

Gegenstand dieser Arbeit ist die Entwicklung effizienter und robuster Methoden zur Beschreibung von Ladungs- und ladungsneutralen Anregungen von kernnahen Zuständen in molekularen Systemen mittels Vielteilchen-Störungstheorie. Um auch die Anwendbarkeit auf Systeme, die schwere Elemente beinhalten, zu gewährleisten, wird der Formalismus in einem zwei-komponentigen Kramers-symmetrischen Rahmen präsentiert. Dies erlaubt neben skalarrelativistischen Effekten auch die explizite Beschreibung der Spin-Bahn-Wechselwirkung. Die erarbeiteten Ansätze bleiben jedoch auch im ein-komponentigen, nichtrelativistischen Grenzfall gültig. Es wird eine neue Methode zur Berechnung von Quasiteilchenenergien in der *GW*-Näherung vorgestellt und bewertet. Dabei wird die Beschreibung von Ladungsanregungen, den Ionisierungsenergien und Elektronenaffinitäten, gleichermaßen für Valenz- und Rumpfelektronen ermöglicht. Diese Technik verringert gerade für die letztere Anwendung den Aufwand drastisch im Vergleich zu etablierten Methoden und besitzt zudem auch Vorteile für Systeme mit einer hohen Zustandsdichte. Die so erhaltenen Quasiteilchenenergien werden im Weiteren als Ausgangspunkt zur Berechnung von ladungsneutralen Anregungen, wie sie zur Beschreibung von Experimenten aus der Röntgenabsorptionsspektroskopie benötigt werden, mittels der Bethe-Salpeter Gleichung verwendet. Es werden zwei Ansätze diskutiert, die bereits im Rahmen der Dichtefunktionaltheorie und *post*-Hartree–Fock Methoden bekannt sind. Erstere folgt der gedämpften linearen Antworttheorie und führt eine künstliche Lebenszeit für angeregte Zustände ein. Dies ermöglicht die Berechnung dynamischer Polarisierbarkeiten für beliebige Frequenzen. Die zweite Methode nutzt die schwache Kopplung zwischen den Anregungen rumpfnaher und Valenzelektronen in der elektronischen Hesse-Matrix. Das Problem wird in einem entsprechenden Unterraum der Einfachanregungen von Rumpfelektronen gelöst. Beide Methoden werden im Folgenden zusammen mit den entsprechenden Implementierungen vorgestellt und auf die Möglichkeit zur Beschreibung von Anregungen von kernnahen Elektronen bewertet. Die Ergebnisse werden mit weiteren Methoden, sowie experimentellen Daten verglichen, und auf reale Fragestellungen angewandt.

Abstract

Subject of the present work is the development of efficient and robust methods for the description of charge and charge neutral excitations of low-lying states in molecular systems within many-body perturbation theory. To ensure a sensible description for systems containing heavy elements, the general formalism is presented in a quasirelavistic two-component Kramers symmetric framework. This allows for the explicit description of scalar-relativistic effects and spin-orbit interactions. However, the considerations presented in the following remain valid in the non-relativistic one-component limit. A new method for the evaluation of quasiparticle energies within the *GW* approximation is proposed and assessed, which is specifically geared towards the description of charge excitations, the ionization potentials and electron affinities, for valence and core electrons in a balanced manner. This technique results in large efficiency gains over well-established methods, especially in the latter case, but also provides a considerable improvement for systems with a particular high density of states. The quasiparticle energies obtained here act as a starting point for the calculation of charge neutral excitations used to simulate X-ray experiments by using the Bethe-Salpeter equation. This technique is then combined with two methods, known from their formulations in the context of density functional theory and *post*-Hartree–Fock approaches. The first technique introduces artificial lifetimes, following damped linear response theory. This allows for the direct evaluation of dynamic polarizabilities for arbitrary frequencies. The second method exploits the weak coupling between the excitations of core and valence electrons in the electronic Hessian. The underlying equations are then solved in the subspace of singly excitated states of core electrons. Both methods, as well as aspects regarding the respective implementations, are presented in the following, where they are then assessed for their description of core-excited states in selected systems. The results are compared with similar methods, as well as experimental data, and is then applied to real-life problems.

Contents

Kurzfassung . . . . . **i**

Abstract . . . . . **iii**

1 Introduction and Motivation **1**

2 Notation **3**

3 Fundamental Concepts in Relativistic Density Functional Theory **5**
3.1 Quasirelativistic Methods in Quantum Chemistry 6
3.2 Self-Consistent Field Theory in Quasirelativistic Two-Component Methods 8
3.3 Kramers' Time Reversal Symmetry 9
3.4 Aspects of Quasirelativistic Kohn–Sham Density Functional Theory 10
3.5 Time-Dependent Kohn–Sham Equations and Linear Response Theory 11
3.6 Damped Response Theory 15

4 Green's Function based Methods in Quantum Chemistry **17**
4.1 The One-Particle Green's Function 17
4.2 Hedin's Equations 20
4.3 The *GW* Approximation 22
4.4 Practical Approximations Towards Self-Consistent *GW* 26

5 *GW* Subspace Methods **29**
5.1 Subspace Representation of the Dielectric Function 29
5.2 Analytic Continuation of the Self-Energy 32
5.3 Contour Deformation Technique in *GW* 34
5.4 Analytic Continuation of the Screened Exchange 36
5.5 Analytic Continuation using an Adaptive Frequency-Sampling Technique 37
5.5.1 Evaluation of the Screened Exchange 38
5.5.2 The fsCD-*GW* Algorithm 40
5.6 Assessment of fsCD-*GW* 45
5.6.1 Quasi-Degeneracies in Core-Level States: the C_{60} Molecule 46
5.6.2 Validation of the Accuracy for Valence States in Coinage Metal Complexes 47
5.6.3 Performance for Core-Electron Binding Energies for Cd Clusters 49

6 Bethe-Salpeter Equation for Core-Excited States **51**
6.1 Fundamental Aspects of the Bethe-Salpeter Equation 52
6.2 Damped Bethe-Salpeter Equations 54
6.2.1 Solution of the Damped Response Equations 56
6.2.2 Practical Considerations of the Damped Response Formalism 60
6.3 Core-Valence Separation in *GW*-BSE 61

7 Origin-Independent Oscillator Strength **65**
7.1 Semi-Classical Light-Matter Interaction 65
7.2 Gauge-Invariant Oscillator Strength 67

7.3 Implementation and Validation . . . 69

8 Assessment of the Starting Point Dependence of GW for Vertical Ionization Potentials . . . 71
8.1 Ionization Potential of Valence Electrons: the GW27 and GW100 Test Sets . . . 72
8.2 Core-Electron Binding Energies: the CORE65 Test Set . . . 76

9 Assessment of *GW*-BSE for Core-Excited States . . . 79
9.1 Assessment of K-edge Absorption Spectra for Light Systems . . . 80
9.2 Assessment of *GW*-BSE for K- and $L_{1,2,3}$-Edges in Inorganic Systems . . . 81

10 Application to Core-Excited States of Lanthanum Compounds . . . 85

11 Summary and Conclusion . . . 89

A Appendix . . . 91
A.1 Performance of fsCD-*GW* for Cd Clusters of Varying Size . . . 91
A.2 Ionization Potentials for the GW27 Test Set . . . 93
A.3 Ionization Potentials for the GW100 Test Set . . . 95
A.4 Ionization Potentials of the CORE65 Test Set . . . 101
A.5 Core-Excited States within *GW*-BSE . . . 113
A.6 Statistical Data for Core-Excited States within *GW*-BSE for aligned spectra . . . 115

List of Figures . . . 117

List of Tables . . . 119

Acronyms and symbols . . . 121

Permissions to Print . . . 123

Bibliography . . . 125

Acknowledgments . . . 143

1 Introduction and Motivation

Since the initial discovery of X-ray radiation, spectroscopic methods using highly energetic radiation have evolved into a well-established tool for the investigation of the electronic structure of materials.[1] These techniques provide unique insights into the local environments of individual elements by selectively exciting their core electrons. Here, one may choose between different regions, associated with the specific ionization thresholds of low-lying states, to take advantage of the selection rules for electronic transitions and achieve an angular momentum resolution. This allows the probing of the individual orbital contributions, which in turn provides information regarding the bonding situation. These spectra are highly sensitive to the local density at a site, which is related to the formal oxidation state of an atom.[2–4] Recent studies, for example, demonstrated how high resolution X-ray absorption experiments can offer insights into the topic of bond covalency in lanthanum compounds.[1,5–8] These experiments usually require highly sophisticated setups and are mostly limited to large synchrotron facilities in order to provide the necessary coherence and intensity for X-ray spectroscopy.[1,9] However, novel techniques are being developed, which may allow for X-ray absorption experiments also on a laboratory scale, extending the use of these methods to exciting new problems in the future.[1,7,8]

For many experiments, the measurements are complemented by computational studies using quantum chemical methods, in order to provide further insights and rationalize the initial observations. For energetically low-lying excitations, in UV/Vis experiments, a variety of well-established tools are available and are routinely applied in many computational studies. However, the high energy regime encountered in X-ray spectroscopy provides additional challenges to these methods. Many common approximations used for the description of valence excitations, suddenly start to break down. One example, is the electric dipole approximation to the light-matter interaction in the semi-classical picture. As the wavelength of the electromagnetic radiation approaches the extend of a molecule, this approximation may begin to fail, and higher interaction terms become necessary to properly relate the simulated transition rates to the experimental observations.[10,11] Other examples, are the stark increase in magnitude of relativistic effects, as one tries to model properties of electrons in the vicinity of the nucleus.[12] Especially when considering heavier elements, the spectra may start to be even qualitatively wrong, if these effects are carelessly neglected. The spin-orbit interaction for inner shells can give rise to multiple branches, which may overlap, depending on the element considered. Since perturbative approaches do not suffice in these cases, a more rigorous framework based on a self-consistent (quasi-)relativistic theory is highly desirable. These complications arise independently from the method used to optimize ground and excited states, in order to provide a description of the electronic structure of the system under investigation. Here, either density functional based methods or wavefunction based methods are usually considered. Density functional theory (DFT) or more specifically, its time-dependent extension, has been successfully applied for the description of X-ray experiments in many molecular systems.[13–15] Although, care must be taken as these results are often highly sensitive to the choice of the approximate density functional employed.[16–18] On the other hand, wavefunction based methods usually carry an inherent high computational complexity, which limits these approaches to only simple systems. If molecules of sizes typically encountered in most everyday applications are to be examined, derived low-cost methods are needed. However, these often rely on a favourable cancellation of errors.[19–21] An alternative third category are the Green's function based methods, introduced in the context of many-body perturbation theory. In particular, the Bethe-Salpeter equation (BSE), in combination with the quasiparticle energies obtained within the *GW* approximation, has been shown to provide a reasonable alternative to DFT based methods for the description of excited states in recent years. This approach has been demonstrated to improve in areas, where common density functional approximations tend to struggle.[22–26] However, the studies were mostly limited

to the description of valence excitations and its performance regarding core-excited states has seen less attention. As such, it is yet to be thoroughly assessed. A key feature of the *GW* method, is its ability to provide reasonable approximations to electron binding energies and electron affinities not only for valence states, but also for the energetically low-lying core electrons. In the latter case, the popular ΔSCF based methods, where the ionization potentials are obtained as differences between self-consistent (ground) states, have to account for the variational collapse during the self-consistent optimization, and become less straightforward in their application.[27–29] Having access to quasiparticle energies for these states, enables the evaluation of excitation energies of core electrons by employing the Bethe-Salpeter equation. This equation is used to describe the interaction of the hole and particle states accounting for the dielectric screening effects in a system. For most applications, this composite *GW*-BSE approach is used in a perturbative way, as a correction of a density functional or Hartree–Fock reference ground state.

Subject of this thesis is the development and assessment of robust approximations to the *GW*-BSE method within a framework suitable for the description of relativistic effects, including spin-orbit effects. This allows for its use in the study of molecules containing heavy elements and extends the range to low-lying states for systems of sizes typically encountered in most real-life applications.

The further contents of this work are structured as follows: After a brief introduction of the notation in chapter 2, chapter 3 introduces fundamental aspects of single-reference electronic structure and density functional theories for the description of ground and excited states. This is done in the context of a two-component framework. In chapter 4, important concepts of the description of quantum chemical systems using Green's function based methods are discussed and commonly used approximations are introduced. This is followed by common techniques for the evaluation of the quasiparticle energies using the auxiliary subspace representation of the dielectric function are presented in chapter 5 . Here, a frequency sampling extension is proposed, which was developed within this thesis. Different aspects regarding its performance for core and valence states are assessed. Chapter 6 introduces the Bethe-Salpeter formalism, including further developments introduced in the context of this thesis. This encompasses the combination of the damped response formalism, as well as the core-valence separation ansatz with the BSE, which allows for the efficient evaluation of highly excited states. In order to provide a description of the intensities in quantum mechanical methods beyond the electric dipole approximation, chapter 7 discusses the implementation of the gauge-invariant second order oscillator strength for closed-shell systems in a two-component framework, done as part of this thesis. All practical implementations were done in the `TURBOMOLE` program suite.[30–33] Having established a set of tools, the perturbative *GW* method is then examined for various modern density functionals in chapter 8, including local hybrid functionals, for valence and core levels. The study is then extended to the description of charge neutral excitations within the *GW*-BSE method in chapter 9. This included an assessment for molecules, where the correct description of spin-orbit effects is mandatory. The *GW*-BSE method is then applied to two lanthanum compounds in chapter 10, which is followed by a general summary in chapter 11.

2 Notation

We briefly introduce the notation used throughout this thesis in the following.
All quantities, if not stated otherwise, will be given in Hartree atomic units, for which

$$e = 4\pi\epsilon_0 = a_0 = \hbar = m_e = 1, \tag{2.1}$$

where e is the elementary charge, ϵ_0 is the vacuum permittivity, a_0 the Bohr radius, $\hbar$ the reduced Planck constant, and m_e the mass of an electron.
Operators, matrices and vectors will be denoted using bold face letters. As much of the formalism presented in the following will be presented at a two-component level of theory, many of the underlying quantities become (2×2) matrices to account for the different spin blocks. These blocks will be indicated by the generalized momenta α and β, which are related to the common spin indices at the one-component level. If not further elaborated in the text, the quantities are assumed to be diagonal in spin space and the mixed block $\alpha\beta$ and $\beta\alpha$ are assumed to vanish.
To indicate states with respect to the Fermi level, we will adopt a common convention, where occupied states are indicated by the lower case letters,

$$i, j, k, l, \ldots, \tag{2.2}$$

while

$$a, b, c, d, \ldots, \tag{2.3}$$

will be used to for unoccupied (virtual) states states, in most matrix representations.

$$p, q, r, s, \ldots \tag{2.4}$$

are then used for general indices. In chapter 4, we will briefly use the capital letters,

$$I, A, M, \ldots, \tag{2.5}$$

to indicate many-electron states. For the rest of this thesis, capital letters, such as $P, Q, \ldots$, will be used to indicate auxiliary basis functions. Any deviation of this will be specifically indicated in the text.
Two-electron integrals will be represented using the standard Dirac notation. The 4-center Coulomb integrals can thus be written as

$$\langle pq|rs\rangle = \iint \Phi_p^*(\boldsymbol{r}_1)\Phi_q^*(\boldsymbol{r}_2)\frac{1}{|\boldsymbol{r}_1-\boldsymbol{r}_2|}\Phi_r(\boldsymbol{r}_1)\Phi_s(\boldsymbol{r}_2) = (pr|qs). \tag{2.6}$$

The real and imaginary contributions of matrices and operators will be denoted as $\mathfrak{Re}\left[\boldsymbol{O}\right]$ and $\mathfrak{Im}\left[\boldsymbol{O}\right]$, respectively, where $\boldsymbol{O}$ is an arbitrary operator or matrix.

3 Fundamental Concepts in Relativistic Density Functional Theory

This chapter aims at giving a brief summary of methods commonly used for the description of molecular systems in ground and excited states. The underlying concepts are discussed in order to establish a suitable framework for the inclusion of spin-orbit coupling (SOC) effects, as they become increasingly important when considering molecules containing heavy elements. To this end the formalism is based on the Dirac equation instead of the Schrödinger equation. The former is invariant with respect to a Lorentz transformation, a strict requirement to be able to agree with the principle of special relativity.[34] The Dirac equation offers a concise way of introducing not only SOC, but also scalar-relativistic effects and intrinsically includes the spin of an electron.[35] However, the structure of the Dirac equation requires the wavefunction to feature four distinct components, making it a 4-spinor.[12] It does not only describe electronic states, but also states associated with the positron. This greatly increases the complexity of even simple problems such as the hydrogen atom.[12] Many applications circumvent this issue by introducing effective core potentials (ECPs), which directly incorporate scalar-relativistic effects and can even be used to model SOC.[36] However, the description of SOC effects requires at least a two-component formalism, as it is intrinsically tied to the structure of the SOC operator.[37]

In this thesis, we will be mostly concerned with properties regarding core electrons, more specifically core-electron binding energies (CEBEs) and core-excited states (CESs), which may be used to predict and complement experimental techniques such as X-ray photoelectron spectroscopy (XPS) and X-ray absorption spectroscopy (XAS). Since ECPs replace the inner shell structure of an atom by a pseudo-potential, they cannot be employed for this purpose. In general, relativistic effects are far larger for core electrons. For example, SOC splits the $2p$ state of lanthanum by several hundred eVs and cannot be disregarded easily.[38] In order to provide an adequate description of relativistic effects without attempting the solution of the full four-component Dirac equation, the exact two-component (X2C) theory is applied. This technique allows for the decoupling of the positronic and electronic states, requiring only two-component spinors, which is similar to the effort associated with SOC-ECPs and the Pauli equation.[39] While an extensive discussion regarding relativistic effects in quantum chemistry and the typical approximations is far beyond the scope of this thesis, some key aspects of the fundamental theories will be briefly discussed, for more elaborate overviews, the reader is referred to refs. 40, 41 and 12. Furthermore, the systems for which SOC will be considered here, are generally closed-shell systems in the absence of (external) magnetic fields. As such, these systems feature a symmetry somewhat similar to what is observed for closed-shell system in a non-relativistic framework, the so-called Kramers- or time-reversals symmetry. This concept will be briefly discussed, as all implementations presented in the following chapters strictly assume this symmetry if SOC effects are considered. The two-component formalism will be shortly discussed in the context of self-consistent field theories and density functional theory. Lastly, linear response theory in its regular and its damped formulations will be presented, which not only allows for the calculation of (dynamic) response properties, but will also be used in later chapters for the description of the polarizability in Green's function based methods and the damped formulation of the Bethe-Salpeter equation.

3.1 Quasirelativistic Methods in Quantum Chemistry

In relativistic quantum chemistry, it is often convenient to distinguish between scalar- and spin-orbit effects. Here, the Schrödinger equation does not offer a suitable starting points, as it does not account for any of these effects, which can only be introduced in an heuristic manner. If Einstein's laws of special relativity are to be obeyed, the motion of an free electron may instead be best described in the context of the Dirac equation.[34] This equation offers a more general framework consistent with the requirements of special relativity.[35] It takes a form reminiscent of the time-dependent Schrödinger equation and reads

$$i\frac{\partial}{\partial t}\boldsymbol{\Psi} = \left(c\boldsymbol{\alpha}\cdot\boldsymbol{p} + \boldsymbol{\beta}c^2\right)\boldsymbol{\Psi}, \tag{3.1}$$

where $\boldsymbol{p}$ is the linear momentum operator, c is the speed of light ($\approx 137\ a_0 E_h/\hbar$ in atomic units) and $\boldsymbol{\alpha}$ is a vector. The elements of this vector and $\boldsymbol{\beta}$ are (4×4) super-matrices defined by

$$\boldsymbol{\alpha} = (\boldsymbol{\alpha}_x\ \ \boldsymbol{\alpha}_y\ \ \boldsymbol{\alpha}_z)^T \quad \text{with} \quad \boldsymbol{\alpha}_i = \begin{pmatrix} \mathbf{0}_2 & \boldsymbol{\sigma}_i \\ \boldsymbol{\sigma}_i & \mathbf{0}_2 \end{pmatrix} \quad \text{for} \quad i\in\{x,y,z\} \quad \text{and} \quad \boldsymbol{\beta} = \begin{pmatrix} \mathbf{1}_2 & 0 \\ 0 & -\mathbf{1}_2 \end{pmatrix} \tag{3.2}$$

where $\mathbf{1}_2$ is the (2×2) identity matrix and $\boldsymbol{\sigma}_i$ are the Pauli spin matrices

$$\boldsymbol{\sigma}_x = \begin{pmatrix} 0 & 1 \\ 1 & 0 \end{pmatrix},\ \boldsymbol{\sigma}_y = \begin{pmatrix} 0 & -i \\ i & 0 \end{pmatrix},\ \boldsymbol{\sigma}_z = \begin{pmatrix} 1 & 0 \\ 0 & -1 \end{pmatrix}. \tag{3.3}$$

As stated before, the Dirac equation intrinsically accounts for the spin angular momentum of the electrons. In addition to the positive energy spectrum, the solutions also include a complementary negative energy spectrum. These are associated with the anti-particle of the electron, the positron.[41–45] The super-matrix structure of $\boldsymbol{\alpha}$ and $\boldsymbol{\beta}$ increase the dimension of the wavefunction, which requires the use of a 4-spinor, which is written as

$$\boldsymbol{\Psi}(\boldsymbol{r},t) = \begin{pmatrix} \psi^1(\boldsymbol{r},t) \\ \psi^2(\boldsymbol{r},t) \\ \psi^3(\boldsymbol{r},t) \\ \psi^4(\boldsymbol{r},t) \end{pmatrix} = \begin{pmatrix} \boldsymbol{\psi}^{\mathrm{L}}(\boldsymbol{r},t) \\ \boldsymbol{\psi}^{\mathrm{S}}(\boldsymbol{r},t) \end{pmatrix}. \tag{3.4}$$

These components are usually collected in the two-component *large* and *small* spinors, $\boldsymbol{\psi}^{\mathrm{L}}$ and $\boldsymbol{\psi}^{\mathrm{S}}$. This designation is derived from the positive energy spectrum for which $\boldsymbol{\psi}^{\mathrm{L}}$ is far larger than $\boldsymbol{\psi}^{\mathrm{S}}$ by a factor roughly the speed of light in the limit of large $\boldsymbol{r}$. For an electron moving in a static potential, $\boldsymbol{V}$, the time-dependence can be conveniently separated and the Dirac equation takes a time-independent form. An analogues procedure, used in order to obtain the static Schrödinger equation, results in

$$\begin{pmatrix} \boldsymbol{V} & c\boldsymbol{\sigma}\cdot\boldsymbol{p} \\ c\boldsymbol{\sigma}\cdot\boldsymbol{p} & \boldsymbol{V} - 2c^2\mathbf{1}_2 \end{pmatrix} \begin{pmatrix} \boldsymbol{\psi}^L \\ \boldsymbol{\psi}^S \end{pmatrix} = E \begin{pmatrix} \boldsymbol{\psi}^L \\ \boldsymbol{\psi}^S \end{pmatrix} \quad \text{with} \quad \boldsymbol{V} = \begin{pmatrix} V & 0 \\ 0 & V \end{pmatrix} \quad \text{and} \quad \boldsymbol{\psi}(\boldsymbol{r},t) \to \boldsymbol{\psi}(\boldsymbol{r}), \tag{3.5}$$

where the left-hand side is just the Dirac-Hamiltonian acting on the large and small components, while E are the energy-eigenvalues. We choose to shift the energy spectrum for it to coincide with the non-relativistic limit, by subtracting the rest

mass of the electron. For most quantum chemical systems, the energies encountered are far below the pair-creation threshold and therefore it is usually sufficient to only consider the positive energy spectrum. It is therefore desirable to instead derive and work in a quasirelativistic framework, which only describes these electronic states. One could argue as to work with the Pauli Hamiltonian instead, which already incorporates relativistic effects without any reference to postironic states.[39] However, using the Pauli Hamiltonian is rather limiting as it is highly singular and is generally unsuitable for variational calculations.[40] Therefore, other methods are applied in order to extract the positive energy spectrum, reducing the dimension of $\mathbf{\Phi}$ in eq. 3.4. Comprehensive reviews and extensive discussions of these methods can be found in the literature, see refs. 41, 44, 46, and 45. Here, we will only briefly discuss some of the fundamental ideas in order to motivate these techniques, more specifically the exact two-component theory.

Foldy and Wouthuysen suggested a decoupling scheme based on a unitary transformation, which may be written as[47]

$$\boldsymbol{U}^\dagger \boldsymbol{h}^{4c} \boldsymbol{U} = \begin{pmatrix} \boldsymbol{h}^+ & \mathbf{0}_2 \\ \mathbf{0}_2 & \boldsymbol{h}^- \end{pmatrix} \quad \text{with} \quad \boldsymbol{U}^\dagger \boldsymbol{U} = \mathbf{1}_4, \tag{3.6}$$

where the four-component Dirac-operator $\boldsymbol{h}^{4c}$ in eq. 3.5 is brought into block-diagonal structure. The diagonal blocks $\boldsymbol{h}^+$ and $\boldsymbol{h}^-$ are associated with the positive and negative energy spectrum, respectively. Since the primary interest are the electronic states, only the former part needs to be considered, resulting in what is called a quasirelativistic two-component framework, in contrast to the fully relativistic four-component framework. In the static Dirac equation, the large and small components are related by the operator $\boldsymbol{X}$, which can be written as[44,48,49]

$$\Psi^S = \boldsymbol{X} \Psi^L \quad \text{with} \quad \boldsymbol{X} = \frac{1}{2c^2 - \boldsymbol{V}} \left(c\boldsymbol{\sigma} \cdot \boldsymbol{p} - [\boldsymbol{X}, \boldsymbol{V}] - \boldsymbol{X} \left(c\boldsymbol{\sigma} \cdot \boldsymbol{p} \right) \boldsymbol{X} \right). \tag{3.7}$$

For the unitary operator in eq. 3.6 follows[48]

$$\boldsymbol{U} = \begin{pmatrix} \frac{1}{\sqrt{1+\boldsymbol{X}^\dagger \boldsymbol{X}}} & \frac{-\boldsymbol{X}^\dagger}{\sqrt{1+\boldsymbol{X}^\dagger \boldsymbol{X}}} \\ \frac{\boldsymbol{X}^\dagger}{\sqrt{1+\boldsymbol{X}^\dagger \boldsymbol{X}}} & \frac{1}{\sqrt{1+\boldsymbol{X}^\dagger \boldsymbol{X}}} \end{pmatrix}, \tag{3.8}$$

where aside from the transformation of the large and small components, a renormalization is carried out. However, $\boldsymbol{X}$, in the form presented in eq. 3.7, is highly singular, even if the two-electron interaction is neglected and the resulting two-component Hamiltonian can quickly become unstable.[49] These problems can be avoided by directly working with the matrix representations in a finite basis, instead of working with these quantities at the operator level. This follows the initial works of Dyall for the normalized elimination of the small component (NESC),[50–53] which already introduces many aspects of modern X2C theory.[40,44,54–58] As the X2C approach is used in many calculations throughout this thesis, we will briefly reiterate the basic ideas in the following.[40,44,54–57] In the non-relativistic limit, the large and small components are related by the kinetic balance condition,[59]

$$\boldsymbol{\psi}^{\mathrm{S}} = \frac{\boldsymbol{\sigma} \cdot \boldsymbol{p}}{2c} \boldsymbol{\psi}^{\mathrm{L}}. \tag{3.9}$$

In this limit, the positronic and electronic states can be decoupled exactly. By expansion of the large and small components in a basis of one-particle functions, in a way that incorporates eq. 3.9, we may work in the matrix representation of the static Dirac equation, eq. 3.5, and solve the one-electron problem including the external potential at the full four-component level. Note that the interaction of the electrons with each other is not considered, and linear dependencies have to be taken care of.

The resulting generalized matrix eigenvalue problem can be efficiently solved using standard techniques, for which we obtain the eigenvalues, $\boldsymbol{E}_{\pm}$, and eigenvectors, $\boldsymbol{C}_{\pm}$. The operator equation in eq. 3.7 is replaced by a simple matrix or vector identity. By considering the expansion coefficients of the spinors, the small component is effectively eliminated using

$$\boldsymbol{\psi}^{\mathrm{S}} = \boldsymbol{X}\boldsymbol{\psi}^{\mathrm{L}} \longrightarrow \boldsymbol{C}_{+}^{\mathrm{S}} = \boldsymbol{X}\boldsymbol{C}_{+}^{\mathrm{L}} \quad \text{with} \quad \boldsymbol{X} = \boldsymbol{C}_{+}^{\mathrm{S}} \left(\boldsymbol{C}_{+}^{\mathrm{L}}\right)^{-1}. \tag{3.10}$$

$\boldsymbol{X}$ is then the matrix representation of the decoupling operator in eq. 3.7, which is expressed using the eigenvectors of the positive and negative energy solutions. The two-electron interaction in principle should be transformed in a similar manner. This however, would require a computational effort comparable with the full solution of the four-component problem, making it impractical. Incorporating special relativity directly in the two-electron interaction is particularly difficult. While approximate operators to the true relativistic two-electron interaction exist, such as the Coulomb-Breit operator, these are mostly limited to small model sized systems, often in the context of perturbation theory and are not considered here.[60] Instead the bare two-electron Coulomb interaction is used and added afterwards, where the relativistic corrections can be accounted for in an approximate manner.[61–63] Aside from the X2C approach, alternative decoupling techniques are given by the zeroth-(or higher-)order regular approximation (ZORA)[64–67], the Douglas-Kroll-Hess (DKH)[12,68–74] method or the approach by Barysz, Sadlej, and Snijders (BSS)[75,76], but were not used in the context of this thesis and as such are not further discussed.

3.2 Self-Consistent Field Theory in Quasirelativistic Two-Component Methods

Assuming a quasirelativistic two-component Hamiltonian has been obtained, either in the context of X2C theory or similar methods, the static Dirac equation can be brought into the form of a two-dimensional super-matrix eigenvalue problem. For an N-electron system, the wavefunction may be represented by a Slater determinant,

$$\Psi(\boldsymbol{r}_1, \boldsymbol{r}_2, \ldots, \boldsymbol{r}_N) \approx \Psi_{\mathrm{SD}}(\boldsymbol{r}_1, \boldsymbol{r}_2, \ldots, \boldsymbol{r}_N) = \frac{1}{\sqrt{N}} \det\left[\boldsymbol{\Phi}_1(\boldsymbol{r}_1) \otimes \boldsymbol{\Phi}_2(\boldsymbol{r}_2) \otimes \cdots \otimes \boldsymbol{\Phi}_N(\boldsymbol{r}_N)\right], \tag{3.11}$$

where $\boldsymbol{\Phi}$ are one-particle functions. Due to the structure of the off-diagonal blocks, these functions are required to be complex and two-dimensional. The two-component spinors read

$$\boldsymbol{\Phi}_{p\sigma}(\boldsymbol{r}) = \begin{pmatrix} \phi_{p\sigma}^{\alpha}(\boldsymbol{r}) \\ \phi_{p\sigma}^{\beta}(\boldsymbol{r}) \end{pmatrix} \quad \text{with} \quad \sigma \in \{\alpha, \beta\}. \tag{3.12}$$

α and β the Kramers-indices or generalized momenta. Both momenta are coupled via the off-diagonal blocks of the quasirelativistic Hamiltonian. By neglecting the SOC terms, the Kramers-indices reduce to the regular spin-indices known from non-relativistic theory and the spinors can be chosen to be real and only contain α or β blocks, resulting in

$$\boldsymbol{\Phi}_{p\sigma}(\boldsymbol{r}) = \begin{pmatrix} \phi_{p\sigma}^{\alpha}(\boldsymbol{r}) \\ \phi_{p\sigma}^{\beta}(\boldsymbol{r}) \end{pmatrix} \longrightarrow \boldsymbol{\Phi}_{p\alpha}(\boldsymbol{r}) = \begin{pmatrix} \phi_{p\alpha}^{\alpha}(\boldsymbol{r}) \\ 0 \end{pmatrix} \quad \text{and} \quad \boldsymbol{\Phi}_{p\beta}(\boldsymbol{r}) = \begin{pmatrix} 0 \\ \phi_{p\beta}^{\beta}(\boldsymbol{r}) \end{pmatrix}, \tag{3.13}$$

where $\phi_{\alpha}^{\alpha}(\boldsymbol{r})$ and ϕ_{β}^{β} are spinorbitals. The generalized canonical Hartree–Fock equations[77,78] may be derived in an analogues fashion as is done in regular theory. They resemble the non-relativistic analogues and read[46,79,80]

$$\boldsymbol{F}_p \left|\boldsymbol{\Phi}'_p\right\rangle = \epsilon_p \left|\boldsymbol{\Phi}'_p\right\rangle, \tag{3.14}$$

where $\boldsymbol{F}_p$ is the complex Hermitian (quasi-)relativistic Fock-Operator, $\boldsymbol{\Phi}'$ are the spinors in canonical Hartree–Fock basis and ϵ are the real eigenvalues. The spinors in eq. 3.14 can be expanded in a basis of of real-valued atom-centered cartesian one-electron functions, as long as external magnetic fields are not considered. This is the LCAO-ansatz at the two-component level.[37,81,82] The eigenfunctions are expandend according to

$$\boldsymbol{\Phi}_{p\sigma}(\boldsymbol{r}) = \begin{pmatrix} \phi^{\alpha}_{p\sigma}(\boldsymbol{r}) \\ \phi^{\beta}_{p\sigma}(\boldsymbol{r}) \end{pmatrix} = \sum_{\mu}^{N_{\text{basis}}} \begin{pmatrix} c^{\alpha}_{p\sigma,\mu} \\ c^{\beta}_{p\sigma,\mu} \end{pmatrix} \varphi_{\mu}(\boldsymbol{r}), \tag{3.15}$$

where φ are real atom-centered basis functions. Using the above expansion, the generalized-complex Roothaan-Hall equations can be derived, which read[79]

$$\boldsymbol{FC} = \boldsymbol{SC}\boldsymbol{\epsilon}. \tag{3.16}$$

Here, $\boldsymbol{F}$ is the Fock matrix, $\boldsymbol{C}$ collects the expansion coefficients, $\boldsymbol{S}$ is the overlap and $\boldsymbol{\epsilon}$ are the eigenvalues. The Fock-operator can be written as to indicate the structure of the one- and two-electron terms with respect to the spin blocks which becomes[81,82]

$$\boldsymbol{F} = \begin{pmatrix} \boldsymbol{h}^0 + \boldsymbol{h}^z_{\text{SO}} & \boldsymbol{h}^x_{\text{SO}} - i\boldsymbol{h}^y_{\text{SO}} \\ \boldsymbol{h}^x_{\text{SO}} + i\boldsymbol{h}^y_{\text{SO}} & \boldsymbol{h}^0 - \boldsymbol{h}^z_{\text{SO}} \end{pmatrix} + \begin{pmatrix} \boldsymbol{J} - \boldsymbol{K}^{\alpha\alpha} & -\boldsymbol{K}^{\alpha\beta} \\ -\boldsymbol{K}^{\beta\alpha} & \boldsymbol{J} - \boldsymbol{K}^{\beta\beta} \end{pmatrix}. \tag{3.17}$$

$\boldsymbol{h}^0$ contains the one-electron terms, including contributions from scalar-relativistic effects and $\boldsymbol{h}^i$ with $i \in \{x, y, z\}$ are the spin-orbit contributions. $\boldsymbol{J}$ and $\boldsymbol{K}$ are the Coulomb- and exchange-contributions, respectively, defined as

$$\begin{aligned} \langle \Phi_{q\tau} | \boldsymbol{J}_{p\sigma} | \Phi_{q\tau} \rangle &= \langle p\sigma q\tau | p\sigma q\tau \rangle \\ \langle \Phi_{q\tau} | \boldsymbol{K}_{p\sigma} | \Phi_{q\tau} \rangle &= \langle p\sigma q\tau | q\tau p\sigma \rangle . \end{aligned} \tag{3.18}$$

$\boldsymbol{J}$ is diagonal in spin space, and as such only features non-zero contributions for the $\alpha\alpha$ and $\beta\beta$ blocks, while the Hartree–Fock-exchange term, $\boldsymbol{K}$, can additionally feature contributions for all spin blocks. By neglecting the spin-orbit terms in eq. 3.17, the spin-components are decoupled and the spinors may be chosen according to eq. 3.13 from which the scalar-relativistic equations can be extracted.

3.3 Kramers' Time Reversal Symmetry

In the quasirelativistic framework, the two-components are generally coupled if SOC effects are considered. Therefore, closed-shell systems do not provide the same symmetry with respect to the electron spin, as is commonly used at the non-relativistic (one-component) level. Instead a similar and more general symmetry can be used, as long as magnetic fields are ignored. To this end, consider the anti-unitary operator, $\boldsymbol{K}$, given by[83]

$$\boldsymbol{K} = -i\boldsymbol{\sigma}_y \boldsymbol{K}_0, \tag{3.19}$$

where $\boldsymbol{\sigma}_y$ is just one of the Pauli spin matrices in eq. 3.3 and $\boldsymbol{K}_0$ performs a complex conjugation. $\boldsymbol{K}$ is called the time-reversal operator and can be used to relate two states in the absence of magnetic fields of a closed-shell system. This operator applied to a state $\boldsymbol{\Phi}_p$ results in a new state $\bar{\boldsymbol{\Phi}}_p$, following the relation

$$\boldsymbol{K}\boldsymbol{\Phi}_{p\sigma} = \boldsymbol{K}\begin{pmatrix}\phi^{\alpha}_{p\sigma}\\ \phi^{\beta}_{p\sigma}\end{pmatrix} = \begin{pmatrix}-\left(\phi^{\beta}_{p\sigma}\right)^*\\ \left(\phi^{\alpha}_{p\sigma}\right)^*\end{pmatrix} = \bar{\boldsymbol{\Phi}}_{p\sigma} \quad \text{and} \quad \boldsymbol{K}\bar{\boldsymbol{\Phi}}_{p\sigma} = -\boldsymbol{\Phi}_{p\sigma}. \tag{3.20}$$

The states $\boldsymbol{\Phi}_{p\sigma}$ and $\bar{\boldsymbol{\Phi}}_{p\sigma}$ are said to form a Kramers pair and have degenerate eigenvalues. For quantum chemical systems exhibiting time-reversal symmetry all states occur pair-wise, obeying the above relation and are either both occupied or unoccupied. This property readily applies not only at the two-component, but also at the four-component level.[84,85] Assuming time-reversal symmetry the Hamiltonian operator commutes with $\boldsymbol{K}$, that is

$$[\boldsymbol{H}, \boldsymbol{K}] = 0 \Longleftrightarrow \boldsymbol{K}\boldsymbol{H}\boldsymbol{K}^{-1} = \boldsymbol{H}, \tag{3.21}$$

as does the Fock operator. The similarity transformed Fock matrix from eq. 3.17 becomes[86,87]

$$\boldsymbol{K}\begin{pmatrix}\boldsymbol{F}^{\alpha\alpha} & \boldsymbol{F}^{\beta\alpha}\\ \boldsymbol{F}^{\alpha\beta} & \boldsymbol{F}^{\beta\beta}\end{pmatrix}\boldsymbol{K}^{-1} = \begin{pmatrix}\boldsymbol{F}^{\beta\beta} & -\boldsymbol{F}^{\alpha\beta}\\ -\boldsymbol{F}^{\beta\alpha} & \boldsymbol{F}^{\alpha\alpha}\end{pmatrix}, \tag{3.22}$$

for which the matrix elements can be related according to[71,86]

$$\boldsymbol{F}^{\alpha\alpha} = \boldsymbol{F}^{\beta\beta}, \;\; \boldsymbol{F}^{\alpha\beta} = -\left(\boldsymbol{F}^{\beta\alpha}\right)^* \quad \text{and} \quad \boldsymbol{F}^{\beta\alpha} = -\left(\boldsymbol{F}^{\alpha\beta}\right)^*, \tag{3.23}$$

where $\boldsymbol{F}^{\alpha\alpha}$ is Hermitian and $\boldsymbol{F}^{\alpha\beta}$ is antisymmetric. Since this structure is valid for any operator in time-reversal symmetric systems, the components of the spin-density vanish for every point $\boldsymbol{r}$, greatly simplifying the evaluation of the exchange-correlation potential in density functional theory.[37,81,88] Note that in later chapters, if not stated otherwise, the systems at the two-component level are assumed to be Kramers symmetric. The equations and implementations presented are therefore limited to closed-shell systems if spin-orbit effects are included, while no such limitation is required at the one-component level.

3.4 Aspects of Quasirelativistic Kohn–Sham Density Functional Theory

Density functional theory offers an alternative approach to wavefunction based methods for the description of quantum mechanical systems. Hohenberg and Kohn demonstrated that the total energy of a system may, at least in principle, be described by its total density.[89] The original proof was later shown to be insufficient and has since been reformulated by Levy and Lieb.[90,91] Much of the success of DFT derives from the works of Kohn and Sham,[92–94] who substituted the problematic kinetic energy term by that of a non-interacting reference system. This was done by introducing the idea of auxiliary orbitals, which reproduce the correct density of the fully-interacting system.[95] DFT offers an interesting and flexible starting point,

especially for perturbative approaches like the non-self-consistent Green's function based methods examined in later chapters (see chapters 4 and 5). These concepts have since been extended to the relativistic and quasirelativistic frameworks, a full discussion of which would be far beyond the scope of the current work and are given, for example, in refs. 81, 96, and 37. This section will focus only on selected aspects of DFT, introducing ideas which may be expanded in latter sections in the context of time-dependent theories. In analogy to the formulation in a non-relativistic one-component level, the (static) quasirelativistic Kohn–Sham equations take the form of an eigenvalue problem, given by

$$\boldsymbol{F}_p^{\mathrm{KS}} \left|\boldsymbol{\Phi}_p\right\rangle = \epsilon_p^{\mathrm{KS}} \left|\boldsymbol{\Phi}_p\right\rangle , \tag{3.24}$$

where $\boldsymbol{F}^{\mathrm{KS}}$ is a Fock-like operator, including the exchange-correlation potential instead of the Hartree–Fock-exchange term. The one-particle density matrix, $\boldsymbol{\gamma}$, of an N-electron system can be calculated using the Kohn–Sham spinors according to[82]

$$\boldsymbol{\gamma}(\boldsymbol{r}_1, \boldsymbol{r}_2) = \sum_i^N \boldsymbol{\Phi}(\boldsymbol{r}_1)\boldsymbol{\Phi}^\dagger(\boldsymbol{r}_2) = \begin{pmatrix} \boldsymbol{\gamma}^{\alpha\alpha}(\boldsymbol{r}_1, \boldsymbol{r}_2) & \boldsymbol{\gamma}^{\beta\alpha}(\boldsymbol{r}_1, \boldsymbol{r}_2) \\ \boldsymbol{\gamma}^{\alpha\beta}(\boldsymbol{r}_1, \boldsymbol{r}_2) & \boldsymbol{\gamma}^{\beta\beta}(\boldsymbol{r}_1, \boldsymbol{r}_2) \end{pmatrix} \tag{3.25}$$

and can be separated into the particle number density, n, and the spin magnetization vector, $\boldsymbol{m}$,

$$n(\boldsymbol{r}_1, \boldsymbol{r}_2) = \mathrm{tr}\left(\boldsymbol{\gamma}(\boldsymbol{r}_1, \boldsymbol{r}_2)\right) \quad \text{and} \quad m_i(\boldsymbol{r}_1, \boldsymbol{r}_2) = \mathrm{tr}\left(\boldsymbol{\sigma}_i\boldsymbol{\gamma}(\boldsymbol{r}_1, \boldsymbol{r}_2)\right) \quad \text{with} \quad i \in \{x, y, z\}, \tag{3.26}$$

where $\boldsymbol{\sigma}_{x,y,z}$ are the Pauli spin matrices introduced in eq. 3.3. In contrast to the non-relativistic one-component framework, the exchange-correlation potential, $\boldsymbol{V}_{\mathrm{xc}}$, now includes additional contributions from the spin-densities. The potential becomes

$$\boldsymbol{V}_{\mathrm{xc}}(\boldsymbol{r}) = \frac{\delta E_{\mathrm{xc}}(\boldsymbol{r})}{\delta n(\boldsymbol{r})}\mathbf{1}_2 + \sum_i \boldsymbol{\sigma}_i \frac{\delta E_{\mathrm{xc}}(\boldsymbol{r})}{\delta m_i(\boldsymbol{r})} \quad \text{for} \quad \boldsymbol{r} = \boldsymbol{r}_1 = \boldsymbol{r}_2. \tag{3.27}$$

Here, E_{xc} is the exchange-correlation energy functional. The second term reproduces the spin-density terms in the non-relativistic limit.[82] If the system is Kramers symmetric, the spin-density vanishes, except for $\mathfrak{Im}\left[m_z\right]$ and the exchange-correlation potential in eq. 3.27 becomes diagonal, assuming no Hartree–Fock exchange is included.[81]

3.5 Time-Dependent Kohn–Sham Equations and Linear Response Theory

While the Hohenberg-Kohn theorems establish a formal basis for the description of static quantum chemical systems, this prove needs to be extended in order to apply it to the time-dependent domain.[89] This addition is usually associated with Runge and Gross, who presented a way to establish an one-to-one correspondence between the time-dependent density and the potential of an electronic system.[97,98] It should be noted, that the initial prove given in ref. 97 is incomplete and can lead to a causality violation in later expressions. This was later resolved independently by van Leeuwen using the Keldysh formalism[99–101] and Vignale[102,103], who pointed out an error in the boundary considerations of the action integral. The extension to the relativistic framework was given by Rajagopal.[104] According to these results, the time-dependence of an N-electron system in the context of Kohn–Sham-DFT is governed by the time-dependent Kohn–Sham equations, which take the form of effective one-particle equations:

$$i\frac{\partial}{\partial t}\left|\boldsymbol{\Phi}(\boldsymbol{r}, t)\right\rangle = \boldsymbol{F}^{\mathrm{KS}} \left|\boldsymbol{\Phi}(\boldsymbol{r}, t)\right\rangle . \tag{3.28}$$

$\boldsymbol{\Phi}(\boldsymbol{r},t)$ are time-dependent spinors and $\boldsymbol{F}^{\mathrm{KS}}$ is the (quasirelativistic) Kohn–Sham operator, given by

$$\boldsymbol{F}^{\mathrm{KS}} = \boldsymbol{h} + \boldsymbol{V}^{\mathrm{KS}}[\boldsymbol{\gamma}](t) \quad \text{with} \quad \boldsymbol{V}^{\mathrm{KS}}[\boldsymbol{\gamma}](t) = \boldsymbol{V}_{\mathrm{ext}}(\boldsymbol{r},t) + \boldsymbol{V}_{\mathrm{H}}[\mathrm{tr}\,(\boldsymbol{\gamma})](\boldsymbol{r},t) + \boldsymbol{V}_{\mathrm{xc}}[\boldsymbol{\gamma}](\boldsymbol{r},t), \tag{3.29}$$

where $\boldsymbol{h}$ collects quasirelativistic Dirac-Hartree–Fock-like one-electron terms and $\boldsymbol{V}^{\mathrm{KS}}$ is the Kohn–Sham potential, which contains the external potential, $\boldsymbol{V}_{\mathrm{ext}}$, as well as the Hartree and exchange-correlation potentials, $\boldsymbol{V}_{\mathrm{H}}$ and $\boldsymbol{V}_{\mathrm{xc}}$. In X2C theory, these equations need to be directly written in their matrix representations of the operators instead. However, the following considerations remain unaffected. The external potential includes the perturbative scalar time-dependent potential, $\boldsymbol{U}$, which is diagonal in spin space, such that

$$\begin{aligned} \boldsymbol{V}_{\mathrm{ext}}(\boldsymbol{r},t) &= \boldsymbol{V}^{(0)}_{\mathrm{ext}}(\boldsymbol{r}) + \boldsymbol{V}^{(1)}_{\mathrm{ext}}(\boldsymbol{r},t) \\ &= \boldsymbol{V}^{(0)}_{\mathrm{ext}}(\boldsymbol{r}) + \boldsymbol{U}(\boldsymbol{r},t). \end{aligned} \tag{3.30}$$

From eq. 3.28 it follows that the time evolution of the one-electron density is governed by the Liouville–von Neumann equation[105,106]

$$i\frac{\partial}{\partial t}\boldsymbol{\gamma}(\boldsymbol{r},t) = \left[\boldsymbol{F}^{\mathrm{KS}}, \boldsymbol{\gamma}(\boldsymbol{r},t)\right] \quad \text{with} \quad \boldsymbol{\gamma}(\boldsymbol{r},t) = \boldsymbol{\gamma}(\boldsymbol{r},\boldsymbol{r},t). \tag{3.31}$$

While this problem can in principle be solved in real-time using propagator methods,[107,108] it is more convenient to instead work in frequency-space directly and solve the problem within the context of response theory. Many properties correspond to small perturbations and are already well represented by considering only the linear density response. The response equations can be arrived by expanding the density and the Kohn–Sham or Fock operator in a Taylor series. The density then becomes

$$\boldsymbol{\gamma} = \boldsymbol{\gamma}^{(0)} + \boldsymbol{\gamma}^{(1)} + \boldsymbol{\gamma}^{(2)} + ... \tag{3.32}$$

The linear response is extracted by inserting eq. 3.32 into eq. 3.31 and only considering the terms first order in the perturbation. The Lehmann representation of the linear response equation is then given by

$$\omega\boldsymbol{\gamma}^{(1)} = \left[\boldsymbol{F}^{\mathrm{KS}(1)}, \boldsymbol{\gamma}^{(0)}\right] + \left[\boldsymbol{F}^{\mathrm{KS}(0)}, \boldsymbol{\gamma}^{(1)}\right], \tag{3.33}$$

where the arguments were dropped for clarity. The above equation can be solved by evaluating the commutator expression and introducing a suitable expansion for the first order density response. $\boldsymbol{\gamma}^{(1)}$ can also be expressed using the response function of the non-interacting reference system, $\boldsymbol{\chi}^{\mathrm{KS}}$, which is

$$\boldsymbol{\gamma}^{(1)}(\mathbf{1}) = \int \boldsymbol{\chi}^{\mathrm{KS}}(\mathbf{1},\mathbf{2})\boldsymbol{V}^{\mathrm{KS}(1)}(\mathbf{2})\mathrm{d}\mathbf{2} \quad \text{with} \quad \mathbf{1} = (\boldsymbol{r}_1, t_1). \tag{3.34}$$

The response function of the KS reference system has a well-known spectral representation, derived from time-dependent perturbation theory and reads[98,109,110]

$$\boldsymbol{\chi}^{\mathrm{KS}}(\boldsymbol{r}_1,\boldsymbol{r}_2,\omega)=\sum_a\sum_i\left(\frac{\boldsymbol{\Phi}_i^*(\boldsymbol{r}_1)\boldsymbol{\Phi}_a(\boldsymbol{r}_1)\boldsymbol{\Phi}_a^*(\boldsymbol{r}_2)\boldsymbol{\Phi}_i(\boldsymbol{r}_2)}{\omega-\epsilon_a+\epsilon_i+i\eta}-\frac{\boldsymbol{\Phi}_a^*(\boldsymbol{r}_1)\boldsymbol{\Phi}_i(\boldsymbol{r}_1)\boldsymbol{\Phi}_i^*(\boldsymbol{r}_2)\boldsymbol{\Phi}_a(\boldsymbol{r}_2)}{\omega+\epsilon_a-\epsilon_i+i\eta}\right). \tag{3.35}$$

Here, ϵ are the Kohn–Sham eigenvalues and η is a infinitesimal positive parameter. The density response in eq. 3.34 can also be written using the response function of the fully interacting system, given by

$$\boldsymbol{\gamma}^{(1)}(\mathbf{1})=\int\boldsymbol{\chi}(\mathbf{1},\mathbf{2})\boldsymbol{V}^{(1)}(\mathbf{2})\mathrm{d}\mathbf{2}, \tag{3.36}$$

where $\boldsymbol{V}^{(1)}$ is the first order change of the exact potential. The frequency representation of the true response function is given as follows:

$$\boldsymbol{\chi}(\boldsymbol{r}_1,\boldsymbol{r}_2,\omega)=\sum_{m\neq0}\left(\frac{\langle0|\boldsymbol{\rho}(\boldsymbol{r}_1)|m\rangle\langle m|\boldsymbol{\rho}(\boldsymbol{r}_2)|0\rangle}{\omega-(E_m+E_0)+i\eta}-\frac{\langle0|\boldsymbol{\rho}(\boldsymbol{r}_2)|m\rangle\langle m|\boldsymbol{\rho}(\boldsymbol{r}_1)|0\rangle}{\omega+(E_m+E_0)+i\eta}\right). \tag{3.37}$$

E_0 and E_m are the total energies of the ground and excited states and $\boldsymbol{\rho}$ is the density operator. As the frequency approaches any true excitation energy, obtained as the difference between the total energy of excited state m and the ground state energy, the response function becomes singular. In contrast, the Kohn–Sham response function, $\boldsymbol{\chi}^{\mathrm{KS}}$, has poles at the differences of occupied and virtual Kohn–Sham states, which we will later assume to not coincide with the poles of the true response function. Since both response functions can be used to describe the same density response, after some algebraic manipulations, it follows that[111,112]

$$\begin{aligned}\boldsymbol{\chi}(\mathbf{1},\mathbf{2})&=\boldsymbol{\chi}^{\mathrm{KS}}(\mathbf{1},\mathbf{2})+\iint\frac{\delta\boldsymbol{\gamma}(\mathbf{1})}{\delta\boldsymbol{V}^{\mathrm{KS}}(\mathbf{3})}\frac{\delta\boldsymbol{V}^{\mathrm{KS}}(\mathbf{3})}{\delta\boldsymbol{\gamma}(\mathbf{4})}\frac{\delta\boldsymbol{\gamma}(\mathbf{4})}{\delta\boldsymbol{V}_{\mathrm{ext}}(\mathbf{2})}\bigg|_{\boldsymbol{V}_{\mathrm{ext}}[\gamma^{(0)}]}\mathrm{d}\mathbf{4}\mathrm{d}\mathbf{3}\\&=\boldsymbol{\chi}^{\mathrm{KS}}(\mathbf{1},\mathbf{2})+\iint\boldsymbol{\chi}^{\mathrm{KS}}(\mathbf{1},\mathbf{3})\left(\frac{\delta(t_3,t_4)}{|\boldsymbol{r}_3-\boldsymbol{r}_4|}+\boldsymbol{f}_{\mathrm{xc}}(\mathbf{3},\mathbf{4})\right)\boldsymbol{\chi}(\mathbf{4},\mathbf{2})\mathrm{d}\mathbf{4}\mathrm{d}\mathbf{3}\\&\quad\text{with}\quad\boldsymbol{f}_{\mathrm{xc}}(\mathbf{3},\mathbf{4})=\frac{\delta\boldsymbol{V}_{\mathrm{xc}}(\mathbf{3})}{\delta\boldsymbol{\gamma}(\mathbf{4})},\end{aligned} \tag{3.38}$$

where we have repeatedly made use of the chain rule and introduced the exchange-correlation kernel $\boldsymbol{f}_{\mathrm{xc}}$. Eq. 3.38 is the Dyson equation of the response function and connects $\boldsymbol{\chi}$ with $\boldsymbol{\chi}^{\mathrm{KS}}$. This relation may also be used to extract ground state properties and potentials.[98,113,114] As we will see later, the response functions are directly connected to the Green's function, a connection repeatedly used in chapters 4 and 5.[109]

By considering the matrix representations of the above quantities, eq. 3.33 may be recast in the form of an linear system of equations:[115,116]

$$\left[\begin{pmatrix}\boldsymbol{A}&\boldsymbol{B}\\\boldsymbol{B}^*&\boldsymbol{A}^*\end{pmatrix}-\omega\begin{pmatrix}\mathbf{1}&\mathbf{0}\\\mathbf{0}&-\mathbf{1}\end{pmatrix}\right]\begin{pmatrix}\boldsymbol{X}\\\boldsymbol{Y}\end{pmatrix}=-\begin{pmatrix}\boldsymbol{U}\\\boldsymbol{U}^*\end{pmatrix}. \tag{3.39}$$

$\boldsymbol{U}$ contains the matrix elements of the perturbative potential, also called the property gradient.[117] The super-matrix containing $\boldsymbol{A}$ and $\boldsymbol{B}$ is the electronic Hessian, whose elements are

$$\begin{aligned} A_{iajb} &= (\epsilon_a - \epsilon_i)\delta_{ab}\delta_{ij} + \langle ib|aj\rangle + \langle ib|f_{\text{xc}}|aj\rangle \\ B_{iajb} &= \langle ij|ab\rangle + \langle ij|f_{\text{xc}}|ab\rangle \end{aligned} . \tag{3.40}$$

$\boldsymbol{X}$ and $\boldsymbol{Y}$ are the generalized orbital rotation parameters, associated with excitation and de-excitation, and represent the (linear) density response according to[118,119]

$$\begin{aligned} \boldsymbol{\gamma}^{(1)}(\boldsymbol{r}_1, \boldsymbol{r}_2, \omega) &= \sum_a \sum_i \left(\boldsymbol{\Phi}_i^\dagger(\boldsymbol{r}_2)\boldsymbol{\Phi}_a(\boldsymbol{r}_1)\boldsymbol{U}_{ai}^{(1)}(\omega) + \boldsymbol{\Phi}_a^\dagger(\boldsymbol{r}_1)\boldsymbol{\Phi}_i(\boldsymbol{r}_2) \left[\boldsymbol{U}_{ai}^{(1)}(-\omega)\right]^* \right) \\ &= \sum_a \sum_i \left(\boldsymbol{\Phi}_i^\dagger(\boldsymbol{r}_2)\boldsymbol{\Phi}_a(\boldsymbol{r}_1)\boldsymbol{X}_{ai}(\omega) + \boldsymbol{\Phi}_a^\dagger(\boldsymbol{r}_1)\boldsymbol{\Phi}_i(\boldsymbol{r}_2)\boldsymbol{Y}_{ai}(\omega) \right), \end{aligned} \tag{3.41}$$

where $\boldsymbol{U}_{ai}^{(1)}(\omega)$ and $\left[\boldsymbol{U}_{ai}^{(1)}(-\omega)\right]^*$ are Fourier coefficients. The rotations amidst the occupied or the virtual blocks are zero at the linear response level, due to the normalization condition and the idempotency of the density.[119,120] $\boldsymbol{X}$ and $\boldsymbol{Y}$ are normalized according to

$$\begin{pmatrix} \boldsymbol{X}^\dagger & \boldsymbol{Y}^\dagger \end{pmatrix} \begin{pmatrix} \mathbf{1} & 0 \\ 0 & -\mathbf{1} \end{pmatrix} \begin{pmatrix} \boldsymbol{X} \\ \boldsymbol{Y} \end{pmatrix} = \mathbf{1}. \tag{3.42}$$

Eq. 3.39 is equivalent to the Hartree–Fock response equations, where the Hartree–Fock exchange terms is substituted by the exchange-correlation kernel $\boldsymbol{f}_{\text{xc}}$,[121] i.e.,

$$-\langle ib|ja\rangle \rightarrow \langle ib|f_{\text{xc}}|aj\rangle \qquad \text{and} \qquad -\langle ij|ba\rangle \rightarrow \langle ij|f_{\text{xc}}|ab\rangle . \tag{3.43}$$

The exchange-correlation kernel in eqs. 3.38 and 3.40 is not frequency-independent and contains a memory effects with respect to the density at earlier times. This history dependence is usually neglected in what is called the adiabatic approximation. $\boldsymbol{f}_{\text{xc}}$ is thus approximated as to only depend on the instantaneous density and becomes local in time[98,100,122,123] At the two-component level an important issue arises for practical calculations, due to way the spin-magnetization vector may be incorporated. This gives rise to collinear and non-collinear formulations, which have been extensively discussed in the literature and the reader is referred to refs. 124, 125, 126, 127, 128, and 119.

The problem in eq. 3.39 may be recast in the form of a generalized eigenvalue equation oftentimes referred to as Casida's equation. This can be found by explicitly searching for the singularities associated with the true excitations, for which the term in brackets in eq. 3.39 becomes singular.[112,118,129–135] This results in the linear response eigenvalue equations, given by

$$\begin{pmatrix} \boldsymbol{A} & \boldsymbol{B} \\ \boldsymbol{B}^* & \boldsymbol{A}^* \end{pmatrix} \begin{pmatrix} \boldsymbol{X} \\ \boldsymbol{Y} \end{pmatrix} = \omega \begin{pmatrix} \mathbf{1} & 0 \\ 0 & -\mathbf{1} \end{pmatrix} \begin{pmatrix} \boldsymbol{X} \\ \boldsymbol{Y} \end{pmatrix} . \tag{3.44}$$

The size of the electronic Hessian even in the space of singly-excited states in eq. 3.39 and 3.44 requires roughly a computational effort of $\mathcal{O}\left(N^6\right)$ for its solution, where N is a measure of the size of a system. The required memory quickly grows beyond what is available even on modern platforms. Therefore, the equations are solved only approximately, by employing subspace

methods, where only small subset of eigenvalues is extracted, for most applications. Common approaches such as the Jacobi-Davidson algorithm excel at the extraction of the extreme eigenvalues of large eigenvalue problems.[25,115,116,135–138] In chapter 6 a derived technique is discussed, which was implemented in the context of this thesis in order to solve a variant of the linear system presented in eq. 3.39.

3.6 Damped Response Theory

The structure of the linear response equations in eq. 3.39 make them unsuitable to solve for a given frequency region, as they diverge as one approaches any true excitation energy. As mentioned in the previous section, this can be avoided by instead focusing on the extraction of these poles directly and can be done efficiently if only a small subset of eigenvalues is of interest for an application. If one is instead interested in properties associated with interior eigenvalues, these methods become much more involved and sometimes difficult to converge properly.[139–142] An alternative approach is to consider the response of a system in a damped formalism, where one tries to obtain a variant of eq. 3.39, which is regular even at the excitation energies and can be solved for specific frequencies in a stable manner. The explicit extraction of the roots can then be avoided completely, which becomes especially relevant for systems with a high density of states (DOS) or for spectral regions associated with internal eigenvalues of the Casida's equation such as in XAS.[143,144]
The damped response formalism can be derived by modifying the Liouville-von Neumann equation (eq. 3.31), introducing a complex bias term, which then results in[114,120,143–148]

$$i\frac{\partial}{\partial t}\bar{\boldsymbol{\gamma}}(\boldsymbol{r},t) = \left[\boldsymbol{F}^{\mathrm{KS}}, \bar{\boldsymbol{\gamma}}(\boldsymbol{r},t)\right] - i\Gamma\left(\bar{\boldsymbol{\gamma}}(\boldsymbol{r},t) - \boldsymbol{\gamma}_0(\boldsymbol{r})\right), \tag{3.45}$$

where Γ is a damping parameter and controls the rate with which the system drives towards the equilibrium state, $\boldsymbol{\gamma}_0$, in the limit $t \to \infty$. $\boldsymbol{\gamma}_0$ will be taken to be the ground state density, which does not carry an explicit time-dependence, whereas $\bar{\boldsymbol{\gamma}}$ corresponds to the density of the system at time t. $\bar{\boldsymbol{\gamma}}$ can be conveniently split into the static ground state part and the dynamic contribution, according to

$$\bar{\boldsymbol{\gamma}}(\boldsymbol{r},t) = \boldsymbol{\gamma}_0(\boldsymbol{r}) + \boldsymbol{\gamma}_\Gamma(\boldsymbol{r},t), \tag{3.46}$$

where the time-dependence is solely carried in $\boldsymbol{\gamma}_\Gamma(\boldsymbol{r},t)$. It may be written as

$$\boldsymbol{\gamma}_\Gamma(t) = \sum_{m\neq 0} \boldsymbol{\gamma}_m(t)\mathrm{e}^{-\Gamma_m t} \to \mathrm{e}^{-\Gamma t}\sum_{m\neq 0}\boldsymbol{\gamma}_m(t), \tag{3.47}$$

where $\boldsymbol{\gamma}_m$ is the density response associated with the m'th excited state. By setting $\Gamma_m \to \Gamma$ a common lifetime is adopted for all excited states. If only the linear response is of interest, it is sufficient to consider the contributions, mixing occupied and virtual states in the respective matrix representations following eq. 3.41 and incorporating the finite lifetime parameter. Since $\boldsymbol{\gamma}_0$ only contains non-zero in the occupied-occupied block for which it is diagonal, it does not directly couple with the mixed blocks at the linear approximation. The final working equations then can be solved in the occupied-virtual block directly. The damped linear response equations are derived in an analogues manner to the standard linear response equations, where instead of the Fourier transform the Laplace transform is used to include the finite lifetime. The latter is given by

$$\mathcal{L}\left[f(t)\right] = \int f(t)\mathrm{e}^{i\omega t+\Gamma t}\mathrm{d}t \tag{3.48}$$

and results in the damped linear response equations after some algebraic manipulations:

$$\left[\begin{pmatrix} \boldsymbol{A} & \boldsymbol{B} \\ \boldsymbol{B}^* & \boldsymbol{A}^* \end{pmatrix} - (\omega + i\Gamma) \begin{pmatrix} \mathbf{1} & \mathbf{0} \\ \mathbf{0} & -\mathbf{1} \end{pmatrix}\right] \begin{pmatrix} \boldsymbol{X} \\ \boldsymbol{Y} \end{pmatrix} = - \begin{pmatrix} \boldsymbol{U} \\ \boldsymbol{U}^* \end{pmatrix}. \tag{3.49}$$

The matrices $\boldsymbol{A}$ and $\boldsymbol{B}$ are identical to the form given for standard linear response theory in eq. 3.40. The damped response equations differ from the regular linear response equations by frequency argument, which becomes complex, setting

$$\omega \to \bar{\omega} = \omega + i\Gamma. \tag{3.50}$$

As the poles are shifted into the imaginary plane, the damped response equations can be solved for arbitrary real frequencies. The damped response vectors, $\boldsymbol{X}$ and $\boldsymbol{Y}$, are complex quantities at both, the one- and two-component levels. For close-lying states the damped response vectors, obtained as solutions of eq. 3.49, contain contributions from multiple resonances as function of the distance between the associated excitation energies and the damping parameter.[144] $\boldsymbol{X}$ and $\boldsymbol{Y}$ are then used to calculate the complex polarizability, which in turn is used to obtain the absorption cross section, σ, via the isotropic average of its imaginary part. In the electric dipole approximation, this simplifies to

$$\sigma(\omega) = \frac{4\pi\omega}{3c} \mathfrak{Im} \left[\mathrm{tr}\left(\boldsymbol{\alpha}\right)\right]. \tag{3.51}$$

The evaluation of the absorption cross section for a single frequency in the electric dipole approximation requires the solution of the damped linear response equations for all three components of the electric dipole moment individually. At the one-component level the damped response formalism requires the use of complex algebra, increasing the computational effort compared to the standard eigenvalue problem. However, at the two-component level the density is already complex and hence no additional complications compared to the solution of the eigenvalue problem introduced in eq. 3.44.[145,149,150]

4 Green's Function based Methods in Quantum Chemistry

Green's function techniques are a standard tool in the study of inhomogeneous linear differential equations.[151] From a conceptual point, the quantum mechanical Green's function may be associated with the propagation of a particle or hole in time and space. While initially much of the framework was developed in the context of quantum field theory, these methods have since been widely adopted for the description of solids and molecules in quantum chemistry. The central object is the one-particle Green's function. It can be related to properties such as the one-particle density and total energies, but is most commonly used in order to obtain ionization potentials (IPs) and electron affinities (EAs).[109,152–154] The latter are connected to the quasiparticles, which will be the primary interest in this chapter. Green's function based methods are convenient alternatives to other common approaches used to obtain IPs and EAs, such as the ΔSCF method, Koopmans' theorem, or similar methods based on DFT or (post)-Hartree–Fock theories.[155–157] Following Hedin's initial work, a set of five interdependent integro-differential equations can be formulated,[152] from which aside from the Green's function other useful quantities such as the self-energy may be derived. The self-energy can also be used to construct effective ground state potentials.[158,159] Starting from an initial reference, Hedin's equations can be used to obtain subsequently better approximations to the Green's function.[152] Using a simple Hartree–Fock or Kohn–Sham calculation as a starting point, many-body effects are introduced during an iterative process. This chapter will be structured as follows: First, the one-particle Green's function will be briefly introduced in the context of quantum mechanics. The Green's function is then related to other quantities comprising Hedin's equations, for which the popular *GW* approximation will be introduced. Lastly, related methods and common approximations based on the presented methodology are briefly discussed. The following chapter aims at giving a short but general introduction to the Green's function based methods used throughout this thesis, while the more practical aspects are subject of later chapters. The methodology will be extended in chapter 6 in order to describe charge-neutral excitations using the Bethe-Salpeter equation, specifically geared towards CESs.[26,160]

4.1 The One-Particle Green's Function

Let $\boldsymbol{H}$ be the Hamiltonian operator of an N-electron system given by

$$\boldsymbol{H} = \boldsymbol{h}(\boldsymbol{r}_1) + \boldsymbol{v}(\boldsymbol{r}_1, \boldsymbol{r}_2). \tag{4.1}$$

where, $\boldsymbol{h}$ collects, the kinetic energy operator, $\boldsymbol{t}$, the static potential, $\boldsymbol{V}$, and the operator for the spin-orbit coupling, $\boldsymbol{h}^{\text{SO}}$,[44,161] and $\boldsymbol{v}$ is the bare two-electron Coulomb interaction. $|N_0\rangle$ is the normalized ground state of this N-electron system and E_{N_0} the associated ground state energy. For convenience the space- and time-coordinates are again collected in a time-space coordinate vector, according to

$$\mathbf{1} = (\boldsymbol{r}_1, t_1),\ \mathbf{2} = (\boldsymbol{r}_2, t_2)\ \ \ldots\ . \tag{4.2}$$

The one-particle Green's function associated with this Hamiltonian operator is defined as [152,162]

$$\begin{aligned} \boldsymbol{G}(\mathbf{1},\mathbf{2}) &= -i \left\langle N_0 | \mathcal{T} \left(\psi(\mathbf{1}) \psi^\dagger(\mathbf{2}) \right) | N_0 \right\rangle \\ &= -i\theta(\tau) \left\langle N_0 | \psi(\mathbf{1}) \psi^\dagger(\mathbf{2}) | N_0 \right\rangle + i\theta(-\tau) \left\langle N_0 | \psi^\dagger(\mathbf{2}) \psi(\mathbf{1}) | N_0 \right\rangle \qquad \text{with} \qquad \tau = t_1 - t_2. \end{aligned} \tag{4.3}$$

Here, $\mathcal{T}$ is Wick's time-ordering operator, which for two operators can be easily expressed using the Heaveside step function, θ, given by

$$\theta(\tau) := \begin{cases} 1 & \text{if } \tau > 0 \\ 0 & \text{if } \tau \leq 0 \end{cases}. \tag{4.4}$$

$\psi^\dagger(\mathbf{1})$ and $\psi(\mathbf{2})$ are the common field operators in the interaction picture, given by [163]

$$\psi^\dagger(\mathbf{1}) = \mathrm{e}^{-i\boldsymbol{H}t_1} \psi^\dagger(\boldsymbol{r}_1) \mathrm{e}^{i\boldsymbol{H}t_1} \qquad \text{and} \qquad \psi(\mathbf{2}) = \mathrm{e}^{i\boldsymbol{H}t_2} \psi(\boldsymbol{r}_2) \mathrm{e}^{-i\boldsymbol{H}t_2}, \tag{4.5}$$

creating or annihilating a particle at point $\boldsymbol{r}$ at time t. The one-particle Green's function shown in eq. 4.3 describes the propagation of either a particle (electron) or a hole state depending on whether τ is positive or negative. It can be interpreted as the probability amplitude of a particle or hole state created at $\boldsymbol{r}_1$ or $\boldsymbol{r}_2$ to have traveled to $\boldsymbol{r}_2$ or $\boldsymbol{r}_1$, where it is annihilated. The Green's function reduces to the one-particle density matrix in the limit $t_2 \to t_1^+ = t_1 + 0^+$, where 0^+ is an infinitesimal small positive shift in time. The Lehmann representation of the one-particle Green's function is obtained by inserting a projector onto a complete set of the $(N \pm 1)$-electron states and subsequent Fourier transformation. The spectral representation reads

$$\begin{aligned} \boldsymbol{G}(\boldsymbol{r}_1, \boldsymbol{r}_2, \omega) &= \sum_A \frac{\boldsymbol{\Lambda}_A(\boldsymbol{r}_1) \boldsymbol{\Lambda}_A^\dagger(\boldsymbol{r}_2)}{\omega - \epsilon_A + i\eta} + \sum_I \frac{\boldsymbol{\Lambda}_I(\boldsymbol{r}_1) \boldsymbol{\Lambda}_I^\dagger(\boldsymbol{r}_2)}{\omega - \epsilon_I - i\eta} \\ &= \sum_M \frac{\boldsymbol{\Lambda}_M(\boldsymbol{r}_1) \boldsymbol{\Lambda}_M^\dagger(\boldsymbol{r}_2)}{\omega - \epsilon_M + i\eta \, \mathrm{sgn}(\epsilon_M - \omega^\mathrm{F})}, \end{aligned} \tag{4.6}$$

where ω^F is the energy of the Fermi level and A, I indicate electron and hole states respectively, collected in M, and $\boldsymbol{\Lambda}$ are the Lehmann amplitudes, also referred to as Dyson orbitals. ϵ are the quasiparticle energies and correspond to a charge excitation of $|N\rangle$ to either $|N \pm 1\rangle$. The quasiparticle energies can be obtained from the total energy expression by

$$\epsilon_A = E_{(N+1)_A} - E_N \qquad \text{and} \qquad \epsilon_I = E_N - E_{(N-1)_I}. \tag{4.7}$$

From this, the relation to the EAs and IPs becomes clear. The one-particle Green's function has singularities at the quasiparticle energies. By considering a reference system such as the Kohn–Sham system, a non-interacting Green's function, $\boldsymbol{G}_0$, can be constructed from the Kohn–Sham one-particle states and eigenvalues. Its Lehmann amplitudes are then the spinors associated with either occupied or virtual states. $\boldsymbol{G}_0$ has poles at the Kohn–Sham eigenvalues, which replace the true quasiparticle energies. The one-particle Green's function obeys the equation of motion

$$\left(i\frac{\partial}{\partial t}\mathbf{1}_2 - \boldsymbol{h}(\mathbf{1}) - \boldsymbol{U}(\mathbf{1})\right)\boldsymbol{G}(\mathbf{1},\mathbf{2}) + i\int \boldsymbol{v}(\mathbf{1},\mathbf{3})\boldsymbol{G}_2(\mathbf{1},\mathbf{3}^+,\mathbf{2},\mathbf{3}^{++})\mathrm{d}\mathbf{3} = \delta(\mathbf{1},\mathbf{2}), \tag{4.8}$$

where an external perturbative potential, $\boldsymbol{U}$, was introduced, which is local in time. This potential can eventually be set to zero in the final expressions. The analogues equation using the time-derivative with respect to t_2 takes a similar form. A detailed derivation of which is presented in ref. 163. $\boldsymbol{G}_2$ is the two-particle Green's function, which can be related to the correlated propagation of a pair of particle or hole states, as well as possible combinations. It will be briefly revisited in order to describe charge-neutral excitations in later sections. The two-particle Green's function can be eliminated by using Schwinger's functional derivative technique, using the relation[164–166]

$$\boldsymbol{G}_2(\mathbf{1},\mathbf{3},\mathbf{2},\mathbf{3}^+) = \boldsymbol{G}(\mathbf{1},\mathbf{2})\boldsymbol{G}(\mathbf{3},\mathbf{3}^+) - \frac{\delta\boldsymbol{G}(\mathbf{1},\mathbf{2})}{\delta\boldsymbol{U}(\mathbf{3})}. \tag{4.9}$$

Inserting this expression in eq. 4.8, results in two terms. The first term is the potential of a simple charge-distribution and corresponds to the bare Hartree-potential, $\boldsymbol{V}^{\mathrm{H}}(\boldsymbol{r}_1)$, which is

$$\boldsymbol{V}^{\mathrm{H}}(\boldsymbol{r}_1) = -i\int \boldsymbol{v}(\mathbf{1},\mathbf{2})\boldsymbol{G}(\mathbf{2},\mathbf{2}^+)\mathrm{d}\mathbf{2}. \tag{4.10}$$

The second term must therefore include the exchange and correlation effects. These are gathered in the self-energy, $\boldsymbol{\Sigma}$, which is defined in accordance with Hedin's original formulation[152] by

$$\boldsymbol{\Sigma}(\mathbf{1},\mathbf{2}) = i\int \boldsymbol{v}(1^+,\mathbf{3})\frac{\delta\boldsymbol{G}(\mathbf{1},\mathbf{4})}{\delta\boldsymbol{U}(\mathbf{3})}\boldsymbol{G}(\mathbf{4},\mathbf{2})\mathrm{d}\mathbf{3}\mathrm{d}\mathbf{4} \tag{4.11}$$

and is identical to the so-called mass operator. Inserting eqs.. 4.9, 4.10, and 4.11 in eq. 4.8, the equation of motion of the one-particle Green's function is obtained as

$$\left(i\frac{\partial}{\partial t}\mathbf{1}_2 - \boldsymbol{h}(\mathbf{1}) - \boldsymbol{V}^{\mathrm{H}}(\mathbf{1}) - \boldsymbol{U}(\mathbf{1})\right)\boldsymbol{G}(\mathbf{1},\mathbf{2}) + \int \boldsymbol{v}(\mathbf{1},\mathbf{3})\boldsymbol{\Sigma}(\mathbf{1},\mathbf{3})\mathrm{d}\mathbf{3} = \delta(\mathbf{1},\mathbf{2}). \tag{4.12}$$

Similarly, for the non-interacting Green's function, the equation of motions reads

$$\left(i\frac{\partial}{\partial t}\mathbf{1}_2 - \boldsymbol{h}(\mathbf{1}) - \boldsymbol{V}^{\mathrm{H}}(\mathbf{1}) - \boldsymbol{U}(\mathbf{1})\right)\boldsymbol{G}_0(\mathbf{1},\mathbf{2}) = \delta(\mathbf{1},\mathbf{2}), \tag{4.13}$$

for which the self-energy, $\boldsymbol{\Sigma}$, vanishes, as it does not contain many-body effects. By invoking the identity for the Green's function

$$\int \boldsymbol{G}(\mathbf{1},\mathbf{3})\boldsymbol{G}^{-1}(\mathbf{3},\mathbf{2})\mathrm{d}\mathbf{2} = \delta(\mathbf{1},\mathbf{2}), \tag{4.14}$$

the equation of motion of the non-interacting Green's function can be inserted into eq. 4.12, which constitutes the Dyson equation:

$$\boldsymbol{G}(\mathbf{1},\mathbf{2}) = \boldsymbol{G}_0(\mathbf{1},\mathbf{2}) + \int \boldsymbol{G}_0(\mathbf{1},\mathbf{3})\boldsymbol{\Sigma}(\mathbf{3},\mathbf{4})\boldsymbol{G}(\mathbf{4},\mathbf{2})\mathrm{d}\mathbf{3}\mathrm{d}\mathbf{4}. \tag{4.15}$$

In principle, the above equations allow for the calculation of the fully-interacting one-particle Green's function starting from a suitable reference and having knowledge of the self-energy. $\boldsymbol{\Sigma}$ is a functional of the exact one-particle Green's function and needs to be approximated. Choosing either a Hartree–Fock or Kohn–Sham solution to construct the non-interacting Green's function, the approximate exchange- and correlation-potentials need to be substracted in order to avoid double counting. Thereby, it is convenient to modify the expression for the self-energy according to

$$\boldsymbol{\Sigma} \rightarrow \boldsymbol{\Sigma} - \boldsymbol{V}_{\mathrm{xc}}, \tag{4.16}$$

where $\boldsymbol{V}_{\mathrm{xc}}$ is an approximation to the many-body effects described by the self-energy, here, given by the (KS-)exchange-correlation potential. If the one-particle Green's function is available, the quasiparticle energies can be obtained through eq. 4.12. By using the spectral representation of the Green's function in eq. 4.6, in eq. 4.15 and using the fact, that the equation of motion becomes singular near the quasiparticle energies, a non-Hermitian eigenvalue problem can be derived, which reads [162]

$$\int \left(\delta(\boldsymbol{r}_1,\boldsymbol{r}_2)(\epsilon_p - \boldsymbol{h}(\boldsymbol{r}_2) - \boldsymbol{\Sigma}(\boldsymbol{r}_1,\boldsymbol{r}_2,\epsilon_p)\right)\boldsymbol{\Lambda}_p(\boldsymbol{r}_2)\mathrm{d}\boldsymbol{r}_2 = \mathbf{0}, \tag{4.17}$$

where, $\boldsymbol{\Lambda}$ is the Lehmann amplitude associated with the state p and the quasiparticle energie ϵ_p. This equation assumes, that as the limit $\omega \rightarrow \epsilon$ is approached, the singulartiy is primarily associated with the Green's function, which is the quasiparticle approximation. [167] Since the self-energy is a non-Hermitian energy-dependent term, this equation is non-linear and its solutions are complex and not unique. In the following, we will only consider the real part, associated with the IPs and EAs and refere to these as the quasiparticle energies. The imaginary contribution corresponds to a finite lifetime, which is not considered. The above equation reduces to the Hartree–Fock equations if the self-energy is replaced by its zero'th order expansion in $\boldsymbol{v}$, which is equivalent to the Hartree–Fock-exchange potential.

4.2 Hedin's Equations

The one-particle Green's function is dependent on the self-energy, involving complicated functional derivatives with respect to the perturbative potential, $\boldsymbol{U}$. This form is unsuitable for a systematic evaluation, as it explicitly contains a dependence on the nature of the perturbation term. A solution independent of $\boldsymbol{U}$ can be obtained following Hedin, who presented a set of five differential equations from which the self-energy and the one-particle Green's function may be obtained for arbitrary $\boldsymbol{U}$. [152,162,168] These equations show a cyclic dependence and connect functions, for which well-established theories and techniques exist in order to obtain approximate solutions. Their hierarchical structure suggests an iterative approach in order to obtain a solution, for which the Green's function is subsequently improved towards the exact results. The first of these equations is the Dyson equation in eq. 4.15, introduced in the preceding section. It connects the non-interacting Green's function to the fully-interacting one using the non-local frequency-dependent potential, that is the self-energy, $\boldsymbol{\Sigma}$. Using the identity of the Green's function in eq. 4.14, eq. 4.11 can be recast as

$$\boldsymbol{\Sigma}(\mathbf{1},\mathbf{2}) = -i\int \boldsymbol{v}(\mathbf{1}^+,\mathbf{3})\boldsymbol{G}(\mathbf{1},\mathbf{4})\frac{\delta\boldsymbol{G}^{-1}(\mathbf{4},\mathbf{2})}{\delta\boldsymbol{U}(\mathbf{3})}\mathrm{d}\mathbf{3}\mathrm{d}\mathbf{4}. \tag{4.18}$$

The functional derivative of the inverse Green's function with respect to the potential $\boldsymbol{U}$ is expanded by using the chain rule

$$\frac{\delta \boldsymbol{G}^{-1}(\mathbf{1},\mathbf{2})}{\delta \boldsymbol{U}(\mathbf{3})} = \int \frac{\delta \boldsymbol{G}^{-1}(\mathbf{1},\mathbf{2})}{\delta \boldsymbol{V}_{\text{tot}}(\mathbf{4})} \frac{\delta \boldsymbol{V}_{\text{tot}}(\mathbf{4})}{\delta \boldsymbol{U}(\mathbf{3})} \mathrm{d}\mathbf{4} \quad \text{with} \quad \boldsymbol{V}_{\text{tot}}(\mathbf{1}) = \boldsymbol{U}(\mathbf{1}) - i \int \boldsymbol{V}(\mathbf{1},\mathbf{3}) \boldsymbol{G}(\mathbf{3},\mathbf{3}^{+}) \mathrm{d}\mathbf{3}, \tag{4.19}$$

where $\boldsymbol{V}_{\text{tot}}$ is the total potential. This equation allows for the identification of a screened interaction, $\boldsymbol{W}$, which will be defined according to

$$\boldsymbol{W}(\mathbf{1},\mathbf{2}) = \int \boldsymbol{v}(\mathbf{1},\mathbf{3}) \frac{\delta \boldsymbol{V}_{\text{tot}}(\mathbf{2})}{\delta \boldsymbol{U}(\mathbf{3})} \mathrm{d}\mathbf{3}. \tag{4.20}$$

By inserting eq. 4.14 and again invoking the chain rule, the screened interaction is rewritten as

$$\begin{aligned} \boldsymbol{W}(\mathbf{1},\mathbf{2}) &= \boldsymbol{v}(\mathbf{1},\mathbf{2}) + i \int \boldsymbol{v}(\mathbf{1},\mathbf{3}) \boldsymbol{v}(\mathbf{2},\mathbf{4}) \boldsymbol{G}(\mathbf{4},\mathbf{5}) \frac{\delta \boldsymbol{G}^{-1}(\mathbf{5},\mathbf{6})}{\delta \boldsymbol{U}(\mathbf{3})} \boldsymbol{G}(\mathbf{6},\mathbf{4}^{+}) \mathrm{d}\mathbf{3}\mathrm{d}\mathbf{4}\mathrm{d}\mathbf{5}\mathrm{d}\mathbf{6} \\ &= \boldsymbol{v}(\mathbf{1},\mathbf{2}) + \int \boldsymbol{W}(\mathbf{1},\mathbf{3}) \boldsymbol{P}(\mathbf{3},\mathbf{4}) \boldsymbol{v}(\mathbf{4},\mathbf{2}) \mathrm{d}\mathbf{3}\mathrm{d}\mathbf{4}, \end{aligned} \tag{4.21}$$

where $\boldsymbol{P}$ is the polarization function,

$$\boldsymbol{P}(\mathbf{3},\mathbf{4}) = i \int \boldsymbol{G}(\mathbf{4},\mathbf{5}) \frac{\delta \boldsymbol{G}^{-1}(\mathbf{5},\mathbf{6})}{\delta \boldsymbol{V}_{\text{tot}}(\mathbf{3})} \boldsymbol{G}(\mathbf{6},\mathbf{4}^{+}) \mathrm{d}\mathbf{5}\mathrm{d}\mathbf{6}. \tag{4.22}$$

In eq. 4.21, the screened interaction is written as the sum of the bare Coulomb interaction, plus a correction describing the polarization effects in the system. The interaction is symmetric with respect to the interchange of two particles and can be thought of as the potential experienced by a (quasi-)particle felt at $\mathbf{1}$ due to the presence of a test charge located at $\mathbf{2}$, screened by the dielectric medium. It differs from the Coulomb interaction by taking the immediate environment of the electrons into account and instead considers them as collective constructs, so-called quasiparticles, indicated in fig. 4.1.

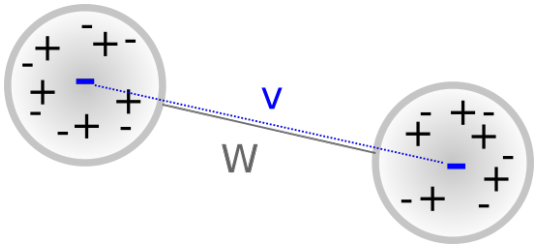

Figure 4.1: The screened interaction, $\boldsymbol{W}$, of two (quasi-)particles takes the dielectric screening effects of the environment into account compared to the bare Coulomb interaction, $\boldsymbol{v}$.

Eq. 4.20 can be rewritten using the dielectric function, $\boldsymbol{\epsilon}$, which in turn is related to the charge fluctuation potential.[169–172] The functional derivative of the inverse Green's function with respect to the total potential is the vertex function, $\boldsymbol{\Gamma}$, given by

$$\begin{aligned}\boldsymbol{\Gamma}(\mathbf{1},\mathbf{2},\mathbf{3}) &= -\frac{\delta \boldsymbol{G}^{-1}(\mathbf{1},\mathbf{2})}{\delta \boldsymbol{V}_{\text{tot}}(\mathbf{3})} \\ &= \delta(\mathbf{1},\mathbf{2})\delta(\mathbf{1},\mathbf{3}) + \frac{\delta \boldsymbol{\Sigma}(\mathbf{1},\mathbf{2})}{\delta \boldsymbol{V}_{\text{tot}}(\mathbf{3})}\end{aligned} \tag{4.23}$$

and is the final quantity required to formulate Hedin's equations. The second line of eq. 4.23 follows directly by inversion of eq. 4.15 and applying the chain rule. The dependence on the external potential $\boldsymbol{U}$ is eliminated and the equation becomes valid for an arbitrary perturbation. The vertex function then reads

$$\boldsymbol{\Gamma}(\mathbf{1},\mathbf{2},\mathbf{3}) = \delta(\mathbf{1},\mathbf{2})\delta(\mathbf{1},\mathbf{3}) + \int \frac{\delta \boldsymbol{\Sigma}(\mathbf{1},\mathbf{2})}{\delta \boldsymbol{G}(\mathbf{4},\mathbf{5})} \boldsymbol{G}(\mathbf{4},\mathbf{6})\boldsymbol{G}(\mathbf{7},\mathbf{5})\boldsymbol{\Gamma}(\mathbf{6},\mathbf{7},\mathbf{3})\mathrm{d}\mathbf{4}\mathrm{d}\mathbf{5}\mathrm{d}\mathbf{6}\mathrm{d}\mathbf{7}. \tag{4.24}$$

Eqs. 4.18 and 4.22 can be rewritten using the vertex function. The polarization function and the self-energy then become

$$\boldsymbol{P}(\mathbf{3},\mathbf{4}) = i \int \boldsymbol{G}(\mathbf{4},\mathbf{5})\boldsymbol{G}(\mathbf{6},\mathbf{4}^{+})\boldsymbol{\Gamma}(\mathbf{5},\mathbf{6},\mathbf{3})\mathrm{d}\mathbf{5}\mathrm{d}\mathbf{6}, \tag{4.25}$$

and

$$\boldsymbol{\Sigma}(\mathbf{1},\mathbf{4}) = i \int \boldsymbol{G}(\mathbf{1},\mathbf{4})\boldsymbol{W}(\mathbf{1}^{+},\mathbf{3})\boldsymbol{\Gamma}(\mathbf{4},\mathbf{2},\mathbf{3})\mathrm{d}\mathbf{3}\mathrm{d}\mathbf{4}. \tag{4.26}$$

Eqs. 4.15, 4.24, 4.20, 4.25, and 4.26 constitute Hedin's five equations. Due to their dependence on each other the solution is non-trivial. The suggested iterative procedure is shown in Ffig. 4.2 and should be followed in a clockwise manner, using either Hartree–Fock or DFT starting points. Provided the equations are solved until self-consistency is reached, the solutions becomes independent of the initial reference. Unfortunately, the complex structure makes a straightforward solution difficult and further simplifications need to be devised, most commonly using model vertex functions.[173] The most prominent of which is the *GW* approximation, as proposed by Hedin, which will be discussed in the following section.[152,162,174,175]

4.3 The *GW* Approximation

The *GW* approximation is most easily derived by following Hedin's pentagon in fig. 4.2 for a given reference. Starting from the non-interacting Green's function, the polarizability function is obtained by only keeping the first order term of the vertex function, which is given by

$$\boldsymbol{\Gamma}_0(\mathbf{1},\mathbf{2},\mathbf{3}) \approx \delta(\mathbf{1},\mathbf{2})\delta(\mathbf{1},\mathbf{3}). \tag{4.27}$$

This neglects all excitonic effects as well as the interaction of the screening electrons and is consistent with the non-interacting starting.[171] The polarizability reduces to

$$\boldsymbol{P}_0(\mathbf{1},\mathbf{2}) = i\boldsymbol{G}(\mathbf{2},\mathbf{1})\boldsymbol{G}(\mathbf{1},\mathbf{2}^{+}), \tag{4.28}$$

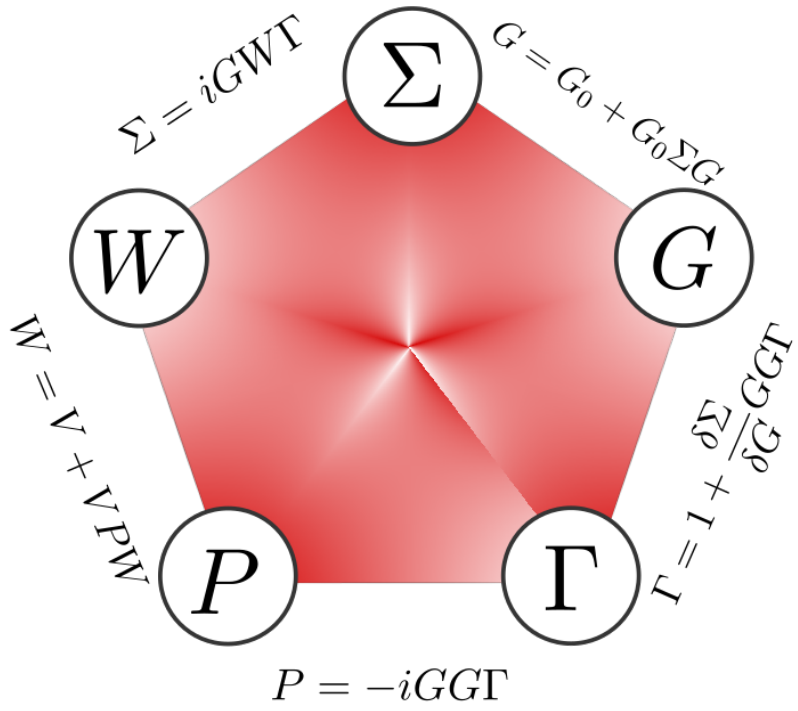

Figure 4.2: Schematic representation of Hedin's five equations. The equations are arranged as to indicate the cyclic dependence and the manner in which a self-consistent solution may be obtained iteratively. The solutions can be solved in a clockwise manner. $\boldsymbol{G}$ and $\boldsymbol{G}_0$ are the Green's function of the system and its non-interacting counterpart. $\boldsymbol{\Gamma}$ is the vertex function and $\boldsymbol{P}$ is the polarizability function. $\boldsymbol{W}$ is the screened exchange from which the self-energy $\boldsymbol{\Sigma}$ is obtained. In subsequent iterations $\boldsymbol{G}_0$ is set to the approximate Green's function obtained prior, while also taking into account its any approximate self-energy contributions in order to avoid double counting.

which corresponds to the random-phase approximation (RPA), containing only non-interacting particle-hole pairs.[168,176–180] In the first iteration, the polarizability is obtained from the non-interacting Green's function and is readily available using eq. 4.6. Having found an expression for the polarziation function, the screened exchange can be evaluated. In practice, instead of directly considering the polarizability, as suggested by the above equation, $\boldsymbol{W}$ is evaluated by using the dielectric function in eq. 4.20 as[172,181]

$$\boldsymbol{W}(\mathbf{1},\mathbf{2}) = \int \boldsymbol{\epsilon}^{-1}(\mathbf{3},\mathbf{2})\boldsymbol{v}(\mathbf{1}^{+},\mathbf{3})\mathrm{d}\mathbf{3} \quad \text{with} \quad \boldsymbol{\epsilon}^{-1}(\mathbf{3},\mathbf{2}) = \frac{\delta \boldsymbol{V}_{\text{tot}}(\mathbf{3})}{\delta \boldsymbol{U}(\mathbf{2})}. \tag{4.29}$$

This is done, since the inverse of the dielectric function is directly connected to the (RPA) response function introduced in sec. 3.5. The relation is given by

$$\boldsymbol{\epsilon}^{-1}(\mathbf{1},\mathbf{2}) = \delta(\mathbf{1},\mathbf{2}) + \int \boldsymbol{v}(\mathbf{1},\mathbf{3})\boldsymbol{\chi}(\mathbf{3},\mathbf{2})\mathrm{d}\mathbf{3}. \tag{4.30}$$

This quantity can be conveniently evaluated in the frequency domain in the context of linear response theory. Following sec. 3.5, the spectral representation of the (RPA) response function, $\boldsymbol{\chi}(\boldsymbol{r}_1, \boldsymbol{r}_2, \omega)$, is given by[161,162]

$$\begin{aligned}\boldsymbol{\chi}(\boldsymbol{r}_1,\boldsymbol{r}_2,\omega) &= \sum_{n\neq 0}\left[\frac{\boldsymbol{\rho}_{0n}(\boldsymbol{r}_1)\boldsymbol{\rho}^{\dagger}_{0n}(\boldsymbol{r}_2)}{\omega-\omega_n+i\eta} - \frac{\boldsymbol{\rho}^{\dagger}_{0n}(\boldsymbol{r}_1)\boldsymbol{\rho}_{0n}(\boldsymbol{r}_2)}{\omega+\omega_n-i\eta}\right] \\ &\text{with} \quad \boldsymbol{\rho}_{0n}(\boldsymbol{r}) = \sum_a\sum_i (\boldsymbol{X}+\boldsymbol{Y})_{ia,n}\boldsymbol{\Phi}^{\dagger}_a(\boldsymbol{r})\boldsymbol{\Phi}_i(\boldsymbol{r}),\end{aligned} \tag{4.31}$$

where $\boldsymbol{\rho}_n(\boldsymbol{r}_1)$ and ω_n are the transition densities and excitation energies corresponding theH n'th charge-neutral excitation in the random-phase approximation and $(\boldsymbol{X}+\boldsymbol{Y})_{ia,n}$ are the eigenvectors of Casida's equation (eq. 3.44) associated with ω_n.[25,161] This is equivalent to the time-dependent Hartree problem, which can be reliably solved by using well-established methods.[131–134,182] η is again used as an infinitesimal small positive shift. Using the spectral representation of the linear response function in order to describe the dielectric screening, $\boldsymbol{W}$, is written as

$$\begin{aligned}\boldsymbol{W}(\boldsymbol{r}_1,\boldsymbol{r}_2,\omega) &= \boldsymbol{v}_n(\boldsymbol{r}_1\boldsymbol{r}_2) + \sum_{n\neq 0}\left[\frac{\tilde{\boldsymbol{V}}^{\dagger}_n(\boldsymbol{r}_1)\tilde{\boldsymbol{V}}_n(\boldsymbol{r}_2)}{\omega-\omega_n+i\eta} - \frac{\tilde{\boldsymbol{V}}_n(\boldsymbol{r}_1)\tilde{\boldsymbol{V}}^{\dagger}_n(\boldsymbol{r}_2)}{\omega+\omega_n-i\eta}\right] \\ &\text{with} \quad \tilde{\boldsymbol{V}}_n(\boldsymbol{r}_1) = \int \boldsymbol{v}(\boldsymbol{r}_1,\boldsymbol{r}_2)\boldsymbol{\rho}_{0n}(\boldsymbol{r}_2)\mathrm{d}\boldsymbol{r}_2,\end{aligned} \tag{4.32}$$

where the fluctuation potential, $\tilde{\boldsymbol{V}}(\boldsymbol{r})$, has been introduced. From eq. 4.32, it can be seen that as the frequency approaches a charge neutral excitation within the RPA, the screened exchanges becomes singular in the limit $\eta \to 0^+$. Inserting the model vertex function, $\boldsymbol{\Gamma}_0$, in the self-energy expression results in

$$\boldsymbol{\Sigma}(\mathbf{1},\mathbf{2}) = i\boldsymbol{G}(\mathbf{1},\mathbf{2})\boldsymbol{W}(\mathbf{1}^+,\mathbf{2}). \tag{4.33}$$

The self-energy simplifies to a product of the Green's function and the screened interaction. This is the origin of the name "*GW*", where the vertex function is kept fixed at the $\boldsymbol{\Gamma}_0$ level, also in subsequent iterations. The above equation is transformed into the frequency domain and reads[183]

$$\boldsymbol{\Sigma}(\boldsymbol{r}_1,\boldsymbol{r}_2,\omega) = \frac{i}{2\pi}\int \boldsymbol{G}(\boldsymbol{r}_1,\boldsymbol{r}_2,\omega+\omega')\boldsymbol{W}(\boldsymbol{r}_1,\boldsymbol{r}_2,\omega')\mathrm{e}^{i\omega'\eta}\mathrm{d}\omega', \tag{4.34}$$

where we used the fact that $\boldsymbol{W}$ is symmetric. η as a regularization parameter. The above equation resembles the Hartree–Fock self-energy, where the exchange potential is replaced by a (dynamically) screened interaction. $\boldsymbol{W}$ may be split into the bare Coulomb potential and a screened exchange. The former leads to the Hartree–Fock exchange, while the latter introduces static and dynamic correlation effects. Note that this terminology should not be confused with the one used in post-Hartree–Fock methods. The self-energy is then written as

$$\begin{aligned}\boldsymbol{\Sigma}(\boldsymbol{r}_1,\boldsymbol{r}_2,\omega) &= \frac{i}{2\pi}\int \boldsymbol{G}(\boldsymbol{r}_1,\boldsymbol{r}_2,\omega+\omega')\boldsymbol{v}(\boldsymbol{r}_1,\boldsymbol{r}_2)\mathrm{e}^{i\omega'\eta}\mathrm{d}\omega' \\ &+ \frac{i}{2\pi}\int \boldsymbol{G}(\boldsymbol{r}_1,\boldsymbol{r}_2,\omega+\omega')\left(\boldsymbol{W}(\boldsymbol{r}_1,\boldsymbol{r}_2,\omega') - \boldsymbol{v}(\boldsymbol{r}_1,\boldsymbol{r}_2)\right)\mathrm{e}^{i\omega'\eta}\mathrm{d}\omega' \\ &= \boldsymbol{\Sigma}^{\mathrm{X}}(\boldsymbol{r}_1,\boldsymbol{r}_2,\omega) + \boldsymbol{\Sigma}^{\mathrm{c}}(\boldsymbol{r}_1,\boldsymbol{r}_2,\omega).\end{aligned} \tag{4.35}$$

If the RPA problem is solved and the full spectral representation of $\boldsymbol{W}$ is known, this equation can be evaluated analytically,[175] resulting in the Hartree–Fock exchange self-energy

$$\boldsymbol{\Sigma}^{\mathrm{X}}(\boldsymbol{r}_1, \boldsymbol{r}_2, \omega) = \boldsymbol{\Sigma}^{\mathrm{X}}(\boldsymbol{r}_1, \boldsymbol{r}_2) = \boldsymbol{v}(\boldsymbol{r}_1, \boldsymbol{r}_2), \tag{4.36}$$

which does not carry any explicit frequency-dependence, and a correlation contribution[25]

$$\boldsymbol{\Sigma}^{\mathrm{c}}(\boldsymbol{r}_1, \boldsymbol{r}_2, \omega) = \sum_{n \neq 0} \left[\sum_i \frac{\tilde{\boldsymbol{V}}_n^\dagger(\boldsymbol{r}_1) \tilde{\boldsymbol{V}}_n(\boldsymbol{r}_2) \boldsymbol{\Phi}_i(\boldsymbol{r}_1) \boldsymbol{\Phi}_i^\dagger(\boldsymbol{r}_2)}{\omega - \omega_i - i\eta} + \sum_a \frac{\tilde{\boldsymbol{V}}_n(\boldsymbol{r}_1) \tilde{\boldsymbol{V}}_n^\dagger(\boldsymbol{r}_2) \boldsymbol{\Phi}_a(\boldsymbol{r}_1) \boldsymbol{\Phi}_a^\dagger(\boldsymbol{r}_2)}{\omega + \omega_a + i\eta} \right], \tag{4.37}$$

for which we used the screened interaction given in eq. 4.32 and set $2\eta \to \eta$. Expressions 4.35 to 4.37 may be evaluated by projecting the quantities onto a set of suitable one-particle spinor functions, which in the first iteration are given by the eigenvalues of the reference system. Having a better approximation to the self-energy a new Green's function can be obtained using the Dyson equation, by inverting $\boldsymbol{G}$ or in the quasiparticle approximation (eq. 4.17). The self-energy is generally not Hermitian, which results in separate left and right eigenvectors, which both need to be considered. Without the *GW* approximation, subsequent iterations involve so-called vertex corrections and use polarizabilities and self-energies beyond the RPA. By considering these corrections only in the polarizability, the results may be observed to deteriorate with respect to the non-iterative solutions at the RPA level for both $\boldsymbol{P}$ and $\boldsymbol{\Sigma}$.[184] As pointed out by Shirley, the effect of self-consistency may even cancel out possible vertex corrections for quasiparticle energies, as they are of similar magnitude, but opposite sign.[185] Here, the non-iterative solution can often benefit from favourable cancellation of errors. The development of robust approximations to the vertex function in eq. 4.24 in order to obtain a systematic improvement with respect to the *GW* approximation are fields of active research, and are often much more computationally demanding, while a systematic and efficient improvement over *GW* is difficult to achieve.[186–192]

Instead of trying to achieve self-consistency, other more pragmatic approaches aim at choosing a suitable starting point, close to the true solution, and stop after the first iteration. This is referred to as *single-shot GW* or G_0W_0 method and avoids the complicated structure of the self-energy of subsequent iterations.[161,193–196] The self-energy is expressed in the canonical Kohn–Sham or Hartree–Fock basis from which the quasiparticle energies are calculated according to

$$\epsilon_p = \epsilon_{0,p} + Z_p(\epsilon_{0,p}) \left(\mathfrak{Re} \left[\langle p | \boldsymbol{\Sigma}[\boldsymbol{G}_0](\epsilon_{0,p}) | p \rangle \right] - \langle p | \boldsymbol{V}_{\mathrm{xc}} | p \rangle \right). \tag{4.38}$$

Here, $\epsilon_{0,p}$ are the zeroth order approximation to the quasiparticle energies, the Kohn–Sham or Hartree–Fock eigenvalues associated with state p. $\boldsymbol{V}_{\mathrm{xc}}$ is the exchange-correlation potential, which needs to substracted as to avoid double counting. Z is a renormalization parameter given by[172,197–199]

$$Z_p(\omega) = \left(1 - \mathfrak{Re} \left[\langle p | \frac{\partial \boldsymbol{\Sigma}(\omega')}{\partial \omega'} |_{\omega' = \omega} | p \rangle \right] \right)^{-1} \qquad \text{with} \qquad 0 \leq Z(\omega) \leq 1. \tag{4.39}$$

Eq. 4.38 is the linear approximation of the quasiparticle equation. Due to the energy-dependence of the self-energy, the quasiparticle equations are non-linear and multiple possible solutions may be found. The renormalization parameter corresponds to the weight of a specific solution, where $Z_p \ll 1$ hints at the one-particle state p not being a good approximation to the proper quasiparticle state.[200–202] Casting the quasiparticle equations in this linearized form assumes that the initial starting point is sufficiently close to the exact solution. This assumption gets progressively problematic for core electrons starting from a standard Kohn–Sham reference.[29,203–205] In practice, spurious values for Z_p are not uncommon, as one considers states far from the valence levels. This is due to the complicated structure the self-energy and associated spectral function typically

show in these frequency ranges.[28] Therefore, the self-energy often deviates strongly from the assumed linearity, resulting in numerical instabilities and spurious quasiparticle energies.[201] We may therefore choose to solve the quasiparticle equations iteratively or to fix the renormalization parameter to a fixed value, e.g. to one. The latter is equivalent to substituting the exchange-correlation potential by the self-energy in terms of the Kohn–Sham eigenvalues. The resulting quasiparticle energies are not solutions to the quasiparticle equations in eq. 4.17. Aside from the already mentioned techniques, other approaches exist in order to go beyond the G_0W_0 method, including partial or fully-consistent methods using additional constraints. Some of these techniques will be briefly discussed in the following section in order to better differentiate the various and sometimes ambiguously named variants commonly used, which derive from the *GW* ansatz. The different levels of self-consistency for the most common approaches are shown in fig. 4.3, where they are compared to the original solution of Hedin's equations (left), where in a first step, the vertex function is only represented by its leading term, which is the *GW* approximation. This set of equations may then be solved in an fully self-consistent manner, using only partial self-consistency or in an one-shot manner altogether.

4.4 Practical Approximations Towards Self-Consistent *GW*

While the self-consistent solution of the *GW* equations does not carry any dependence on the initial starting point, quasiparticle energies obtained within the perturbative G_0W_0 approach, do not share this property. Here, the Green's function and screened interaction remain fixed at the Kohn–Sham or Hartree–Fock level.[206] However, even if the vertex corrections are neglected at the *GW* level, the self-consistent solution still requires considerable computational effort and quickly becomes intractable as systems approach sizes routinely encountered in quantum chemistry. Therefore, the self-consistent solution of Hedin's equations even within the *GW* are ill-suited for most practical applications. As mentioned before, some studies on the self-consistent *GW* (sc*GW*) method indicate that converged results do not necessarily improve the quasiparticle energies with respect to the non-iterative approaches, although total energies were shown to improve over the G_0W_0 method.[193,195,207–210] Especially if high-accuracy solutions are sought after, additional issues need to be addressed. One is the self-interaction error, resulting from the missing vertex corrections.[188,190,191,204] This effect may result in a deterioration of the quasiparticle energies for self-consistent solutions. We may choose to calculate the screened interaction from the initial reference and only iterate the Green's function which constitutes the partial self-consistent GW_0 method. This method has the added benefit of not requiring $\boldsymbol{W}$ to be evaluated repeatedly, as the spectral representation does not change, this results in a computational effort comparable to the G_0W_0 method. These method may be constitute the subsequent introduction of approximations to the self-consistent solution of Hedin's equation, as shown in fig. 4.3. Other approaches, such as the quasiparticle self-consistent *GW* method (qs*GW*), aim at first obtaining an improved ground state by employing an approximate self-energy expression suitable for mean-field calculations. Faleev and co-workers suggested an energy-independent Hermitian self-energy, $\tilde{\boldsymbol{\Sigma}}$, for the construction of an effective one-particle Hamiltonian, given by[211–214]

$$H = -\frac{1}{2}\Delta + \boldsymbol{V}_{\mathbf{H}} + \tilde{\boldsymbol{\Sigma}}. \tag{4.40}$$

This constitutes a new non-interacting reference system, from which a new $\boldsymbol{G}_0$ is obtained and used in order to construct a new model self-energy. Since the Green's function is used in order to construct the non-interacting one, this approach basically acts in reverse when compared to the other iterative approaches. The approach is said to construct the reference ground state in order to minimize the correction at the G_0W_0 level and has been observed to converge to the same quasiparticle states, independent of the starting point.[215] If the reference one-particle states are instead assumed to be already sufficiently accurate, and only the quasiparticles are updated, the eigenvalue-only self-consistent *GW* (ev*GW*) method is recovered.[198,215,216] This approach is computationally much more feasible and can be applied to a wide range of chemically relevant systems. By iterating the

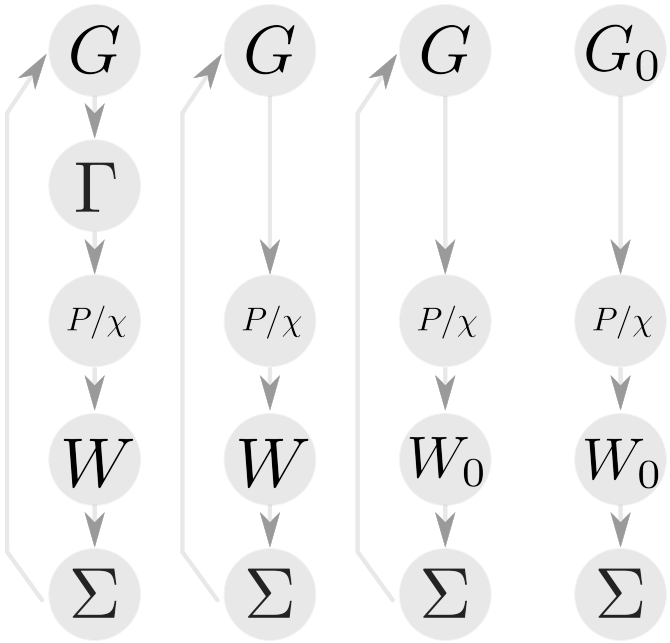

Figure 4.3: Schematic representation of different approaches and their relation. Starting from some approximation to the Green's function, the self-consistent solution of Hedin's equation includes the vertex corrections. The *GW* approximation is obtained by neglecting the non-linear terms in $\boldsymbol{\Gamma}$, resulting in a simple form for the polarization function and susceptibility from which we obtain the screened interaction $\boldsymbol{W}$ and the self-energy $\boldsymbol{\Sigma}$. By keeping the screened interaction fixed at the reference an underscreening can be avoided and the computational effort is lowered significantly, which is referred to as the GW_0 method. The G_0W_0 method completely neglects the self-consistency and stops after the first iteration. The Green's function and the screened exchange correspond to those of the reference system, usually employing a mean-field reference.

quasiparticles the starting point dependence can already be significantly reduced.[215] Especially for references employing (semi-)local density functionals, ev*GW* has been shown to reduce the errors when compared with G_0W_0 at least for the highest occupied state.[27] For low-lying states an analogous improvement is usually not observed, as these are regularly shifted towards too low energies with respect to the experimental values.[216,217] This can be partially attributed to an underscreening in $\boldsymbol{W}$. Golze *et al.* suggested that the partial-self-consistent GW_0 ansatz may strike a balance between a good description of the Green's function while avoiding the issues associated with the self-consistent solution of the screened exchange.[29,204,218]

5 *GW* Subspace Methods

The *GW* method, introduced in the preceding chapter, offers a comprehensive approach towards the calculation of quasiparticle energies, in order to describe the charge excitations, i.e., IPs and EAs, of a quantum chemical system. However, in order to describe the dielectric screening effects, the solution of the full RPA problem is required. This scales formally as $\mathcal{O}\left(N^6\right)$, where N measures the size of the system considered. In a two-component framework, the computational effort increases dramatically, roughly by a factor of 256, for Kramers symmetric systems, with respect to the one-component level. This is due to the use of complex algebra and the increased dimension of the electronic Hessian and does not account for additional requirements to the basis set in order to properly describe SOC effects.[25,161,219–222] The *GW* method at the two-component level, using the spectral representations of the response function, is therefore limited to only small systems. In order to extend the range of this method, techniques need to be devised which avoid the full solution of the RPA problem. A common approach in reducing the computational complexity, associated with the calculation of the four-center electron-repulsion integrals (ERIs), is the resolution of the identity (RI) approximation. This technique has seen considerable effort in improving overall efficiency, while maintaining a very small error overall.[82,137,223–227,227] In the context of *GW*, the RI approximation may be used, not only to reduce the computational effort necessary for the calculation of the ERIs, but also to avoid the solution of the RPA problem and the inversion of the dielectric function in its standard 4-indexed matrix representation completely.[25] In this chapter, some key considerations regarding the projection of the dielectric function in the auxiliary subspace are discussed. This is followed by the introduction of two of the common low-scaling *GW* variants, namely, the analytic continuation[228–234] (AC) and the contour deformation[27,28,137,183,199,230,235–237] (CD) *GW* methods. Both methods can be used to efficiently describe quasiparticle energies of valence states, but become considerably worse if states far from the Fermi level are of concern. These states often introduce severe numerical instabilities in AC-*GW*, and feature a stark increase in the cost, in the case of CD-*GW* . Therefore, a third approach, combining aspects of both, is examined. This method was implemented in the context of this thesis, for which an extension is presented, allowing for an application to a wide variety of problems. It introduces a simple sampling strategy in order to provide a basis for the description of quasiparticle energies, not only in close proximity to the Fermi level, but also including those associated with core electrons. This technique is then later used to provide quasiparticle energies for valence and core states in combination with the BSE in order to describe CESs.

5.1 Subspace Representation of the Dielectric Function

In this section, we will briefly introduce the dielectric function in its auxiliary subspace representation. This is a key step in order to avoid the solution of the full RPA problem and can be used to reduce the formal cost associated with the calculation of a single quasiparticle from $\mathcal{O}\left(N^6\right)$ by one or two orders of magnitude, depending on the method and state of interest.
The central idea was proposed by Aryasetiawan and Gunnarsson in the context of solids,[181] but was later adopted for the description of molecules.[209,210] We start by considering the screened exchange in eq. 4.29, which is given by

$$\boldsymbol{W}(\mathbf{1},\mathbf{2}) = \int \boldsymbol{\epsilon}^{-1}(\mathbf{1},\mathbf{3})\boldsymbol{v}(\mathbf{3},\mathbf{2})\mathrm{d}\mathbf{3}, \tag{5.1}$$

where we have made use of the symmetry of the screened exchange with respect to the interchanging of its arguments. In the full spectral *GW* approach, this equation is evaluated by first expressing the dielectric function using the response function and later introducing its spectral representation, obtained by solving the full RPA problem. The latter step is the bottleneck in this approach and needs to be avoided in order to devise methods for an efficient calculation of the quasiparticle energies. Here, instead of using the spectral representation of the linear response function, its Dyson series expansion is employed. In sec. 3.5 the linear response equation, $\boldsymbol{\chi}$, was related to its non-interacting counterpart within Kohn–Sham theory, $\boldsymbol{\chi}^{\mathrm{KS}}$. Here, we instead consider these quantities within the RPA and replace $\boldsymbol{\chi}^{\mathrm{KS}}$ by $\boldsymbol{\chi}^{0}$, which is the equivalent expression for the non-interacting Hartree system. The inverse dielectric function in eq. 4.30 is represented by the series expansion of the RPA response equations, according to 3.38, for which we write

$$\begin{aligned}\boldsymbol{\epsilon}^{-1}(\mathbf{1},\mathbf{2}) &= \delta(\mathbf{1},\mathbf{2}) + \int \boldsymbol{v}(\mathbf{1},\mathbf{3})\boldsymbol{\chi}(\mathbf{3},\mathbf{2})\mathrm{d}\mathbf{3} \\ &= \delta(\mathbf{1},\mathbf{2}) + \int \boldsymbol{v}(\mathbf{1},\mathbf{3})\boldsymbol{\chi}^{0}(\mathbf{3},\mathbf{2})\mathrm{d}\mathbf{3} + \iiint \boldsymbol{v}(\mathbf{1},\mathbf{3})\boldsymbol{\chi}^{0}(\mathbf{3},\mathbf{4})\boldsymbol{v}(\mathbf{4},\mathbf{5})\boldsymbol{\chi}^{0}(\mathbf{5},\mathbf{2})\mathrm{d}\mathbf{5}\mathrm{d}\mathbf{4}\mathrm{d}\mathbf{3} + \dots\end{aligned} \tag{5.2}$$

The response function of the RPA differs from the one of the Kohn–Sham system in eq. 3.38, by discarding the exchange-correlation potential and only keeping the Hartree potential term. Since the Hartree potential is local in time, i.e.,

$$\boldsymbol{v}(\mathbf{1},\mathbf{2}) = \boldsymbol{v}(r_1, r_2)\delta(t_1, t_2), \tag{5.3}$$

eq. 5.2 only depends on the difference of t_1 and t_2. In the frequency domain, only a single frequency variable needs to be regarded explicitly. The quantities are then transformed into their matrix representation in the basis of the reference states, here, the Kohn–Sham eigenfunctions. The Fourier transform of the non-interacting response function in eq. 3.37 and eq. 5.2 reduces to

$$\chi^{0}_{pqrs}(\omega) = \delta_{pr}\delta_{qs}\frac{f_q - f_p}{\omega - (\epsilon_p - \epsilon_q) + i\eta}, \tag{5.4}$$

where f are the occupation numbers, which is diagonal in spin space. η is again used to indicate a small real positive number, shifting the poles into the complex plane. In the final working equations only the limit $\eta \to 0^{+}$ will be considered. Inserting eqs. 5.4 and 5.2 in eq. 5.1, the matrix elements of the screened exchange may be written as

$$\begin{aligned}W_{pqrs}(\omega) &= v_{pqrs} + \sum_{tuvw} v_{pqtu}\chi^{0}_{tuvw}(\omega)v_{vwrs} + \dots \\ &= v_{pqrs} + \sum_{tuvw} v_{pqtu}\delta_{tv}\delta_{uw}\frac{f_u - f_t}{\omega - (\epsilon_t - \epsilon_u) + i\eta}v_{vwrs} + \dots \\ &= v_{pqrs} + \sum_{tu} v_{pqtu}\frac{f_u - f_t}{\omega - (\epsilon_t - \epsilon_u) + i\eta}v_{turs} + \dots .\end{aligned} \tag{5.5}$$

The RI approximation allows for the approximation of the 4-center ERIs using RI-intermediates integrals according to[81,82,225]

$$v_{pqrs} \approx \sum_{P} \left(R^{P}_{pq}\right)^{*} R^{P}_{rs}, \tag{5.6}$$

where R are the complex 3-center integrals, obtained as

$$R_{pq}^{P} = \sum_{Q} \left[\boldsymbol{V}^{-1/2}\right]_{PQ} \langle Qp|1q\rangle \, \mathbf{1}_2 \quad \text{with} \quad V_{PQ} = \langle PQ|11\rangle \,. \tag{5.7}$$

$\boldsymbol{V}$ is the Coulomb metric, where capital letters are used to indicate auxiliary basis functions. Expanding the Coulomb matrix elements in eq. 5.5 using the RI-intermediates, the screened exchange can be rewritten as

$$\begin{aligned} W_{pqrs}(\omega) &= \sum_{P} \left[\left(R_{pq}^{P}\right)^{*} R_{rs}^{P} + \sum_{tu} \left(R_{pq}^{P}\right)^{*} R_{tu}^{P} \frac{f_u - f_t}{\omega - (\epsilon_t - \epsilon_u) + i\eta} \sum_{Q} \left(R_{tu}^{Q}\right)^{*} R_{rs}^{Q} + \dots \right] \\ &= \sum_{PQ} \left(R_{pq}^{P}\right)^{*} \left[\delta_{PQ} + \sum_{tu} R_{tu}^{P} \frac{f_u - f_t}{\omega - (\epsilon_t - \epsilon_u) + i\eta} \left(R_{tu}^{Q}\right)^{*} + \dots \right] R_{rs}^{Q} \\ &= \sum_{PQ} \left(R_{pq}^{P}\right)^{*} \left[\delta_{PQ} - \sum_{tu} R_{tu}^{P} \frac{f_u - f_t}{\omega - (\epsilon_t - \epsilon_u) + i\eta} \left(R_{tu}^{Q}\right)^{*} \right]^{-1} R_{rs}^{Q}. \end{aligned} \tag{5.8}$$

In the last step, the series was collapsed into a closed form. The term in brackets is the dielectric function in its auxiliary subspace representation, which is given by

$$\begin{aligned} \epsilon_{PQ} &= \delta_{PQ} - \sum_{tu} R_{tu}^{P} \frac{f_u - f_t}{\omega - (\epsilon_t - \epsilon_u) + i\eta} \left(R_{tu}^{Q}\right)^{*} \\ &= \delta_{PQ} - \Pi_{PQ}(\omega), \end{aligned} \tag{5.9}$$

where $\mathbf{\Pi}$ is the auxiliary subspace representation of the (non-interacting) response function. While the auxiliary basis sets are usually larger then a regular basis, the response function and the dielectric function are effectively represented by 2-index quantities, instead of their original 4-indexed forms in the original basis. The calculation of the response function scales with approximately $\mathcal{O}\left(N^4\right)$, while the inversion of the dielectric function in the representation scales roughly with $\mathcal{O}\left(N^3\right)$, where N is again a measure of the sytem size.[25,182,238] By first calculating and inverting the dielectric function, the screened exchange is obtained in an efficient manner and is evaluated as

$$W_{pqrs}(\omega) = \sum_{PQ} \left(R_{pq}^{P}\right)^{*} \epsilon_{PQ}^{-1}(\omega) R_{rs}^{Q}. \tag{5.10}$$

Note that the dielectric function does not carry a reference to the indices of the matrix representation of the screened exchange in the full spinor basis. If the (inverse) dielectric function at a given frequency is available, any matrix element of the screened exchange can be easily constructed within comparably little time. For either purely real or imaginary frequencies in the limit $\eta \to 0^{+}$, the response function takes a particularly simple structure, as is becomes real in both cases.[137] As will be seen in the following sections, these cases are especially useful in both AC- and CD-*GW* approaches. For imaginary frequencies, the dielectric function then additionally becomes positive definite, for which the inversion can be done using a Cholesky decomposition. For a more detailed discussion of the symmetries associated with the response function, the reader is referred to ref. 137. In the following sections, methods will be presented which use the above consideration in order to evaluate the self-energy at selected (real) frequencies, allowing for the efficient calculations of quasiparticle energies. These techniques are

mostly used in order to extract only a small subset of quasiparticle energies, which is usually enough for many applications such as photoelectron spectroscopy or the description of excited states within the BSE.

5.2 Analytic Continuation of the Self-Energy

Now having access to the screened exchange for selected frequencies, further consideration can be made in order to evaluate the self-energy within the *GW* approximation presented in eq. 4.34. In the following only the correlation contribution to the self-energy will be discussed, as the Hartree–Fock exchange term is readily available in most quantum mechanical program suites and needs no further explanation. The correlation contribution of the self-energy is given by

$$\begin{aligned} \boldsymbol{\Sigma}^{\mathrm{c}}(r_1, r_2, \omega) &= \frac{i}{2\pi} \int \boldsymbol{G}(r_1, r_2, \omega + \omega') \left(\boldsymbol{W}(r_1, r_2, \omega') - \boldsymbol{v}(r_1, r_2) \right) \mathrm{e}^{i\omega'\eta} \mathrm{d}\omega' \\ &= \frac{i}{2\pi} \int \boldsymbol{G}(r_1, r_2, \omega + \omega') \boldsymbol{W}^{\mathrm{c}}(r_1, r_2, \omega') \mathrm{e}^{i\omega'\eta} \mathrm{d}\omega', \end{aligned} \tag{5.11}$$

where $\boldsymbol{W}^{\mathrm{c}}$ describes the difference between the screened exchange and the regular or Hartree–Fock exchange contribution. In order to evaluate the self-energy for a frequency, ω, this integral has to be solved, which is done analytically using the spectral representation of both quantities. However, the associated cost, especially at the two-component level, is the limiting factor, such that this can only be routinely done for small to medium sized systems.[161,172] Applying the auxiliary subspace technique, discussed in the previous section, grants access to the matrix elements of the screened exchange directly and the integral may instead be evaluated using a numerical quadrature scheme. This can then be done at a cost scaling with the number of quadrature roots, times the effort required for the evaluation of the integrand at these reference points. For most applications, the time-determining step is the calculation of the response matrix Hrequired in the dielectric function. However, the number of grid points required in order to converge the self-energy, may quickly become too large for practical applications. This is due to the complex structure of $\boldsymbol{\Sigma}$ along the real frequency axis.[239,240] The self-energy has many points close to the real axis, where it ceases to be analytic, as both the Green's function and the screened exchange have many poles. These occur at the quasiparticle energies for the Green's function and at the charge-neutral excitations for the screened exchange. Both types can be deduced from their spectral representations, in eqs. 4.6 and 4.32 respectively. These poles can be shifted into the complex plane. However, this may introduce an artificial dependence of the quasiparticle energies for large shifts.
Alternatively, one may try to evaluate the self-energy for imaginary frequencies instead and use this information to obtain the self-energy at the real axis, where it is smooth for complex frequencies and the poles can be easily avoided.[228,229,232,241] Following Ke and others, the matrix elements of the correlation contribution to the self-energy for an imaginary frequency, using the one-particle Green's function in eqs. 4.3 and 4.6 and the screened exchange in eq. 4.29 with eq. 4.30, becomes[137,231,232]

$$\Sigma^{\mathrm{c}}_{pq}(i\omega) = -\frac{1}{2\pi} \sum_m \left(\int \frac{\delta_{pq}}{i(\omega + \omega') - \epsilon_m - i\eta \, \mathrm{sgn}(\epsilon_m - \omega^{\mathrm{F}})} \sum_{PQ} \left(R^P_{pm} \right)^* \left(\epsilon^{-1}_{PQ}(i\omega') - \delta_{PQ} \right) R^Q_{mp} \mathrm{d}\omega' \right), \tag{5.12}$$

where the dielectric function in its auxiliary subspace representation has been used to evaluate the matrix elements of $\boldsymbol{W}^{\mathrm{c}}$. In order to obtain the potential for a real frequency, the self-energy is first evaluated for a set of imaginary ω. Here, the frequency integration converges much quicker, as compared to eq. 5.11. These reference points are then used to obtain a suitable representation of the self-energy, for example, by means of a rational approximation. It is assumed that this

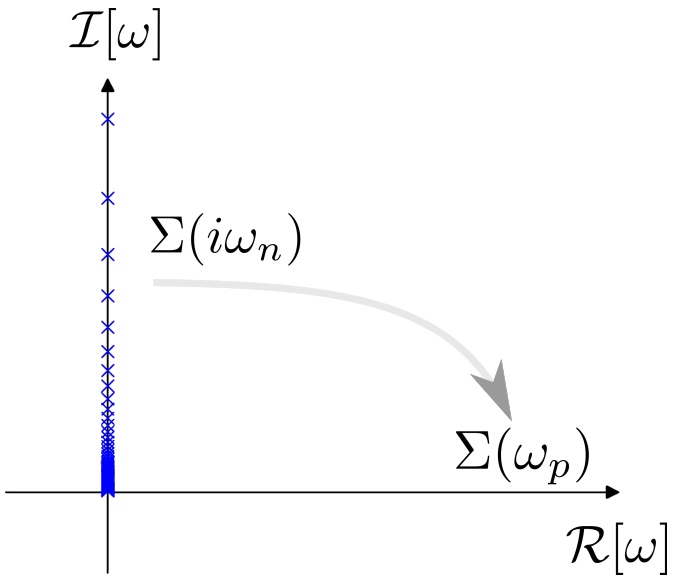

Figure 5.1: The analytic continuation approach uses a set of reference points along the imaginary frequency axis, shown in blue, which are then used to determine a suitable function, whose domain is then extended to the real frequency axis, where it is used to evaluate the self-energy. By choosing purely imaginary frequencies, the structure of the response function becomes particularly simple for the one- and two-component formalism, enabling an efficient evaluation of the dielectric matrix and screened exchange, as shown by Holzer *et al.* and avoids the singularities along the real axis.[25,137] The default setting of the TURBOMOLE program suite employs an identical grid in the construction of the rational approximation, used in the analytic continuation, and the evaluation of the frequency integral over the Green's function and screened exchange in eq. 5.12.

function stays valid as its domain of definition is extended to the real frequency axis, where it is used to approximate the self-energy contribution of the quasiparticles. The self-energy is therefore analytically continued from $i\omega$ to ω as depicted in fig. 5.1.[242–244] Early implementations employed a two-pole model for $\boldsymbol{\Sigma}$.[229,232] Later, more robust forms based on the Padé expansion were introduced. The general form of a Padé approximation is given by

$$\Sigma_{pq}(z) = \frac{P_n(z)}{Q_m(z)}, \tag{5.13}$$

where P_n and Q_m are polynomials of degrees n and m, respectively. The diagonal Padé approximation, which sets $n = m$, can be equivalently expressed as a continued fraction.[243] The rational approximation of the self-energy then reads

$$\Sigma_{pq}(z) = c_0 \left(1 + \frac{c_1(z - z_1)}{1 + \frac{c_2(z-z_2)}{1+\ldots+c_N(z-z_N)}} \right)^{-1}, \tag{5.14}$$

where z are the reference points, here chosen to be purely imaginary, and c are the complex expansion coefficients. In order to obtain a stable solution, these points should be chosen as to provide the correct asymptotic behaviour.[243] This method has been demonstrated to provide more reliable results, when compared to the simple two-pole model[240] and is the default method in the TURBOMOLE program suite. Further details regarding the implementation are provided in ref. 25. If not stated otherwise, the imaginary frequency grid employed for the analytic continuation approach, is chosen to be equal to the roots of the mapped Gauss-Legendre grid used for the frequency integration in eq. 5.12. Here, the default number of Gauss-Legendre quadrature roots is set to 128 and is identical to the number of the expansion coefficients in eq. 5.14. This technique, however, has certain drawbacks as a large number of coefficients can quickly lead to numerical instabilities. Therefore, large grid sizes can sometimes result in spurious solutions even for valence states. The analytic continuation becomes unreliable as frequencies far from the Fermi level are considered, effectively limiting this technique mostly to the valence region.[245]

5.3 Contour Deformation Technique in *GW*

As pointed out in the previous section, the AC-*GW* is suited to describe the self-energy near the Fermi level, but cannot be used to reliably predict the complex structure of the self-energy for low-lying states and core levels. Golze and co-workers observed, that even for small molecules containing only light elements, the predicted qausiparticle energies may already feature errors of several eV in magnitude.[28] In order to provide a more rigorous framework for the description of quasiparticle energies associated with core electrons, an alternative approach is required. Here, the initial ansatz proposed by Godby *et al.* can be employed, who used the contour deformation technique to evaluate the self-energy for real frequencies directly.[158] The correlation contribution of the self-energy in eq. 4.34 is split into an integral along the imaginary frequency axis and a contour integral, along a complex path in frequency space. Following refs. 28, 137, and 236, the correlation self-energy is expressed as

$$\begin{aligned}\boldsymbol{\Sigma}^{\mathrm{c}}(r_1, r_2, \omega) = &\frac{i}{2\pi} \oint \boldsymbol{G}(r_1, r_2, \omega + \omega')(\boldsymbol{W}(r_1, r_2, \omega') - \boldsymbol{v}(r_1, r_2))\mathrm{d}\omega' \\ &- \frac{1}{2\pi} \int_{\infty}^{\infty} \boldsymbol{G}(r_1, r_2, \omega + i\omega')(\boldsymbol{W}(r_1, r_2, i\omega') - \boldsymbol{v}(r_1, r_2))\mathrm{d}\omega' \\ &= \boldsymbol{R}^{\mathrm{c}}(r_1, r_2, \omega) + \boldsymbol{I}^{\mathrm{c}}(r_1, r_2, \omega)\ ,\end{aligned} \tag{5.15}$$

where $\boldsymbol{R}^{\mathrm{c}}$ is the contribution from the contour and $\boldsymbol{I}^{\mathrm{c}}$ represents the integral along the imaginary axis. Note the similar structure of $\boldsymbol{I}^{\mathrm{c}}$ with respect to the imaginary frequency integral in AC-*GW* in to eq. 5.12. The integration path of the contour integral is indicated by the grey line in fig. 5.2. It extends into the first and third quadrant of the complex plane and encloses some, but not all, of the poles of the self-energy. These can be attributed to the Green's function, while the poles of the screened exchange are avoided completely and are not shown in fig. 5.2.[236,244] Besides the poles of the Green's function, the self-energy is analytic everywhere inside the area enclosed by the integration path. Since the position of the poles is known, we may choose to evaluate the integral using the residue theorem. The contour integral is then given by the sum of the residues of the integrand enclosed in the path and $\boldsymbol{R}^{\mathrm{c}}$ simplifies to

$$\boldsymbol{R}^{\mathrm{c}}(r_1, r_2, \omega) = \sum_{z_p \in \mathrm{Z}} \mathrm{Res}\left[\boldsymbol{G}(r_1, r_2, z)\boldsymbol{W}^{\mathrm{c}}(r_1, r_2, z), z_p\right] \quad \text{with} \quad \mathrm{Res}\left[f(z), z_p\right] = \lim_{z \to z_p} (z - z_p) f(z), \tag{5.16}$$

where Z is the set of poles of the Green's function entering the contour in the first quadrant in fig. 5.2.[244] The required residues are easily identified as the quasiparticle energies, resulting in

$$\mathrm{Res}\left[\boldsymbol{G}(r_1, r_2, z)\boldsymbol{W}^{\mathrm{c}}(r_1, r_2, z), z_p = \epsilon_p - i\eta\ \mathrm{sgn}(\epsilon_p - \epsilon^{\mathrm{F}})\right] = \boldsymbol{\Phi}_p(r_1)\boldsymbol{\Phi}_p^*(r_2)\boldsymbol{W}^{\mathrm{c}}(r_1, r_2, z_p). \tag{5.17}$$

By using the canonical Kohn–Sham basis, the matrix representation of the contour integral becomes

$$R^{\mathrm{c}}_{pq}(\omega) = \sum_m \delta_{pq} \tilde{f}_m W^{\mathrm{c}}_{pmpm}(|\omega - \epsilon_m| + i\eta), \tag{5.18}$$

where $\tilde{f}$ is used to indicate if the associated quasiparticle energy enters the first quadrant, in which case the corresponding residue is added to R^{c}_{pq}. $\tilde{f}$ is given by

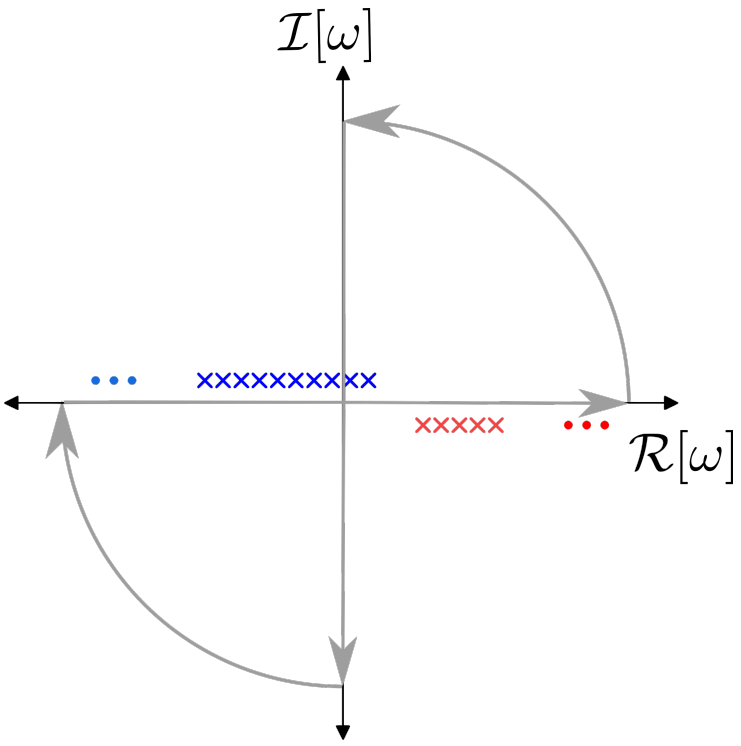

Figure 5.2: Evaluation of the self-energy by using the contour deformation technique. The poles of the Green's function are depicted as blue and red crosses (dots) and lie at the difference between the frequency argument and the quasiparticle energies, ϵ. The residues enter the first quadrant for quasiparticle energies according to $\mathfrak{Re}\left[\omega\right] < \epsilon < \omega^{\mathrm{F}}$, where they need to be included in the contour integrals. The poles of the screened exchange do not extend into the first quadrant and need not to be considered.

$$\tilde{f}_m = \begin{cases} +1 & \text{if} \quad \epsilon^{\mathrm{F}} \leq \epsilon_q < \omega \\ -1 & \text{if} \quad \epsilon^{\mathrm{F}} > \epsilon_q > \omega \\ +\frac{1}{2} & \text{if} \quad \epsilon^{\mathrm{F}} \leq \epsilon_q = \omega \\ -\frac{1}{2} & \text{if} \quad \epsilon^{\mathrm{F}} > \epsilon_q = \omega \\ 0 & \text{else} \end{cases} . \tag{5.19}$$

The limit $\eta \to 0^+$ was specifically addressed by Holzer and Klopper, and assumes a factor of $\frac{1}{2}$ for residues associated with $\omega \to \epsilon_p$, as is the case in self-consistent solutions of the quasiparticle equations in eq. 4.17. Therefore, any dependence on a finite η can be avoided and the response function, used in order to calculate the screened exchange, becomes real.[25,137]
The integral along the imaginary axis is given by

$$I^{\mathrm{c}}_{pq}(\omega) = -\frac{\delta_q}{2\pi} \sum_m \int_{-\infty}^{\infty} \frac{\delta_{pq}}{\omega + i\omega' - \epsilon_m - i\eta \, \mathrm{sgn}(\epsilon^{\mathrm{F}} - \epsilon_m)} W^{\mathrm{c}}_{pmpm}(i\omega') \mathrm{d}\omega'. \tag{5.20}$$

It resembles the self-energy integral used in the analytic continuation technique in sec. 5.2 and can be efficiently evaluated using Gaussian quadrature. We therefore employ the same Gauss-Legendre grid used before in AC-*GW*. As only the real part of the quasiparticle energies are relevant in the context of this study, the above equation is rearranged to extract the real contribution of I^{c}_{pq} only.
Since eq. 5.20 is structurally identical to eq. 5.12 its computational complexity increases similarly approximately as $\mathcal{O}\left(N^4\right)$, due to the computation of the calculation of the response matrix needed in order to evaluate the inverse of dielectric function in its auxiliary subspace representation. When evaluating the contribution of the contour integral, the number of residues entering

the first quadrant is central for the estimating of the scaling behaviour. From eqs. 5.18 and 5.19 it can be seen, that as lower-lying states are to be considered, the number of residues contributing to the contour integral increases, such that this approach formally scales with $\mathcal{O}\left(N^5\right)$ for core states. If the self-energy is to be evaluated at multiple frequencies, the dielectric function required for the evaluation of the screened exchange in eq. 5.18 is generally different for non-degenerate states and two or more energetically close-lying states each require roughly the same computational effort. This is due to the frequency argument in eq. 5.18 being shifted by the quasiparticle energies, independently. Since the Gauss-Legendre roots are chosen to be identical for all states, the dielectric function needs to be evaluated only once at every imaginary frequency reference point. As more and more states are considered, even if they all appear close to the Fermi level, the computational effort shifts from the imaginary frequency integration in I^{c}_{pq} to the calculation of the residues $\boldsymbol{R}^{\mathrm{c}}_{pq}$. Compared to the analytic continuation of the self-energy to the real axis, the contour deformation approach in principle allows for a balanced description of the self-energy at any given frequency and present a more reliable basis for the calculation of CEBEs.[28] However, the scaling for core states, due to the increased number of residues entering the first quadrant, limits the application at the two-component level to small and medium sized systems. In order to extend the range of this method, robust approximations to the residues have to be devised, which will be addressed in the following sections. In the context of this thesis, the initial implementation of the contour deformation approach for *GW* by Holzer[25,137] was extended to be compatible with multiple subsets of quasiparticles, e.g., quasiparticle energies associated with core and valence states. This is used in order to describe core and valence electrons without explicitly evaluating the quasiparticle energies associated with all states in between. Furthermore, additional considerations regarding the stability of this approach, when applied to energetically (quasi-)degenerate states have to be made, as core levels, even at the Kohn–Sham level, are much harder to converge properly and show an increased numerical uncertainty. The finite precision of close deep-lying states may result in spurious divergence in $\boldsymbol{R}^{\mathrm{c}}$ and $\boldsymbol{I}^{\mathrm{c}}$ and will be addressed in the following sections.

5.4 Analytic Continuation of the Screened Exchange

The contour deformation technique allows in principle for a direct description of self-energy for any (real) frequency, which can be used to evaluate CEBEs without relying on the full spectral solution approach or the AC-*GW* method. In an initial step, the self-energy is split into a contour integral and one along purely imaginary frequencies according to fig. 5.2 and eqs. 5.15 to 5.20. While the efficiency of this approach is comparable to the AC-*GW* method for the first few states close to the Fermi level, this changes as the number of states with an energy between the Fermi energy and the target frequency increases. Here, the number of residues entering the area enclosed by the contour grows, due to eq, 5.19. The evaluation of the self-energy within the contour deformation method scales with $\mathcal{O}\left(N^4\right)$ to $\mathcal{O}\left(N^5\right)$, depending on whether valence- or core-level states are of interest. Note that an analogues considerations can be made for high-lying virtual states, but since these are rarely of interest, they will not be explicitly discussed here. In comparison to the CD-*GW* approach, the self-energy as obtained in the context of the analytic continuation *GW* method, requires formally the exact same effort for any frequency. However, the quality of the analytic continued self-energy may deteriorate relatively quickly for large frequencies, noting the complicated structure of $\boldsymbol{\Sigma}$, due to eqs. 4.6 and 4.32.

Duchemin and Blase proposed combining aspects of both methods and adapted the contour deformation technique in a simple way:[246,247] Following the regular contour deformation approach, the self-energy is rewritten according to eq. 5.15, the screened exchange is evaluated using a rational approximation of the screened exchange instead. While in AC-*GW* the self-energy is represented by a rational function, this can be done in an completely analogues manner for the screened exchange. The contour integral thus becomes

$$R^{\mathrm{c}}_{pq}(\omega) \approx \sum_m \delta_{pq} \tilde{f}_m \tilde{W}^{\mathrm{c}}_{pmpm}(|\omega - \epsilon_m| + i\eta) \quad \text{with} \quad \tilde{W}^{\mathrm{c}}_{pmpm}(z) = c_0 \left(1 + \frac{c_1(z - z_1)}{1 + \frac{c_2(z-z_2)}{1+\ldots+c_N(z-z_N)}}\right)^{-1}, \tag{5.21}$$

where the coefficients, c, are implicitly dependent on the considered matrix element W_{pmpm}. Assuming the rational approximation can be used to adequately represent all required residues, employing only a few reference frequencies, the formal scaling of evaluating eq. 5.21 is reduced to $\mathcal{O}\left(N^4\right)$. This function may similarly be used in order to reduce the number of frequencies, for which the dielectric function is evaluated along the imaginary frequency. By calculating the dielectric function at only a subset of the true Gauss-Legendre roots in eq. 5.20, we may try to approximate the remaining ones using the same rational approximation as for the real residues.[246] The advantage of using analytically continuing the screened exchange, instead to the self-energy directly, lies in the much simpler structure of $\boldsymbol{W}$. It only contains the poles associated with the charge-neutral excitations. The rational approximation is therefore assumed to be much more well-behaved, staying valid for larger frequency ranges.[246]
In order to stabilize the analytic continuation further, the imaginary frequency grid may be extended by a set of reference points along the real axis. Duchemin and Blase employed a set of additional supporting points, linearly spaced along the real axis and shifted by η into the imaginary plane, where η was chosen between 0.1 and 1.5 eV. They further modified the continued fraction method by imposing the symmetry of the screened exchange. The reference points included in their Padé approximation, were selected, as to minimize the least-square error, while using as few points, as possible.[246] The convergence of the Padé type approximations is often impaired by so-called "Froissart doublets", corresponding to pole-zero pairs.[248,249] By limiting the number of coefficients in the continued fraction method, the function may return more reliable results, compared to trying to provide a rational approximation of the maximum degree available. This avoids overfitting of the screened exchange.

5.5 Analytic Continuation using an Adaptive Frequency-Sampling Technique

To recap the central idea of the preceding section: Using the analytic continuation of the screened exchange in order to obtain the residues in CD-*GW*, the explicit calculation of the dielectric function for all frequencies individually can be avoided. This becomes especially relevant, as the number of contributing residues increases, as is the case for lower-lying or especially core states. The evaluation of the response function required for the inverse dielectric function at the real frequencies, then quickly becomes a bottleneck in the standard CD-*GW* approach. This step is replaced by an analytic continuation of the rational approximation of the screened exchange in eq. 5.21. If multiple quasiparticle states are considered, the advantage of this approach becomes even more obvious. Here, a common frequency grid can be employed and the dielectric function needs to be calculated and inverted only once for all unique ω. In principle, these can be used to obtain all required matrix elements of the screened exchange. However, the original approach was found to be unreliable for core states, even in small molecules.[246] It employed a linearly spaced grid starting from zero and a second grid at the largest frequency required. These frequencies correspond to the differences between the target frequency, the quasiparticle energy of concern, and the quasiparticle energies of all other states entering the area enclosed by the contour, as seen in eqs. 5.18 and 5.21. In tab. 5.1 results are shown, where a variant of this approach, using a different slightly different form for the analytic continuation described in sec. 5.5.1 is employed, in order to describe the three lowest-lying states of the noble gases Ar, Kr and Xe. We find the quasiparticle energies of the $1s$ state to be reasonable well described with respect to standard CD-*GW* . However, large discrepancies are observed for some of the remaining states, showing deviations as high as several eV. This agrees with the initial results by Duchemin and Blase.[246] We aim here, at improving this approach, by employing a more concise and flexible frequency grid. This grid is ideally chosen in an adaptive manner, with respect to the individual requirements of the system itself, By constructing this grid for systems directly, a balanced description for a wider range of molecules and states may be provided. We start by considering the full frequency grid, including all frequencies of the contributing residues for the selected quasiparticle states according to eq. 5.19. These frequencies often occur in relative proximity, forming groups, which for atoms can be related to

the different shells. A strategy can be devised by simply exploiting this sparsity, assuming the dielectric function to be well represented by a suitable rational approximation having a reference point in close proximity. The target set is build in reverse, by first constructing the complete frequency grid, which is then subsequently reduced, by discarding close values according to some thresholds. The criteria used here, were optimized by a series of test calculations and aim at accounting for the different requirements for core and valence states, due to their difference in magnitude. A frequency is eliminated if it is found either within $5 \cdot 10^{-6}$ E_h of another grid point, or if their relative magnitude differs by less than 0.01 %. For a core state the residues associated with valence electrons, are therefore ideally represented by only few actual frequencies, since the relative energies are similar. Employing this grid for the Ar, Kr and Xe, the errors were found to be largely reduced with respect ot the values presented in tab. 5.1. The largest error was found for the Xe $1s$ state at $9 \cdot 10^{-8}$ eV. The respective quasiparticle energy is found at approximately -34 694.34 eV. All other errors were negligible. Note, the values presented here for Xe, differs strongly from the experimentally measured ionization potential, as further considerations need to be made in order to properly describe ionization potentials at these energy levels.[250] The frequency grid for the Xe $1s$ state includes ten real frequency grid points, roughly half of what is required for the standard CD-*GW* method. By adopting a common frequency grid for all states, the

Table 5.1: Quasiparticle energies as obtained using the contour deformation techniques (CD-*GW*)[25] and the analytic continuation technique for the residuals (acCD-*GW*), employing 10 grid points above zero and the difference of the individual $1s$ states and the HOMO energy, respectively, separated by 1 eV. The linearization parameter was kept fixed (Z=1) in all calculations. All calculations were done using the PBE0[251] density functional with a fine grid (size 5a in `TURBOMOLE`)[252–254]. Scalar relativistic effects were included using the X2C one-component Hamiltonian employing the x2c-TZVPPall basis set and suitable auxiliary basis sets.[221,255] For the CD-*GW* calculations, default parameters as provided by the `TURBOMOLE` program suite, were employed. All energies are given in eV.

Element	State	CD-*GW*	acCD-*GW*	abs. deviation
Ar	$1s$	-3210.17	-3210.17	$7.80 \cdot 10^{-7}$
	$2s$	-323.65	-312.96	$1.07 \cdot 10^{1}$
	$2p$	-248.85	-248.85	$1.70 \cdot 10^{-7}$
Kr	$1s$	$-14\,375.11$	$-14\,375.11$	$5.00 \cdot 10^{-8}$
	$2s$	-1936.89	-1926.86	$1.00 \cdot 10^{1}$
	$2p$	-1704.45	-1704.45	$8.98 \cdot 10^{-5}$
Xe	$1s$	$-34\,694.34$	$-34\,694.34$	$4.46 \cdot 10^{-4}$
	$2s$	-5479.94	-5480.47	$5.34 \cdot 10^{-1}$
	$2p$	-4910.78	-4910.72	$6.56 \cdot 10^{-2}$

dielectric function needs to be evaluated only once for all reference points, allowing for a similar strategy employed in the calculation of the imaginary integral. The formal scaling of this is given by $\mathcal{O}(N_\omega \cdot N^4)$, where N_ω is the number of real frequencies. In the following sections, some additional aspects of this technique will be presented, including a description of the implementation done and used in the context of this thesis. This approach will then be tested and compared against the regular CD-*GW* approach, as provided by the `TURBOMOLE` program suite, in order to assess its performance for CEBEs, but also for cases, where a high number of states at the valence level is required.

5.5.1 Evaluation of the Screened Exchange

We define a reference set of functional values at frequencies for which the matrix elements of the screened exchange have been evaluated explicitly. In order to obtain the contour integral in eq. 5.21, the remaining residues are evaluated by means of an analytic continuation. This implies a suitable form for the function has been found, here, given by a rational approximation. While these types of functions have been successfully applied in the context of *GW*,[228–234,246] they can be difficult to converge, as the number of coefficients is increased.[249] This is due to overfitting and the occurrence of spurious poles in many rational approximations. To this end, the solution has to be optimized in a way, that not only fit the functional values, but ideally

using the minimal complexity possible. In the following, the Adaptive Antoulas-Anderson (AAA) algorithm presented by Nakatsukasa *et al.* will be used, which will be briefly presented in the following.[256,257] This algorithm tries to find an optimal function, by subsequently increasing the complexity, until convergence is found or the number coefficients exceeds a predefined threshold. Here, the matrix elements of the screened exchange are expressed as

$$W_{pmpm}(z) \approx f(z) = \frac{P(z)}{Q(z)} = \sum_j^n \frac{w_j f(z_j)}{z - z_j} \Bigg/ \sum_j^n \frac{w_j}{z - z_j} \ , \tag{5.22}$$

where n is the number of complex reference points z and $f(z_j)$ are the corresponding function values. w are the weights, which are unknown and subject of the optimization step. This is the barycentric form of a rational approximation, which is oftentimes better conditioned and offers higher stability, when compared to some other common Padé type forms.[257–259] This function has poles at the incorporated reference points, for which the values can be obtained by interpolation.
The AAA algorithm is an iterative technique. We choose to start this algorithm at $z = 0$. This point is always included in our reference set and corresponds to the residue arising from the pole associated with the selected quasiparticle itself. It sits right on top of the contour and occurs for every single selected quasiparticle energy. In order to obtain the weights, eq. 5.22 is rearranged to

$$\sum_j^n \frac{w_j}{z - z_j} r(z) = \sum_j^n \frac{w_j f(z_j)}{z - z_j} \qquad \text{with} \qquad z \notin Z_s. \tag{5.23}$$

The denominators become singular at the sample points included in the set Z_s, which have to be explicitly excluded. The weights can be found by minimizing the error for all remaining reference points not already in Z_s. Setting $r(z) = f(z)$ we find

$$\begin{aligned} &\text{minimize} \left\| \sum_j^n \frac{w_j f(z)}{z - z_j} - \sum_j^n \frac{w_j f(z_j)}{z - z_j} \right\| \\ &\text{with} \quad z \in Z \setminus Z_s \quad \text{and} \quad \sum_j^n \|w_j\|^2 = 1, \end{aligned} \tag{5.24}$$

where Z is the complete set of reference points provided. The above problem comprises of solving a linear system of equations, which can be expressed more conveniently in matrix form, arriving at

$$\boldsymbol{L}\boldsymbol{w} = \boldsymbol{b}, \tag{5.25}$$

where $\boldsymbol{L}$ is the non-square complex Löwener matrix,[260] whose elements are given by

$$L_{ij} = \frac{f(z_i) - f(z_j)}{z_i - z_j}. \tag{5.26}$$

We are interested in the solution of the above equation for which the elements of the right-hand side become zero. These solutions correspond to the null space of matrix $\boldsymbol{L}$ and are easily obtained by means of a singular value decomposition (SVD).[249] The solution vector is usually non-unique and can even contain vanishing elements, corresponding to a weight of

zero assigned to a point in the set. In this manner the rational approximation to the matrix elements of the screened exchange according to eq. 5.22 is obtained.
The adaptive part of the AAA algorithm refers to the expansion of the set, Z_s, containing the supporting points for the rational function. This is done by searching for the largest deviation of the last approximation and adding this to the set Z_s and the next iteration is performed. The iterative procedure terminates, if either all errors are below a predefined threshold or the number of included points exceeds the maximum number of supporting points allowed, which can be chosen to be smaller or equal to the total number of reference points. In the context of this thesis, the algorithm was assumed to be converged if the maximum absolute error for all remaining sample points was found to be smaller than 10^{-10}. The poles and residues of the underlying rational function can be determined using a matrix eigenvalue problem.[257,261,262] If the target value approaches a pole its function value is obtained by a simple interpolation, except, for poles corresponding to a reference point. In this case, the target value may be directly approximated by the closest reference, assuming the frequency dependence to be negligible. The threshold for which the variation of the dielectric function is assumed to be negligible is set to $5 \cdot 10^{-6}$ E_h by default, which is the same threshold used for the construction of the reference set. In an additional step, pole-zero pairs may be removed, by evaluating the residues at the poles. A pole is assumed to be spurious if its residue is close to zero. Here, a threshold of 10^{-13} is adopted. These poles often vanish upon removal of the closest lying supporting point in the set used for the rational approximation.[257] In the context of this thesis, most states were found to converge relatively quickly with respect to the number of reference points, such that these spurious poles were found to be exceedingly rare and as such, are not further discussed. The implementation follows directly from the steps outlined above and is similar to the initial presentation by Nakatsukasa *et al.* in ref. 257. The Löwener matrix in eq. 5.26 needs to be reassembled in every step. The weights are obtained using a SVD, which is the time-determining step in this algorithm, which is done using the routine ZGESDD for complex generalized matrices of the LAPACK package.[263] However, the number of grid points, including real and imaginary frequencies, rarely exceeds 200 and compared to the calculation of the matrix elements, can be done in negligible time.

5.5.2 The fsCD-*GW* Algorithm

Following the considerations in the preceding sections and assuming a suitable ground state, the quasiparticle energies within the fsCD-*GW* algorithm require three distinct steps:

1. The calculation of the RI-intermediates according to eq. 5.6.
2. The construction of the frequency grid.
3. The evaluation of the real part of the self-energy and quasiparticle energies.

The generation of the 3-index-intermediates needs to be done only once at the beginning of the calculation, which are then stored on disc. Note however, that depending on the size of the system considered and the basis set employed, these quantities can become large relatively quickly for both one- and two-component calculations, the latter of which adds roughly a factor of two to four. The RI-intermediates are readily available in the `TURBOMOLE` program suite, following implementations and techniques described and assessed in refs. 224, 225, 227, and 82. The second step in the above is straightforward to implement. The construction of the frequency grid only requires knowledge of the current approximations to the quasiparticle states, taken as the Kohn–Sham eigenvalues in the first iteration, and comes with a negligible cost. A description of the frequency selection strategy, employed throughout this thesis, was given in previous sections. Here, we will primarily be concerned with the last step, which pertains the evaluation of the self-energy. It involves both the frequency integration along the imaginary axis and the calculation of the residues. In the following discussion, this last step will again be split into three distinct steps:
The first part is completely analogues to the standard CD-*GW* method and follows the implementation by Holzer presented in

ref. 25. The necessary steps are shown in fig. 5.3 and are required in order to evaluate the real part of the imaginary frequency integral I^{c}_{pp} in eq. 5.20. The matrix elements of the screened exchange W_{pmpm} at the imaginary Gauss-Legendre quadrature points, $i\omega_I$, are obtained as intermediate quantities and are saved for latter use in the calculation of the residues by an analytic continuation. This part of the algorithm scales formally with $\mathcal{O}\left(N_I \times N^4\right)$, where N_I is the number of Gauss-Legendre quadrature points and N is again used to indicate the system size. The time-determining step is step 2 in fig. 5.3, which is the calculation of response function, in order to obtain the dielectric function. The Cholesky decomposition in step 4 can only be used for purely imaginary frequencies, for which the dielectric matrix becomes positive definite.[25,137] In the context of this work, this part was only slightly modified and follows the original implementation by Holzer in ref. 25. The quadrature in step 9 can quickly become numerically unstable, if two or more large quasiparticle energies are in close energetic proximity. This latter part is commonly encountered for CEBEs, since the numerical noise for core-excited states is comparatively large and can result in an spurious splitting of degenerate states. These cases are especially problematic if (partial) self-consistency is to be achieved, where small numerical instabilities can result in feedback effects, amplifying initially small differences, which then converge to spurious solutions. Specifically, these instabilities arise from the real part of $I^{\mathrm{c}}_{pp}(i\omega_I)$ in eq. 5.20, as the Gauss-Legendre roots become small compared to the energetic difference between two quasi-degenerate states. To illustrate this, consider the real part of the integral along the imaginary frequency axis in eq. 5.20, which can be rewritten as

$$\begin{aligned}
\mathfrak{Re}\left[I^{\mathrm{c}}_{pp}(\epsilon_p)\right] &= -\frac{1}{2\pi} \sum_{\omega_I \in S_{\omega_I}} w_I \sum_m \mathfrak{Re}\left[\frac{1}{\epsilon_p + i\omega_I - \epsilon_m - i\eta\ \mathrm{sgn}(\epsilon^{\mathrm{F}} - \epsilon_m)}\right] W^{\mathrm{c}}_{pmpm}(i\omega_I) \\
&= -\frac{1}{2\pi} \sum_{\omega_I \in S_{\omega_I}} w_I \sum_m \frac{\epsilon_p - \epsilon_m}{(\epsilon_p - \epsilon_m)^2 + (\omega_I - \eta\ \mathrm{sgn}(\epsilon^{\mathrm{F}} - \epsilon_m))^2} W^{\mathrm{c}}_{pmpm}(i\omega_I),
\end{aligned} \tag{5.27}$$

where w_I is the Gauss-Legendre weight, associated with root ω_I. Consider the following limit

$$\omega_I - \eta\ \mathrm{sgn}(\epsilon^{\mathrm{F}} - \epsilon_k) \ll \epsilon_p - \epsilon_k, \tag{5.28}$$

where p and k are energetically close quasi-degenerate states. The real sum in eq. 5.27 then becomes

$$\begin{aligned}
\mathfrak{Re}\left[I^{\mathrm{c}}_{pp}(\epsilon_p)\right] &= -\frac{w_S}{2\pi} \frac{(\epsilon_p - \epsilon_k) W^{\mathrm{c}}_{pkpk}(i\omega_S)}{(\epsilon_p - \epsilon_k)^2 + (\omega_I - \eta\ \mathrm{sgn}(\epsilon^{\mathrm{F}} - \epsilon_k))^2} - \frac{1}{2\pi} \sum_{\omega_I \in S_{\omega_I} \setminus \{\omega_S\}} \dots \\
&= -\frac{w_S}{2\pi} \frac{W^{\mathrm{c}}_{pkpk}(i\omega_S)}{\Delta} - \frac{1}{2\pi} \sum_{\omega_I \in S_{\omega_I} \setminus \{\omega_S\}} \dots .
\end{aligned} \tag{5.29}$$

As Δ approaches zero, while still being larger than ω_I, the first term diverges. $\mathfrak{Re}\left[I^{\mathrm{c}}_{kk}(\epsilon_k)\right]$ is obtained in a similar manner. The associated term then has the exact opposite sign, as the pole is approached from the other site. The screened exchange is symmetric with respect to pairwise interchanging of the indices. As these values are close to a singularity in $\boldsymbol{G}$, they can become arbitrarily large, which results in spurious self-energies. The initial small difference, is then amplified, especially for self-consistent solutions. This behaviour stems from the finite numerical quadrature and it is not associated with a physically sensible self-energy. A possible solution involves the use of a finite shift along the imaginary plane, as is done, e.g., in the spectral *GW* method. In order to be consistent, this would require the introduction of the same finite η in the screened exchange, which would destroy the simple structure of the dielectric function it has for $\eta \to 0^+$.[137] Instead we may identify these grid points, by testing for instabilities and interpolate between both terms, if we assume these states to belong to degenerate

Calculation of the self-energy matrix element $\Sigma_{pp}(\epsilon_p)$

input : S_{ω_I} Gauss-Legendre roots; (N_I)

S_{ω_R} sampled real frequency grid; (N_R)

S_p selected quasiparticle states; (N_p)

R^P_{ai}, R^P_{pm} RI-intermediates ; $(N_{\text{aux}} \times (N_{\text{virt}} \times N_{\text{occ}} + N_p \times N_m))$

output: $\mathfrak{Re}\left[\Sigma^c_{pp}\right]$ using eq. 5.15 for all selected states p; (N_p)

Z_p quasiparticle weights given in eq. 4.39; (N_p)

Loop 1: Imaginary grid points $W_{pmpm}(i\omega_I)$ and $\mathfrak{Re}\left[I^{\text{c}}_{pp}\right]$

forall *elements* ω_I *in* S_{ω_I} **do**

  Calculate response function in the auxiliary subspace $\Pi(\omega)$ at imaginary frequencies $i\omega_I$ using the RI-intermediates R^P_{ai} using eq. 5.9;

  Obtain the auxiliary subspace representation of the dielectric function $\epsilon_{PQ}(i\omega_I) = (\delta_{PQ} - \Pi_{PQ})$ from eq. 5.9;

  Calculate the Cholesky factorization of the dielectric function $\epsilon_{PQ}(i\omega_I) = LL^{\text{T}}$;

  Obtain the inverse $\left[L^{-1}\right]_{QP}$ of the Cholesky matrices;

  forall *elements* p *in* S_p **do**

    Scale RI-intermediates $\tilde{R}^P_{pm}(i\omega) = \sum_Q R^Q_{pm}\left[L^{-1}\right]_{QP}$;

    Calculate the correlation contribution of screened exchange $W^{\text{c}}_{pmpm}(i\omega_I) = \sum_P \left(\tilde{R}^P_{pm}(i\omega_I)\tilde{R}^{P*}_{pm}(i\omega_I) - R^P_{pm}R^{P*}_{pm}\right)$;

    Add the matrix element of the screened interaction scaled by the Gauss-Legendre weight to $I^{\text{c}}_{pp}(\epsilon_p)$, as in eq. 5.20;

  end

end

$\vdots$

Figure 5.3: First part of the evaluation of the self-energy, where the intermediate quantity I^{c}_{pp} at the required quasiparticle energies along purely imaginary frequencies and the sample points $W^{\text{c}}_{pmpm}(i\omega_I)$ is calculated. The dimensions of selected quantities are shown in parenthesis. ω_I are the N_I mapped Gauss-Legendre quadrature roots, N_R is the number of real frequency grid points chosen in accordance with the strategy outlined in sec. 5.5 and p are the indices of the selected states for which the quasiparticle energies shall be determined. N_{aux}, N_{occ} and N_{virt} is the number of (RI-)auxiliary basis functions, occupied and virtual states respectively. N_m is the number of all states. The algorithm scales roughly as $\mathcal{O}\left(N_I \times N^4\right)$, where N describes the size of the system considered. This first loop follows the implementation of the CD-*GW* approach by Holzer in `TURBOMOLE` presented in ref. 25, on which this work is based on.

orbitals, they would cancel out completely. These features often result from numerical artefacts and do not carry any physical meaning. In the context of this work, these instabilities were only identified for low-lying states with high energies, for which a simple criterion based for (quasi-)degeneracies based on absolute and relative energies can be used.

Calculation of the self-energy matrix element $\Sigma_{pp}(\epsilon_p)$ (continued)

input : S_{ω_I} Gauss-Legendre roots; (N_I)

S_{ω_R} sampled real frequency grid; (N_R)

S_p selected quasiparticle states; (N_p)

R^P_{ai}, R^P_{pm} RI-intermediates in eq. 5.9; $(N_{\text{aux}} \times (N_{\text{virt}} \times N_{\text{occ}} + N_p \times N_m))$

output: $\mathfrak{Re}\left[\Sigma^c_{pp}\right]$ using eq. 5.15 for all states p selected; (N_p)

Z_p quasiparticle weights given in eq. 4.39; (N_p)

⋮

Loop 2: Real grid points $W_{pm'pm'}(\omega_R)$

forall *elements* ω_R *in* S_{ω_R} **do**

  Calculate response function in the auxiliary subspace $\Pi(\omega)$ for real frequencies ω_R using the RI-intermediates R^P_{ai} similar using eq. 5.9 for real frequencies;

  Obtain the auxiliary subspace representation of the dielectric function $\epsilon_{PQ}(i\omega_I) = (\delta_{PQ} - \Pi(\omega_I))$ from eq. 5.9;

  Calculate inverse dielectric function $\epsilon^{-1}_{PQ}(\omega_R)$;

  Compute the unit-shifted inverse dielectric function $\bar{\epsilon}^{-1}_{PQ} = \epsilon^{-1}_{PQ}(\omega_R) - \delta_{PQ}$;

  forall *elements* p *in* S_p **do**

    forall m' *with frequencies* $\omega_{pm'} = |\epsilon_p - \epsilon_{m'}|$, *whose residues enter the 1. quadrant according to eq. 5.19* **do**

      Calculate $W^{\text{c}}_{pm'pm'}(\omega_R) = \sum_P R^P_{pm'} \sum_Q \bar{\epsilon}^{-1}_{PQ} R^{Q*}_{pm'}$;

    end

  end

end

⋮

Figure 5.4: Second part and continuation of the algorithm presented in fig. 5.3. The supporting points along the real axis, i.e. the selected sampled real frequencies ω_R are constructed. m' refers to states m which enter the first quadrant and includes a small subset of all residues for most states. See description of fig. 5.3 for an explanation of the quantities and dimensions.

Calculation of the self-energy matrix element $\Sigma_{pp}(\epsilon_p)$ (continued)

input : S_{ω_I} Gauss-Legendre roots; (N_I)

S_{ω_R} sampled real frequency grid; (N_R)

S_p selected quasiparticle states; (N_p)

R^P_{ai}, R^P_{pm} RI-intermediates in eq. 5.6; $(N_{\text{aux}} \times (N_{\text{virt}} \times N_{\text{occ}} + N_p \times N_m))$

output: $\mathfrak{Re}\left[\Sigma^c_{pp}\right]$ using eq. 5.15 for all states p selected; (N_p)

Z_p quasiparticle weights given in eq. 4.39; (N_p)

$\vdots$

Loop 3: Contribution from residues $R^c_p(\omega_N)$ and $\mathfrak{Re}\left[\Sigma_{pp}(\epsilon_P)\right]$

forall *elements* p *in* S_p **do**
  forall m' *with frequencies* $\omega_{pm'} = |\epsilon_p - \epsilon_{m'}|$, *whose residues enter the 1. quadrant according to eq. 5.19* **do**
    if $\|\omega_{pm} - \omega_R\| \leq \tau_1 \; \forall \; \omega_R \in S_R$ **then**
      Set $W_{pmpm}(\omega_{pm}) = W_{pmpm}(\omega_R)$;
    else
      Calculate rational approximation of $W_{pmpm}(\omega_{pm})$ via the Adaptive Antoulas-Anderson algorithm in sec. 5.5.1
    end
    Add $W_{pmpm}(\omega_{pm})$ to $R^c_{pp}(\epsilon_p)$;
  end
  Evaluate $\mathfrak{Re}\left[\Sigma_{pp}(\epsilon_P)\right] = I^c_{pp}(\epsilon_p) + R^c_{pp}(\epsilon_p)$;
  if *linearized* G_0W_0 **then**
    Calculate Z_p
  else
    Set Z_p to 1
  end
end

Figure 5.5: Continuation of figs. 5.3 and 5.4. In the final step the second contribution to the self-energy is evaluated using the imaginary and real frequency points obtained in the first two steps. The frequency dependence of the screened exchange is assumed to be negligible for frequencies within τ_1 of a given reference point. The remaining points are evaluated using the AAA algorithm in sec. 5.5.1.

The next step encompasses the evaluation of the matrix elements of the screened exchange at the real frequency grid points selected previously. The general algorithm is presented in fig. 5.4. In contrast to the standard CD-*GW* approach, is given in sec. 3.5.6 of ref. 25, the set S_{ω_R} of real frequencies is usually smaller then the set of imaginary frequencies needed for the Gauss-Legendre quadrature S_{ω_I}. While the inverse of the dielectric function in the first step is positive definite, this is not ensured for real frequencies.[137] Instead of using a Cholesky decomposition, as in the step 4 in fig. 5.3, the contraction with the 3-index-intermediates is done in a straightforward manner in order to obtain the screened exchange. Since only a subset of the poles of the Green's function enter the first quadrant, not all states need to be considered. Matrix elements of the screened exchange that do not contribute to the contour integral, $\boldsymbol{R}^{\mathrm{c}}_{pp}(\epsilon_p)$, need not to be evaluated. In practice instead of using eq. 5.19 directly, poles are selected within a certain range around ϵ_p for which degeneracy is assumed. This is done in a consistent manner with the integration along the imaginary frequency and the third step. To account for numerical noise, we use two thresholds: The first is used to directly compare the absolute difference of two states and is chosen to be 10^{-6} E_h. The second parameter is used to compare relative energies and is set to 0.01%. This latter parameter is again required in order to account for the numerical uncertainty typically found for core-levels.
In the last step, shown in fig. 5.5, the self-energy and the renormalization parameter are calculated from the sample points along the imaginary and real frequency axes. Residues of real frequencies in the set S_{ω_R} are taken directly, and would correspond to poles in the rational approximation in eq. 5.22 if they are included as supporting points. Furthermore, the deviation of the screened exchange is assumed to be negligible within $5 \cdot 10^{-6}$ E_h. For all other grid points the matrix elements are obtained using the AAA algorithm discussed in sec. 5.5.1. The renormalization parameter Z_p is only required for linearized G_0W_0 and is evaluated by numerical differentiation. In contrast to the standard CD-*GW* approach, fsCD-*GW* uses an outer frequency loop for the screened exchange for both, the imaginary and the real frequencies. Therefore, the response matrix needs to be calculated only once for every grid point, while in standard CD-*GW* the real frequency is done separately for every quasiparticle state selected. In fsCD-*GW*, the computational effort of the second part roughly becomes $\mathcal{O}(N_{\omega_R} \cdot N^4)$, where N_{ω_R} is the number of grid points along the real axis, while the time for the evaluation of the residues is usually negligible. The scaling behaviour will be further assessed in sec. 5.6.3. We close this section by briefly discussing the partial self-consistent GW_0 method. Since the matrix elements of the screened exchange do not change, as the dielectric function is kept fixed at the Kohn–Sham level, we may choose to forgo the construction of a new reference grid. By using the matrix elements of the screened exchange from the first iteration, the imaginary frequency integral, as well as the residues, may be evaluated in negligible time. The effort associated with the GW_0 method then becomes comparable to the G_0W_0 method. In standard CD-*GW* the residues need to be recalculated in every iteration, as the poles of the Green's function shift, as the quasiparticle energies are updated. The computational effort for GW_0 and ev*GW* in the standard variation is therefore comparable for low-lying states, if a similar convergence behaviour can be assumed. For ev*GW*, the dielectric matrix changes and all the matrix elements of the screened exchange need to be reevaluated.

5.6 Assessment of fsCD-*GW*

The fsCD-*GW* algorithm in principle allows for the efficient calculation of quasiparticle energies for a wide range of states at a reasonable cost. Using this approach the error of the analytic continuation approach in the case of the noble gas atoms Ar, Kr and Xe, discussed in sec. 5.4 was found to decrease substantially, when compared to the an approach based on the ref. 246. In this section, this method is further assessed, in the context of selected systems in order to demonstrate its ability in providing quasiparticle energies for core and valence state. The considerations regarding the numerical instabilities for low-lying (quasi-)degenerate states are discussed for the $1s$ states in the C_{60} molecule. In order to estimate the applicability for valence states, a series of three coinage metal complexes, previously investigated in ref. 264, are used. Finally, the scaling behaviour at the one- and two-component level is assessed for a series of small Cd clusters of varying sizes, using the structure provided in ref. 265.

5.6.1 Quasi-Degeneracies in Core-Level States: the C_{60} Molecule

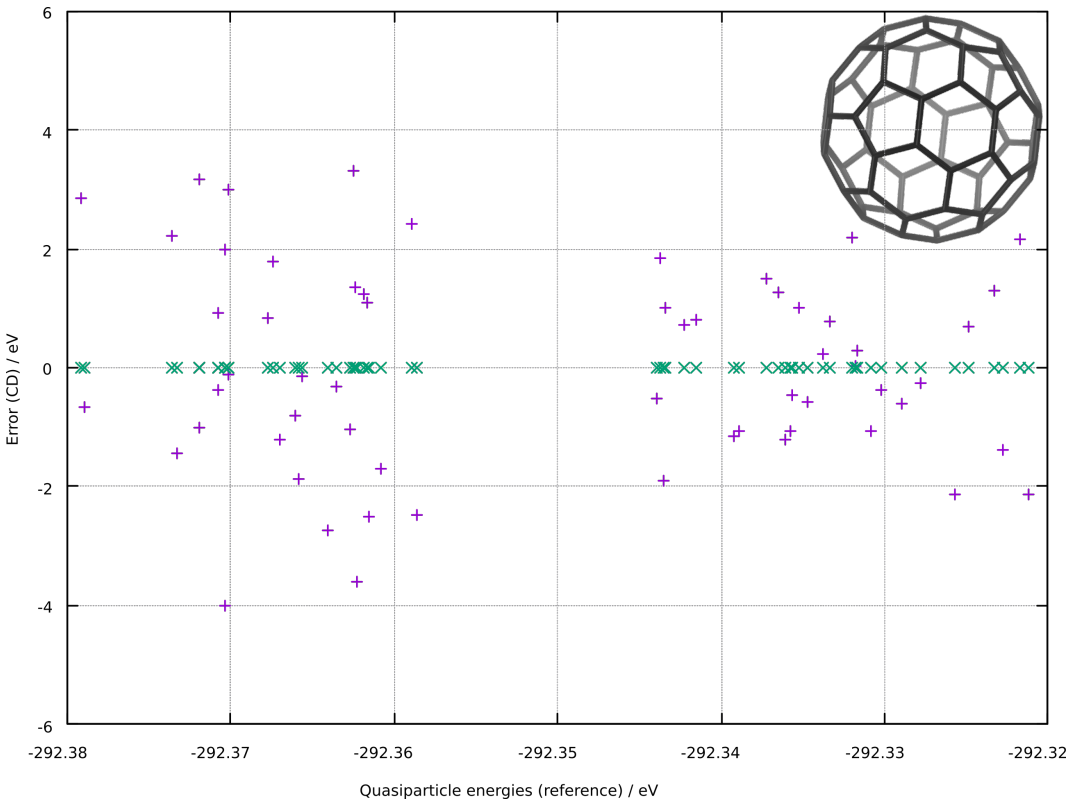

Figure 5.6: Errors of the quasiparticle energies for the lowest-lying 60 carbon $1s$ type orbitals of C_{60}, at the one-component G_0W_0 level, setting the renormalization parameter to one. The solution of the spectral *GW* method were used as a reference, where a finite imaginary shift of 0.001 is used, following eq. 83. in 172. Ground state was optimized employing the PBE0 [251] density functional, integrated on a fine grid [252–254], using the def2-SVP basis. [224,266,267] Ground state energies were converged to 10^{-10} E_h in the energy and 10^{-9} in the density. Data shown in violet corresponds to the regular CD-*GW* approach, using the standard Gauss-Legendre quadrature grid, while data shown in green disregards instabilities according to the strategy discussed in sec. 5.5.2. The maximum error introduced by using the frequency sampling strategy in the latter approach, was found to be lower than $2 \cdot 10^{-8}$ eV, which are therefore presented.

The Buckminsterfullerene, C_{60}, offers a interesting benchmark system, to test the behaviour of the contour deformation technique and the frequency sampling strategies. Here, the system is evaluated at the one-component level without any constrains regarding point group symmetry. Computational details are given in fig. 5.6, where the different CD-*GW* approaches are compared to a reference, which is provided by using the full spectral representation of the self-energy expression, described in sec. 4.3. We limit ourselves to the 60 lowest-lying quasiparticle states, associated with the carbon $1s$ orbitals in the context of G_0W_0. The renormalization parameter is set to one in order to avoid introducing additional errors arising due to the numerical differentiation in the following. The Kohn–Sham eigenvalues are found ranging from -279.84 to -279.80 eV. Using the *GW* method, employing the full spectral representation of the self-energy, the corresponding quasiparticle energies are then shifted to values between -292.38 and -292.32 eV. For the standard CD-*GW* method using all Gauss-Legendre quadrature points along the imaginary frequency axis, the mean signed error (MSE) is found to at approximately $2 \cdot 10^{-5}$ eV, while the mean absolute deviation (MAD) is found at 1.40 eV. The standard deviation is 1.69 eV. The largest absolute deviation is 4.02 eV and does not appear to be associated with any specific property of the particular state. The vanishingly small MSE suggests the distribution to be centered closely around the reference quasiparticle energies. From fig. 5.6, the original CD-*GW* approach in violet, appears to fail for theses states. The errors appear to be mostly statistical in nature, with no clear pattern. This behaviour can be understood from the discussion provided in sec. 5.5.2. If two states are considered to be quasi-degenerate, the resulting instabilities should appear similar in magnitude, but with opposite sign for the terms arising in both states. This argument

can be extended to three or more states in close proximity, as needed for the above example. A summation of all states would then be expected to roughly cancel out. This seems to agree with the above observation. While the MAD is relatively large, the MSE vanishes. These features are clearly spurious. If the corresponding poles are identified beforehand and the respective Gauss-Legendre weight set to zero, the spurious shifts of the quasiparticle states is reduced or vanishes completely. This approach corresponds to the data shown in green in fig. 5.6. The MSE seems to be not affected, while the MAD now decreases to less then 3 meV. The largest deviation is reduced to 5 meV and the STD likewise decreases to 3 meV. We note, that the error introduced by the use of the frequency sampling algorithm (fsCD-*GW*) compared to the above appears negligible in this example. The largest deviation was found to be less then $2 \cdot 10^{-8}$ eV. The fsCD-*GW* approach uses a frequency grid consisting of 14 reference points along the real axis and an additional 128 frequencies along the imaginary axis. The real frequency points only contain a single frequency close to the core levels, while the rest correspond to frequencies associated with valence levels. For residues arising from energetically close quasiparticle energies, the immediate frequency range appears to be well represented by the static limit, plus the 128 imaginary frequencies, while higher frequencies are stabilized by additional reference points. All three contour deformation calculations were done on a Intel Xeon Gold 6254 processor using 20 of the 36 threads. The computational effort reduces from initially five days in the case of standard CD-*GW* to merely two hours, with respect to the CPU time. By explicitly calculating the lowest-lying 60 states in the above way, the computational effort in standard CD-*GW* requires roughly 60 times the effort for a single state, since the residues are evaluated for all frequencies individually. While this demonstrates the possible speed ups, it should be noted, that for highly symmetric systems, the use of symmetry would likewise be expected to lower the computational demand dramatically.

5.6.2 Validation of the Accuracy for Valence States in Coinage Metal Complexes

To demonstrate the performance of the fsCD-*GW* algorithm in the context of valence states, a series of coinage metal complexes are examined, which were previously synthesized by Dahlen and co-workers.[264,268] The structures consist of two $N,N'-$bis[(2-dinphenylphosphino)phenyl]formamidinate)] (dpfam), offering four coordination sites, for which the two outer most are connected by two gold atoms. This results in two cavities, which can then be reacted with different coinage metal salts, resulting in the dicationic species $[\mathrm{dpfam_2Au_2M_2}]^{2+}$, where M is either Cu, Ag, or Au.[268] These species have a high density of states near the HOMO-LUMO gap, making them an interesting test system for the fsCD-*GW* approach, in order to test its capabilities for system real life applications. The optimized structures are shown in 5.7, together with the computational details. These system are too large for a comparison with the spectral *GW* approach, as the tensor space dimension of the

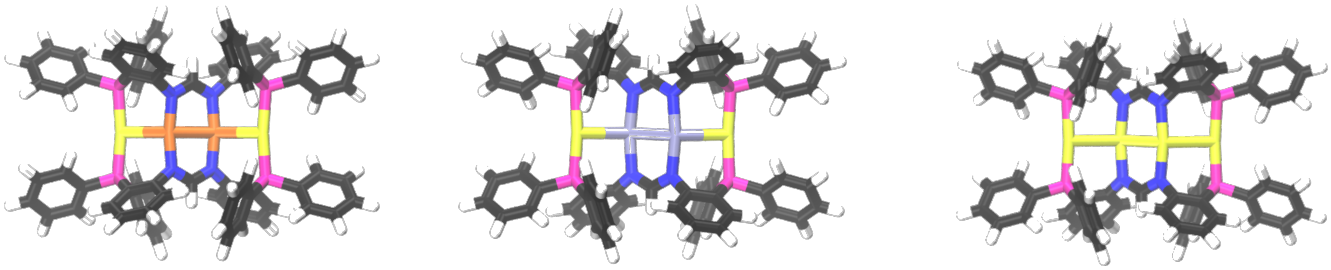

Figure 5.7: Optimized structures of $N,N'-$bis[(2-diphenylphosphino)phenyl]formamidinate)] coinage metal complexes, showing $[\mathrm{dpfam_2Au_2Cu_2}]^{2+}$ (left), $[\mathrm{dpfam_2Au_2Ag_2}]^{2+}$ (middle) and $[\mathrm{dpfam_2Au_4}]^{2+}$ (right). Ground states were optimized employing the PBE0 functional[251] integrated using a fine grid (size 4).[252,253] A mixed basis set, consisting of dhf-TZVPP basis set for Cu, Ag and Au, including effective core potentials for the latter two, while the dhf-SVP was used for all remaining atoms, with appropriate auxiliary basis sets.[220,224,266,267,269] All calculations were done at the one-component level. Note, that the dhf basis sets are synonymous to the def2 basis sets for light elements. The counter anions are omitted in all calculations, where the conductor-like screening (COSMO) model was used instead, employing default parameters, as given in the `TURBOMOLE` program suite.[270,271] Elements a color-coded as follows: carbon (black), hydrogen (white), phosphorous (pink), nitrogen (blue), gold (yellow), silver (grey), and copper (orange).

RPA problem, required for the spectral representation of the response function in eq. 3.37, is already close to half a million

in size for all three systems. The accuracy is therefore only assessed with respect to the standard CD-*GW* approach. The primary concern will be the assessment of the error introduced by using the fsCD-*GW* approach. The quasiparticle states were explicitly calculated for Kohn–Sham energies between -10 eV and 0 eV, while all remaining states were shifted by the difference between the quasiparticle energy and the Kohn–Sham eigenvalues of the HOMO or LUMO, respectively. At the Kohn–Sham level, the HOMO-LUMO gaps are found to lie between 4 and 5 eV for all three systems. Note, the fsCD-*GW* is fully equivalent to regular CD-*GW* if only the HOMO and LUMO are considered, as only a single residue with the frequency zero enters the first quadrant in both cases. The above considerations results in 79 states in Cu and 74 states for Ag and Au for which the quasiparticle states are explicitly evaluated. Errors of the fsCD-*GW* method with respect to standard CD-*GW* are shown in tab. 5.2 for different approaches based on the *GW* approximation. As expected the errors increase slightly in the case of linearized G_0W_0 , due to introducing errors in both, the contour integral, as well as the renormalization parameter, which is obtained via numerical differentiation in both implementations. However, the total errors appear negligible in theses examples, and are found to be below 10^{-5} eV. These values were obtained by using only few real frequencies, usually three or

Table 5.2: Mean signed error (MSE), mean absolute error (MAD) and standard deviation (STD) for the three coinage metal dicationic complexes $[\mathrm{dpfam_2Au_2M_2}]^{2+}$ in fig. 5.7 with M = Cu, Ag, Au for $G_0W_0\,(Z=1)$, linearized (lin.) G_0W_0 and ev*GW* for the fsCD-*GW* with respect to the standard CD-*GW* approach. All values are with respect to energies in eV.

	G_0W_0			lin. G_0W_0			ev*GW*		
M	MSE	MAD	STD	MSE	MAD	STD	MSE	MAD	STD
Cu	$2\cdot10^{-7}$	$2\cdot10^{-7}$	$1\cdot10^{-6}$	$8\cdot10^{-7}$	$1\cdot10^{-6}$	$5\cdot10^{-6}$	$-9\cdot10^{-10}$	$2\cdot10^{-7}$	$8\cdot10^{-7}$
Ag	$9\cdot10^{-9}$	$1\cdot10^{-8}$	$5\cdot10^{-7}$	$5\cdot10^{-8}$	$6\cdot10^{-8}$	$3\cdot10^{-8}$	$-2\cdot10^{-9}$	$3\cdot10^{-7}$	$2\cdot10^{-6}$
Au	$-3\cdot10^{-8}$	$1\cdot10^{-7}$	$6\cdot10^{-7}$	$2\cdot10^{-5}$	$2\cdot10^{-5}$	$2\cdot10^{-4}$	$-1\cdot10^{-9}$	$1\cdot10^{-6}$	$5\cdot10^{-6}$

four, depending on the method and iteration in case of ev*GW* . The latter converged within four iterations in all calculations. The number of residues calculated in the standard CD-*GW* approach was found between 1400 and 1700 frequencies per iteration. Using numerical differentiation for the calculation of the renormalization parameter roughly doubles this number. In comparison the frequency grid used for the fsCD-*GW* approach only consists of the imaginary frequencies, also required in the standard approach, and adds three to four additional real frequency points, in the above examples in order to sample the frequencies close to the Fermi energy. From these, the less then 100 residues are exact, in the sense, that they are part of the reference set, while remaining residues were obtained by analytic continuation using the AAA algorithm. This resulted in a stark reduction of the computational effort in all calculations. While the computational load of the respective nodes was not controlled, the CPU time for the eigenvalue-only self-consistent *GW* approach was measured at approximately 39.5 days for standard CD-*GW* and 2.5 days for fsCD-*GW* using 10 threads of an Intel Xeon Gold 6154 processor @ 3.00 GHz for M=Cu. Similar gains could be observed for the other systems. This is easily explained by the number of times the response matrix needs to be evaluated for real frequencies. For fsCD-*GW*, the real frequency grid is small compared to the number of imaginary frequencies, for which by default 128 Gauss-Legendre roots are used. The time-determining step is then the first loop in sec. 5.5.2 (see fig. 5.3). In contrast, the regular CD-*GW* calculates the frequencies independently for all residues. It shares the first frequency loop with the fsCD-*GW* approach, but as the number of states increases, the evaluation of the residues becomes the bottleneck even for valence states. Due to the close energetic proximity of all states considered, the list of frequencies needed for the fsCD-*GW* approach is limited to a small energetic range close to zero, where the analytic continuation of the screened exchange can be done most easily, using the imaginary frequency grid. A comparison with the AC-*GW* was not possible for these molecules, as the analytic continuation of the self-energy became unstable within the first the ten occupied states closest to the Fermi level and resulted in spurious quasiparticle energies ranging between -50 and +5 eV. This hints at the CD-*GW* approach being more reliable not only for low-lying states, but also as the density of states becomes large near the Fermi level.

5.6.3 Performance for Core-Electron Binding Energies for Cd Clusters

We conclude this chapter by briefly examining the efficiency regarding the calculation of quasiparticle energies associated with core-electron binding energies at the one- and two-component level of theory, where the (spin-free) X2C-Hamiltonian was used, applying the DLU approximation.[56,272,273] Here, a series of small Cd cluster ranging from four to 18 atoms is used to investigate the scaling behaviour of this algorithm. The parameter N describing the system size can be directly compared with the number of Cd atoms for these examples. The geometries were taken from ref. 265. Ground states were optimized at the PBE0[251] level using a fine grid (size 5a)[252–254] and tight convergence criteria, where the energy was converged to 10^{-12} E_h and the density to 10^{-10}. The x2c-TZVPPall-2c basis was employed in all calculations, using suitable complementary auxiliary basis set.[221,255] Only the lowest-lying state, corresponding to a single Cd $1s$ stater were optimized. Note that its Kramers partner is implicitly included. Point group symmetries were not exploited at any level. The CPU times are depicted in fig. 5.8. The corresponding wall times are given in sec. A.1 in the appendix. All calculations were done on a Intel E5-2687W

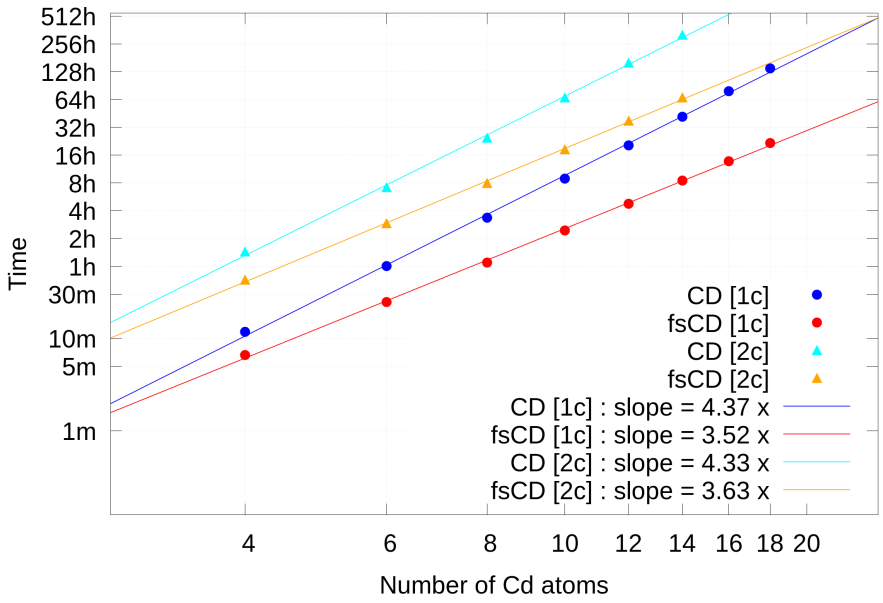

Figure 5.8: CPU timings for fsCD-*GW* (red and orange) and CD-*GW* (light and dark blue) for Cd clusters of varying sizes in one- (circles) and two-component (triangles) calculations for the lowest-lying state in C_1 symmetry. Quasiparticle energies were obtained at the non-iterative G_0W_0 level, where the renormalization parameter was set to one. The scaling behaviour or computational complexity is estimated from the slope of a linear regression using a logarithmic scales for system size and CPU time and are shown in the graphs. The timings were recorded employing the default Gauss-Legendre grid, using 128 frequency points along the imaginary axis in the calculation of $I^{c}_{pp}(\epsilon_p)$. Errors for the fsCD-*GW* algorithm were found to be approximately 10^{-5} eV or lower in the above examples.

v4 processor @ 3.00 Ghz using 8 threads (without hyper-threading). The quasiparticle errors were found to be comparatively large at 10^{-5} eV and may increase if self-consistent schemes were invoked. Note that the energies considered here, are found at approximately -26 778 eV, varying slightly with the size of the cluster. The computational complexity is estimated via linear regression using a double logarithmic scale, with the slopes given in fig. 5.8. The efficiency gain using frequency sampling in fsCD-*GW* compared to the standard CD-*GW* algorithm appears to be roughly of order $\mathcal{O}\left(N^{0.8}\right)$ to $\mathcal{O}\left(N^{0.9}\right)$, close to the formal difference in scaling of $\mathcal{O}\left(N^{1}\right)$. The observed scaling for both approaches is lower than the expected asymptotic computational complexity of $\mathcal{O}\left(N^{5}\right)$ and $\mathcal{O}\left(N^{4}\right)$ for CD-*GW* and fsCD-*GW* respectively. This may be attributed to a variety of optimizations, like the blocking algorithm employed and related steps. The sizes considered here, appear too far from the asymptotic limit, as the effort associated with the remaining steps is non-negligible. For example, while the calculation of the imaginary frequency integrals is technically a $\mathcal{O}\left(N^{4}\right)$ step. it involves the number of Gauss-Legendre quadrature points, which introduces a factor of 128 in all calculations and may be comparable to the calculation of the residues for small systems

in standard CD-*GW* . By reducing the number of imaginary frequency grid points, the slope is expected to become closer to the asymptotic behaviour, as the large prefactor of the $\mathcal{O}\left(N^4\right)$ step required in the imaginary frequency integration, is reduced. The resulting graph is shown in the sec. A.1 in the appendix. However, in fsCD-*GW* residues are obtained by the analytic continuation using both imaginary and real reference points. A change in the Gauss-Legendre grid size is therefore expected to also strongly influence the quality of the rational approximation used in the calculation of the required residues, especially in the small and intermediate frequency ranges. The advantage of the fsCD-*GW* lies again in the small number of residues evaluated explicitly, which is the second step in the algorithm explained in sec. 5.5.2. At the one-component level the dielectric matrix is only evaluated for nine real frequencies, while this number increases to eleven at the two-component level. The number of reference at the one- or two-component level stays the same in all sizes examined here. This is due to the energetic proximity of the additional states, also for larger systems, which allow for an especially efficient sampling. For more complex system, this requirements on the grid may increase and the reference set is expanded accordingly. In the limit of a continuum of states, the associated grid along the real axis, would appear to be linearly spaced in the small frequency limit, while the separation of frequencies is expected to follow an exponential increase. The timings for selected steps are listed in tab. 5.3 for Cd_4, Cd_8 and Cd_{12}. In fsCD-*GW* the number of residues evaluated explicitly only scale with N_{ω_R} times

Table 5.3: CPU times for Cd_4, Cd_8 and Cd_{12} for the construction of I^{c}_{pp} and R^{c}_{pp} at the quasiparticle energies ϵ_p in the context of contour deformation *GW* approaches for G_0W_0 with Z_p fixed to one. For fsCD-*GW* the construction of the matrix elements of the screened exchange, $W^{\mathrm{c}}_{pmpm}(\omega_R)$, at the real frequency reference points is given (see fig. 5.4), since the construction of the residues is done in negligible time. See the text for computational details. Values are given in seconds and as a percentage of the total time.

		Cd_4		Cd_8		Cd_{12}	
Method	Step	1c	2c	1c	2c	1c	2c
CD-*GW*	$I^{\mathrm{c}}_{pp}(\epsilon_p)$	259 s 38 %	2338 s 45 %	3028 s 25 %	22927 s 26 %	13550 s 18 %	105679 s 18 %
	$R^{\mathrm{c}}_{pp}(\epsilon_p)$	360 s 51 %	2574 s 50 %	8585 s 71 %	62841 s 71 %	237480 s 84 %	457591 s 80 %
fsCD-*GW*	$I^{\mathrm{c}}_{pp}(\epsilon_p)$	295 s 75 %	2074 s 81 %	3124 s 79 %	22420 s 80 %	13876 s 81 %	108160 s 80 %
	$W^{\mathrm{c}}_{pmpm}(\omega_R)$	35 s 9 %	295 s 12 %	408 s 11 %	3600 s 13 %	5605 s 11 %	17649 s 13 %
	$R^{\mathrm{c}}_{pp}(\epsilon_p)$	2 s 1 %	2 s 0 %	6 s 0 %	6 s 0 %	9 s 0 %	10 s 0 %

the computational effort for the construction of the response matrix in its auxiliary subspace representation. The evaluation of the residues using the AAA algorithm is usually done in a few seconds for the above examples and is negligible, as it scales only with the number of reference points. The size of the Gauss-Legendre quadrature grid was set to 128 and corresponds to the number of imaginary reference points for the matrix elements of the screened exchange, which are an intermediate quantity in the calculation of $I^{\mathrm{c}}_{pp}(\epsilon_p)$. For states further from the HOMO-LUMO gap, the evaluation of the residues quickly becomes the time-determining step in regular CD-*GW* . In contrast, in the case of fsCD-*GW*, the evaluation of $I^{\mathrm{c}}_{pp}(\epsilon_p)$ and the associated exchange matrix elements, usually stays the time-critical step. The above considerations are made on a per state level. If multiple states are to be considered the real frequency grid is shared in the case of fsCD-*GW* . While the errors appear small, care must be taken if self-consistent solutions are sought. Especially for system without a clear energetic separation of states, small errors introduced in fsCD-*GW* may result in a feedback, deviating from the correct solution. For these cases, the description using regular CD-*GW* may also be problematic, as the question of whether a residue enters the first quadrant, and relies on numerical thresholds. Ultimately, these problems can oftentimes be tackled by adjusting the thresholds discussed in this chapter, as to properly include or exclude these residues in real-life applications.

6 Bethe-Salpeter Equation for Core-Excited States

In the last two chapters, general and practical aspects regarding the calculation of charge excitations in the context of many-body perturbation theory were discussed. This chapter now focuses on the extension of this formalism in order to obtain the charge neutral excitations of molecular systems. Specifically, techniques for the description of highly excited states are discussed, which are required for the simulation of X-ray experiments. The formalism can be derived from the variation of the one-particle Green's function with respect to external perturbations, which is governed by the BSE.[163,274] This equation can be formally related to the response equations introduced in the context of TDDFT in sec. 3.5 and offers a compelling alternative to the popular DFT based methods, especially, if charge-transfer excitations are of concern. In these cases, the BSE equation has been shown to often yield superior results with respect to many common density functional approximations, since it includes the correct asymptotic for $\boldsymbol{r}$.[24,275–279] Most calculations employ the quasiparticle energies, as they are provided by methods based on the *GW* approximation, which is then collectively referred to as the *GW*-BSE approach.[26,160] Here, we will employ the strategies presented in chapters 4 and 5 in order to obtain approximations to the quasiparticle energies.
The BSE is subject of current developments, more recent studies include the effects of TDDFT correlation in the BSE kernel,[280] the study of dynamic screening effects,[281–283] as well as the description of atoms and molecules in strong magnetic fields.[284,285] Using its connection to the response function, the BSE can also be used in order to obtain other properties, such as NMR coupling constants,[286] or dynamic polarizabilities from a damped formulation of the BSE, the latter of which will be subject of this chapter.[150] In its static formulation, the computational complexity associated with the (*GW*-)BSE approach is comparable to TDDFT calculations using a hybrid functional.[25] Here, we use the RI approximation in order to evaluate the screened exchange, following the ideas presented in sec. 5.1. The *GW*-BSE approach was previously implemented in the `TURBOMOLE` program package by Krause *et al.*[287] and later reworked and extended by Holzer.[24,25,137]
We will start this chapter, by giving a brief discussion of the concepts from which the BSE equation can be derived in the context of molecular systems. This is then extended in order to obtain complex dynamic polarizabilities in the damped BSE formalism, as was introduced in the context of this thesis. The solution of the underlying equations requires the use of dedicated subspace techniques. Here, an adaption of the generalized Jacobi-Davidson solver, presented in refs. 25 and 137, was developed in collaboration with C. Holzer and Y. J. Franzke.[150,288] This allows for the stable solution of the linear response-like equations at the two-component level, which is the used to evaluate the complex dynamic polarizability at specific frequencies directly. From this the absorption cross section for arbitrary energies can be obtained, which becomes especially convenient in the description of CESs. An alternative to this, which will also be examined in this chapter, uses the energetic separation of the core and valence electrons. The space of the electronic Hessian is then restricted in such a way, as to only include the subspace required for the description of CESs. This is the so-called core-valence separation (CVS) ansatz.[289,290] It directly reduces the dimension of the underlying matrices and oftentimes allows for large time-savings.[15,21,291] The CVS for the BSE follows closely from the TDDFT problem, and only the screening effects mediated by the dielectric function have to be properly accounted for. In the context of this thesis, the CVS-BSE approach was implemented at the one- and two-component level of theory and is later used in order to assess the performance of the *GW*-BSE approach for CESs in chapter 9 for a series of small inorganic molecules.

6.1 Fundamental Aspects of the Bethe-Salpeter Equation

The BSE describes the variation of the one-particle Green's function with respect to an external time-dependent potential. In order to derive the BSE, it is convenient to first introduce the generalized four-point susceptibility, $\boldsymbol{L}$, which is also called two-particle correlation function. It is given by [26,163]

$$\boldsymbol{L}(\mathbf{1},\mathbf{2},\mathbf{1}',\mathbf{2}') = \frac{\delta \boldsymbol{G}(\mathbf{1},\mathbf{1}')}{\delta \boldsymbol{U}(\mathbf{2}',\mathbf{2})}, \tag{6.1}$$

where the perturbative potential, $\boldsymbol{U}$, is local in time and is defined as

$$\boldsymbol{U}(\mathbf{1},\mathbf{2}) = \boldsymbol{U}(\boldsymbol{r}_1,\boldsymbol{r}_2,t_1)\delta(t_1,t_2). \tag{6.2}$$

By comparing the correlation function in eq. 6.1 to eq. 4.9, it can be related to the two-particle Green's function, $\boldsymbol{G}_2$. The correlation function describes the difference between the correlated and uncorrelated motions of two particle states, hole states, or any combination thereof. For the description of optical properties of molecular systems, we will be only concerned with the interaction of a particle-hole pair, created upon the excitation of an electron, subject to the dielectric screening of the environment. In the equations above, this corresponds to the two time-orderings $t_1, t_{1'} > t_2, t_{2'}$ and $t_1, t_{1'} < t_2, t_{2'}$.[292] The correlation function is closely connected to the vertex function in eq. 4.23, which was introduced in the context of Hedin's equations. It is required in the description of polarization effects beyond the RPA, e.g., to account for the response of the dielectric medium to a perturbation and is required to remove the self-interaction error in the *GW* approximation.[188,191] The direct relation can be derived from eq. 6.1, by repeatedly applying the chain rule in eq. 4.19, first with respect to the total potential, $\boldsymbol{V}_{\text{tot}}$, then for the one-particle Green's function. The vertex function then follows after invoking the Green's function identity in eq. 4.14.[163,293] Following a similar approach as was outlined in chapter 4 for $\boldsymbol{\Gamma}$, the correlation function may be brought into a form, for which the limit $\boldsymbol{U} \to 0$ can be considered explicitly and as such, is independent on the type of perturbation. The correlation function is then written as

$$\begin{aligned}\boldsymbol{L}(\mathbf{1},\mathbf{2},\mathbf{1}',\mathbf{2}') &= \boldsymbol{G}(\mathbf{1},\mathbf{2}')\boldsymbol{G}(\mathbf{2},\mathbf{1}') + \int \boldsymbol{G}(\mathbf{1},\mathbf{3})\boldsymbol{G}(\mathbf{3}',\mathbf{1}')\boldsymbol{\Xi}(\mathbf{3},\mathbf{4}',\mathbf{3}',\mathbf{4})\boldsymbol{L}(\mathbf{4},\mathbf{2},\mathbf{4}',\mathbf{2}')\mathrm{d}\mathbf{3}\mathrm{d}\mathbf{3}'\mathrm{d}\mathbf{4}'\mathrm{d}\mathbf{4} \\ &= \boldsymbol{L}_0(\mathbf{1},\mathbf{2},\mathbf{1}',\mathbf{2}') + \int \boldsymbol{L}_0(\mathbf{1},\mathbf{3}',\mathbf{1}',\mathbf{3})\boldsymbol{\Xi}(\mathbf{3},\mathbf{4}',\mathbf{3}',\mathbf{4})\boldsymbol{L}(\mathbf{4},\mathbf{2},\mathbf{4}',\mathbf{2}')\mathrm{d}\mathbf{3}\mathrm{d}\mathbf{3}'\mathrm{d}\mathbf{4}'\mathrm{d}\mathbf{4}.\end{aligned} \tag{6.3}$$

Here the non-interacting correlation function, $\boldsymbol{L}_0$, was introduced, which is just a simple product of two one-particle Green's functions. $\boldsymbol{\Xi}$ is the so-called BSE Kernel, which is given by

$$i\boldsymbol{\Xi}(\mathbf{3},\mathbf{4}',\mathbf{3}',\mathbf{4}) = \delta(\mathbf{3},\mathbf{3}')\delta(\mathbf{4}^+,\mathbf{4}')\boldsymbol{v}(\mathbf{3},\mathbf{4}) + i\frac{\delta \boldsymbol{\Sigma}(\mathbf{3},\mathbf{3}')}{\delta \boldsymbol{G}(\mathbf{4},\mathbf{4}')}, \tag{6.4}$$

where $\boldsymbol{v}$ is the instantaneous Coulomb potential and $\boldsymbol{\Sigma}$ is just the self-energy, as defined according to eq. 4.11. Eq. 6.3 has the form of a Dyson equation and is related to the response function in eq. 3.38, which was introduced in the context of TDDFT in sec. 3.5. Both quantities can be easily related, by taking considering eq. 6.1 in the limit $\mathbf{1}' \to \mathbf{1}^+$ and $\mathbf{2}' \to \mathbf{2}^+$. Following the definition of the correlation function, this then results in

$$-i\boldsymbol{L}(\mathbf{1},\mathbf{2},\mathbf{1}^+,\mathbf{2}^+) = -i\frac{\delta \boldsymbol{G}(\mathbf{1},\mathbf{1}^+)}{\delta \boldsymbol{U}(\mathbf{2}^+,\mathbf{2})} = \frac{\delta \boldsymbol{\gamma}(\mathbf{1})}{\delta \boldsymbol{U}(\mathbf{2})} = \boldsymbol{\chi}^{\mathrm{BSE}}(\mathbf{1},\mathbf{2}), \tag{6.5}$$

where the linear response function was obtained by inverting eq. 3.41. It expresses the (first order) variation of the density with respect to the perturbation $\boldsymbol{U}$. Now, by considering the same limit in the Dyson equation of the correlation function in eq. 6.3, we arrive at [26]

$$\boldsymbol{\chi}^{\mathrm{BSE}}(\mathbf{1},\mathbf{2}) = \boldsymbol{\chi}_0^{\mathrm{BSE}}(\mathbf{1},\mathbf{2}) + \int \boldsymbol{\chi}_0^{\mathrm{BSE}}(\mathbf{1},\mathbf{3})\boldsymbol{\Xi}(\mathbf{3},\mathbf{4},\mathbf{3},\mathbf{4})\boldsymbol{\chi}^{\mathrm{BSE}}(\mathbf{4},\mathbf{2})\mathrm{d}\mathbf{3}\mathrm{d}\mathbf{4}, \tag{6.6}$$

which connects the BSE response of the interacting system with the non-interacting (BSE) response function, $\boldsymbol{\chi}_0^{\mathrm{BSE}}$, which follows from $\boldsymbol{L}_0$. In linear response theory, the self-energy term in the BSE Kernel is just replaced by the exchange-correlation kernel, $\boldsymbol{f}_{\mathrm{xc}}$, introduced in eq. 3.38, where it becomes

$$\boldsymbol{\Xi}(\mathbf{3},\mathbf{4},\mathbf{3},\mathbf{4}) \to \boldsymbol{\Xi}^{\mathrm{TDDFT}}(\mathbf{3},\mathbf{4},\mathbf{3},\mathbf{4}) = \boldsymbol{v}(\mathbf{3},\mathbf{4}) + \frac{\delta \boldsymbol{V}_{\mathrm{xc}}(\mathbf{3})}{\delta \boldsymbol{\gamma}(\mathbf{4})}. \tag{6.7}$$

Likewise, the response function of the time-dependent Hartree–Fock method is recovered by replacing the exchange-correlation kernel by a Hartree–Fock exchange term in the above, which is just the first order expansion of the screened exchange in the Coulomb potential. [152] The BSE kernel includes functional derivatives of the self-energy. The latter can be conveniently expressed in the context of the *GW* approximation, where this becomes a simple product of the one-particle Green's function and the screened exchange. The BSE kernel in the *GW* approximation can be written as [26,160,292]

$$\begin{aligned} i\boldsymbol{\Xi}(\mathbf{3},\mathbf{4}',\mathbf{3}',\mathbf{4}) &= \delta(\mathbf{3},\mathbf{3}')\delta(\mathbf{4}^+,\mathbf{4}')\boldsymbol{v}(\mathbf{3},\mathbf{4}) - \frac{\delta\left[\boldsymbol{G}(\mathbf{3},\mathbf{3}')\boldsymbol{W}(\mathbf{3}^+,\mathbf{3}')\right]}{\delta \boldsymbol{G}(\mathbf{4},\mathbf{4}')} \\ &= \delta(\mathbf{3},\mathbf{3}')\delta(\mathbf{4}^+,\mathbf{4}')\boldsymbol{v}(\mathbf{3},\mathbf{4}) - \delta(\mathbf{3},\mathbf{4})\delta(\mathbf{3}',\mathbf{4}')\boldsymbol{W}(\mathbf{3}^+,\mathbf{3}'), \end{aligned} \tag{6.8}$$

where in the second step the variation of the screened exchange with respect to the Green's function has been neglected. This avoids the inclusion of higher-order terms in $\boldsymbol{W}$. [26,160,168] While the Coulomb interaction is instantaneous, even within the *GW* approximation, the screened exchange is dynamic in nature. Here, it is common to only consider its static limit, which is similar to the adiabatic approximation for the exchange-correlation kernel in TDDFT. [26,160,168,294] Explicitly including the dynamic effects in the screened exchange destroys the simple structure of the underlying response equations, which would results in a non-linear eigenvalue problem. Techniques to efficiently solve this issue have been recently suggested in the literature, [282,283] but are beyond the scope of this thesis. The frequency representation of the BSE response function using the static limit of the screened exchange can be is obtained by a Fourier transformation. $\boldsymbol{\chi}_0^{\mathrm{BSE}}$ and $\boldsymbol{\chi}^{\mathrm{BSE}}$ in eq. 6.6 take an analogues form to the TDDFT response functions in eqs. 3.35 and 3.41. By projecting the problem onto a suitable basis, provided, e.g., by the Kohn–Sham eigenfunctions, the problem can be transformed into the form of an matrix eigenvalue problem, reminiscent of Casida's equation shown in eq. 3.44, which then reads [26,160]

$$\begin{pmatrix} \boldsymbol{A}^W & \boldsymbol{B}^W \\ \boldsymbol{B}^{W*} & \boldsymbol{A}^{W*} \end{pmatrix} \begin{pmatrix} \boldsymbol{X} \\ \boldsymbol{Y} \end{pmatrix} = \omega \begin{pmatrix} \mathbf{1} & \mathbf{0} \\ \mathbf{0} & -\mathbf{1} \end{pmatrix} \begin{pmatrix} \boldsymbol{X} \\ \boldsymbol{Y} \end{pmatrix}, \tag{6.9}$$

where ω are the excitations energies, corresponding to the poles of the (interacting) BSE response function, while $\boldsymbol{X}$ and $\boldsymbol{Y}$ are the orbital or spinor rotation parameters. The sub matrices of the electronic Hessian, $\boldsymbol{A}^W$ and $\boldsymbol{B}^W$, differ from their TDDFT equivalent in eq. 3.40. They contain the matrix elements of the static screened exchange interaction, replacing the adiabatic exchange-correlation kernel, and are given by

$$\begin{aligned} A^W_{iajb} &= (\epsilon_a - \epsilon_i)\delta_{ab}\delta_{ij} + \langle ib|aj\rangle - W_{ijab}(\omega = 0) \\ B^W_{iajb} &= \langle ij|ab\rangle + W_{ibaj}(\omega = 0), \end{aligned} \tag{6.10}$$

Instead of the Kohn–Sham eigenvalues, ϵ_a and ϵ_i correspond to the quasiparticle energies obtained within the *GW* approximation. Following eq. 5.10, the matrix elements of the screened exchange required in the above, can be evaluated as

$$\begin{aligned} W_{pqrs}(\omega = 0) &= R^P_{pq}{\epsilon_{PQ}}^{-1}(\omega = 0)R^Q_{rs} \\ &= \sum_{PQ} \tilde{R}^P_{pq}\tilde{R}^Q_{rs} \\ \text{with} \quad \tilde{R}^Q_{rs} &= \sum_P R^P_{rs}\,[L]^{-1}_{PQ} \quad \text{and} \quad \boldsymbol{\epsilon}(\omega = 0) = \boldsymbol{L}\boldsymbol{L}^{\mathrm{T}}, \end{aligned} \tag{6.11}$$

where $\boldsymbol{L}$ is a triangular matrix obtained by a Cholesky decomposition of the dielectric matrix. Following the same considerations as done in TDDFT, the dimension of the screened exchange, projected onto the space of singly excited states, is far too large to hold in memory, even on modern machines. The explicit construction of the full matrix, therefore needs to be avoided, where we will follow a common strategy, which will be presented in sec. 6.2.1. The BSE approach described in this section offers an competitive alternative to conventional TDDFT calculations for the description of singly excited states. Even in its static approximation, it has seen reasonable success for the description of singlet excitations. However, triplet excitations have been observed to be problematic and tend to be predicted at too low excitation energies.[22–24] This error can be partially reduced by reintroducing the correlation contribution of the exchange-correlation kernel in the matrices $\boldsymbol{A}^W$ and $\boldsymbol{B}^W$, thereby creating a TDDFT-BSE hybrid kernel. This approach was dubbed the correlation-kernel augmented BSE or cBSE method and was introduced in ref. 280. In the following sections, methods regarding the solution of the BSE, aiming at the description of CESs are presented, as they haven been implemented and used throughout this thesis. Specifically, the BSE approach was extended as to directly evaluate complex dynamic polarizabilities, via the solution of linear response-like equation in the context of damped response theory. Furthermore, the CVS approximation was introduced for the BSE. Both approaches offer ways to significantly reduce the computational effort for high-lying optically excited states, where a description using standard methods becomes increasingly difficult, especially at the two-component level.

6.2 Damped Bethe-Salpeter Equations

Complementary to the solution of the BSE in the form of an eigenvalue problem, given in eq. 6.9, one may prefer to solve the BSE for a selected frequency region instead. This has several advantages over the standard approach, based on the eigenvalue form of the BSE. In order to describe the optical excitations of a molecular system using the standard methodology, its eigenvalue and eigenvectors are required. These eigenvalues correspond to the excitation energies. For most applications only a few are explicitly required, which can be extracted by using techniques, such as the (Jacobi-)Davdison algorithm or similar methods. Here, the problem is projected in an appropriate subspace, where it is solved using the Rayleigh-Ritz

method.[136,295] These techniques are mostly geared towards the calculation of extreme eigenvalues and commonly struggle when solutions corresponding to interior eigenvalues are sought after. In these cases, the Ritz-pairs tend to converge towards the extreme eigenvalues or spurious solutions altogether.[139,296] Therefore, more sophisticated methods such as the generalized preconditioned locally harmonic residual (GPLHR) algorithm have been proposed in order to extract the interior eigenvalues and eigenvectors associated with selected frequency ranges,[142,297,298] relying on the so-called harmonic Ritz-pairs instead.[296] However, these can be difficult to converge, as energies corresponding to spurious or pseudo-continuum solutions may appear in the same frequency domain.[299]The spectrum associated with interior solutions can instead be represented using the damped response formalism. Here, the dynamic complex polarizability may be calculated directly for a given frequency, avoiding the eigenvalue problem completely and replacing it by a complex linear set of equations. Aside from core excitations this method can also prove beneficial for systems system of particular high density of states.[300,301] However, it can not account for possible spurious continuum excitation from valence states, which may appear randomly in the selected regions. Following sec. 3.6, in order to arrive at the damped form of the static Bethe-Salpeter equations, the time-dependent density response due to the nth excited state, is damped by introducing an artificial lifetime parameter, Γ_n,. It is most convenient to adopt a single lifetime parameter for all excited states, i.e. setting

$$\Gamma_n \to \Gamma. \tag{6.12}$$

This is identical to standard damped response theory and may be understood as an analytic continuation of the response function, $\boldsymbol{\chi}$, into the complex plane, setting

$$\boldsymbol{\chi}(\omega) \to \boldsymbol{\chi}(\bar{\omega}) = \boldsymbol{\chi}(\omega + i\Gamma), \tag{6.13}$$

where $\bar{\omega}$ is complex and is comprised of the real frequency ω and an the imaginary lifetime parameter $i\Gamma$. Using a finite non-zero lifetime, the poles of the response function at the true excitation energies are avoided. In contrast to sec. 3.6, the response functions are given by their BSE analogues within the *GW*-BSE method, writing

$$\boldsymbol{\chi}_0 \to \boldsymbol{\chi}_0^{\mathrm{BSE}} \quad \text{and} \quad \boldsymbol{\chi} \to \boldsymbol{\chi}^{\mathrm{BSE}}, \tag{6.14}$$

where $\boldsymbol{\chi}^{\mathrm{BSE}}$ is defined according to eq. 6.6. We again only consider the static limit of the BSE kernel, which can then be easily transformed into the frequency domain. The (Coulomb-)exchange-correlation kernel, $f_{H\mathrm{xc}} = \boldsymbol{v} + f_{\mathrm{xc}}$, within TDDFT is replaced by the static BSE kernel from eq. 6.4. The damped Bethe-Salpeter equations in matrix form read

$$\left[\begin{pmatrix} \boldsymbol{A}^W & \boldsymbol{B}^W \\ \boldsymbol{B}^{W*} & \boldsymbol{A}^{W*} \end{pmatrix} - (\omega + i\Gamma) \begin{pmatrix} \mathbf{1} & \mathbf{0} \\ \mathbf{0} & -\mathbf{1} \end{pmatrix} \right] \begin{pmatrix} \boldsymbol{X} \\ \boldsymbol{Y} \end{pmatrix} = - \begin{pmatrix} \boldsymbol{U} \\ \boldsymbol{U}^* \end{pmatrix}, \tag{6.15}$$

which is a generalized Hermitian system of equations. In two-component calculations, the right-hand side is constructed from the matrix elements,

$$\boldsymbol{U} = \langle n|\boldsymbol{O}|0\rangle\,, \tag{6.16}$$

where n and 0 indicate the nth excited state and the ground state respectively. $\boldsymbol{O}$ is an operator, describing the perturbation, which, following the discussion in chapter 4.1, is of the general form

$$\boldsymbol{O}_\nu = \begin{pmatrix} \boldsymbol{O}_\nu^0 + \boldsymbol{O}_{\mathrm{SO},\nu}^z & \boldsymbol{O}_{\mathrm{SO},\nu}^x - i\boldsymbol{O}_{\mathrm{SO},\nu}^y \\ \boldsymbol{O}_{\mathrm{SO},\nu}^x + i\boldsymbol{O}_{\mathrm{SO},\nu}^y & \boldsymbol{O}_\nu^0 + \boldsymbol{O}_{\mathrm{SO},\nu}^z \end{pmatrix}, \tag{6.17}$$

where 0, x, y and z refer to the spin components associated with the respective Pauli matrices in eq. 3.3. $\boldsymbol{O}_\nu^0$ is real symmetric, while $\boldsymbol{O}_{\mathrm{SO},\nu}^x$, $\boldsymbol{O}_{\mathrm{SO},\nu}^y$, and $\boldsymbol{O}_{\mathrm{SO},\nu}^z$ are imaginary and skew-symmetric, making $\boldsymbol{O}$ Hermitian. ν is used to indicate the dimensionality of the perturbation operator, e.g., the three cartesian components of the electronic dipole operator. SO is used to indicate spin-orbit contributions. We will only consider the interaction of a system with a dynamic electric field in the following and further limit ourselves to the electronic dipole approximation, as is required in the zeroth order description of the semi-classical light-matter interaction. This will be further discussed in sec. 7. The dipole operator does not intrinsically contain spin-orbit interaction terms.[12] However, when working in a quasirelativistic two-component framework, for example, by employing decoupling techniques such as in X2C theory, this is not necessarily true anymore. To be fully consistent with the ground state X2C Hamiltonian, the dipole operator needs to be transformed similarly to the other one-electron integrals by the X2C decoupling matrix and becomes complex Hermitian.[302–304] This is the so-called picture-change correction (PCC) and results in finite spin-orbit contributions even for the matrix elements of the electric dipole operator.[150,288] Since the solution of the damped response equations explicitly incorporate the right-hand side, it is also dependent on this transformation. Note however, for the solution of the generalized eigenvalue problem in eqs. 3.44 and 6.9, the solution is independent from the dipole moment. Here, the picture-change error can only introduce errors in the transition moments and oscillator strengths. In order to evaluate the complex dynamic polarizabilty for a single frequency, the dipole integrals provide three distinct right-hand side vectors, which, without considering symmetries, need to be solved individually. In contrast to the corresponding linear response eigenvalue equations, solutions to the eq. 6.15 can be found in a stable manner for any finite ω, provided the damping factor is sufficiently large. In the context of this thesis, no convergence problems were observed for damping factors as small as 0.1 eV, which is typically adopted for comparison to the experimental broadened spectra in linear response theory.
Here, a generalized Hermitian solver for the linear system of equations is employed, which was implemented in the context of this thesis.[150] Note, the solution of the damped response equations was previously implemented at the one-component level of theory by Parket *et al.*,[305] and required only small modifications in order to account for the complex damped response vectors for the calculation of the screened exchange. Therefore, the focus lies in the extension to the quasirelativistic two-component regime, which is not limited to use in the context of the BSE, but can also be used for TDDFT. The details of this approach will be subject of the discussion provided in the following section.

6.2.1 Solution of the Damped Response Equations

The solution of the damped response equations was realized, starting from the Jacobi-Davidson solver for the generalized eigenvalue problem encountered in two-component calculations, for TDDFT without the Ziegler approximation.[116,118,125,138,182] The algorithm for the solution of the linear response eigenvalue equations is given in refs. 137 and 25, while in this section, we will present some of the results published in ref. 150. In damped response theory, instead of the eigenvalue problems in eqs. 3.44 or 6.9, the complex linear system of equations, shown in eqs. 3.49 and 6.15, needs to be solved. The implementation was done as part of an collaboration with Y. J. Franzke and C. Holzer, the static solution has already been discussed in ref. 288, for which the (complex) frequency, ω ($\bar{\omega}$), in eqs. 3.49 and 6.15 is set to zero. This can be used in order to obtain static response properties. The following will thereby only address the dynamic problem. Complications arise from the dimension associated with the matrix quantities in the linear response equations. The square matrices $\boldsymbol{A}$ ($\boldsymbol{A}^W$) and $\boldsymbol{B}$ ($\boldsymbol{B}^W$), which comprise the electronic Hessian, are of the dimensions $(N_{\mathrm{occ}} \times N_{\mathrm{virt}})$, where N_{occ} and N_{virt} are the number of occupied and virtual spinors respectively. Due to the super matrix structure of the electronic Hessian, the full dimension of the problem grows twice as fast, compared to $\boldsymbol{A}$ and $\boldsymbol{B}$. The solutions of systems of linear equations scale usually with $\mathcal{O}\left(N^3\right)$. For

the problem above, the computational effort thus becomes $\mathcal{O}\left(N^6\right)$ in the asymptotic limit, which effectively prohibits the direct solution of these equations for all but small molecules. Therefore, in most applications, it is required to solve the problem in an suitable subspace instead, whose solutions are build in order to be as close to the true solutions of the full problem as possible. The general algorithm is depicted in fig. 6.1 and continued in fig. 6.2. It is a direct extension of the algorithm presented for the solution of linear response eigenvalue problem to complex frequencies at the two-component level of theory.[115,137] The general idea follows from the systematic expansion of the subspace, in which the electronic Hessian is projected. The initial set of trial vectors in eq. 6.18, which is step 4 in fig. 6.1, is obtained by neglecting the two-electron contributions. These vectors are carefully orthogonalized using the modified Gram-Schmidt procedure. Since we intend to solve the problem only in its subspace, the Hessian is never explicitly required. Instead the trial vectors are directly contracted with the Hessian. In practice, these matrix-vector products are only evaluated for two-electron part, as the differences between the quasiparticle energies or Kohn–Sham eigenvalues contribute only to the diagonal, and can simply be added latter at no significant cost. This dramatically reduces the memory requirement. In most applications the evaluation of the two-electron interaction constitutes the time-depending step of an iteration. In the BSE formalism, this corresponds to the contraction of the screened exchange-matrix with the trial vectors. This matrix-vector product is then used to construct the subspace representation of the Hessian and the right-hand side vector. The right-hand side vector is projected into the subspace accordingly. This corresponds to eq. 6.20 in fig. 6.1. The computation of the metric is trivial, due to the trial vectors being orthogonalized in every step. The solution of the complex linear system of equations in eq. 6.21, which is step 7 in fig. 6.1, is implemented in many linear algebra packages. Here, the routines ZPOTRF and ZPOTRS of the LAPACK package are used, for which first the Cholesky decomposition of the left-hand side matrix is calculated via ZPOTRF. Since the Cholesky matrix is triangular, the linear system then becomes trivial to solve using forwards and backwards substitution in ZPOTRS. The approximate solutions to the full problem, can then be easily constructed by mapping the trial solution to the full space spanned by the trial vectors in eq. 6.22. The error is estimated by the norm of the residual in eq. 6.23.[136] The algorithm terminates if the residual is found to be below a predefined threshold, usually of the order 10^{-5}. If multiple frequencies are requested, convergence is only assumed if the errors for all residuals falls below the convergence threshold. Otherwise, the subspace is further expanded and the next iteration is started. Here, the subspace expansion is done in an (Jacobi-)Davidson step, from which new trial vectors are obtained using the diagonal of the electronic Hessian as a preconditioner.[136,295,306] The Jacobi-Davidson algorithm tries to skew the direction, in which the subspace is expanded, and has been extensively been discussed in the literature.[295,306] The presented algorithm is used for the iterative solution of the complex Hermitian linear system of equations, which is required in the context of damped response theory at the quasirelativistic two-component level of theory. It was usually found to converge within a few up to a maximum of twenty cycles for most cases examined in the context of this thesis. Since the difference between the static BSE and the linear response equations in TDDFT or TDHF is limited to the way the exchange and correlation contributions are evaluated, the general structure is retained in all three approaches, where this technique was easily adopted for.

Solution of the generalized (damped) response equation

input : $\Omega = \{\omega_1, \omega_2, \ldots, \omega_{n_\omega}\}$ is the set of requested frequencies; (N_ω)

Γ is the damping factor;

ϵ_p are quasiparticle energies or KS-eigenvalues;

$\boldsymbol{U}^\nu$ is the right-hand side vector with N_ν unique components;

τ_{max} is the convergence threshold;

output: $\tilde{\boldsymbol{V}} = \{\tilde{\boldsymbol{v}}, \ldots, \tilde{\boldsymbol{v}}_{N_\omega}\}$ is the set containing the solution vectors; $(N_\omega \times N)$

Initialize subspace

1 Add $N_\omega \times N_\nu$ trial vectors

$$\boldsymbol{v} = \begin{pmatrix} \boldsymbol{x}^\nu \\ \boldsymbol{y}^\nu \end{pmatrix} \quad \text{with} \quad x_{ai}^\nu = \frac{U_{ai}^\nu}{\epsilon_a - \epsilon_i - \omega} \text{ and } y_{ai}^\nu = \frac{U_{ai}^{\nu *}}{\epsilon_a - \epsilon_i + \omega}; \tag{6.18}$$

2 Orthogonalize all trial vectors in the set using the modified Gram-Schmidt algorithm;

Solve linear system of equations

3 **while** $\tau > \tau_{max}$ **do**

4 Obtain the matrix-vector product of the electronic Hessian, $\boldsymbol{H}$, and the trial vectors

$$\boldsymbol{W} = \boldsymbol{H}\boldsymbol{V} \quad \text{with} \quad \boldsymbol{W} = \{\boldsymbol{w}_1, \ldots, \boldsymbol{w}_{N_v}\} = \{\boldsymbol{H}\boldsymbol{v}_1, \ldots, \boldsymbol{H}\boldsymbol{v}_{N_v}\}; \tag{6.19}$$

5 Calculate the subspace projections of $\boldsymbol{H}$ and the right-hand side vectors, according to

$$\boldsymbol{M} = \boldsymbol{V}^\dagger \boldsymbol{W} \quad \text{and} \quad \boldsymbol{u}^\nu = \boldsymbol{V}^\dagger \boldsymbol{U}^\nu \tag{6.20}$$

(The subspace projections of the metric, $\boldsymbol{s}$, is trivial);

7 Construct the left-hand side of eq. 6.15 in the subspace spanned by $\boldsymbol{V}$

$$(\boldsymbol{M} - \bar{\omega}\boldsymbol{s})\, \boldsymbol{t}^\nu = \boldsymbol{u}^\nu \quad \text{with} \quad \bar{\omega} = \omega + i\Gamma, \tag{6.21}$$

and solve for $\boldsymbol{t}^\nu$;

⋮

Figure 6.1: Solving the generalized linear system of equations required in damped response theory, following the (Jacobi-)Davidson algorithm described in refs. 137 and 25. Instead of calculating the electronic Hessian, only its contraction with the trial vectors is calculated. The Hessian is therefore never fully kept in memory and is only solved in the comparatively small subspace. The references to the individual frequencies are omitted for clarity. t^ν is the Ritz(-like)-vector used in the calculation of the approximate solution to the full problem. The trial vectors are complex in both one- and two-component calculations, due to the complex damping factor Γ. The algorithm is continued in fig. 6.2.

Solution of the generalized (damped) response equation (continued)

input : $\Omega = \{\omega_1, \omega_2, \ldots, \omega_{n_\omega}\}$ is the set of requested frequencies; (N_ω)

Γ is the damping factor;

ϵ_p are quasiparticle energies or KS-eigenvalues;

$\boldsymbol{U}^\nu$ is the right-hand side vector with N_ν unique components;

τ_{max} is the convergence threshold;

output: $\tilde{\boldsymbol{V}} = \{\tilde{\boldsymbol{v}}, \ldots, \tilde{\boldsymbol{v}}_{N_\omega}\}$ is the set containing the solution vectors; $(N_\omega \times N)$

Solve linear system of equations

$\vdots$

10 Construct the trial solution, $\tilde{\boldsymbol{t}}$, from the solution of in the subspace according to,

$$\tilde{\boldsymbol{t}} = \boldsymbol{V}\boldsymbol{t} \tag{6.22}$$

11 and calculate the residuals, $\boldsymbol{r}^\nu$, and the corresponding euclidean norm, τ, as

$$\boldsymbol{r}^\nu = (\boldsymbol{m}^\nu - \bar{\omega}\boldsymbol{s})\boldsymbol{t}^\nu - \boldsymbol{u}^\nu \quad \text{and} \quad \tau = \|\boldsymbol{r}^\nu\|_2; \tag{6.23}$$

12 **if** *maximum residual norm* τ *is less then* τ_{max} **then**

13 Set $\tilde{v} = \tilde{t}$ and exit the loop;

14 **else**

15 Expand the trial space by (Jacobi-)Davidson step, as

$$\begin{gathered} \boldsymbol{c} = \zeta \boldsymbol{D}\tilde{\boldsymbol{t}} - \boldsymbol{D}\boldsymbol{r} \\ \text{with} \quad \boldsymbol{D} = (\boldsymbol{H} - \bar{\omega}\boldsymbol{S}) \quad \text{and} \quad \zeta = \frac{\tilde{\boldsymbol{t}}^\dagger \boldsymbol{D}^{-1}}{\tilde{\boldsymbol{t}}^\dagger \boldsymbol{D}^{-1}\tilde{\boldsymbol{t}}}\tilde{\boldsymbol{r}}, \end{gathered} \tag{6.24}$$

where $\boldsymbol{S}$ is the metric in the full problem.

16 $\boldsymbol{c}$ is orthogonalized against the set of trial vectors using the modified Gram-Schmidt algorithm and added to $\boldsymbol{V}$.

17 **end**

18 **end**

Figure 6.2: Continuation of the algorithm in fig. 6.1. The algorithm is assumed to be converged, if the maximum residual norm is less then the convergence threshold, τ_{max}. Convergence is estimated using the maximum norm of all residuals. See description of fig. 6.1 for further information.

6.2.2 Practical Considerations of the Damped Response Formalism

The damped response equations offer direct access to the complex polarizability at any frequency points of choice. However, aside of certain advantages, it also has certain drawbacks compared to standard linear response formulations, especially if valence states are to be considered. Since the linear response equations inherently depend on the perturbation, a proper description of the interaction term becomes especially important, as small deficiencies of the perturbation operator, may provide unsatisfactory results or even spurious solutions. For standard applications, the dynamic polarizability may be already well-described using the electric dipole approximation. The operator of the electric dipole moment has three distinct components, corresponding the three cartesian coordinates. These components need to be solved individually. In practice, here, only a single subspace is constructed and expanded, in which all three components are solved in simultaneously. This can have major advantages, if the response of the systems does not feature any preference with respect to the polarization of the electric field with respect to molecule.

Complications may arise, if we are instead interested in the description of CESs. Here, the wavelength of the photons becomes comparable to the spatial extend of the molecule and the electric dipole approximation may start to fail. Going beyond the electric dipole approximation, first introduces the magnetic dipole and electric quadrupole contributions, which may be required, in order to describe the absorption cross section of these systems. We will later see in chapter 7, that even higher moments may be needed to be introduced, in order to achieve gauge-invariant forms of the amplitudes beyond the electric dipole approximation.[10,307] Then, each element of the multipole moments considered, requires the solution of its own set of equations. For example, the magnetic dipole introduces an additional set of three components, while the electric quadrupole has nine entries, for which six are unique. This number grows as higher multipole moments are to be considered. This becomes impractical, especially as the solution explicitly depends on the right-hand side vector and the picture-change correction may need to be addressed. Alternatively, the full semi-classical light-matter interaction may be considered, but comes with its own drawbacks and may not be easily introduced here.[11] Therefore, the damped response formalism employing the electric dipole approximation may fail to describe important spectral features in an X-ray absorption spectrum, which may be dipole forbidden, but may appear if higher transition moments are properly introduced.

Another drawback of non- and scalar-relativistic damped response theory compared to standard linear response theory, stems from the fact, that it requires the use of complex vectors already at the one-component level. This then requires complex algebra, which increases the computational complexity roughly by a factor of four. However, at the two-component level this does not increase the computational effort, since the transition densities are complex also for regular response theory. Here, the number of possible solution increases dramatically, since transitions are no longer pure singlet or triplet transitions. Since damped response vectors are usually not associated with a single excited state, we can use the same number of reference frequencies to describe systems of varying size. This number may be selectively increased, in order to better resolve the underlying features provided by the dynamic polarizability. Especially for systems with a particular high density of states, a description of the spectral features on the basis of few eigenvalues, may quickly become prohibitively expensive at the one- or two-component level, as more and more roots need to be extracted.[300,301] To illustrate this case, consider a set of the three Cd clusters, Cd_4, Cd_6, and Cd_8. Fig. 6.3 depicts the molar absorbance calculated in the context of the *GW*-BSE method, either using 50 frequencies in the context of damped response theory, adopting a common lifetime of 0.1 eV, or extracting the first 50 lowest-lying roots from the eigenvalue equation. Due to the increasing density of states, which grows as the cluster size increases, the lowest-lying 50 roots are only able to cover a decreasing spectral range, such that for Cd_8 the highest energy excitation extracted is at an energy of roughly 2.5 eV, approximately 1 eV lower than for Cd_4, which is not sufficient to simulate the spectral features in this energetic range. In contrast, in damped response theory, the area is described with the same number of frequency points. Since the complex polarizability features contributions from neighbouring transitions, the spectra even contain information of transitions from excitation outside the spectral window considered here, as can be seen from the decreasing flanks of Cd_4 and Cd_8. Note that each frequency point at the electronic dipole approximation requires the consideration of all three cartesian components, making them more expensive than the individual roots in standard theory, by

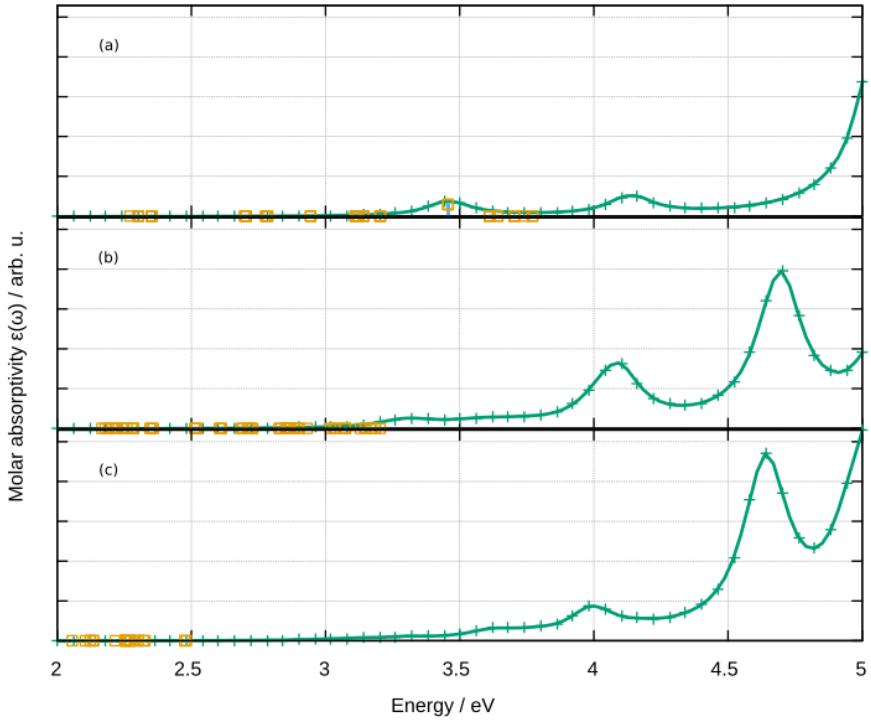

Figure 6.3: Molar absorption coefficient as obtained using damped and linear response formulations for small Cd clusters. 50 equally spaced frequency points were chosen to simulate the spectrum between 2 and 5 eV shown as green crosses, adopting a common lifetime parameter of 0.1 eV. The green lines are obtained by interpolation using cubic splines. The individual roots obtained from the eigenvalue equation are shown in orange and only cover an decreasing spectral area as the system size increases. Geometries were taken from ref. 265. Ground states were optimized at the PBE0[251] level, employing a fine grid (size 5a)[252–254]. The x2c-TZVPPall-2c basis set in combination with suitable auxiliary basis sets were used throughout.[221,255] The ground state energies were converged to 10^{-12} E_h, while the density was converged to 10^{-10}. Relativistic effects were introduced by using the two-component X2C-Hamiltonian in the DLU approximation.[56,272,273] The graphs shown correspond to the cluster sizes Cd_4 (a), Cd_6 (b), and Cd_8 (c).

roughly a factor of three. Furthermore, it is more difficult to extract additional information of these features from the damped response vectors, as these contain information, not only from a single excitation, but also from neighbouring features. If the underlying excitations are properly separated, e.g., by using a smaller damping factor, the damped response vectors may start to contain information associated with individual excitations.

The above example already illustrates, how this method can help in extending the chemical space for which response calculations can be done, especially at the two-component level, not only in relation to X-ray experiments, but also for systems of an increasing density of states.

6.3 Core-Valence Separation in *GW*-BSE

In the preceding two sections, the absorption spectra were described using the complex polarizability within the damped response theory, where spectral features were directly obtained at selected frequencies in a predefined energy window. In this section, an alternative approach, specifically geared towards the description of core-excited states is presented. Here, the excitation energies, which correspond to interior eigenvalues, are directly extracted from the electronic Hessian. It relies on the restriction of the space of single excitations, which span the electronic Hessian. The idea is, by neglecting the usually small coupling elements between core and valence states, the underlying problems, associated with valence and core excitations, can be assumed to be sufficiently decoupled.[308] In order to obtain the excitation energies of CESs, the linear response eigenvalue

equations are then only solved for a small sub matrix, only involving occupied core and the full virtual space. This approach is commonly referred to as core-valence separation or CVS and was initially proposed by Cederbaum and co-workers.[289,290] By neglecting the valence states, the lowest-lying solutions of the linear response eigenvalue problem then correspond to CESs, which are readily extracted using standard techniques.[136,295,306] The CVS approach has been applied to a variety of methods, including ADC,[20,308–310] linear response CC[19] and equation-of-motion-CC.[311,312] The errors from neglecting the coupling to valence states are oftentimes found to be small.[19] For standard TDDFT and TDHF methods it is trivial to implement, as it involves only restricting the excitation space, while for post Hartree–Fock methods further considerations are required. Likewise, in CVS-BSE the contributions of valence electrons can not be fully neglected. While, the coupling matrix elements between valence and core states can be assumed to be small, their contribution may become important in order to describe the valence-particle-core-hole interaction subject to the dielectric screening of all electrons. Both approaches were implemented in the context of this thesis, allowing for the inclusion or exclusion of screening effects of frozen occupied states or frozen virtual states independently in the dielectric matrix. In tab. 6.1 this effect is illustrated by comparing results for the two lowest-lying core-excited states close to the carbon K-edge in C_2H_3F. Computational details are given in the description of tab. 6.1. These features can be assigned to the transition from the C $1s$ core levels to the π^* system of the C-C double bond and have been experimentally observed at 285.0 and 287.1 eV respectively.[313] The order of the transitions can be easily explained by considering the reduction of the electron density, due to the presence of the electronegative fluorine at one carbon atom, which draws electron density. This also lower the screening of the carbon nucleus, resulting in an increase of the CEBE of the core electrons. This increases the excitation energies compared to the core electrons of the other carbon atom. To test our approach, reference values are obtained by solving the eigenvalue problem in the full tensor space dimension, which we will be simply denoted as BSE. In CVS-BSE*, contributions of the valence electrons to the dielectric matrix are neglected, while in CVS-BSE, the full static screening, identical to the one used in non-CVS or reference BSE calculations is employed. The values for the CVS-BSE are in excellent agreement to the reference values, the error of which is observed to be 0.01 eV or lower for this example. In contrast, the error for the incomplete screening increases to several eV (CVS-BSE*). This illustrates the importance of using the full dielectric matrix in CVS. For valence excitations, the effect of freezing the core electrons has not be examined, but is assumed to be far smaller, as the screening of the corresponding hole and particle states due the core electrons is assumed to be small, for the resulting particle and hole states in the valence region. Using the full dielectric screening matrix fortunately does not result in an stark increase in the overall cost for most systems, since the BSE kernel in its static approximation requires the evaluation of the dielectric matrix only once, which is then used in order to transform the RI intermediate, which is then used throughout the solution of the standard eigenvalue problem in its reduced space. Depending whether the quasiparticle energies are obtained self-consistently or at the G_0W_0 level, the deviation to the experiment is found to be within 1.0 or 0.2 eV in this example. Note, that the error for the quasiparticle energies at the evGW level are found to increase with respect to G_0W_0. This is a well-known phenomenon and is related to the underscreening of electrons, if the screened interaction is evaluated in an self-consistent manner, as is done in evGW.[204] The observed electron binding energies are then usually found to be too large, which in turn overestimates the excitation energies. This agrees well with our observations here. We also find our results in comparable and in general good agreement with the values provided by Wenzel and Dreuw, who used different (CVS-)ADC variants in order to describe this system. Methods derived within the framework of ADC, are a commonly used for the description of core-excited states of small molecules.[308] While these results are in no way representative, they are at least encouraging. The GW-(CVS-)BSE approach is further assessed in chapter 9 for a set of small inorganic molecules for several GW variants.

We conclude this chapter by considering some key differences for these methods. In this work, both the damped response and the CVS approach are considered for their application in order to provide reliable ways for the description of core-excited states. While in damped response theory the polarizability may be evaluated for any frequency directly, it still requires the solution of the linear system in the full space of the single excitations. In CVS, this space is considerably reduced. For many applications, the calculation of excited states can then be done in negligible time, compared to the evaluation of the quasiparticle energies for the GW-BSE method. As the density of states increases this may change. However, in these cases

Table 6.1: The lowest two core-excited states at the carbon K-edge in CH_2CHF, obtained by using the *GW*-BSE method and compared to experimental values and results obtained using the algebraic diagrammatic construction scheme (ADC). Experimental values are taken from ref. 313. ADC results were taken from ref. 308, where "2x" refers to the extended ADC(2) (ADC(2)-x) method. Reference values using the full tensor space spanned by all single-excitations are referred to by BSE, while CVS is used to indicate an restricted space for which valence electrons are kept frozen. The CVS-BSE* does not feature contributions of the frozen valence electrons in the construction of the (static) dielectric matrix, in contrast to CVS-BSE, which considers all contributions. The quasiparticle energies were optimized using the fsCD-*GW* approach described prior and explicitly evaluated for all states below 10 eV with respect to the initial KS-eigenvalues, either in a one-shot manner setting the renormalization parameter to one (G_0W_0-1) or self-consistently via the ev*GW* method. Ground states were optimized using the PBE0[251] function, integrated over a fine grid (size 5a)[252–254] Scalar-relativistic effects were included by usage of the DLU-X2C-Hamiltonian,[56,272,273] here, employing the x2c-TZVPPall-2c basis set and suitable auxiliary basis sets in all steps.[221,255]

	G_0W_0-1			ev*GW*			ADC		
Transition	BSE	CVS-BSE*	CVS-BSE	BSE	CVS-BSE*	CVS-BSE	ADC(2x)	ADC(3)	Exp.
C $1s$ (CH2) $\rightarrow \pi^*$	284.95	278.71	284.95	285.98	279.80	285.97	285.05	287.17	285.0
C $1s$ (CHF) $\rightarrow \pi^*$	286.96	280.82	286.95	287.99	281.15	287.98	287.33	289.07	287.1

combining both approaches may prove to be beneficial, in order to describe the optical spectra of highly excited states of very large systems. This combination has not been explored in the context of this work. Furthermore, damped response does not provide means to exclude pseudo-continuum solutions, which are excitations from valence states to high-lying diffuse virtual states. In the above example spurious transitions involving the F $2s$ state were found within close proximity to the carbon K-edge for the reference calculation. These transitions do not occur in the reduced tensor space used in the CVS approach.[299] For damped response theory, these states may become difficult to identify, as the complex polarizability does not provide much information to the true nature of the underlying transitions. These transitions are usually found to be sensitive to changes diffuse functione in the basis set.[143] However, this may become impractical for many applications, as it increases the effort in order to check for spurious amplitudes.

7 Origin-Independent Oscillator Strength

The interaction between a static or dynamic electromagnetic field and a molecular system is commonly described in a semi-classical picture. Here, the full interacting term can usually be expanded in a series of multipole moments, allowing for easy access to derived quantities such as the transition dipole moments, in order to describe the transition probabilities or similar properties associated with excited states. For monochromatic dynamic electromagnetic fields the leading term, the electric dipole moment, is usually sufficient. This assumes, that the associated wavelength is far larger than the spatial extend of the molecular system, which is usually given in the case of UV/Vis spectroscopy. The interaction is then modelled by a simple scalar potential.[314] As one is interested in dipole-forbidden transitions or starts approaching shorter wavelengths, this approximation may start to break down and second order interaction terms are required to describe the correct structure and recover important features. When going beyond the electric dipole approximation special care must be taken in order to ensure the correct physical behaviour of the properties of concern, as higher terms may inadvertently carry an spurious dependency on the gauge origin. This chapter introduces the basics of the semi-classical description of light-matter interaction. Gauge-invariant second order oscillator strengths are discussed, as they were implemented and used in the context of this thesis, in order to describe highly excited states, associated with core electrons.

7.1 Semi-Classical Light-Matter Interaction

The interaction of charged particles with (classical) external electromagnetic fields, in the context of quantum mechanics, may be realised through the application of the minimal coupling principle.[315,316] The momentum operator, $\boldsymbol{p}$, acting on a particle of charge q is substituted by the generalized momentum operator, $\boldsymbol{\pi}$, following

$$\boldsymbol{p} \longrightarrow \boldsymbol{\pi} = \boldsymbol{p} - \boldsymbol{A}(\boldsymbol{r}, t), \tag{7.1}$$

where $\boldsymbol{A}(\boldsymbol{r}, t)$ is the vector potential. The electric and magnetic fields, $\boldsymbol{E}(\boldsymbol{r}, t)$ and $\boldsymbol{B}(\boldsymbol{r}, t)$, may be expressed using the vector potential, as

$$\boldsymbol{E}(\boldsymbol{r}, t) = -\boldsymbol{\nabla}\varphi(\boldsymbol{r}, t) - \frac{1}{c}\frac{\partial}{\partial t}\boldsymbol{A} \quad \text{and} \quad \boldsymbol{B}(\boldsymbol{r}, t) = \boldsymbol{\nabla} \times \boldsymbol{A}(\boldsymbol{r}, t), \tag{7.2}$$

where $\varphi(\boldsymbol{r}, t)$ is a scalar potential. From these expression, it can be seen, that the electric and magnetic fields remain invariant with respect to different forms of the vector and scalar potentials, which can be related by so-called gauge transformations. The vector and scalar potentials are therefore not uniquely defined.[44,316–318] In the Coulomb gauge, the vector potential is chosen to be divergence-free, i.e., it satisfies

$$\boldsymbol{\nabla} \cdot \boldsymbol{A} = 0, \tag{7.3}$$

and therefore commutes with the momentum operator. Note that the Coulomb gauge is not strictly Lorentz invariant and can not describe retardation effects, which therefore cannot occur in the following.[12] Applying the minimal coupling principle to the non-relativistic Hamiltonian results in[319,320]

$$\boldsymbol{H} = \sum_i^n \frac{1}{2}\left(\boldsymbol{p}_i - \frac{1}{c}\boldsymbol{A}(\boldsymbol{r}_i,t)\right)^2 + \boldsymbol{V}(\boldsymbol{x}_1,\boldsymbol{x}_2,...,\boldsymbol{x}_n,t) - \varphi(\boldsymbol{x}_1,\boldsymbol{x}_2,...,\boldsymbol{x}_n,t)\mathbf{1}_2 - \frac{1}{2}\sum_i \boldsymbol{\sigma}\cdot\boldsymbol{B}(\boldsymbol{r}_i,t), \tag{7.4}$$

where $\boldsymbol{\sigma} = (\boldsymbol{\sigma}_x, \boldsymbol{\sigma}_y, \boldsymbol{\sigma}_z)^{\mathrm{T}}$, with $\boldsymbol{\sigma}_{x,y,z}$ being the Pauli matrices. The additional term corresponds to the spin-Zeeman interaction. Further assuming the electric and magnetic fields to be sufficiently weak, the terms quadratic in $\boldsymbol{A}(\boldsymbol{r},t)$ can be neglected. The interaction potential of an electron with electromagnetic radiation can therefore be written as

$$\boldsymbol{V}^{\mathrm{in}}(\boldsymbol{x}_1,\boldsymbol{x}_2,...,\boldsymbol{x}_n,t) = -\frac{1}{c}\sum_i^n \boldsymbol{A}(\boldsymbol{r}_i,t)\cdot\boldsymbol{p} - \varphi(\boldsymbol{r}_1,\boldsymbol{r}_2,...,\boldsymbol{r}_n,t)\mathbf{1}_2 - \frac{1}{2}\sum_i \boldsymbol{\sigma}\cdot\boldsymbol{B}(\boldsymbol{r}_i,t), \tag{7.5}$$

where we used the fact, that $\boldsymbol{p}$ and $\boldsymbol{A}$ commute in the Coulomb gauge, according to eq. 7.3. In the following, we will only consider the external electromagnetic field as a small perturbation to a Kramers symmetric system in its ground states.[84,86] Here, the spin-Zeeman term is neglected. The vector potential of a monochromatic linearly polarized electromagnetic field is given as[321]

$$\boldsymbol{A}(\boldsymbol{r},t) = \tilde{\boldsymbol{A}}_0\boldsymbol{\varepsilon}\mathrm{e}^{i\boldsymbol{k}\cdot\boldsymbol{r}-\omega t} + \tilde{\boldsymbol{A}}_0^*\boldsymbol{\varepsilon}\mathrm{e}^{-i\boldsymbol{k}\cdot\boldsymbol{r}-\omega t} \quad \text{with} \quad \tilde{\boldsymbol{A}}_0^* = \tilde{\boldsymbol{A}}_0^\dagger \quad \text{and} \quad \varphi(\boldsymbol{r},t) = 0, \tag{7.6}$$

where $\tilde{\boldsymbol{A}}_0$ and $\tilde{\boldsymbol{A}}_0^*$ are the Fourier coefficients. $\boldsymbol{\varepsilon}$ is the polarization vector, $\boldsymbol{k}$ the wave vector and ω the frequency. The latter two are related according to

$$|\boldsymbol{k}| = k = \frac{\omega}{c} = \frac{2}{\pi\lambda}. \tag{7.7}$$

The transition rate between the ground state and nth excited state is obtained by applying Fermi's golden rule,[317,322] from which the dimensionless oscillator strength is obtained according to

$$f_{0n} = \frac{2}{E_{0n}}|\boldsymbol{T}_{0n}|^2, \tag{7.8}$$

with the transition moment, $\boldsymbol{T}_{0n}$, of the full semi-classical interaction is given as

$$\boldsymbol{T}_{0n} = \sum_i \langle 0|\mathrm{e}^{i\boldsymbol{k}\cdot\boldsymbol{r}_i}\boldsymbol{\varepsilon}\cdot\boldsymbol{p}_i|n\rangle\,. \tag{7.9}$$

The oscillator strength is thus connected to the probability of a transition and is often used in order to model the absorption spectrum of an molecule, which can then be used to relate quantum chemical calculations of excited states to experimental observations.

7.2 Gauge-Invariant Oscillator Strength

The exact form of the transition moment, even in its semi-classical approximation, is difficult to calculate. More commonly, it is only considered in low-order approximations. To this end, the exponential in eq. 7.9 is first expanded in a Taylor series, from which the transition moments are obtained as

$$\boldsymbol{T}_{0n} = \boldsymbol{T}_{0n}^{(0)} + \boldsymbol{T}_{0n}^{(1)} + \boldsymbol{T}_{0n}^{(2)} + ... \tag{7.10}$$

The zeroth-order approximation of this expansions results the electric dipole approximation of the oscillator strength , i.e,

$$\boldsymbol{T}_{0n} \approx \boldsymbol{T}_{0n}^{(0)} = \boldsymbol{T}_{0n}^{(\boldsymbol{\mu})}. \tag{7.11}$$

Continuing this expansion, the first order correction is given by

$$\boldsymbol{T}_{0n}^{(1)} = -\frac{1}{2}\sum_i \langle 0|(\boldsymbol{k}\cdot\boldsymbol{r}_i)(\boldsymbol{\varepsilon}\cdot\boldsymbol{p}_i)|n\rangle = \boldsymbol{T}_{0n}^{(\boldsymbol{Q})} + \boldsymbol{T}_{0n}^{(\boldsymbol{m'})}, \tag{7.12}$$

which are the electric quadrupole, $\boldsymbol{T}_{0n}^{(\boldsymbol{Q})}$, and magnetic dipole transition moments, $\boldsymbol{T}_{0n}^{(\boldsymbol{m'})}$. The electric quadrupole operator and the magnetic dipole operator, $\boldsymbol{Q}$ and $\boldsymbol{m'}$, correspond to the symmetric and skew-symmetric terms with respect to a permutation of $\boldsymbol{\varepsilon}$ and $\boldsymbol{k}$.[10] The elements of the electric quadrupole and magnetic dipole operators in the so-called velocity gauge are

$$Q_{\mu\nu} = \frac{i}{2}(r_\mu p_\nu + p_\mu r_\nu) \quad \text{and} \quad {m'}_\mu = \frac{1}{2c}(\boldsymbol{r}\times\boldsymbol{p})_\mu \quad \text{with} \quad \mu,\nu \in \{x,y,z\}. \tag{7.13}$$

Note, that the prime in $\boldsymbol{m'}$ is used to distinguish this form from the more general magnetic dipole, which includes the spin-dependent contributions associated with the Zeeman interaction, which was neglected in a previous step. The complementary representations in length gauge can be obtained from commutator relations, in the limit of a complete basis.[10,323] While the zeroth-order approximation to the oscillator strength is origin-independent, meaning, it stays invariant with respect to a shift of the molecular origin represented by the simple substitution

$$\boldsymbol{r} \to \boldsymbol{r} + \boldsymbol{O}, \tag{7.14}$$

where $\boldsymbol{O}$ is an arbitrary vector, this is not generally true for higher multipole moments.[324–327] Bernadotte and co-workers demonstrated how this spurious behaviour may be resolved by truncating the multipole expansion in a slightly different manner. Instead of truncating the Taylor expansion of the interaction, they first inserted eq. 7.9 in eq. 7.8 and collected terms in the same order of the wave vector.[10] Using the approach, the second order correction to the oscillator strength becomes

$$f_{0n}^{(2)} = \frac{2}{E_{0n}}\left(|\boldsymbol{T}_{0n}^{(1)}|^2 + 2\mathfrak{Re}\left[\boldsymbol{T}_{0n}^{(0)*}\cdot\boldsymbol{T}_{0n}^{(2)}\right]\right) = \frac{2}{E_{0n}}\left(|\boldsymbol{T}_{0n}^{(1)}|^2 + 2\mathfrak{Re}\left[\boldsymbol{T}_{0n}^{(0)*}\cdot\left(\boldsymbol{T}_{0n}^{(\boldsymbol{O})} + \boldsymbol{T}_{0n}^{(\boldsymbol{M'})}\right)\right]\right), \tag{7.15}$$

where we have introduced the electric octupole moment, $\boldsymbol{O}$, and magnetic quadrupole moment, $\boldsymbol{M'}$, which are defined as

$$O_{\mu\nu\kappa} = (r_\mu r_\nu p_\kappa + r_\mu p_\nu r_\kappa + p_\mu r_\nu r_\kappa) \quad \text{and} \quad M'_{\mu\nu} = (r_\mu(\boldsymbol{r}\times\boldsymbol{p})_\nu + (\boldsymbol{r}\times\boldsymbol{p})_\mu r_\nu). \tag{7.16}$$

Note that this is the first non-zero correction to the oscillator strength, as the terms associated with the products of the electric dipole moment and either the electric quadrupole or magnetic dipole are zero. List *et al.* demonstrated that this behaviour is true for all orders, such that only even orders may give non-trivial contributions, as the products of odd terms are purely imaginary and cancel.[320] If the orientation of a molecular system with respect to the electromagnetic radiation has no preferred direction, as is common in experimental setups, the isotropic averages have to be considered. The individual contributions are given as

$$\langle f_{0n}^{(\boldsymbol{\mu})}\rangle_{\text{iso}} = \frac{2}{3E_{0n}} |\langle 0|\boldsymbol{\mu}|n\rangle|^2 \tag{7.17}$$

$$\langle f_{0n}^{(\boldsymbol{m'})}\rangle_{\text{iso}} = \frac{E_{0n}}{6c^2} |\langle 0|\boldsymbol{m'}|n\rangle|^2, \tag{7.18}$$

$$\langle f_{0n}^{(\boldsymbol{Q})}\rangle_{\text{iso}} = \frac{E_{0n}}{20c^2}\left(\sum_{\mu\nu} |\langle 0|Q_{\mu\nu}|n\rangle|^2 - \sum_{\mu} |\langle 0|Q_{\mu\mu}|n\rangle|^2\right), \tag{7.19}$$

$$\langle f_{0n}^{(\boldsymbol{\mu},\boldsymbol{O})}\rangle_{\text{iso}} = -\frac{2E_{0n}}{45c^2}\sum_{\mu\nu}\langle 0|\mu_\nu|n\rangle\langle 0|O_{\mu\mu\nu}|n\rangle \tag{7.20}$$

and

$$\langle f_{0n}^{(\boldsymbol{\mu},\boldsymbol{M'})}\rangle_{\text{iso}} = \frac{-E_{0n}}{9c^2}\tilde{\varepsilon}_{\mu\nu\kappa}\langle 0|\mu_\nu|n\rangle\langle 0|M'_{\kappa\mu}|n\rangle\,. \tag{7.21}$$

Here, $\tilde{\varepsilon}_{\mu\nu\kappa}$ is the Levi-Civita symbol. In contrast to the electric quadrupole and electric octupole moments, the magnetic quadrupole general does not feature any permutation symmetry with respect to its cartesian components. The isotropic second order oscillator strength becomes

$$\begin{aligned}\langle f_{0n}\rangle_{\text{iso}} &\approx \langle f_{0n}^{(0)}\rangle_{\text{iso}} + \langle f_{0n}^{(2)}\rangle_{\text{iso}} \\ &= \langle f_{0n}^{(\boldsymbol{\mu})}\rangle_{\text{iso}} + \langle f_{0n}^{(\boldsymbol{Q})}\rangle_{\text{iso}} + \langle f_{0n}^{(\boldsymbol{m'})}\rangle_{\text{iso}} + \langle f_{0n}^{(\boldsymbol{\mu},\boldsymbol{O})}\rangle_{\text{iso}} + \langle f_{0n}^{(\boldsymbol{\mu},\boldsymbol{M'})}\rangle_{\text{iso}}\,.\end{aligned} \tag{7.22}$$

Here, $\langle f_{0n}^{(2)}\rangle_{\text{iso}}$ is the first non-trivial correction to the isotropic averaged oscillator strength in the electric dipole approximation $\langle f_{0n}^{(0)}\rangle_{\text{iso}}$, where all quantities are evaluated in the velocity gauge. As shown by Bernadotte *et al.* eqs. 7.20 and 7.21 exactly cancel the spurious origin dependence, which occur for the oscillator strength only considering eqs. 7.18 and 7.19 as corrections to the zeroth order expression.[10] Special care must be taken when the oscillator strengths are to be considered in length gauge instead. Sørensen and co-workers demonstrated that by using the appropriate expressions for the electric moments in length gauge, the oscillator strength becomes dependent on the origin again.[328] A problem of using the oscillator strength in 7.22, is due to the fact that transitions with large dipole strengths may result in negative and therefore spurious transition probabilities.[307] This has been attributed to the different requirements of the second order terms in the multipole expansion.[328] The correct behaviour may be restored if even higher orders are considered, but is impractical, as it has

been observed to converge slowly in some cases.[320] Additional effort has been made in the literature in going beyond the usual multipole expansion entirely and using the full semi-classical interaction term in eq. 7.9 directly, which require more sophisticated techniques for an adequate evaluation.[11,320,329,330] Therefore, while the second order approximation should be used carefully, especially in cases where basis set deficiencies are observed, here, we will limit ourselves to the second order form described above, as going beyond the electric dipole approximation becomes increasingly important if the X-ray regime is subject of interest.

7.3 Implementation and Validation

In the context of this thesis, the second order oscillator strength, as given by eq. 7.22, was implemented in the TURBOMOLE program suite at the one-component level for closed-shell systems as well as two-component Kramers-symmetric systems. The latter extension is easily realised by further considering the imaginary contributions to the matrix elements of the multipole moments, resulting from the complex spinor functions, generally required at the two-component level of theory. Here, the interaction with dynamic magnetic fields were not considered. At the one-component, non-relativistic or including scalar-relativistic effects, this contribution exactly cancels for closed-shell systems and non-zero contributions can occur only (spin-)unrestricted calculations, for which the oscillator strengths vanishes due to spin-selection rule. This also follows for Kramers-symmetric densities, although one should note, that in the presence of a magnetic field, the Kramers symmetry is generally lost. When using schemes for the elimination of the small component in the Dirac equation such as in X2C or DKH theory, a correct description of the matrix elements of the multipole moments likewise would require a analogues unitary transformation, starting from the four-component expressions .[302–304] This is the picture-change correction, which was previously discussed in sec. 6.2, and is neglected in the following. As most of the necessary expressions are already available in the TURBOMOLE program suite, only the matrix elements of the electric octupole moments and magnetic quadrupole moments in velocity gauge needed to be implemented. The required integrals can be efficiently evaluated using Gauss-Hermite quadrature. From eq. 7.16 it is easy to see the symmetry of the electric octupole moments with respect to interchanging the indices. Therefore, only a total of ten unique matrix elements need to be calculated explicitly, with respect to the cartesian coordinates. For the electric quadrupole, this same consideration results in six unique elements. The magnetic quadrupole may be conveniently rearranged using the canonical commutator relations relating the position and angular momentum operators,[331] which results in simple expressions, suitable for the evaluation using the Gauss-Hermite quadrature. The implementation is validated by verifying the gauge-invariance of the resulting second order oscillator strengths. Tab. 7.1 depicts the second order terms of the 3$^{\text{rd}}$ lowest-lying transition at the Fe K-edge in $FeCp_2$ for shifts with respect to the origin. The resulting spectrum is depicted in fig. 7.1. The premier peak is dipole forbidden and the resulting feature only

Table 7.1: Gauge-dependent and -invariant isotropically-averaged oscillator strengths and correction terms as proposed by Bernadotte *et al.*[10] for the 3$^{\text{rd}}$lowest-lying transition at the Fe K-edge in $FeCp_2$, found at 7120.76 eV. The ground state was optimized using the PBE0 functional and the x2c-TZVPPall-2c basis set employing the X2C-Hamiltonian.[221,255] Geometries were obtained at the one-component level of theory. Excited states were optimized using the CVS-BSE@(fs-CD)GW method. The molecule was shifted by 10^3 a$_0$ along the cartesian axes, with $\boldsymbol{\varepsilon}_{x,y,z}$ being the unit vectors, indicating the direction of the shift. The complete second order term, $\langle f_{0n}^{(2)} \rangle_{\text{iso}}$, stays gauge-invariant in all cases shown.

	Ref.	$\boldsymbol{\varepsilon}_x \cdot 10^3$ a$_0$	$\boldsymbol{\varepsilon}_y \cdot 10^3$ a$_0$	$\boldsymbol{\varepsilon}_z \cdot 10^3$ a$_0$	$\frac{\boldsymbol{\varepsilon}_x+\boldsymbol{\varepsilon}_y}{\sqrt{2}} \cdot 10^3$ a$_0$	$\frac{\boldsymbol{\varepsilon}_x+\boldsymbol{\varepsilon}_y+\boldsymbol{\varepsilon}_z}{\sqrt{3}} \cdot 10^3$ a$_0$
$\langle f_{0n}^{(\boldsymbol{Q})} \rangle_{\text{iso}} + \langle f_{0n}^{(\boldsymbol{m'})} \rangle_{\text{iso}}$	2.77×10^{-6}	9.36×10^{-5}	6.68×10^{-5}	5.13×10^{-5}	7.50×10^{-5}	4.76×10^{-5}
$\langle f_{0n}^{(\boldsymbol{\mu},\boldsymbol{O})} \rangle_{\text{iso}} + \langle f_{0n}^{(\boldsymbol{\mu},\boldsymbol{M'})} \rangle_{\text{iso}}$	4.29×10^{-13}	-9.08×10^{-5}	-6.40×10^{-5}	-4.85×10^{-5}	-7.22×10^{-5}	-4.48×10^{-5}
$\langle f_{0n}^{(2)} \rangle_{\text{iso}}$	2.77×10^{-6}	2.77×10^{-6}	2.77×10^{-6}	2.77×10^{-6}	2.77×10^{-6}	2.77×10^{-6}

becomes visible using higher orders of the oscillator strength. It corresponds to Fe $1s \rightarrow Cp_2$ e_g-like transitions with a strong metal $3d$-character.[333] Electric dipole contributions are found to be vanishingly small at less than 10^{-9}, requiring second

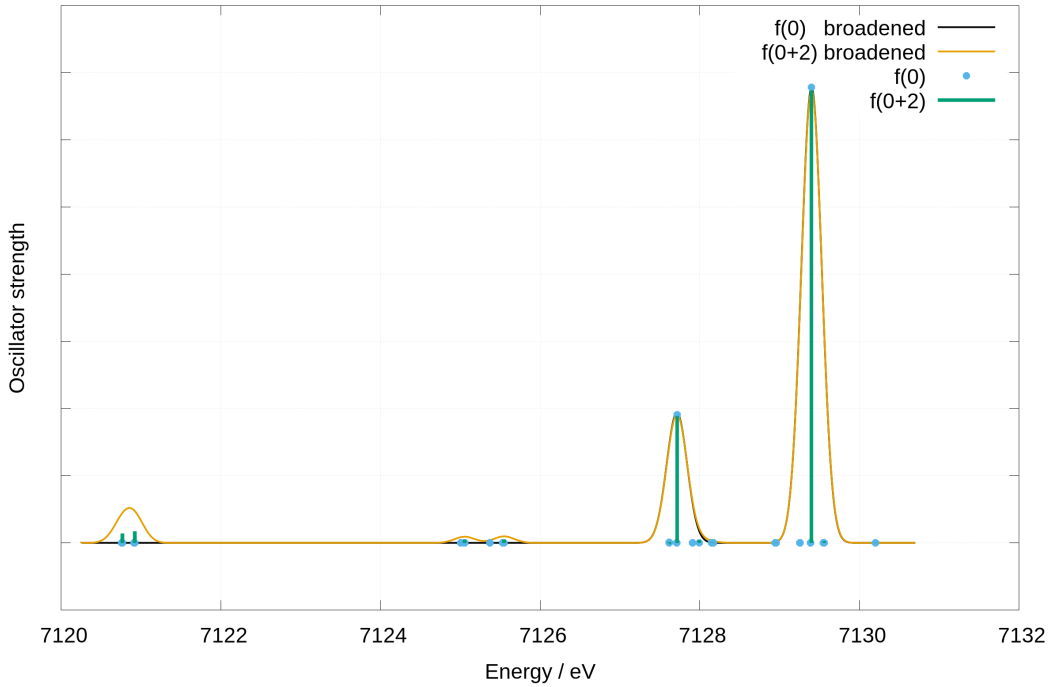

Figure 7.1: Simulated XAS spectrum for the Fe K-edge in $FeCp_2$ obtained using the *GW*-BSE method. Quasiparticle energies were obtained using the G_0W_0 method fixing Z_p to one and using the fsCD-*GW*approach discussed in sec. 5.5. Oscillator strengths were calculated in both zeroth and second order, shown in $f^{(0)}$ (blue dots) and $f^{(2)}$ (green bars), respectively. Broadened spectra were obtained by superimposing Gaussian distributions with a FWHM (full width at half maximum) of 0.3 eV. The quasiparticle energies were calculated for the highest occupied and the 15 energetically lowest-lying unoccupied spinors. The remaining states were shifted by the quasiparticle energies the highest-lying occupied or lowest-lying virtual state respectively. Ground states were optimized using the PBE0 251 functional employing a fine grid (size 5a)[252,254] and the x2c-TZVPPall-2c basis set.[221] The RI-approximation was used throughout. Relativistic effects were modelled using the two-component X2C-Hamiltonian, using the DLU approximation.[56,272,273] The finite nucleus model was used.[273,332] The mSNSO approach was used to account for relativistic effects on the two-electron interactions.[61–63] Kramers symmetry was enforced in ground and excited state calculations.

order terms for comparison with the experiment. This feature was experimentally found at an energy of 7123 eV, which is within few eV of the results using the CVS-BSE technique employed here.[333] Upon translating the molecule by 10^3 a_0 in multiple directions, the translational variance of the initial formulation of the second order oscillator strengths, including only the magnetic dipole and electric quadrupole terms becomes obvious as the oscillator strengths becomes orders of magnitude larger. The translational invariance is retained by including all terms shown in eq. 7.22, as the additional terms exactly cancel out the spurious behaviour of the initial approximation in all cases examined. While this approximation allows to go beyond the electric dipole approximation in a systematic manner, including higher orders might be unsatisfactory due to the slow convergence behaviour in some cases. Future efforts could entail the use of the exact semi-classical interaction, which is beyond the scope of this thesis.

8 Assessment of the Starting Point Dependence of GW for Vertical Ionization Potentials

The quasiparticle energies obtained within the *GW* approach provide approximations to the ionization potentials and electron affinities of a system. While the fully self-consistent solution of Hedin's equations in the *GW* approximation is independent of the starting point, this property is only retained by some approximate iterative schemes, such as the quasiparticle self-consistent *GW* method.[212,214,215] System sizes commonly encountered in real-life applications often prohibit the use of these approaches and rely on fixing the Lehmann amplitudes at the Hartree–Fock or Kohn–Sham levels. This results in a clear dependence on the initial reference, as the self-energy is always constructed within the space spanned by the approximate Lehmann amplitudes. These approaches have previously been assessed from different perspectives.[29,334–336] Here, we intend to extend these studies by examining new approaches within DFT, such as local hybrid functionals (LHFs), in this discussion and evaluate them with respect to other density functional approximations (DFAs) commonly used for both core and valence states.[337] LHFs interpolate between the Hartree–Fock and semilocal DFT exchange, as a function of the electronic coordinate. This tries to differentiate between areas where either type is known to be superior compared to the other, for example, in order to cancel the self-interaction error, commonly associated with DFAs in one-electron areas. These errors may be identified by finding so-called local mixing functions (LMFs), such as the iso-orbital indicator originally introduced by Jaramillo *et al.*,[337] but has since been extended to much more sophisticated types.[338–343] In this chapter, the performance of different starting points regarding their ability in the description of the first vertical ionization potential, representing the valence states, as well as CEBEs, representing low-lying states, will be assessed. The results for the former, were previously published in ref. 206 for which we will briefly recapitulate some of the results. The initial discussion relating to the GW27 and the GW100 test sets,[172,240,335,344] is then further extended, by considering a non-iterative and non-renormalized G_0W_0 variant. The GW27 and GW100 test sets considered here, include 27 and 100 small molecules, respectively, for which data from highly precise methods is available in the literature.[335,344] In order to assess the viability of these approaches in the context of CEBEs, we will use these same DFAs for the CORE65 test set.[29,345] This set includes 65 ionization potentials associated with the $1s$ states of light elements in small organic and inorganic systems.[29,345] The CORE65 set uses experimental reference data, as charge excitations involving core states are generally more difficult to obtain in a reliable manner, especially as approaches such as ΔSCF may become problematic to converge to sensible solutions. For approximate *GW* methods, the linearized G_0W_0 method often fails in these cases, resulting in spurious renormalization factors, as initial references are often far from the true quasiparticle energies. The assumed linearity of the self-energy may then start to break down, especially as $\boldsymbol{\Sigma}$ is known to feature a complicated structure for the energy ranges concerned here.[28,29,204] Similarly, we observed difficulties regarding the convergence of the self-consistent solution of the eigenvalue equations at the G_0W_0 level, which proved unreliable, at times resulting in spurious solutions. We therefore choose not to attempt to compare our results with respect to ones obtained from solving the quasiparticle equations in the context of G_0W_0 at this point. Instead, the renormalization parameter is set to one without iterating the quasiparticle energies. This implicitly assumes that the quasiparticle energy for the converged solution to be close to a simple substitution of the exchange-correlation potential with the self-energy at the Kohn–Sham level. This constitutes a somewhat pragmatic approach, where the quasiparticle energies can be obtained in a stable manner, also for larger systems. However, these quasiparticle energies are then no longer true solutions of the Dyson equation. In the context of the first ionization potentials, which are associated with valence states, we will compare our results for the

linearized G_0W_0 method, the eigenvalue-only self-consistent *GW* method (ev*GW*), and the non-interative non-renormalized scheme, which we will denote as G_0W_0-1 in the following. For the CORE65 test set, we will further replace the linearized G_0W_0 method and instead consider the GW_0 approach. This method only features self-consistency in the Green's function and describes the screened exchange at the Kohn–Sham level. This is done since self-consistency in the screened exchange tends to result in an underscreening of the electrons, due to the overestimation of the HOMO-LUMO gap. For CEBEs, this issues then results in an noticeable trend, where the ionization potentials of low-lying states are overestimated, i.e., the quasiparticle energies are too low.[204] As such, results at the G_0W_0 level may often provide a more balance description, attributed to a favourable cancellation of errors.

8.1 Ionization Potential of Valence Electrons: the GW27 and GW100 Test Sets

In this section, the first ionization potentials for molecules part of the GW27 and the GW100 test sets are assessed, containing 27 and 100 closed-shell molecules, respectively. The following discussion includes sections previously published as part of ref. 206 and will be briefly discussed. Reference values were taken from literature and correspond to the first ionization potentials described within the ΔSCF CCSD(T) method, which will be referred to as ΔCCSD(T).[344] All presented calculations are done at the one-component level of theory, chosen to be consistent with the computational approach used for the reference data above. Ground states were optimized, adopting the same geometry and basis sets, as used by Krause and co-workers. The calculations were done using the def2-TZVPP basis for all elements.[266,346] Ground states were converged to at least 10^{-9} E_h in the energy and 10^{-6} with respect to variations in the density. Various DFAs were employed, which were integrated on a fine grid (size 5).[252,253] The tested DFA include representatives of different commonly used types, as well as more modern approaches. For the pure DFAs, the BP86,[347,348] PBE,[349] and TPSS,[350] were included, which do not feature any form of Hartree–Fock exchange. For hybrid functionals, the BH&HLYP,[348,351,352] B3LYP,[348,351,353] and PBE0[251] DFAs, were included, while LC-ωPBE,[354–356] ωB97D-X,[354,355,357] and CAM-B3LYP,[354,355,358] were used as representatives of the class of range-separated hybrid (RSH) DFAs. We also include the LHFs LH07t-SVWN[359], LH12ct-SsirPW92[360], LH14t-calPBE[361], which will be abbreviates as LH07t, LH12ct and LH14t, respectively, as well as LH20t,[362] LHJ14,[342] and mPSTS.[206,338–340] This choice covers different types of local mixing functions further elaborated in ref. 206. The starting point dependence is evaluated for three different *GW* variants, which are the linearized G_0W_0 method, the non-iterative non-renormalized G_0W_0 method, denoted as G_0W_0-1, and the eigenvalue-only self-consistent ev*GW* method. Especially the linearized G_0W_0 method and the ev*GW* method are popular approaches commonly used to approximate the full self-consistent *GW* methods, based on the spectral representations, for the use in many applications.[363–367] Quasiparticle energies were optimized using the AC-*GW* method, employing the standard grid with 128 Gauss-Legendre quadrature roots and the same number of Padé approximants. Here, only the quasiparticle energies associated with the HOMO and LUMO are optimized explicitly, which is sometimes referred to as the "scissor operator" approach.[368] For the HOMO, the quasiparticle energies obtained using the analytic continuation and the contour deformation techniques are expected to be nearly indistinguishable, as the self-energy is expected to be much more well-behaved for these frequencies. The fsCD-*GW* method, when only optimizing the HOMO and LUMO levels is completely equivalent to the standard CD-*GW* method and is therefore not considered. The results for the 27 first ionization potentials in the GW27 test set are shown in fig. 8.1. The individual quasiparticles are provided in the supporting information of ref. 206 for the linearized G_0W_0 and the ev*GW*, while the results for the non-iterative non-renormalized G_0W_0-1 approach, are listed in sec. A.2 in the appendix. Using the linearized G_0W_0 method (top in fig. 8.1) the pure DFAs are found to consistently underestimate the ionization potentials, where the mean signed error (MSE) and the mean absolute deviation (MAD) are found to be roughly -0.4 and 0.4 eV, respectively. This error is reduced when considering hybrid functionals, where Becke's half-and-half approach shows the overall lowest error, here. The

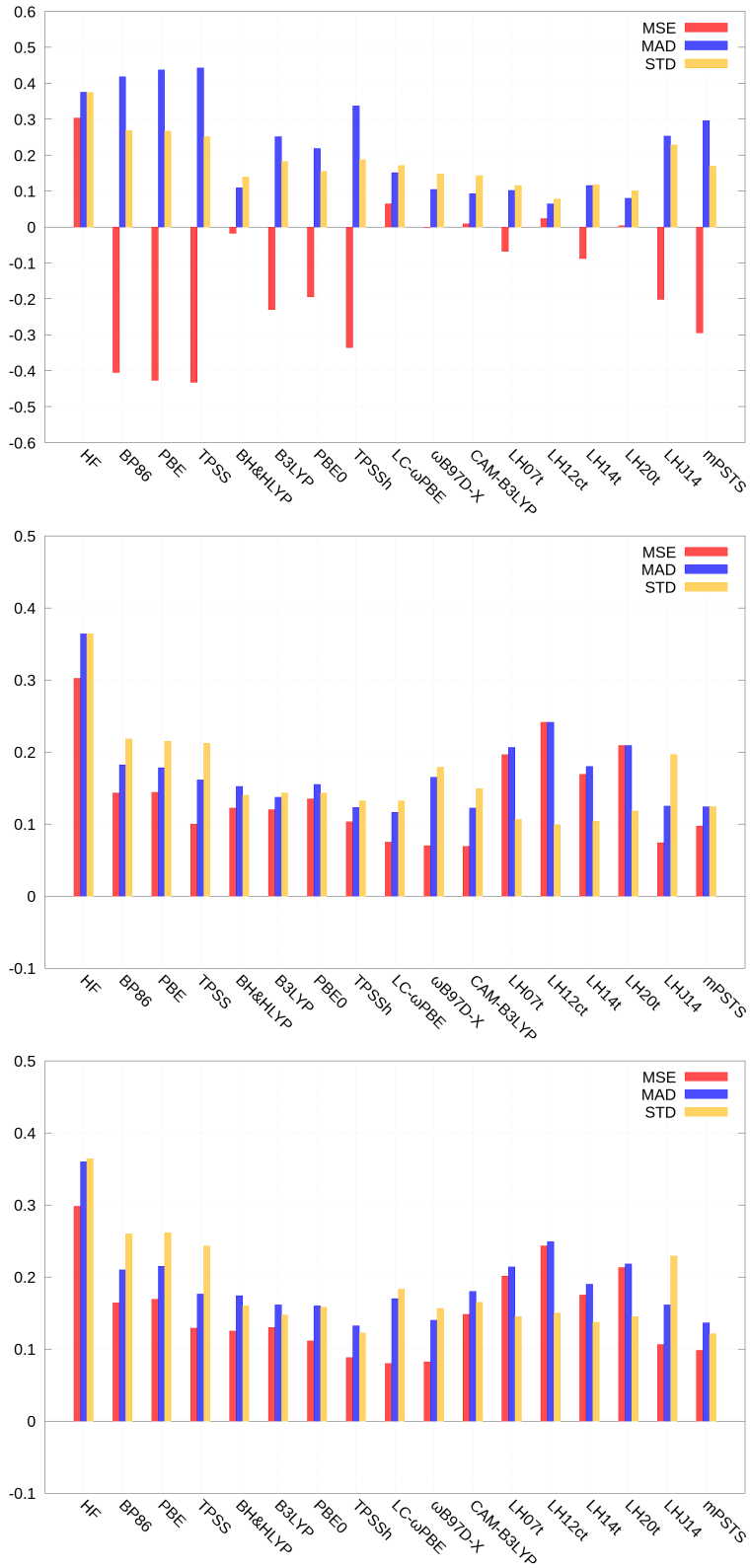

Figure 8.1: Comparison of various DFAs for the GW27 test set. Errors are shown for the ionization potential of the highest occupied orbital with respect to reference values provided by Krause and co-workers.[344] The graph corresponds to the quasiparticle energies obtained using linearized G_0W_0 (top), non-iterative non-renormalized G_0W_0-1 (middle) and eigenvalue-only self-consistent evGW (bottom). The means signed error (MSE), mean absolute deviation (MAD) and the standard deviation (STD) are shown in red, blue and yellow, respectively. Computational details are given in the text.

performance of the BH&HLYP functional is consistent with the results provided by Bruneval *et al.* and Golze *et al.*, who found that errors for hybrid DFAs with a large Hartree–Fock exchange contributions, such as BH&HLYP, which incorporates 50% Hartree–Fock exchange, are lower compared to those featuring only little or no exact exchange at all, in the case of small molecules.[29,369,370] Deviations were found to be further reduced when using RSHs. Here, the MAD is observed to be less than $0.2\,\text{eV}$ for LC-ωPBE, ωB97D-X, and CAM-B3LYP, while the MSE is found between 0.1 and $-0.1\,\text{eV}$, suggesting the negative of the quasiparticle energies to be closely centered around the reference. The improvement for LHFs is less obvious. Here, ionization potentials for LHFs using a local mixing function based on the iso-orbital indicator, such as LH07t, yield results comparable to the RSH, where LH12ct and the highly parameterized LH20t show the lowest deviations for all DFAs considered. Comparing these results to the ionization potentials obtained at the ev*GW* level, which is shown in the bottom graph in fig. 8.1, we find the errors for the pure DFAs to be largely reduced, becoming closer to the hybrid DFAs. Overall, the differences between the various starting points appear to be largely diminished, even though the orbital coefficients correspond to those of the initial Kohn–Sham references. For the best performing DFAs at the G_0W_0 level, the error does not appear to improve when switching to the self-consistent ev*GW* approach. For some, such as the LH07t or the LH12ct the errors are even larger. We find the results obtained at the G_0W_0-1 level, which is the middle graph in fig. 8.1, to be remarkably close to the eigenvalue self-consistent scheme, where the differences are in the range of a few 100ths of an eV for many functionals investigated here. The best performing DFAs are the standard hybrid and the RSH DFAs, followed by the LHJ14 and the mPSTS LHFs. The ionization potentials for the Hartree–Fock reference are similar for all *GW* schemes used. The MAD and MSE are approximately 0.4 and 0.3 eV, with a comparable high STD of 0.4 eV. Using the full Hartree–Fock exchange, results in an overestimation of the ionization potential. Similarly, we find the DFAs provided by either ev*GW* or G_0W_0-1, to overestimate the quasiparticle energies for most molecules in this set, although this overestimating is comparably small in the range of 0.2 eV. For ev*GW*, this is expected, due to the overestimation of the gap, which results in an underestimation of the dielectric screening of the electrons, which in turn stabilizes the occupied states. This problem will be revisited in the context of CEBEs, as these effects then tends to be much more pronounced for higher energies, for example, when dealing with core electrons. The errors for the G_0W_0-1 method resemble the results for ev*GW*, while the screened exchange is here calculated at the initial Kohn–Sham level. These quasiparticle energies do not correspond to proper solutions of the quasiparticle eigenvalue equations, but still manage to largely improve over the renormalized G_0W_0 and show a diminished dependence on the initial DFAs, comparable to what is observed for ev*GW* . We can validate these findings by comparing these with the results obtained for the far larger GW100 test set. The individual ionization potentials are listed in sec. A.3 in the appendix for the G_0W_0-1 method, while the results for the linearized G_0W_0 method and ev*GW* are again given in the supporting information of ref. 206. Note that some molecules are featured in both sets, but may have slightly different geometries. The respective results for the GW100 test set are shown in fig. 8.2. The errors follow a similar trend to what was previously observed for the GW27 test set, where DFAs with a high percentage of Hartree–Fock exchange tend to show lower errors, while the Hartree–Fock method overestimates the ionization potentials. The differences between ev*GW* and G_0W_0-1 are slightly more prominent, but still appear to follow a similar trend. The largest difference is seen for ωB97D-X, which has the largest error for all DFAs in G_0W_0-1, with a MAD of approximately 0.3 eV, while the results at the ev*GW* level are far smaller, having MADs of 0.2 eV. In the latter case, it is one of the best performing DFAs, while the overall differences are comparatively small in hybrid functionals, RSHs and LHFs. Again, we see an the overall error to be clearly reduced at both, the G_0W_0-1 and the ev*GW* levels, when compared to the error seen for linearized G_0W_0 . For most DFAs, the MAD for the former G_0W_0-1 and ev*GW* is observed between 0.2 and 0.1 eV, where ionization potentials are estimated to be too high, when compared to the reference values. We find for both test sets, the G_0W_0-1 method to provide reasonable results, often comparable in quality to the more expensive iterative ev*GW* approach. Both approaches appear to largely reduce the functional dependence, when compared to the linearized G_0W_0 method. This may suggest that the G_0W_0-1 method may be a convenient alternative, with respect to the iterative optimization, in areas where this method is expected to be problematic. Here, the G_0W_0-1 at least provides a reasonable approximation to the quasiparticle energies for valence levels, where we may choose from many different DFA starting points and obtain a similar overall performance.

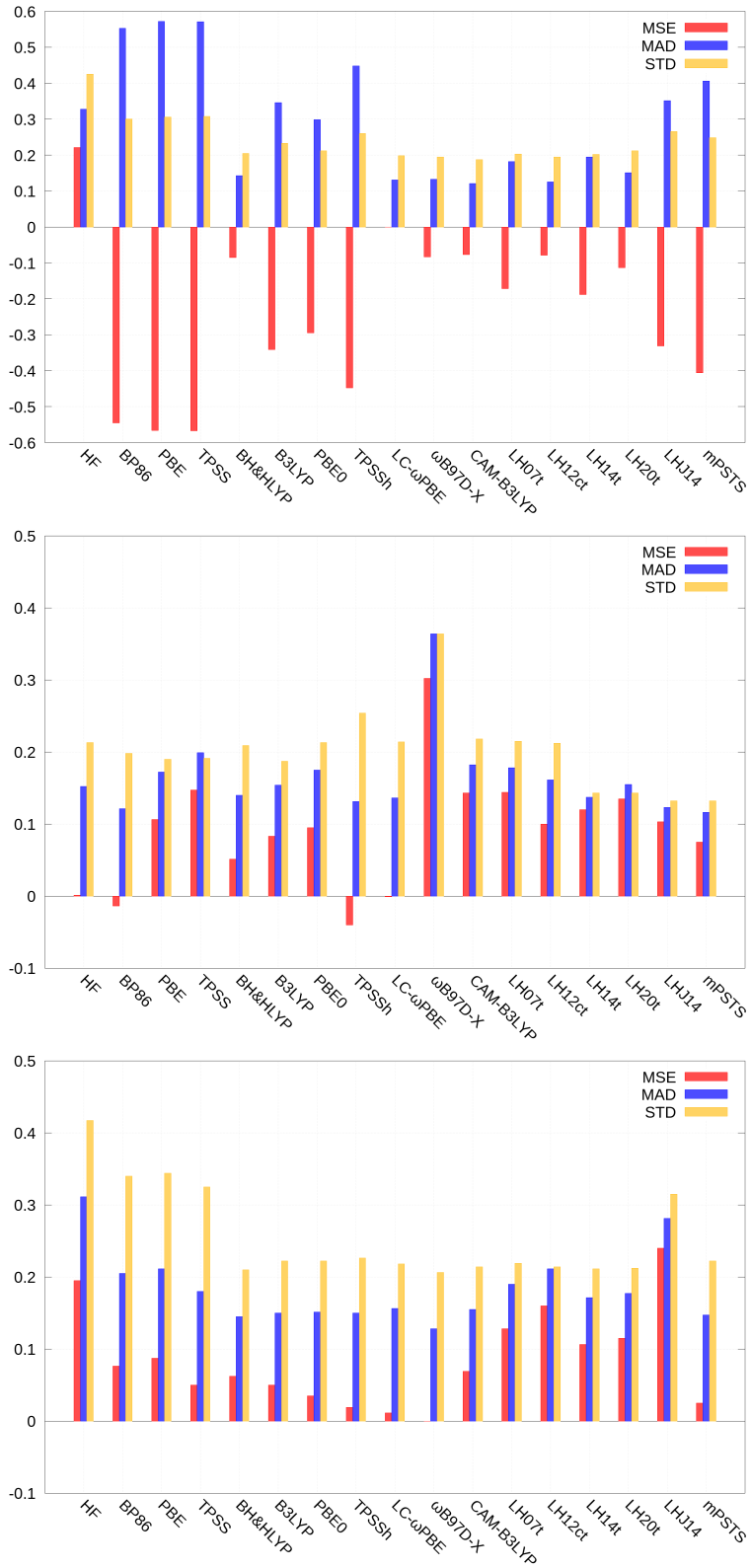

Figure 8.2: Comparison of various DFAs for the GW100 test set. Errors are shown for the ionization potential of the highest occupied orbital with respect to reference values provided by Krause and co-workers.[344] The graph corresponds to the quasiparticle energies obtained using linearized G_0W_0 (top), G_0W_0-1 (middle) and evGW (bottom). The mean signed error (MSE), mean absolute deviation (MAD) and the standard deviation (STD) are shown in red, blue and yellow, respectively. Note that the scale for evGW is slightly extended, in order to account for the larger deviations. Computational details are given in the text.

8.2 Core-Electron Binding Energies: the CORE65 Test Set

Having assessed different DFAs for the first ionization potential, we now turn our attention towards the description of CEBEs. Here, the CORE65 test set compiled by Golze *et al.* will be examined, in order to evaluate the starting point dependence of different *GW* methods and DFA combinations.[29] Ideally, these methods should provide a balanced and robust description of both valence and core properties. The CORE65 test set contains experimental reference values for 65 electron binding energies associated with 30 C, 21 O, 11 N, and 3 F $1s$ states for a set of 32 small organic and inorganic molecules. The individual quasiparticle energies and experimental references are provided in sec. A.4 in the appendix. We use the same experimental references put together by Golze *et al* in ref. 29, and choose here to compare quasiparticle energies using three different *GW* approximations, which are G_0W_0-1, GW_0, and ev*GW* . Since the Kohn–Sham eigenvalues generally do not correspond to good approximations to the ionization potentials, the Taylor expansion of the self-energy may not result in satisfactory quasiparticle energies, which is why it is not considered here.[336] This can also be explained by the complicated structure of the self-energy in this regions, where the renormalization parameter may easily become unstable, resulting in spurious quasiparticle energies.[29] Instead, we include the partial self-consistent GW_0 method, which was previously suggested to provide a more balanced approach, avoiding the issues of ev*GW*, while also going beyond the initial G_0W_0 method. Here, the quasiparticle energies in the Green's function are updated, while the dielectric screening is only considered at the reference level.[28,29,204] We compare these results to the one-shot non-renormalized G_0W_0-1 approach, used in sec. 8.1, as it provided surprisingly close results to the ev*GW* method, which is generally seen as reliable for valence states. Finally, we will also compare these to the ones provided at the ev*GW* level. The geometries used in the following were adopted from ref. 29, which were optimized at the PBE0 level[251]. Scalar-relativistic effects were included, using the one-component (spin-free) DLU-X2C-Hamiltonian operator[56,272,273] and a suitable basis set, here, given by the x2c-TZVPPall basis in combination with a suitable auxiliary basis set.[221,255] The effects of decontraction of the basis set associated with the target state on the quasiparticle energies were not examined. Ground states were converged to 10^{-12} E_h and 10^{-12} in the density. We consider all DFAs given in the previous section. Quasiparticle energies were obtained using the fsCD-*GW* approach, introduced in sec. 5.5.2, which was developed and implemented in the context of this thesis. For the iterative schemes GW_0 and ev*GW*, the quasiparticle energies of states in close energetic proximity to the target state, here, all $1s$ states of the same element, are explicitly optimized. As discussed in sec. 5.5.2, quasiparticle energies are often susceptible to changes of the relative energies to close-lying states, due to poles entering or leaving the first quadrant of the contour integral (see also sec. 5.3). These states are included to provide a consistent description of the relative energies of immediate states, in order to adequately approximate the results obtained by the full spectral approach, while keeping a reasonable cost. Furthermore, the HOMO and LUMO are also explicitly included, where the occupied and virtual blocks, aside from the target set, are then shifted by the difference between the Kohn–Sham eigenvalues and the corresponding quasiparticle energies. This follows the "scissor operator" approach used, for example, in sec. 8.1. For calculations at the GW_0 level, we will employ the "fixed grid" approximation, where the frequency grid used for the evaluation of the residues is kept at the first iteration.

We first examine the G_0W_0-1 approach, which corresponds to the top most graph in fig. 8.3. The pure DFAs, BP86, PBE, and TPSS, show a similar behaviour, as was seen in sec. 8.1 at the valence level, and tend to underestimate the binding energies. Including Hartree–Fock exchange stabilizes the electronic states and the binding energies increase. This results in an overestimation for hybrid functionals. B3LYP and TPSSh, show a MAD of approximately 0.2 eV, while the PBE0 shows a much higher MAD of 0.8 eV for the cases examined here. BH&HLYP was one of the best performing DFAs for valence states, while in the core region, binding energies are consistently overestimated with a MAD and MSE of 1.6 eV, much higher than B3LYP, which incorporates only 20% Hartree–Fock exchange. This is especially interesting, as it suggests that in contrast to the observations for the first vertical ionization energies, a high percentage of exact exchange percentage does not necessarily improve the results, compared to the pure DFAs, but may even be detrimental. The commonly used hybrid functionals, B3LYP, PBE0, and TPSSh, appear to provide a more balanced description, especially when compared to the RSHs and LHFs, based on

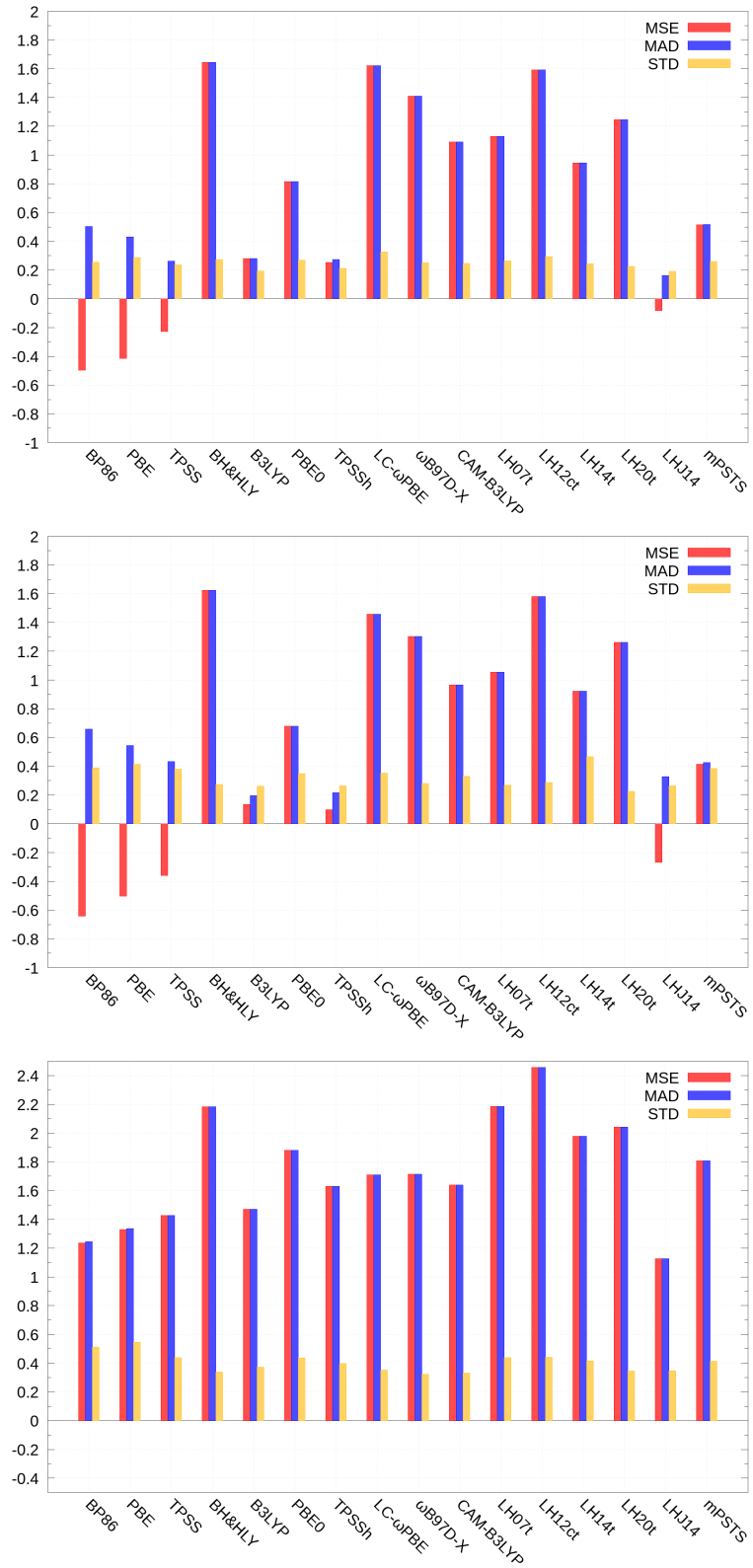

Figure 8.3: Comparison of various DFAs for the CORE65 test set. Errors for 65 individual ionization energies CEBEs of C, O, N, and F 1s states for a set of 32 small molecules. Ionization energies were obtained at the G_0W_0-1 (top), GW_0 (middle) and evGW (bottom) levels. The mean signed error (MSE), mean absolute deviation (MAD) and the standard deviation (STD) are shown in red, blue and yellow, respectively. Computational details are given in the text.

the iso-orbital indicator. These consistently perform worse with respect to simple hybrid functionals, aside from BH&HLYP, or even pure DFAs. Here, LHJ14 and the mPSTS appear comparable to the better performing hybrid DFAs.
Using the GW_0 method (middle graph in fig. 8.3), we find the predicted ionization potentials for the pure DFAs to be slightly worse, while the hybrid DFAs, RSHs and LHFs, aside from LHJ14 and mPSTS, show small improvements of 0.1 eV or less. However, both RSHs and the LHFs, based on the iso-orbital indicator, result in quasiparticle energies, which are still at least 1 eV too high with respect to the experiment. Lastly, we briefly look at the effect of also iterating the screened exchange. The ev*GW* approach consistently predicts too high binding energies, also for pure DFAs, as shown in fig. 8.3 at the bottom (note the different scale used). CEBEs are found to be between 1.0 and 2.4 eV too high. This effect is consistent with the discussions in refs. 29 and 217, where the success of non- or partial self-consistent schemes, was attributed to a compensation of the missing vertex function by the Kohn–Sham eigenvalues, which results in an overscreening, due to the underestimation of the gap, and favourable cancellation of errors. Nevertheless, here, we do not find a significant improvement, when comparing GW_0 with the results of G_0W_0-1 for these examples. One benefit of the ev*GW* approach is however, in its ability to diminish the starting point dependence, at a cost of generally too high CEBEs.

9 Assessment of *GW*-BSE for Core-Excited States

Following the assessment of the *GW* approximation for charge excitations in the previous chapter, we now focus our efforts on the description of charge neutral excitations using the (*GW*-)BSE. This method in its static limit has been thoroughly assessed in the context of valence excitations, used, for example, in order to simulate UV/Vis experiments.[24,277–279,292,366,371] Its performance regarding the description of CESs has only been recently addressed in the context of small molecules, mostly limited to light elements.[150,372] The field of X-ray spectroscopy offers a variety of well established methods for the characterization and analysis of solids and molecules.[1,373] These techniques allow for the study of the local environment of selected elements in a system. While this often requires the access to synchrotron light sources, recent efforts have been made, in order to introduce these techniques on a laboratory scale.[1,8] The description of the underlying processes from a theoretical point of view is challenging. DFT based methods, which are usually an excellent tool for the prediction of optical properties associated with valence excitations, may suddenly struggle with the correct description in the higher energy regime. Intrinsic problems in most DFAs, such as the self-interaction error, are typically amplified for these levels.[16–18,21,374] On the other hand, coupled-cluster based techniques are often limited to the description of small molecules, such as diatomics and small hydrocarbons.[19,20,275,310,375–381] The description of SOC effects further becomes prohibitively expensive or is limited to perturbative corrections.[382] These approaches are then most suitable to s type states, responsible for the K- and L_1-edges, or when the splitting is considerably large. Here, the *GW*-BSE approach may provide a reasonable alternative to both, as Green's function based methods have already been demonstrated to offer an efficient tool for the prediction of electron binding energies (see the discussion in the previous chapter and the cited literature therein). As such, the *GW* approach has been shown to prove viable not only for valence, but also for core electron binding energies. In the following chapter, the *GW*-BSE approach will be assessed in the context of CESs. However, it will be limited to the description of bound states in the (pre-)K- and L-edge regions, as continuum solutions add an additional level of complexity with respect to the basis set, which is beyond the scope of this thesis.[383] In the first section, a set of small molecules will be examined using different starting points for the *GW*-BSE method, which will be briefly compared to TDDFT, high level coupled-cluster methods, as well as experimental data. The underlying excitations are mostly attributed to K-edge Rydberg transitions. This section includes results previously published as part of ref. 150, where the damped response formalism was combined with the *GW*-BSE approach in a quasirelativistic framework. In addition, the *GW*-BSE method is tested using a set of inorganic molecules, for which the absorption near the K- and L-edges of transition metals and metalloids are examined. For these systems, the description of SOC effects becomes relevant, as the $2p$ state splits into $2p_{3/2}$ and $2p_{1/2}$ by several eV. The resulting L_2- and L_3-edges often give rise to overlapping spectra, which then require a quasirelativistic two-component framework in order to even qualitatively describe the experimental observations. While some of these systems have previously been investigated using TDDFT,[384] we will focus here on the assessment of practical approximations to the *GW*-BSE method, which may also be applied to larger systems. The quasiparticle energies are provided using the fsCD-*GW* method, while the excitation energies are evaluated within the CVS-BSE approximation. The spectra are simulated using the zeroth and second order oscillator strengths in order to account for dipole forbidden transitions. They are broadened by superimposing Gaussian functions, where the FWHM is chosen in accordance with the experiment.

9.1 Assessment of K-edge Absorption Spectra for Light Systems

The following section contains results previously published as part of ref. 150, regarding the performance of the (damped) *GW*-BSE method and considers the pre-K-edge region of Ne, CO, H_2O, and Xe. Except for Xe, these systems were subject of a recent study by Coriani and co-workers, using damped response coupled-cluster methods.[19] In order to ensure a good comparability between their original data and our results, the same geometries and basis sets were used. The structure correspond to the experimental geometries following refs. 385, 386, and 387, while Dunning's aug-cc-pCVTZ basis set was chosen,[388–390] including a suitable auxiliary basis set.[391] For Xe, the Sapporo-DKH-TZP-diffuse basis set was used.[392] The auxiliary basis set employed was provided by M. E. Harding and is given in the supporting information of ref. 150. To account for the Rydberg states, a series of diffuse functions, following the scheme by Kaufman and co-workers was added,[383] the exact specifications are given in ref. 150 and follow the approach by Coriani and co-workers.[19]. Ground states were optimized for various DFAs and converged to at least 10^{-9} E_h in the energy and 10^{-7} in the density. CAM-B3LYP,[354,355,358] BH&HLYP,[348,351,352] PBE0,[251] and TPSS[350] were used to assess the starting point dependence of the *GW* method. Aside from this, the results were further compared to the ones obtained from TDDFT employing CAM-B3LYP, BH&LYP, and PBE0 as DFAs, integrated on a fine grid (size 5a).[252–254] Reference data for the local hybrid functional LH12ct-SsirPW92,[360] which will be abbreviated as LH12ct in the following, was provided by C. Holzer, were a medium grid (size 3a)[252–254] was employed. LH12ct has been previously reported to provide good results with respect to Rydberg excitations, when compared to other DFAs, including different LHFs.[393] SOC corrections to the two-electron integrals were approximated by the modified screened nuclear spin–orbit (mSNSO) approach.[61–63] Quasiparticle energies were optimized at the ev*GW* level using the spectral representation ansatz.[161,172] The absorption cross section was evaluated using the damped response BSE method, described in sec. 6.2 and ref. 150. The light-matter interaction was considered in the electric dipole approximation, accounting for picture-change effects. Selected results are shown in tab. 9.1, where the transitions are assigned to the maximum of the absorption cross section obtained within the damped response formalism. For the *GW*-BSE method, only the results with

Table 9.1: Comparison of different methods for the description of XAS for Ne, H_2O, CO, and Xe. Results are shown for common DFAs, including the LHF, LH12ct-SsirPW92, abbreviated as LH-12ct, the ev*GW*-BSE method using the PBE0 reference. CCSDR(3) data are reproduced as given in ref. 19. Only the data for the premier peak at both CO edges were explicitly listed and higher excitations were not considered in the reference. Xe was not considered in by Coriani and co-workers. Experimental reference values and the corresponding reference are included.

Excitation	CAM-B3LYP	BH&HLYP	PBE0	LH12ct	*GW*-BSE	CCSDR(3)	Exp.	Ref.
Ne $1s \rightarrow 3p$	844.1	861.5	845.5	862.2	868.1	867.5	867.12	394
Ne $1s \rightarrow 4p$	845.1	862.2	847.1	863.1	870.5	869.1	868.69	394
Ne $1s \rightarrow 5p$	845.5	863.0	848.1	864.0	871.1	869.7	869.27	394
H_2O $O_{1s} \rightarrow 3s(a_1)$	519.8	532.4	521.6	534.4	534.8	534.9	534.0	395
H_2O $O_{1s} \rightarrow 3p(b_2)$	521.5	533.9	523.1	536.1	536.4	536.7	535.9	395
CO $C_{1s} \rightarrow 2\pi^*$	276.1	283.6	277.0	285.2	287.5	288.1	287.4	395
CO $C_{1s} \rightarrow 3s\sigma$	280.0	289.5	280.8	291.8	293.7	-	292.2	396
CO $C_{1s} \rightarrow 3p\pi$	280.8	290.4	281.4	292.8	295.3	-	293.3	396
CO $O_{1s} \rightarrow 2\pi^*$	520.1	532.0	521.7	533.1	535.6	535.0	534.2	397
CO $O_{1s} \rightarrow 3s\sigma$	523.3	536.7	525.0	538.2	540.3	-	538.9	397
CO $O_{1s} \rightarrow 3p\pi$	524.3	537.8	525.6	539.3	542.0	-	539.9	397
Xe $4d_{5/2} \rightarrow 6p$	62.1	64.6	62.0	62.4	65.1	-	65.1	398
Xe $4d_{3/2} \rightarrow 6p$	63.9	66.5	63.9	64.3	66.8	-	67.0	398

respect to the PBE0 reference are shown. The other DFAs provided results of similar quality and are extensively discussed in ref. 150. The different starting points generally were found to be within 1 eV with respect to the experiment, where the error for higher Rydberg excitations was observed to increase to approximately 1.5 eV, depending on the DFA and excitation.

These errors may in part be attributed to additional basis set requirements, but were found to be in good agreement with the results provided at the CCSDR(3) level. As expected, most DFAs greatly underestimated the absolute excitations energies and predict these excitations at too low energies. For CAM-B3LYP, the Ne $1s \rightarrow 3p$, for example, was found at 844.1 eV, 23 eV below the experimentally observed excitation at 867.12 eV, where the error at the PBE0 level is similar.[394] This is largely attributed to the self-interaction error, where DFAs with a high Hartree–Fock exchange contribution are known to show an improved behaviour, due to cancelling some of this effect.[18] This agrees well with the observation for BH&HLYP, which are much closer to the experimentally observed transitions. The absolute deviations of the premier peaks are found within 2 to 6 eV. LH12ct slightly improves upon this, but still tends to predict too low excitation energies. However, for Xe $4p_{5/2}$ and $4p_{3/2}$, it performs similar to CAM-B3LYP and PBE0, and underestimates the transition energies by 2 eV. Here, the results for BH&HLYP are closer to the experimental values, only deviating by 0.5 eV, while *GW*-BSE correctly predicts these transitions within 0.2 eV or less. Note that errors for the different *GW*-BSE starting points were found to be similar overall.[150] When comparing relative energies, the different DFAs appear to either overestimate or underestimate these separations and no clear pattern arises. No particular DFA appears to show a clear improvement over the others. For the systems considered here, the *GW*-BSE method manages to consistently predict the absolute energies with excellent agreement to the experimental observations, especially when compared to common DFAs, such as PBE0. However, the correct description of the relative energies tends to be overestimated. This may also be due to basis set effects, as previously mentioned, where the quasiparticle energies may feature additional basis set requirements not included in TDDFT, which was not examined in detail here.[399]

9.2 Assessment of *GW*-BSE for K- and $L_{1,2,3}$-Edges in Inorganic Systems

In this section, a set of eight small molecules containing transition metals and metalloids are examined. The systems are shown in fig. 9.1. We assess the performance of the *GW*-BSE method using the pre-K- and L-edge features of these compounds. The L-edge has three distinct spectral regions for heavier elements, corresponding to the L_1, L_2, and L_3 edges, the latter two

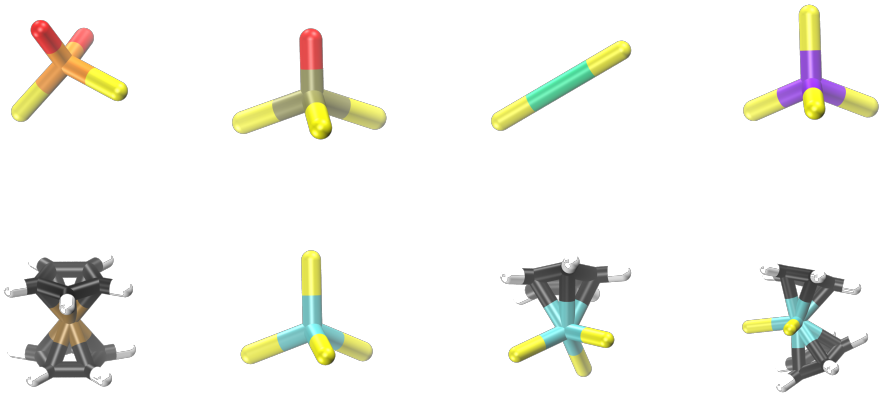

Figure 9.1: Optimized geometries for the molecules in the test set considered in this section. The systems considered are, from left to right, top to bottom, CrO_2Cl_2, $VOCl_3$, $PdCl_2$, $SiCl_4$, $FeCp_2$, $TiCl_4$, $TiCl_3Cp$, and $TiCl_2Cp_2$. Color scheme used here: oxygen (red), chloride (yellow), chromium (orange), vanadium (grey), palladium (green), silicon (violet), iron (brown), titanium (blue), carbon (black), and hydrogen (white).

arise from the $2p$ state, which splits into the $2p_{3/2}$ and $2p_{1/2}$ states, and can only be correctly described within a two- or four-component level of theory. Depending on the compound, these effects may also be required to qualitatively describe the character of valence excitations.[116] From the compounds above, we derive a set of 40 excitations, which correspond to easily identifiable features in the experimental spectra, which are then compared to the calculations. These 40 excitations contain 10

excitations associated with s type core orbitals, i.e., the K- and L_1-edges, and 30 excitations near the L_2- and L_3-edges, which involve the $2p_{3/2}$ or $2p_{1/2}$ electrons of the central metal or metalloid. Note that the energy scales for these transitions range from a hundred to thousands eV. Most common DFAs fail in accurately describing the different energy ranges and require large (uniform) shifts in order to compare to the experimental spectra.[384] Studies concerning the performance of TDDFT in the literature so far, are rare or only consider compounds of light elements, such as hydrocarbons.[17,384,400] This is in part due to the difficulty in producing proper reference data, but also in some ambiguity for the correct description, for example, whether using a uniform shift or nonuniform shift.[384] This makes a direct comparison difficult. We will therefore limit this discussion to the relation to the experimental values listed in the appendix, e.g., in tab. A.11 and only consider *GW*-BSE methods, applicable to a wider range of systems. Only the PBE0 reference Kramers symmetric ground state will be considered, which was found to provide reasonable quasiparticle energies for low-lying states in sec. 8.2. However, one should keep in mind, that this is not necessarily true for virtual states. Geometries and ground states were optimized using the PBE0[251] functional, which was integrated on a fine grid (size 5a)[252–254] and the x2c-TZVPPall-2c basis set, including suitable auxiliary basis sets for all atoms.[221,255] The finite nucleus model was used throughout.[273,332] Ground state energies were converged to at least 10^{-10} E_h and 10^{-9} in the density. Geometries were optimized at the one-component DLU-X2C level of theory,[56,272,273] from which the two-component ground state was obtained by a single point calculation. The effect of SOC on the two-electron integrals was modelled using the mSNSO. approach.[61–63] Quasiparticle energies were obtained using the fsCD-*GW* approximation presented in sec. 5.5.2, at either G_0W_0-1, GW_0, or ev*GW* levels. Only a subset of quasiparticle energies were explicitly evaluated, either including only the highest occupied and lowest unoccupied, thereby correcting the gap, by applying the "scissor operator", or including an additional 5 virtual and occupied Kramers pairs. In the CVS-BSE approach valence states, only contribute indirectly via the dielectric screening matrix. Additionally, we explicitly include the subset of core levels, where for the L-edges, L_1, L_2, and L_3 are included. Note that for calculations of spectra at the K-edge, the L-shell is not included and *vice versa*. The excited states were then optimized using the CVS-BSE method (sec. 6.3), where the lowest 80 roots were extracted in the reduced single excitation space. We supplement this, by data obtained using the correlation-kernel augmented (c)BSE variant. In order to compare our results to the experimental values, the calculated transition energies are broadened by a Gaussian distribution, scaled by the respective oscillator strength. Starting from 0.3 eV, the broadening parameter was subsequently increased, in order to average over multiple transitions, in cases were the experimental resolution was found to be lower, such that individual peaks in the calculations average and resemble the experimental pattern. Oscillator strengths were evaluated at the second order approximation, except in cases, where spurious (negative) values were identified. In these cases the electric dipole approximation was used. The calculated peaks are assigned to experimental features and are listed in sec. A.5 of the appendix. Here, we will only show and discuss the derived statistical quantities. In addition to the mean signed error, mean absolute deviation and the standard deviation, we include the mean absolute percentage deviation (MAPE) and the maximum absolute deviation (Max.AD) We begin by examining the results for the "scissor operator" approach, which is listed in the left column of tab. 9.2. For the G_0W_0-1 method, the MSE is found at 0.84 eV, which is larger than for the GW_0 method, with an MSE of 0.75 eV. However, the MAD for G_0W_0-1 is 1.46 eV, which is 0.21 eV smaller than for GW_0. The error distribution is narrower for G_0W_0-1, showing a standard deviation of 2.31 eV, compared to 3.14 eV in the case of GW_0. The largest error is found at 11.15 eV and 14.04 eV for G_0W_0-1 and GW_0, respectively, which corresponds to the Pd L_1-edge in $PdCl_2$, which is experimentally found at 3610.9 eV, and is overestimated. This is also the energetically highest transition in the set and therefore expected. If we only consider the L_2- and L_3-edges, which require the correct description of splitting due to SOC, the MSE for G_0W_0 and GW_0 is greatly reduced to less than 0.1 eV. Likewise, the MADs are significantly lowered by 0.8 and 0.9 eV. The maximum error is found at 4.05 and 3.67 eV for G_0W_0-1 and GW_0. This again corresponds to transitions of the $PdCl_2$ molecule, but is now attributed to a transition associated with the Pd $2p_{1/2}$ state. For the ev*GW*, MSE and MAD increase significantly. This is, however, expected following the discussion in sec. 8.2 and is mostly due to an overestimation of the CEBEs. In order to assess the relative errors, we briefly compare the mean absolute percentage error. All three approaches manage to predict the absolute peak positions well, as the spectra are only shifted by a few eV, as compared to typical DFAs.[384] This agrees with the initial expectations, as the *GW* method correctly predicts the binding

Table 9.2: Statistical data for the *GW*-BSE approach for CESs of molecules depicted in fig. 9.1 using different *GW* approximations. Individual transitions are listed in sec. A.5. "H/L" refers to the "scissor operator" approach, while (H/L±5) also includes an additional 5 virtual an occupied Kramers pairs explicitly. Computational details are given in the text. All values are in eV.

GW-BSE	(H/L)			(H/L±5)		
	G_0W_0-1	GW_0	evGW	G_0W_0-1	GW_0	evGW
K, L_1+$L_{2,3}$						
MSE	0.84	0.75	1.75	0.75	0.68	1.94
MAD	1.46	1.67	2.11	1.53	1.83	2.15
MAPE	0.18	0.20	0.19	0.19	0.23	0.19
STD	2.31	3.14	3.39	2.25	3.11	3.34
Max.AD	11.15	14.03	17.42	10.27	13.17	16.87
$L_{2,3}$						
MSE	0.07	−0.04	0.97	0.02	−0.10	1.10
MAD	0.77	0.78	0.99	0.92	0.98	1.11
MAPE	0.19	0.20	0.15	0.22	0.24	0.18
STD	1.08	1.05	1.08	1.21	1.22	1.10
Max.AD	4.05	3.67	4.86	4.03	3.61	4.81

energies for lower-lying states with excellent accuracy as well, while DFAs often struggle in this regard (see sec. 8.2 and refs. 336 and 29). As a higher number of states are explicitly considered, the MAD is found to increase singly by roughly 0.1 eV for all three approaches, even though the MSE decreases. This may partly be attributed to additional basis set requirements in order to correctly predict the quasiparticle energies of unoccupied states above the gap and agrees with the initial observation in the preceding section, where the separations of transitions were found to be too large in ev*GW*-BSE.[399] By applying only the "scissor operator", this may then result in a favourable cancellation of errors using the PBE0 reference. For the correlation-kernel augmented BSE approach, the individual transition energies are listed in tab. A.12 in the appendix and we again only present the statistical quantities in the following. The errors are given in tab. 9.3. Here, the transitions energies tend

Table 9.3: Statistical data for the *GW* -cBSE approach for CESs of molecules depicted in fig. 9.1 using different *GW* approaches. All values are in eV. See tab. 9.2 for further information.

GW -cBSE	(H/L)			(H/L±5)		
	G_0W_0-1	GW_0	evGW	G_0W_0-1	GW_0	evGW
K, L_1+$L_{2,3}$						
MSE	1.49	1.36	2.44	1.50	1.42	2.77
MAD	1.71	1.76	2.66	1.84	2.00	2.88
MAPE	0.17	0.17	0.31	0.19	0.21	0.35
STD	2.33	3.13	3.43	2.31	3.14	3.47
Max.AD	11.45	14.96	18.46	10.58	14.33	18.12
$L_{2,3}$						
MSE	0.72	0.56	1.66	0.75	0.61	1.91
MAD	0.91	0.80	1.66	1.10	1.06	1.97
MAPE	0.16	0.15	0.30	0.19	0.19	0.37
STD	1.15	1.09	1.18	1.32	1.35	1.51
Max.AD	4.88	4.46	5.73	4.88	4.43	6.25

to be overestimated, as the MSE and and MAD are increased by approximately 0.7 eV, while the STD is only slightly larger with respect to the standard BSE approach, depending on the method and number of quasiparticle energies explicitly included. The change in MAPE is minor. For ev*GW* the difference to the regular BSE approach increases. This is in part due to the way the screened exchange is calculated within cBSE, as it uses the Kohn-Sham eigenvalues to describe the dielectric screening,

similar to what is done in the GW_0 approach. We briefly try to assess the relative energies, by aligning the experimental and simulated spectra. This is done by identifying a common unambiguous feature, usually the largest band, and shifting all values according to the difference. Note that this reduces the number of data points. The MSE and MAD are then found at 0.41 and 0.40 eV for G_0W_0-1 and GW_0 correcting only the gap, while the error is slightly increased to 0.64 and 0.70 eV, respectively, if higher-lying states are included. This agrees with the observations in sec. 9.1, where the ev*GW*-BSE method was seen to overestimate the separation for most examples, using the spectral representation approach for the calculation of the eigenvalues and may be in part due to additional basis set requirements. For the shifted spectra, the errors for the cBSE method are reduced by approximately 0.1 eV in the MAE, while the MSE and STD are increased similarly, demonstrating that the DFA correlation can provide an improved description in the examples examined here. We estimate the effects of using the screened exchange at the Kohn–Sham level, by neglecting the correlation-augmentation and only use W_0 at the G_0W_0 level for (H/L$\pm$5). The MSE and MAD for the L_2-edges and L_3-edges were found to increase similarly to the results for cBSE, but the relative energies were significantly worse. This indicates the need for the DFT correlation contribution in the cBSE approach. However, by neglecting the quasiparticle energy correction in the screened exchange, its dependence on the initial reference increases and this initial observation may be subject to change.

We find these examples to approximately follow the trends of secs. 8.2 and 9.1. On one hand, self-consistency usually results in an overestimation of the electron binding energies,[29,336] which directly translates to the excitation energies, on the other hand, the relative energies are often overestimated, at least for small systems. Here, further studies regarding the basis set dependence, as well as an extension by considering various types of DFAs may provide a more complete picture, in order to assess more general trends. Also, going beyond the static approximation, at least including perturbative corrections, following the suggestion by Loos *et al.*,[282] may prove to be fruitful and could be subject of further studies. We conclude, that the *GW*-BSE approach manages to predict the absolute energies of CESs with comparatively high precision also for systems containing heavy elements. The *GW* approximation often reproduces the underlying electron binding energies within few eV, such that the resulting spectra are often close to the experimental observations. However, the relative energies tend to be too large. The source of this may be attributed to basis set deficiencies, the *GW* approximation or the static limit of the BSE. The static approximation to the dielectric matrix, is exact in the limit of small frequencies, where the RPA excitations are far higher than the true exitations, within the fully dynamic BSE. Going beyond the static approximation in the form of a perturbative correction scheme, may already provide a reasonable estimation of these effects.[282] In its current form, the *GW*-BSE approach can already be applied to a wide range of systems and recovers the excitation energies within reasonable accuracy. It generally does not suffer from the high self-interaction error usually found in most DFAs, although the RPA in the dielectric screening is not self-interaction free. It provides excitation energies within few eV to the experimental observations, As such, even in its static form, it is a sensible alternative to TDDFT and may proof useful in the description of highly-excited states, for the description of CESs, while maintaining an overall moderate computational effort, comparable to that of TDDFT.

10 Application to Core-Excited States of Lanthanum Compounds

High-energy resolution X-ray absorption near edge structure (HR-XANES) spectroscopy offers insight in the local electronic structure in molecules, by selectively exciting it core electrons. It is highly element specific and sensitive to the local density, which carries information regarding the formal oxidation state of an atom.[1,2] This technique can be used, in order to probe the orbital mixing of unoccupied states, using its intrinsic resolution of angular momenta, by considering different energy ranges, corresponding to the ionization potentials or edges. Recent articles suggested that this method may be helpful, in order to assess the bonding situation of lanthanide (and actinide) compounds, where a low covalent character has been proposed.[5,401–403] In this chapter, we consider two lanthanum compounds, specifically, the endohedral intermetalloid Zintl ion, $[(La@In_2Bi_{11})(\mu\text{-}Bi_2)\ (La@In_2Bi_{11})]^{6-}$, and the much simpler $La(CpMe_4H)_3$, which is its precursor material, and test our approach, based on the *GW*-BSE method, with respect to its capability in the rationalization of XAS experiments. The Zintl ion was first synthesized by Weinert *et al.* and comprises of two nonahedral ($La@In_2Bi_{11}$) units, bridged by two Bi atoms.[404] Its high charge is compensated by six equivalents of $[K\text{-}([2,2,2]crypt)]^+$ in the crystal lattice. In the following, we will be primarily concerned with the description of its optical absorption near the La L_3-edge, as done as preliminary work regarding the interaction of lanthanoids in intermetalloid systems. The HR-XANES spectra of both systems are depicted in fig. 10.1 and were provided by T. Vitova. Both spectra are shifted by 5482 eV, as we will mostly discuss qualitative aspects in the following, related to selected features, by comparing the experimental observations with quantum mechanical calculations.

The geometries were optimized at the scalar-relativistic one-component DLU-X2C level of theory,[56,272,273] employing the PBE0[251] DFA, which was integrated on a fine grid (size 4a).[252–254] The x2c-TZVPPall basis set was used for all atoms, employing suitable auxiliary basis sets.[221,255] The finite nucleus model was used throughout.[273,332] Ground states were converged to at least 10^{-9} E_h and 10^{-8} in the density. The COSMO model with standard parameters, as provided by the `TURBOMOLE` program suite, was used in order to model the counter cations for the Zintl anions.[270,271] For consistency, it was also included in $La(CpMe_4H)_3$. To limit the computational effort, SOC effects were neglected, as the L_2- and L_3-edges, due to the splitting of the La $2p$ orbital, are several hundred eV apart. This results in two distinct spectra, where we will only consider the L_3-edge specifically, which arises from the $2p_{3/2}$ branch. Quasiparticle energies were obtained using the one-component fsCD-ev*GW* approach, including the La $2p$ states, as well as the 80 closest states to the HOMO-LUMO gap for the Zintl anion and 20 states for the precursor. This does not explicitly take the higher-lying f-orbitals of La into account, which will be addressed in further work. The remaining states are shifted by applying the "scissor operator", as was done in the previous chapters. Excited states were obtained using the CVS-BSE approach, where the simulated spectra are obtained from superimposing Gaussian distributions at the first 300 and 100 roots of the CVS-Hessian, with a FWHM of 0.3 eV. Here, the zeroth order oscillator strength is used. Note that while the occupied block is frozen in the CVS approximation, it still contributes indirectly via the dielectric screening. Using the above, the quasiparticle energies associated with the La $2p$ states are found at 5639.6 eV and 5641.5 eV for the cluster and the precursor, respectively. This already indicates a higher electron density at the lanthanum in the Zintl ion, due to decreased screening of the nuclear charge. To account for large SOC shift, a simple approximate correction scheme based on La^{3+} can be devised. Using the x2c-TZVPPall-2c basis set, the $2p_{3/2}$ state is estimated at 146.9 eV higher, when compared to the non-relativistic $2p$ state from the quasiparticle energies, which would be within few eV of the experimental findings. This slight overestimation may be further attributed to the overestimation of

electron binding energies in the ev*GW* approach, addressed in the previous chapters. However, we choose here to align the simulated and experimental spectra and shift the result by 5482 eV, as shown in fig. 10.1. For the precursor material, the

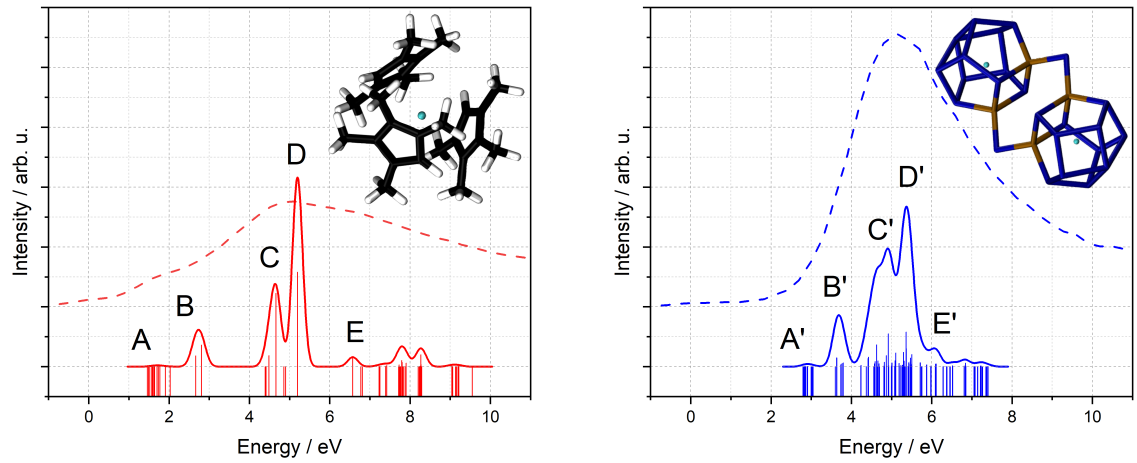

Figure 10.1: Simulated (solid) and experimental (dashed) XAS spectra for $La(CpMe_4H)_3$ (left) and $[(La@In_2Bi_{11})(\mu\text{-}Bi_2)(La@In_2Bi_{11})]^{6-}$ (right). The XAS spectra were simulated by superimposing Gaussian functions with a FWHM of 0.3 eV at the excitation energies, scaled by the oscillator strength. Spectra are shifted and aligned, the experimental spectrum for $La(CpMe_4H)_3$ were scaled by a factor of 1.3 for clarity. Both experimental spectra feature an artificial offset with respect to the simulated spectra. The original maxima were found at 5487 eV. The simulated maxima (features **D** and **D'**) were found at approximately 5491 (5638) eV, with (without) the correction due to the splitting of the La $2p$ state estimated from the splitting of the quasiparticle energies in La^{3+}. Computational details are given in the text. Color scheme used here: lanthanum (light blue), carbon (black), hydrogen (white), bismuth (blue), and iridium (brown).

experimental spectrum shows a few distinct features. Besides the main peak, a small shoulder towards lower energies can be seen. This is followed by a much weaker peak near the zero at this scale. The Zintl anion produces a much narrower band. Similarly, the relative intensity of the pre-edge feature near zero is much weaker, although it appears to be at an similar energy with respect to the precursor material. The simulated spectra roughly follow this trend, where the bands of the precursor material are much broader distributed, as compared to the lanthanum cluster. Although, the separation of the underlying transitions appears to be underestimated, the pattern clearly follows the experimental observations. This underestimation of the relative peak positions may be an artefact, of an slightly imbalanced description of (virtual) valence states, by application of the "scissor operator". Since most features in the spectra are associated with multiple transitions, we use the non-relaxed difference densities to investigate the nature of the transition giving rise to the individual peaks. The contour plots are shown in fig. 10.3. **A** and **A'** can be associated with the La $4f$-states, which give rise to the weak pre-edge peak in fig. 10.1. These transitions are dipole forbidden and gain their intensity from mixing with La $5d$-states. As seen in fig 10.2, the second order correction to the oscillator strength, appears to be only minor in this case, again indicating that the intensity gain is associated with a mixing of La $5d$-orbitals. Note however, that for the Zintl anion, higher-lying transitions were found to feature negative oscillator strengths, which would require even higher orders to correctly cancel out. As these cases only occur, when the dipole strength becomes large, for which the zeroth order approximation is usually sufficient, we choose here to use the electric dipole approximation for the remaining spectrum.[307] The intense shoulder of the precursor at **B** is attributed to the empty La $5d_{z^2}$ orbital, where the z-axis follows the fictitious C_3-axis of an hypothetical ideal D_{3h} symmetric compound, for which it transforms according to the irreducible representation a_1'. The intense peaks, **C** and **D**, are then associated with the La $5d$-orbitals with in a component along the z-axis, i.e., d_{xz} and d_{yz}, which weakly interacts with the π systems of the ligands, transforming as e", as well as the in-plane d_{xy} and $d_{x^2-y^2}$, which transform as e'. The higher-lying feature, **E**, is associated with mostly diffuse mixtures of La $6s, 5d$-character, as they approach the ionization threshold. The precursor follows closely the ligand field splitting expected for an idealized D_{3h} compound, where the La f-orbitals are found at lower energies. By comparing the oscillator strength in the zeroth and second order approximation in fig. 10.2, the intensity of the pre-edge feature

appears to stem mainly from mixtures of these states with La $5d$- and $6s$-orbitals. The Zintl ion consists of two connected nonahedral cages, bridged by two Bi atoms and the splitting is therefore much more complex. However, we find the same weak feature, **A'**, associated with the mixtures of La d, f-orbitals, similar to the precursor. Again, this peak is found at too high energies with respect to the experiment, which is attributed to a qualitatively wrong description using the "scissor operator", shifting these levels by the correction of the LUMO. Since the LUMO of the precursor and Zintl anion are unrelated, the shift differs, and the relative error of **A** and **A'** compared to the experiment is expected to differ accordingly. The further splitting of

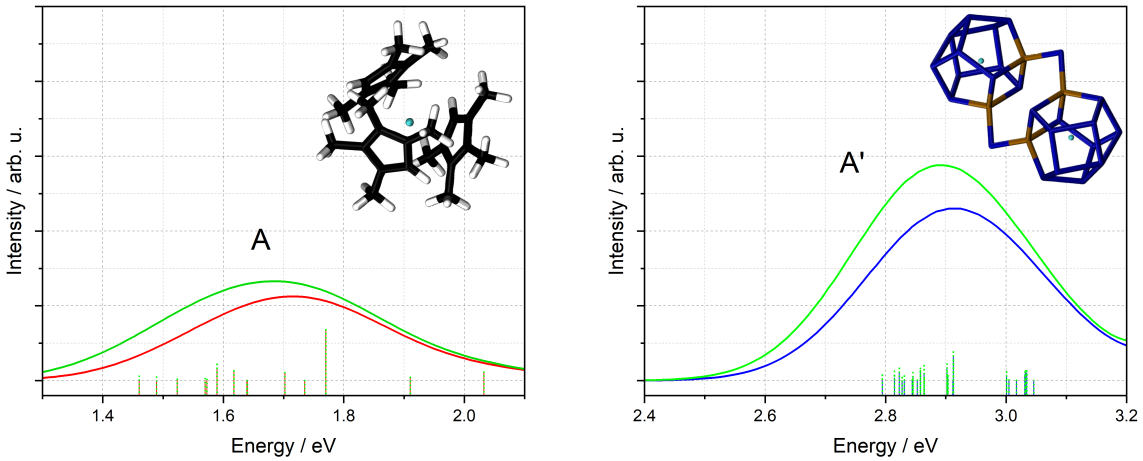

Figure 10.2: Simulated (solid) XAS spectra for $La(CpMe_4H)_3$ (left) and $[(La@In_2Bi_{11})(\mu\text{-}Bi_2)(La@In_2Bi_{11})]^{6-}$ (right) in the region of the pre-edge features A and A' of fig. 10.1. The dipole oscillator strength in red and blue is compared are to the second order oscillator strength in green.

the La $5d$-orbitals is much weaker, due to the complex coordination sphere. The excitations are clear mixtures of La $5d$-states with delocalized orbitals over the whole cage system. They usually occur pairwise, due to the two lanthanum atoms and the symmetry of the system, which is close to an ideal D_{2h}. While the interaction between the lanthanum and the cage is mostly ionic in nature,[404] the final states do feature mixtures of the La d-states and the cage. Slight changes in the pre-edge features have been previously used in order to assess the mixing of ground state orbitals using XANES.[401] The low-lying shoulder, following the pre-edge peak associated with La d, f-mixtures, **B'** corresponds to transfer of density to the cage and bridging Bi atoms with a small lanthanum d-character. Going to higher energies, we find similar mixtures of varying La d-contributions, with a more diffuse character. Note that the delocalized nature is also found for the individual excitations from a single La atom and not a collective effect due to additive nature of the non-relaxed difference density, as was determined by examining the individual excitations and comparing the dominant contributions. For example, the dominant excitations in feature **D'** correspond to two degenerate excitations, originating from the $2p$-orbitals of two different lanthanum and involving the same final state.

We demonstrate here, that the CVS-BSE approach in combination with the fsCD-*GW* method may provide a sensible description of core-excited states, in order to obtain information about the nature of the underlying electronic structure of the excited states. While the simulated spectra are in overall good agreement with the experimental observations, the interesting pre-edge region, involving the lanthanum f-orbitals are difficult to resolve correctly. Here, this can be partly attributed to the "scissor approach". By neglecting the SOC effects and devising a correction from the La^{3+} ion, the simulated spectra are found within a few eV with respect to the experimental observations, but still appear to overestimate the true excitation energies. Following sec. 8.2 and sec. 9.2, this may be attributed to the underscreening in self-consistent *GW* methods with respect to the screened interaction. A further improvement may therefore be expected by instead choosing the non-iterative non-relaxed G_0W_0-1 approach and explicitly including a larger number of virtual orbitals. This is possible using the fsCD-*GW* approach and will be subject of future investigations.

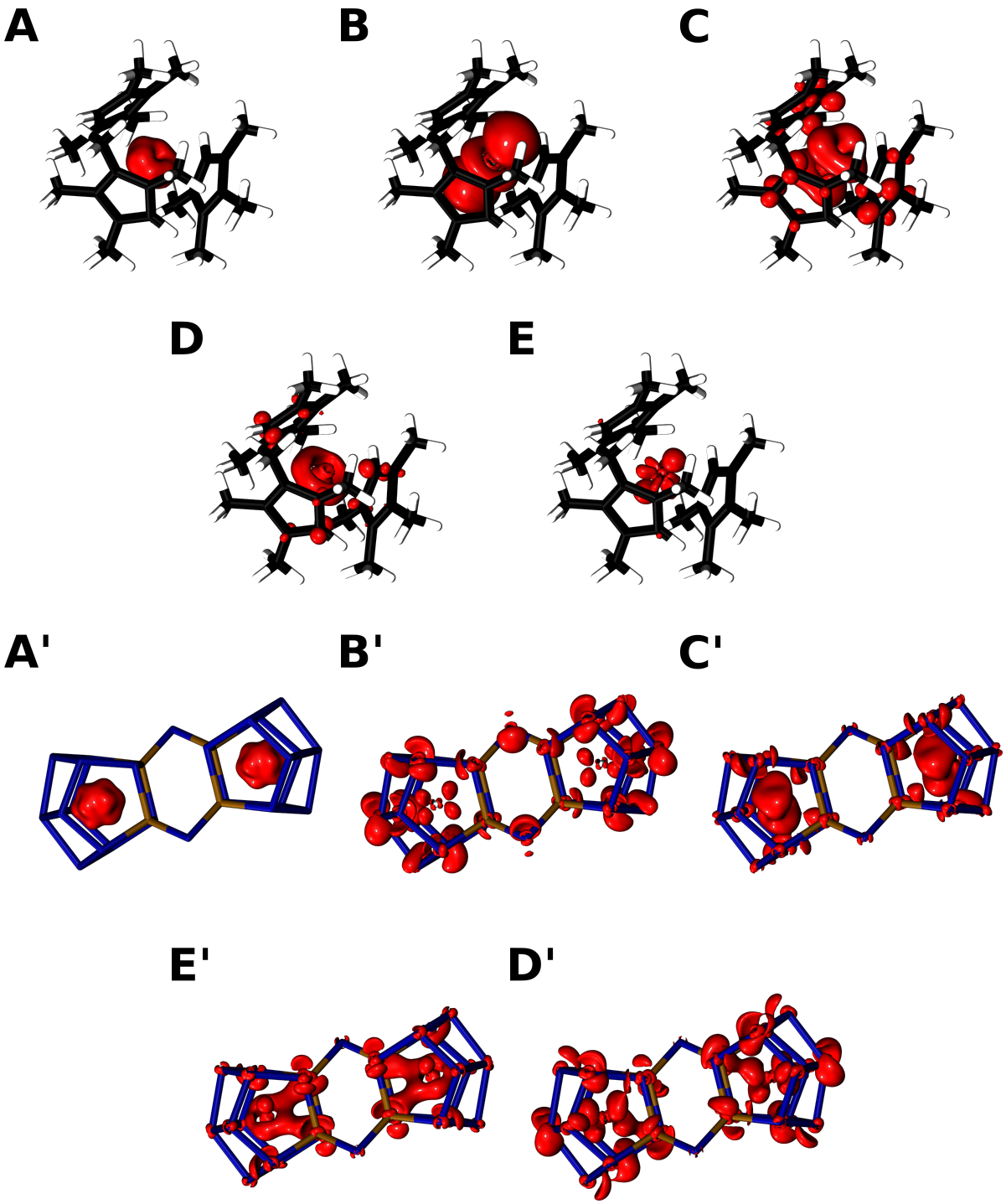

Figure 10.3: Non-relaxed difference densities for features as indicated in fig. 10.1. The density gain is indicated by a red contour, the density loss is localized at the La atoms, corresponding to the excitation from the $2p$ ($2p_{3/2}$) state, and is not depicted here. For La[$CpMe_4H$]$_3$, the contours were drawn at an isovalue of $2 \cdot 10^{-3}$ a_0^{-3} in red, while for [(La@In_2Bi_{11})(μ-Bi_2) (La@In_2Bi_{11})]$^{6-}$ the isovalue is set to $3 \cdot 10^{-4}$ a_0^{-3}. Color scheme used here: lanthanum (light blue), carbon (black), hydrogen (white), bismuth (blue), and iridium (brown).

11 Summary and Conclusion

In the context of this work, new approaches for the description of charge and charge neutral excitations within the framework of the *GW* and the Bethe-Salpeter equation (BSE) have been explored. By employing the *GW* method, the quasiparticle energies of a molecule may be obtained, which are directly related to its vertical ionization potentials and electron affinities. While efficient techniques exist for the evaluation of energies associated with valence orbitals close to the Fermi level, these often struggle if the density of states increases and more than a few are to be optimized explicitly. Especially quasiparticle energies associated with core electrons provide challenges for standard techniques, as they feature a stark increase in the computational cost or become numerically unstable. To improve these aspects and obtain an efficient and robust approach, modern approximations were implemented and extended in the context of this thesis. The key step involved the analytic continuation of the screened exchange in the contour deformation technique for the calculation of the self-energy, which is the central potential in the quasiparticle equations. This consideration was used to address the increased cost for states further away from the Fermi level, and allowed for a much more favourable structure of the *GW* algorithm with respect to the frequency integration. In order to go beyond the initial valence levels, this method was combined with an efficient sampling approach, as well as a robust rational approximation. This was done, in order to address the issue of numerical instabilities, while retaining a favourable scaling behaviour with respect to the system size. It was demonstrated, that this approach allows for the evaluation of the self-energy, at frequencies required for the description of electron binding energies of low-lying states. Furthermore, this technique was found to reduce the formal scaling of the standard contour deformation (CD-)*GW* approach by nearly one order of magnitude for core electrons of systems of chemical relevant sizes. These same considerations further lead to a significant reduction of the computational complexity for valence states, due to the shared frequency grid employed. The frequency-sampled contour deformation *GW* (fsCD-*GW*) method therefore, enables the approximate evaluation of the quasiparticle energies for many states of a system at a reasonable cost, and may be for a routine explicit description of more then a hundred quasiparticle states in future applications. This is required for systems with a high density of states and provides a flexible basis for the description of optically excited states in many applications.

The starting point dependence of the perturbative *GW* approximations was further assessed, using modern density functional approximations (DFAs), including local hybrid functionals (LHFs), not only for valence states, but also with respect to core orbitals. Both areas provide different challenges towards a proper description using DFAs and even *GW* methods. Using a simple substitution of the exchange-correlation potential with the self-energy, was found to provide an overall good agreement with reference and experimental data available. The approximate quasiparticle energies were found to feature a significantly lowered starting point dependence for most DFAs examined, while maintaining a low cost, due to its non-iterative nature.

Charge neutral excitations were then modelled using the BSE, where the quasiparticle energies are evaluated within the *GW* approximation, while the particle-hole interaction is described by the BSE in its static limit. This is the composite *GW*-BSE method. Two different approaches were implemented and considered for the description of the absorption spectrum of low-lying states. The first introduced the damped response formalism to the BSE, where a generalized solver for the underlying equations was implemented. This was used to calculate the dynamic polarizabilities associated with core excitations, directly, but may also be used for systems, where a high density of states effectively prevents a description of the absorption spectrum by extraction of individual roots of the electronic Hessian in a reasonable time frame. The latter aspect was not explored in the context of this work. The second approach considered, was the combination of the core-valence separation (CVS) method with the BSE, which was then applied for the description of molecules including heavy elements. In these examples,

spin-orbit effects were required to obtain even a qualitatively correct picture, consistent with the experimental observations for regions with overlapping features associated with different edges. This approach was assessed with respect to different *GW* approximations to the self-consistent solution of the underlying equations. It was demonstrated to provide an overall efficient and suitable method for the description of core-excited states, and resulted in transition energies in good agreement with experimental observations. In order to describe the high frequency regime, the second order correction of the oscillator strength was implemented at the one- and (Kramers symmetric) two-component level in its gauge-invariant formulation. This was then used to address dipole forbidden transitions in different inorganic molecules, as part of the assessment of the *GW*-BSE method for charge neutral core excitations. The method was then applied in order to rationalize the observations of HR-XANES (high-energy resolution X-ray absorption near edge structure) spectra of two lanthanum compounds, where it was used to provide information regarding the nature of the transitions associated with a weak pre-edge feature, as well as the main spectral band at the La L-edge. Even within the much simpler one-component formalism, the simulated spectrum was within a few eV if the shift due to spin-orbit coupling of the La $2p$ states was addressed using the a simple La^{3+} ion as a model.

In conclusion, the *GW* and the *GW*-BSE methods have been further developed in order to facilitate a description of core electrons, i.e., their charge and charge neutral excitations, enabling their use in a wider range of systems encountered in real-life applications. The latter was found to largely improve upon the incorrect absolute energies typically encountered for most DFAs in time-dependent density functional theory (TDDFT), while maintaining a similar computational effort, previously used for the simulation valence excitations. This was possible due to the efficiency gains in both, the calculation of the quasiparticle energies using the *GW* method, and the evaluation of core-excited states within the *GW*-BSE method. The developments discussed and implemented in this work, provide a reasonable basis for further improvements towards the description of core-excited states within the framework of many-body perturbation theory. Here, the approximate inclusion of the frequency dependence in the BSE kernel, going beyond the initial static limit, may provide an interesting approach for future studies and may help to achieve further improvements in the description of experimental observations.

A Appendix

A.1 Performance of fsCD-*GW* for Cd Clusters of Varying Size

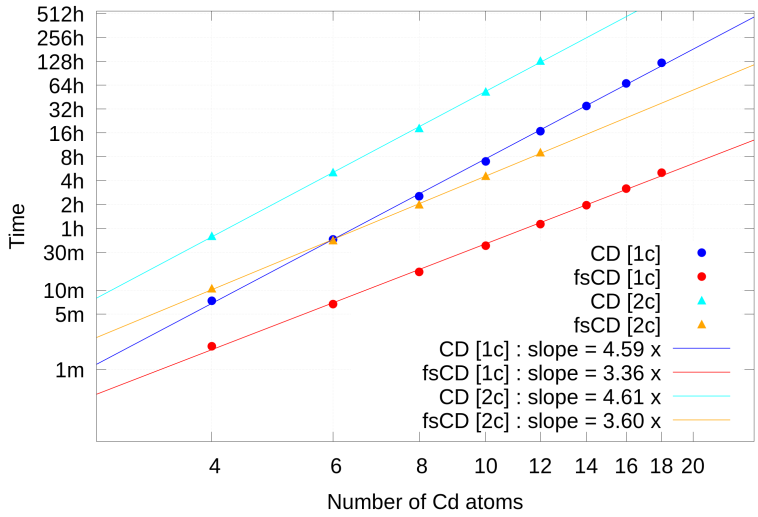

Figure A.1: CPU timings for fsCD-*GW* (red and orange) and CD-*GW* (light and dark blue) for Cd clusters of varying sizes in one- (circles) and two-component (triangles) calculations for the lowest-lying state in C_1 symmetry, employing only six Gauss-Legendre grid points. See fig. 5.8 for further information.

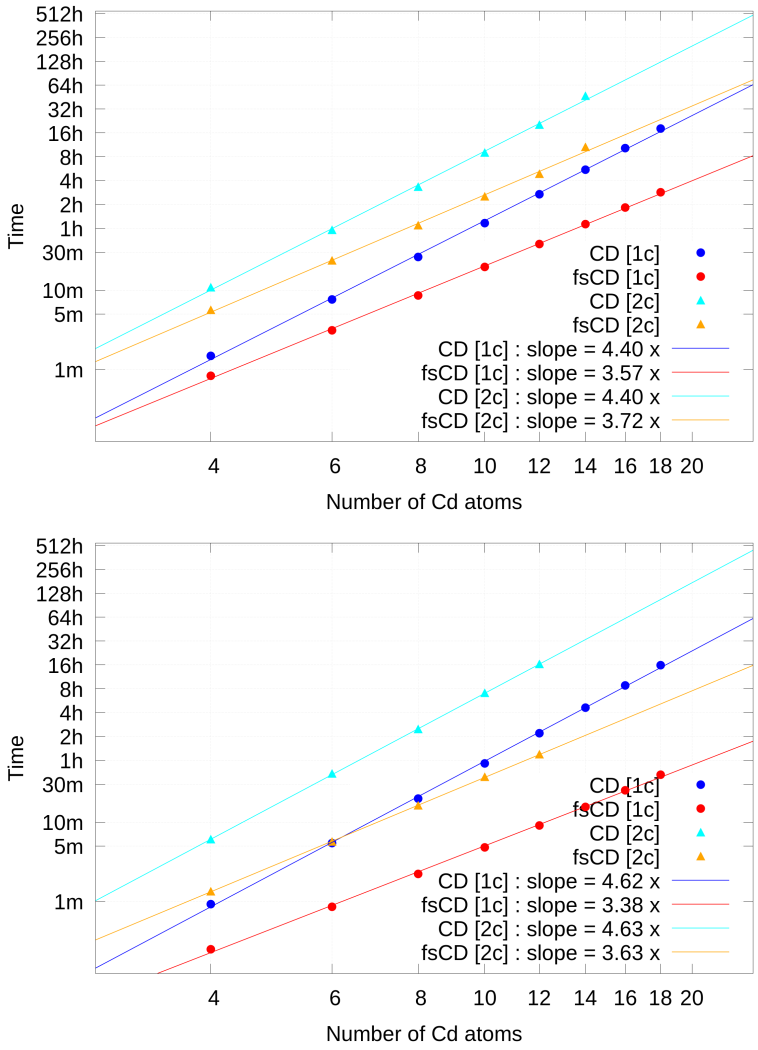

Figure A.2: Wall timings for fsCD-*GW* (red and orange) and CD-*GW* (light and dark blue) for Cd clusters of varying sizes in one- (circles) and two-component (triangles) calculations for the lowest-lying state in C_1 symmetry. The scaling behaviour or computational complexity is estimated from the slope of a linear regression using a logarithmic scales for system size and CPU time and are shown in the graphs. Quasiparticle energies were obtained at the non-iterative G_0W_0 level, where the renormalization parameter was set to one. The top graph shows the default 128 Gauss-Legendre grid points, which correspond to the number of imaginary frequencies considered in the calculation of $I^{c}_{pp}(\epsilon_p)$. The bottom graph uses only very few imaginary frequency points, such that the first step, which is mostly identical in fsCD-*GW* and CD-*GW* (see Fig. 5.3) can be done in negligible time. Errors for the fsCD-*GW* algorithm were found to be approximately 10^{-5} eV in the above examples.

A.2 Ionization Potentials for the GW27 Test Set

Table A.1: Ionization potential for the GW27 test set for various DFAs, obtained using the G_0W_0 -1 method. Computational details are provided in sec. 8.1. Reference values are taken from ref. 344.

Name	CCSD(T)	HF	BP86	PBE	TPSS	BH&HLYP	B3LYP	CAM-B3LYP	PBE0	TPSSh
Butane	11.58	12.13	12.03	12.02	11.74	11.86	12.09	12.14	12.05	11.75
2-Propenal	10.20	11.04	10.16	10.18	10.11	10.48	10.21	10.35	10.25	10.15
Anthracene	7.01	7.53	7.33	7.32	7.31	7.35	7.34	7.31	7.30	7.30
Cesium dimer	3.58	3.53	3.76	3.76	3.71	3.58	3.69	3.52	3.62	3.66
Gold dimer	9.10	8.74	9.95	9.94	9.92	9.03	9.29	9.17	9.16	9.29
Carbon dioxide	13.67	14.08	13.70	13.73	13.65	13.81	13.72	13.83	13.77	13.68
Au4	7.67	7.23	7.98	7.97	7.94	7.51	7.79	7.65	7.66	7.80
Hydrogen	16.21	16.30	16.36	16.35	16.23	16.30	16.32	16.36	16.33	16.24
Boron fluoride	11.14	11.33	11.24	11.22	11.20	11.22	11.20	11.15	11.21	11.19
Lithium dimer	5.20	5.25	5.57	5.59	5.52	5.30	5.44	5.25	5.42	5.46
Disodium	4.92	4.93	5.30	5.30	5.25	5.02	5.17	4.98	5.13	5.18
Acetone	9.71	10.21	9.63	9.64	9.61	9.81	9.69	9.84	9.72	9.65
Benzene	9.34	9.51	9.38	9.37	9.37	9.37	9.38	9.33	9.33	9.35
Methane	14.36	14.72	14.49	14.48	14.48	14.54	14.51	14.56	14.49	14.49
Ethane	13.12	13.12	12.87	12.87	12.86	12.94	12.91	12.95	12.88	12.87
Ethylene	10.70	10.78	10.78	10.77	10.78	10.69	10.74	10.68	10.70	10.75
Propane	12.13	12.46	12.18	12.18	12.17	12.27	12.23	12.28	12.19	12.18
Isobutane	11.68	12.21	11.88	11.88	11.87	11.99	11.94	11.99	11.90	11.89
Lithium hydride	7.93	8.12	7.94	7.92	7.85	8.04	7.97	8.11	8.03	7.91
Ammonia	10.85	11.15	10.95	10.95	10.93	10.95	10.93	10.98	10.94	10.93
Nitrogen	15.54	16.96	15.47	15.47	15.44	15.76	15.56	15.70	15.62	15.50
Water	12.61	12.79	12.65	12.66	12.60	12.61	12.61	12.71	12.64	12.60
Fluorine	15.46	15.79	15.43	15.46	15.36	15.53	15.45	15.62	15.50	15.38
Sulfur tetrafluoride	12.62	13.25	12.57	12.58	12.54	12.86	12.68	12.81	12.67	12.58
Silane	12.70	13.13	12.83	12.83	12.81	12.95	12.89	12.95	12.87	12.83
Naphthalene	8.04	8.37	8.18	8.17	8.16	8.20	8.19	8.16	8.15	8.15
Naphthacene	6.43	7.01	6.80	6.80	6.78	6.83	6.81	6.78	6.77	6.77

Table A.2: Continuation of tab. A.1. Ionization potential for the GW27 test set for various DFAs, obtained using the G_0W_0 -1 method. Computational details are provided in sec. 8.1. Reference values are taken from ref. 344. LH07t-SVWN, LH12ct-SsirPW92, and LH14t-calPBE are abbreviated by LH07t, LH12ct, and LH14t.

Name	CCSD(T)	LC-ωPBE	ωB97X-D	LH07t	LH12ct	LH14t	LH20t	LHJ14	mPSTS
Butane	11.58	12.07	12.08	11.86	11.93	11.84	11.96	11.72	11.77
2-Propenal	10.20	10.39	10.31	10.36	10.44	10.32	10.40	10.16	10.19
Anthracene	7.01	7.18	7.22	7.40	7.44	7.39	7.42	7.26	7.32
Cesium dimer	3.58	3.35	3.40	3.61	3.58	3.60	3.58	3.47	3.66
Gold dimer	9.10	8.97	9.09	9.33	9.27	9.32	9.27	9.96	9.29
Carbon dioxide	13.67	13.82	13.73	13.91	13.98	13.87	13.88	13.66	13.71
Au4	7.67	7.43	7.57	7.84	7.78	7.83	7.79	7.80	7.78
Hydrogen	16.21	16.34	16.34	16.35	16.37	16.29	16.24	16.33	16.27
Boron fluoride	11.14	11.07	11.15	11.28	11.31	11.24	11.25	11.14	11.23
Lithium dimer	5.20	5.17	5.20	5.35	5.35	5.33	5.29	5.28	5.45
Disodium	4.92	4.87	4.88	5.10	5.07	5.09	5.03	4.99	5.18
Acetone	9.71	9.86	9.78	9.87	9.96	9.84	9.92	9.64	9.69
Benzene	9.34	9.18	9.25	9.45	9.48	9.44	9.46	9.29	9.37
Methane	14.36	14.51	14.52	14.61	14.64	14.58	14.62	14.48	14.53
Ethane	13.12	12.89	12.90	12.99	13.44	12.97	13.44	12.87	12.90
Ethylene	10.70	10.54	10.61	10.83	10.85	10.81	10.82	10.66	10.78
Propane	12.13	12.21	12.22	12.41	12.48	12.39	12.49	12.19	12.21
Isobutane	11.68	11.91	11.93	11.94	12.01	11.93	12.02	11.88	11.91
Lithium hydride	7.93	8.15	8.12	8.08	8.13	8.07	8.08	8.04	7.97
Ammonia	10.85	10.96	10.94	11.04	11.08	11.00	11.01	10.87	10.97
Nitrogen	15.54	15.69	15.65	15.81	15.94	15.76	15.85	15.49	15.55
Water	12.61	12.74	12.66	12.75	12.79	12.71	12.69	12.56	12.64
Fluorine	15.46	15.71	15.50	15.68	15.73	15.61	15.61	15.41	15.40
Sulfur tetrafluoride	12.62	12.78	12.64	12.82	12.88	12.79	12.84	12.63	12.58
Silane	12.70	12.94	12.91	13.00	13.05	12.97	13.01	12.86	12.86
Naphthalene	8.04	8.03	8.07	8.26	8.29	8.24	8.28	8.11	8.17
Naphthacene	6.43	6.65	6.69	6.87	6.77	6.81	6.90	6.74	6.79

A.3 Ionization Potentials for the GW100 Test Set

Table A.3: Ionization potential for the GW100 test set for various DFAs, obtained using the G_0W_0 -1 method. Computational details are provided in sec. 8.1. Reference values are taken from ref. 344. LH07t-SVWN, LH12ct-SsirPW92, and LH14t-calPBE are abbreviated by LH07t, LH12ct, and LH14t.

Name	CCSD(T)	HF	BP86	PBE	TPSS	BH&HLYP	B3LYP	PBE0	TPSSh	CAM-B3LYP
Ethylbenzene	8.85	9.08	8.89	8.88	8.88	8.91	8.91	8.85	8.87	8.87
Ozone	12.55	13.51	12.67	12.70	12.61	13.43	12.78	12.84	12.68	12.96
Borone nitride	11.89	11.71	12.45	11.95	11.93	11.72	11.81	11.82	11.86	11.75
Butane	11.57	12.12	11.99	11.99	11.72	12.10	12.05	12.01	11.74	12.11
Toluene	8.90	9.11	8.96	8.95	8.94	8.96	8.96	8.91	8.93	8.92
Phenol	8.70	8.98	8.72	8.72	8.69	8.74	8.72	8.68	8.68	8.71
Pyridine	9.66	9.88	9.64	9.65	9.60	9.75	9.71	9.77	9.65	9.72
Tetracarbon	11.26	8.45	11.40	11.41	11.37	11.38	11.37	11.38	11.41	11.34
Caesium dimer	3.64	3.59	3.81	3.81	3.78	3.64	3.74	3.67	3.72	3.58
Phosphorus dimer	10.47	10.54	10.54	10.54	10.54	10.45	10.49	10.47	10.51	10.38
Silver dimer	7.49	7.17	8.01	8.00	7.94	7.50	7.80	7.67	7.80	7.60
Copper dimer	7.57	7.17	8.95	8.97	8.93	7.53	7.89	7.75	7.98	7.71
Carbon dioxide	13.71	14.12	13.74	13.76	13.69	13.85	13.76	13.81	13.72	13.86
Beryllium oxide	9.94	9.69	10.16	10.19	10.09	9.78	9.99	9.98	10.01	10.01
Magnesium oxide	7.49	8.34	8.06	8.10	7.88	7.66	7.88	7.81	7.79	7.92
Borane	13.28	13.64	13.48	13.46	13.44	13.52	13.49	13.49	13.45	13.54
Hydrogen	16.40	16.49	16.54	16.53	16.35	16.49	16.51	16.52	16.39	16.54
Fluoroborane(1)	11.09	11.28	11.19	11.17	11.15	11.17	11.15	11.16	11.14	11.10
Lithium dimer	5.27	5.32	5.62	5.64	5.58	5.36	5.49	5.48	5.52	5.31
Pentasilane	9.27	9.76	9.24	9.23	9.29	9.46	9.37	9.28	9.31	9.41
Disilane	10.65	11.06	10.69	10.68	10.72	10.83	10.77	10.70	10.73	10.79
Carbon oxide selenide	10.79	11.10	10.92	10.92	10.89	10.94	10.93	10.91	10.88	10.89
Gallium chloride	9.77	9.89	9.85	9.87	9.85	9.78	9.81	9.79	9.82	9.76
Phosphorous nitride	11.74	12.34	11.82	11.84	11.82	12.24	11.83	11.91	11.85	11.90
Diborane	12.26	12.77	12.42	12.41	12.41	12.57	12.49	12.47	12.44	12.57
Arsenic dimer	9.78	9.73	9.74	9.76	9.75	9.65	9.70	9.68	9.71	9.57
Disodium	4.95	4.97	5.33	5.33	5.27	5.05	5.20	5.15	5.21	5.01
Dipotassium	4.06	4.06	4.37	4.36	4.31	4.12	4.26	4.19	4.25	4.06
Rubidium dimer	3.93	3.88	4.15	4.14	4.11	3.94	4.05	3.99	4.05	3.87
Hydrazine	9.72	10.08	9.81	9.82	9.78	9.84	9.80	9.82	9.78	9.86
Hexafluorobenzene	9.93	10.56	9.81	9.81	9.81	10.16	9.97	9.93	9.85	10.04
Sodium tetramer	4.23	4.28	4.55	4.55	4.53	4.30	4.42	4.39	4.47	4.25
Sodium hexamer	4.35	4.45	4.66	4.65	4.63	4.44	4.55	4.51	4.57	4.39
Carbonyl sulfide	11.17	11.51	11.25	11.26	11.22	11.31	11.27	11.26	11.23	11.25
Formaldehyde	10.84	11.26	10.94	10.95	10.87	11.00	10.93	10.98	10.89	11.04

Tetraiodomethane	9.27	9.48	9.00	9.02	9.05	9.20	9.11	9.08	9.07	9.17
Cyclopentadiene	8.68	8.82	8.72	8.71	8.72	8.70	8.72	8.66	8.70	8.66
Cuprous cyanide	10.85	11.20	10.80	10.80	10.82	11.11	10.70	10.60	10.72	10.88
Carbon tetrabromide	10.46	10.69	10.20	10.22	10.21	10.40	10.31	10.28	10.24	10.39
Carbon tetrachloride	11.56	11.92	11.39	11.39	11.38	11.61	11.49	11.48	11.42	11.59
Urea	10.05	10.56	9.97	9.98	9.92	10.15	10.02	10.05	9.96	10.18
Bromoethene	9.27	9.43	9.28	9.28	9.28	9.27	9.28	9.24	9.26	9.25
Iodoethene	9.33	9.47	9.26	9.27	9.28	9.30	9.29	9.25	9.27	9.28
Diethyl ether	9.82	10.36	9.85	9.87	9.79	9.99	9.89	9.93	9.82	10.02
Aniline	7.99	8.29	8.01	8.02	7.99	8.05	8.02	7.99	7.98	8.02
Cyclooctatetraene	8.35	8.64	8.40	8.40	8.40	8.45	8.43	8.38	8.40	8.41
Carbon monoxide	14.21	14.98	14.22	14.21	14.20	14.53	14.31	14.36	14.26	14.40
Ethanol	10.69	11.18	10.73	10.74	10.68	10.82	10.75	10.78	10.70	10.87
Formic acid	11.42	11.81	11.38	11.39	11.32	11.53	11.42	11.47	11.36	11.58
Thymine	9.08	9.62	9.07	9.07	9.04	9.27	9.15	9.13	9.07	9.20
Uracil	10.13	10.02	9.96	9.97	9.91	9.67	9.55	9.54	9.47	9.60
Methanol	11.04	11.46	11.12	11.13	11.07	11.16	11.11	11.14	11.08	11.21
Cytosine	9.51	9.20	8.72	8.73	8.67	8.86	8.76	8.76	8.70	8.84
Benzene	9.29	9.48	9.34	9.33	9.33	9.34	9.34	9.30	9.32	9.30
Adenine	8.33	8.66	8.29	8.29	8.25	8.39	8.33	8.30	8.26	8.35
Guanine	8.03	8.38	7.98	7.98	7.95	8.12	8.04	8.01	7.96	8.07
Methane	14.37	14.73	14.50	14.49	14.50	14.56	14.53	14.51	14.51	14.57
Ethane	13.04	13.14	12.88	12.88	12.88	12.96	12.92	12.89	12.89	12.97
Ethylene	10.67	10.74	10.75	10.74	10.75	10.66	10.71	10.67	10.72	10.64
Acetylene	11.42	11.57	11.50	11.49	11.49	11.45	11.47	11.45	11.47	11.43
Hydrogen cyanide	13.87	13.85	13.74	13.74	13.72	13.72	13.72	13.72	13.71	13.72
Propane	12.05	12.58	12.30	12.30	12.29	12.39	12.35	12.32	12.31	12.40
Krypton	13.94	13.95	13.80	13.82	13.81	13.81	13.82	13.79	13.79	13.82
Neon	21.32	21.25	21.22	21.25	21.16	21.18	21.20	21.21	21.15	21.37
Argon	15.54	15.71	15.54	15.55	15.53	15.56	15.55	15.53	15.52	15.57
Helium	24.51	24.59	24.45	24.45	24.38	24.51	24.47	24.50	24.40	24.58
Sulfur dioxide	13.49	12.85	12.28	12.29	12.24	12.47	12.33	12.37	12.28	12.43
Vinyl chloride	10.09	10.33	10.12	10.12	10.12	10.15	10.13	10.10	10.11	10.11
Fluoroethylene	10.55	10.79	10.59	10.59	10.59	10.61	10.59	10.56	10.57	10.57
Acetaldehyde	10.21	10.69	10.19	10.20	10.15	10.34	10.24	10.27	10.19	10.37
Carbon disulfide	9.98	10.29	10.08	10.09	10.07	10.10	10.08	10.07	10.06	10.05
Cyclopropane	10.87	11.23	10.95	10.95	10.96	11.01	10.98	10.94	10.96	10.99
Carbon tetrafluoride	16.30	16.66	15.98	16.01	15.93	16.30	16.12	16.17	16.00	16.35
Iodine	9.51	9.67	9.39	9.42	9.43	9.46	9.43	9.41	9.42	9.43
Lithium hydride	7.96	8.15	7.97	7.95	7.88	8.07	7.99	8.05	7.94	8.14

Hydrochloric acid	12.59	12.76	12.64	12.64	12.62	12.62	12.63	12.60	12.61	12.62
Sodium chloride	9.03	9.16	9.00	8.99	8.94	9.04	9.02	9.01	8.96	9.09
Hydrofluoric acid	16.03	16.08	16.02	16.03	15.95	15.95	15.97	16.00	15.95	16.11
Ammonia	10.81	11.11	10.90	10.91	10.88	10.90	10.89	10.90	10.88	10.93
Potassium hydride	6.13	6.25	5.97	5.99	5.81	6.13	6.03	6.08	5.89	6.23
Hydrogen peroxide	11.59	11.91	11.59	11.61	11.53	11.64	11.58	11.63	11.54	11.71
Bromine	10.54	10.69	10.45	10.47	10.45	10.50	10.47	10.46	10.45	10.48
Nitrogen	15.57	17.10	15.50	15.50	15.47	15.78	15.59	15.65	15.53	15.73
Water	12.57	12.75	12.61	12.62	12.56	12.57	12.57	12.60	12.56	12.66
Potassium bromide	8.13	8.15	8.04	8.05	8.00	8.03	8.05	8.02	8.00	8.07
Fluorine	15.71	16.13	15.72	15.75	15.65	15.84	15.75	15.79	15.67	15.93
Chlorine	11.41	11.71	11.45	11.46	11.43	11.50	11.46	11.46	11.44	11.48
Germane	12.50	12.85	12.56	12.57	12.54	12.67	12.61	12.60	12.55	12.67
Hydrazoic acid	10.68	11.05	10.83	10.83	10.78	10.84	10.82	10.83	10.79	10.81
Hydrogen sulfide	10.31	10.48	10.39	10.39	10.39	10.36	10.38	10.34	10.37	10.35
Magnesium fluoride	13.71	13.65	13.50	13.49	13.41	13.54	13.51	13.54	13.45	13.77
Sulfur tetrafluoride	12.59	13.22	12.53	12.55	12.50	12.82	12.65	12.64	12.54	12.77
Titanium tetrafluoride	15.48	15.85	14.86	14.88	14.80	15.36	15.07	15.14	14.92	15.42
Aluminum fluoride	15.46	15.44	15.08	15.09	15.02	15.22	15.13	15.18	15.07	15.38
Aluminum iodide	9.82	9.96	9.52	9.54	9.56	9.69	9.61	9.59	9.58	9.67
Arsine	10.40	10.55	10.46	10.48	10.47	10.44	10.47	10.42	10.45	10.42
Magnesium chloride	11.67	11.86	11.59	11.59	11.57	11.67	11.62	11.63	11.58	11.69
Lithium fluoride	11.32	11.17	11.12	11.10	11.01	11.11	11.11	11.13	11.04	11.36
Phosphine	10.52	10.78	10.70	10.70	10.69	10.67	10.69	10.65	10.67	10.65
Silane	12.80	13.21	12.91	12.91	12.89	13.04	12.97	12.96	12.92	13.04

Table A.4: Continuation of tab. A.3. Ionization potential for the GW100 test set for various DFAs, obtained using the G_0W_0 -1 method. Computational details are provided in sec. 8.1. Reference values are taken from ref. 344. LH07t-SVWN, LH12ct-SsirPW92, and LH14t-calPBE are abbreviated by LH07t, LH12ct, and LH14t.

Name	CCSD(T)	LC-ωPBE	ωB97X-D	LH07t	LH12ct	LH14t	LH20t	LHJ14	mPSTS
Ethylbenzene	8.85	8.72	8.79	8.98	9.01	8.96	9.00	8.82	8.89
Ozone	12.55	12.97	12.86	12.99	13.09	12.94	13.00	12.69	12.70
Borone nitride	11.89	11.65	11.72	11.94	11.96	11.90	11.87	11.74	11.91
Butane	11.57	12.04	12.05	11.85	11.92	11.83	11.94	11.71	11.76
Toluene	8.90	8.78	8.84	9.03	9.06	9.01	9.04	8.88	8.95
Phenol	8.70	8.60	8.62	8.80	8.84	8.78	8.81	8.65	8.70
Pyridine	9.66	9.56	9.84	9.87	9.87	9.84	9.85	9.66	9.69
Tetracarbon	11.26	11.27	11.29	11.50	11.56	11.46	11.47	11.31	11.45
Caesium dimer	3.64	3.42	3.46	3.67	3.64	3.66	3.64	3.53	3.72
Phosphorus dimer	10.47	10.26	10.32	10.58	10.60	10.56	10.54	10.36	10.53
Silver dimer	7.49	7.35	7.52	7.77	7.69	7.76	7.69	7.75	7.78
Copper dimer	7.57	7.57	7.64	7.87	7.78	7.86	7.76	9.10	7.91
Carbon dioxide	13.71	13.86	13.76	13.95	14.02	13.91	13.92	13.70	13.74
Beryllium oxide	9.94	9.99	9.93	10.02	10.00	10.00	9.91	10.00	10.04
Magnesium oxide	7.49	7.71	7.82	7.82	7.77	7.81	7.71	7.85	7.80
Borane	13.28	13.52	13.54	13.60	13.64	13.56	13.58	13.49	13.49
Hydrogen	16.40	16.53	16.53	16.53	16.57	16.47	16.41	16.52	16.44
Fluoroborane(1)	11.09	11.02	11.10	11.23	11.26	11.19	11.20	11.09	11.18
Lithium dimer	5.27	5.24	5.26	5.42	5.42	5.39	5.36	5.34	5.51
Pentasilane	9.27	9.32	9.32	9.46	9.51	9.44	9.54	9.28	9.33
Disilane	10.65	10.71	10.71	10.89	10.95	10.86	10.96	10.70	10.76
Carbon oxide selenide	10.79	10.76	10.80	11.02	11.06	11.00	11.00	10.82	10.90
Gallium chloride	9.77	9.70	9.70	9.87	9.89	9.86	9.86	9.75	9.82
Phosphorous nitride	11.74	11.91	11.92	12.03	12.14	12.00	12.36	11.75	11.90
Diborane	12.26	12.54	12.55	12.59	12.63	12.56	12.61	12.48	12.47
Arsenic dimer	9.78	9.48	9.53	9.71	9.73	9.72	9.72	9.55	9.72
Disodium	4.95	4.90	4.91	5.13	5.10	5.12	5.07	5.02	5.21
Dipotassium	4.06	3.91	3.94	4.18	4.15	4.17	4.12	4.03	4.25
Rubidium dimer	3.93	3.72	3.76	3.99	3.96	3.97	3.94	3.83	4.05
Hydrazine	9.72	9.83	9.81	9.91	9.96	9.88	9.89	9.74	9.82
Hexafluorobenzene	9.93	9.94	9.88	10.08	10.14	10.07	10.16	9.91	9.86
Sodium tetramer	4.23	4.18	4.22	4.41	4.40	4.39	4.35	4.27	4.48
Sodium hexamer	4.35	4.30	4.33	4.56	4.56	4.53	4.51	4.40	4.58
Carbonyl sulfide	11.17	11.15	11.15	11.38	11.42	11.35	11.36	11.17	11.24
Formaldehyde	10.84	11.05	10.99	11.07	11.12	11.02	11.02	10.88	10.93
Tetraiodomethane	9.27	9.14	9.19	9.12	9.15	9.13	8.76	9.01	9.07
Cyclopentadiene	8.68	8.52	8.58	8.80	8.83	8.78	8.81	8.63	8.72

Cuprous cyanide	10.85	11.06	10.82	10.82	10.82	10.81	10.77	10.92	10.70
Carbon tetrabromide	10.46	10.39	10.37	10.34	10.40	10.36	10.42	10.21	10.25
Carbon tetrachloride	11.56	11.56	11.52	11.60	11.66	11.58	11.61	11.40	11.43
Urea	10.05	10.23	10.12	10.17	10.24	10.14	10.17	9.98	10.00
Bromoethene	9.27	9.15	9.18	9.35	9.38	9.34	9.37	9.19	9.28
Iodoethene	9.33	9.20	9.26	9.32	9.35	9.33	9.37	9.20	9.28
Diethyl ether	9.82	10.04	9.98	10.01	10.08	9.98	9.98	9.82	9.85
Aniline	7.99	7.91	7.94	8.10	8.14	8.08	8.11	7.94	8.00
Cyclooctatetraene	8.35	8.29	8.33	8.50	8.54	8.49	8.53	8.35	8.42
Carbon monoxide	14.21	14.37	14.37	14.52	14.64	14.48	14.56	14.26	14.31
Ethanol	10.69	10.89	10.82	10.88	10.94	10.84	10.84	10.69	10.74
Formic acid	11.42	11.61	11.51	11.58	11.65	11.55	11.57	11.37	11.40
Thymine	9.08	9.12	9.10	9.24	9.30	9.23	9.27	9.07	9.09
Uracil	10.13	9.52	9.50	9.65	9.71	9.63	9.67	9.46	9.49
Methanol	11.04	11.23	11.17	11.25	11.30	11.21	11.20	11.05	11.11
Cytosine	9.51	8.78	8.74	8.86	8.93	8.85	8.88	8.70	8.71
Benzene	9.29	9.15	9.22	9.42	9.45	9.40	9.42	9.25	9.34
Adenine	8.33	8.25	8.25	8.42	8.47	8.40	8.43	8.25	8.28
Guanine	8.03	7.96	7.96	8.13	8.18	8.12	8.16	7.97	7.98
Methane	14.37	14.52	14.53	14.62	14.66	14.60	14.64	14.49	14.54
Ethane	13.04	12.91	12.91	13.01	13.36	12.98	13.36	12.89	12.91
Ethylene	10.67	10.50	10.57	10.80	10.82	10.77	10.79	10.63	10.75
Acetylene	11.42	11.31	11.38	11.58	11.62	11.56	11.57	11.40	11.50
Hydrogen cyanide	13.87	13.62	13.66	13.88	13.93	13.84	13.85	13.66	13.75
Propane	12.05	12.34	12.35	12.33	12.39	12.31	12.41	12.31	12.33
Krypton	13.94	13.77	13.78	13.86	13.89	13.86	13.89	13.72	13.80
Neon	21.32	21.51	21.21	21.44	21.47	21.37	21.34	21.20	21.17
Argon	15.54	15.50	15.49	15.66	15.70	15.64	15.63	15.45	15.53
Helium	24.51	24.64	24.54	24.64	24.65	24.57	24.55	24.46	24.43
Sulfur dioxide	13.49	12.40	12.33	12.50	12.58	12.47	12.49	12.25	12.30
Vinyl chloride	10.09	10.01	10.04	10.23	10.26	10.21	10.23	10.04	10.13
Fluoroethylene	10.55	10.47	10.48	10.70	10.73	10.67	10.70	10.53	10.60
Acetaldehyde	10.21	10.39	10.32	10.39	10.47	10.36	10.41	10.18	10.23
Carbon disulfide	9.98	9.95	9.96	10.17	10.21	10.15	10.16	9.97	10.07
Cyclopropane	10.87	10.90	10.93	11.09	11.14	11.07	11.12	10.91	10.99
Carbon tetrafluoride	16.30	16.45	16.23	16.32	16.40	16.28	16.30	16.06	16.02
Iodine	9.51	9.38	9.44	9.44	9.47	9.45	9.50	9.33	9.42
Lithium hydride	7.96	8.18	8.15	8.11	8.16	8.10	8.11	8.07	7.99
Hydrochloric acid	12.59	12.54	12.55	12.71	12.74	12.69	12.68	12.53	12.63
Sodium chloride	9.03	9.01	9.01	9.10	9.13	9.09	9.08	8.98	9.00

Hydrofluoric acid	16.03	16.21	16.03	16.15	16.18	16.09	16.06	15.94	15.98
Ammonia	10.81	10.91	10.90	10.99	11.03	10.96	10.97	10.82	10.93
Potassium hydride	6.13	6.26	6.26	6.16	6.23	6.16	6.19	6.15	5.96
Hydrogen peroxide	11.59	11.75	11.65	11.75	11.80	11.70	11.69	11.53	11.57
Bromine	10.54	10.45	10.46	10.51	10.55	10.52	10.55	10.38	10.45
Nitrogen	15.57	15.72	15.68	15.84	15.97	15.79	15.87	15.52	15.58
Water	12.57	12.69	12.62	12.71	12.75	12.66	12.64	12.51	12.60
Potassium bromide	8.13	8.01	8.06	8.07	8.10	8.09	8.11	7.99	8.03
Fluorine	15.71	16.02	15.80	15.97	16.03	15.91	15.90	15.70	15.69
Chlorine	11.41	11.42	11.41	11.57	11.61	11.55	11.55	11.36	11.45
Germane	12.50	12.65	12.64	12.69	12.74	12.68	12.73	12.58	12.57
Hydrazoic acid	10.68	10.71	10.72	10.96	11.00	10.92	10.92	10.73	10.81
Hydrogen sulfide	10.31	10.24	10.28	10.44	10.46	10.42	10.43	10.28	10.39
Magnesium fluoride	13.71	13.92	13.69	13.70	13.74	13.65	13.64	13.56	13.50
Sulfur tetrafluoride	12.59	12.75	12.61	12.79	12.85	12.76	12.81	12.59	12.54
Titanium tetrafluoride	15.48	15.59	15.33	15.26	15.37	15.23	15.29	15.00	14.95
Aluminum fluoride	15.46	15.52	15.29	15.35	15.41	15.30	15.30	15.14	15.10
Aluminum iodide	9.82	9.65	9.69	9.63	9.68	9.65	9.28	9.53	9.59
Arsine	10.40	10.33	10.38	10.46	10.47	10.47	10.50	10.38	10.46
Magnesium chloride	11.67	11.66	11.65	11.73	11.78	11.71	11.72	11.56	11.61
Lithium fluoride	11.32	11.49	11.27	11.28	11.31	11.24	11.21	11.17	11.10
Phosphine	10.52	10.54	10.57	10.73	10.75	10.72	10.74	10.61	10.69
Silane	12.80	13.02	13.00	13.09	13.14	13.06	13.10	12.95	12.94

A.4 Ionization Potentials of the CORE65 Test Set

Table A.5: Continuation of tab. A.3. Ionization potential for the CORE65 test set for various DFAs, obtained using the G_0W_0 -1 method. Computational details are provided in sec. 8.1. Experimental data is taken from the references listed and corresponds to the same data used in ref. 29.

Name	State	BP86	PBE	TPSS	BH&HLYP	B3LYP	PBE0	TPSSh	LC-ωPBE	Exp.	Ref.
Methanol	O 1s	538.67	538.81	538.83	540.47	539.24	539.91	539.27	540.66	538.88	405 , 406, 407
Methanol	C 1s	291.93	291.96	292.42	293.92	292.68	293.05	292.81	293.77	292.3	407 , 405
Formaldehyde	O 1s	539.06	539.19	539.21	540.88	539.65	540.30	539.66	541.10	539.33	405 , 406, 407
Formaldehyde	C 1s	294.03	294.04	294.42	296.18	294.87	295.21	294.86	295.91	294.38	405
Dimethyl Ether	O 1s	538.17	538.33	538.26	539.97	538.72	539.45	538.72	540.21	538.36	405 , 406, 407
Dimethyl Ether	C 1s	291.69	291.73	292.18	293.70	292.46	292.83	292.58	293.57	292.17	408
Formic Acid	O 1s	540.18	540.31	540.34	542.20	540.85	541.52	540.83	542.33	540.69	409
Formic Acid	O 1s	538.39	538.51	538.54	540.43	539.08	539.74	539.04	540.61	539.02	409
Formic Acid	C 1s	294.97	294.96	295.33	297.53	296.00	296.33	295.85	297.09	295.75	409
Acetone	O 1s	537.40	537.53	537.58	539.45	538.10	538.76	538.08	539.72	537.73	405 , 406, 407
Acetone	C 1s	293.04	293.08	293.30	295.31	293.91	294.34	293.79	295.15	293.88	405
Acetone	C 1s	290.60	290.65	291.06	292.59	291.35	291.75	291.47	292.50	291.23	405
Methyl Formate	O 1s	539.45	539.61	539.54	541.41	540.08	540.81	540.03	541.62	539.64	405 , 406, 407
Methyl Formate	O 1s	537.92	538.05	538.09	540.02	538.64	539.31	538.60	540.22	538.24	405 , 406, 407
Acetic Acid	O 1s	539.58	539.71	539.74	541.68	540.29	540.97	540.25	541.83	540.10	409
Acetic Acid	O 1s	537.66	537.79	537.83	539.75	538.38	539.04	538.34	539.98	538.31	409
Acetic Acid	C 1s	294.48	294.49	294.77	297.06	295.51	295.88	295.31	296.70	295.35	409
Acetic Acid	C 1s	291.00	291.05	291.48	293.01	291.76	292.16	291.89	292.89	291.55	409
Water	O 1s	539.45	539.56	539.66	541.20	540.01	540.61	540.08	541.31	539.7	407
Ozone	O 1s	546.56	546.69	546.66	549.37	547.56	548.31	547.32	549.29	546.44	410
Ozone	O 1s	541.37	541.47	541.56	543.85	542.27	542.89	542.13	543.72	541.75	410
Methane	C 1s	290.35	290.40	290.86	292.15	291.02	291.40	291.22	292.09	290.84	407
Nitrogen	N 1s	409.46	409.52	409.70	411.55	410.21	410.72	410.16	411.39	409.93	411
Ammonia	N 1s	405.22	405.31	405.54	407.02	405.81	406.38	405.95	407.04	405.52	405, 411, 406
Hydrogen Cyanide	N 1s	406.40	406.48	406.63	408.39	407.07	407.66	407.09	408.38	406.8	405, 411, 412
Hydrogen Cyanide	C 1s	292.91	292.93	293.21	294.84	293.64	294.01	293.62	294.68	293.5	405, 411, 412
Acetonitrile	N 1s	405.14	405.23	405.40	407.28	405.88	406.48	405.89	407.31	405.58	413
Acetonitrile	C 1s	292.16	292.21	292.62	294.11	292.88	293.29	293.02	294.00	292.88	413
Acetonitrile	C 1s	292.11	292.14	292.33	294.12	292.86	293.28	292.77	294.03	292.60	413
Glycine	O 1s	539.60	539.73	539.76	541.75	540.34	541.01	540.28	541.90	540.2	414
Glycine	O 1s	537.74	537.86	537.91	539.88	538.48	539.14	538.43	540.11	538.4	414
Glycine	N 1s	405.01	405.13	405.29	406.96	405.66	406.29	405.75	407.01	405.4	414
Glycine	C 1s	294.26	294.27	294.56	296.90	295.33	295.70	295.11	296.56	295.2	414
Glycine	C 1s	291.65	291.70	292.08	293.75	292.44	292.85	292.51	293.61	292.3	414
Pyridine	N 1s	404.29	404.42	404.48	406.36	404.97	405.67	404.98	406.50	404.82	415

Pyrrole	N 1s	405.69	405.84	405.87	407.65	406.33	407.03	406.35	407.81	406.18	415
Aniline	N 1s	404.73	404.86	404.98	406.75	405.41	406.06	405.46	406.88	405.31	415
Urea	O 1s	536.54	536.66	536.71	538.64	537.25	537.92	537.22	538.89	537.19	405
Urea	N 1s	405.55	405.67	405.82	407.64	406.28	406.89	406.31	407.66	406.09	405
Urea	C 1s	294.00	294.00	294.31	296.64	295.05	295.42	294.86	296.27	294.84	405
Methylamine	N 1s	404.78	404.90	405.05	406.62	405.38	406.00	405.48	406.69	405.17	405, 411, 406
Ethane	C 1s	290.21	290.27	290.66	292.05	290.88	291.30	291.04	292.02	290.71	407
Nitrobenzene	O 1s	538.06	538.20	538.21	540.50	538.93	539.64	538.81	540.80	538.63	405
Nitrobenzene	N 1s	410.87	410.99	411.04	413.98	412.02	412.74	411.75	413.81	411.6	407
Nitrobenzene	C 1s	291.45	291.51	291.74	293.72	292.30	292.79	292.24	293.66	292.08	405
Nitrobenzene	C 1s	290.58	290.64	290.91	292.80	291.40	291.88	291.39	292.77	291.13	405
Benzene	C 1s	289.88	289.94	290.19	291.88	290.60	291.08	290.63	291.92	290.38	416
Phenylacetylene	C 1s	290.51	290.59	290.78	292.53	291.24	291.74	291.23	292.54	290.88	417
Phenylacetylene	C 1s	289.85	289.92	290.17	291.97	290.63	291.13	290.64	292.02	290.55	417
Phenylacetylene	C 1s	289.85	289.92	290.17	291.97	290.63	291.12	290.64	292.02	290.16	417
Phenylacetylene	C 1s	289.87	289.93	290.18	291.97	290.64	291.13	290.64	292.03	289.75	417
Ethene	C 1s	290.49	290.54	290.86	292.39	291.18	291.61	291.27	292.37	290.82	407
Ethyne	C 1s	290.95	290.99	291.26	292.82	291.62	292.06	291.67	292.79	291.25	407
Carbon Monixide	O 1s	542.08	542.22	542.22	543.84	542.66	543.29	542.65	544.09	542.1	407
Carbon Monixide	C 1s	295.56	295.55	295.86	297.69	296.38	296.73	296.31	297.41	296.23	407
Carbon Dioxide	O 1s	540.85	540.98	541.03	542.91	541.54	542.20	541.53	542.98	541.32	411
Carbon Dioxide	C 1s	296.68	296.65	296.95	299.58	297.87	298.17	297.54	298.94	297.70	407
Tetrafluoromethane	F 1s	694.63	694.76	694.77	696.84	695.42	696.04	695.29	696.95	695.2	407
Tetrafluoromethane	C 1s	300.62	300.61	301.06	303.68	301.93	302.22	301.66	302.85	301.90	407
Fluoromethane	F 1s	692.25	692.39	692.36	693.99	692.82	693.44	692.79	694.34	692.4	418
Fluoromethane	C 1s	292.99	293.01	293.48	295.06	293.79	294.14	293.89	294.85	293.56	407
Trifluoromethane	F 1s	693.82	693.95	693.96	695.91	694.56	695.18	694.45	696.11	694.1	418
Trifluoromethane	C 1s	298.15	298.14	298.60	300.80	299.34	299.58	299.14	300.27	299.16	407
Oxygen	O 1s	543.88	543.96	544.10	546.39	544.84	545.47	544.71	546.27	544.2	407
Oxygen	O 1s	542.97	543.06	543.15	545.16	543.73	544.35	543.66	545.14	543.1	407

Table A.6: Continuation of tab. A.4. Ionization potential for the CORE65 test set for various DFAs, obtained using the ev*GW* method. Computational details are provided in sec. 8.1. Experimental data is taken from the references listed and corresponds to the same data used in ref. 29. LH07t-SVWN, LH12ct-SsirPW92, and LH14t-calPBE are abbreviated by LH07t, LH12ct, and LH14t.

Name	State	ωB97D-X	CAM-B3LYP	LH07t	LH12ct	LH14t	LH20t	LHJ14	mPSTS	Exp.	Ref.
Methanol	O 1s	540.41	540.02	540.18	540.65	539.96	540.11	538.79	539.56	538.88	405 , 406, 407
Methanol	C 1s	293.66	293.35	293.45	293.84	293.30	293.72	292.42	293.05	292.3	407 , 405
Formaldehyde	O 1s	540.83	540.48	540.60	541.08	540.38	540.56	539.23	539.95	539.33	405 , 406, 407
Formaldehyde	C 1s	295.84	295.56	295.69	296.12	295.53	295.92	294.56	295.10	294.38	405
Dimethyl Ether	O 1s	539.96	539.53	539.66	540.15	539.43	539.56	538.29	539.00	538.36	405 , 406, 407
Dimethyl Ether	C 1s	293.45	293.14	293.22	293.60	293.07	293.49	292.20	292.81	292.17	408
Formic Acid	O 1s	542.07	541.70	541.80	542.29	541.58	541.77	540.39	541.11	540.69	409
Formic Acid	O 1s	540.30	539.98	540.02	540.50	539.81	540.03	538.65	539.33	539.02	409
Formic Acid	C 1s	296.99	296.78	296.76	297.22	296.61	297.05	295.66	296.07	295.75	409
Acetone	O 1s	539.39	539.04	539.04	539.54	538.85	539.10	537.70	538.36	537.73	405 , 406, 407
Acetone	C 1s	294.98	294.69	294.63	295.09	294.45	294.79	293.64	293.99	293.88	405
Acetone	C 1s	292.36	292.04	292.06	292.44	291.92	292.31	291.09	291.69	291.23	405
Methyl Formate	O 1s	541.35	540.94	541.03	541.53	540.81	540.96	539.63	540.30	539.64	405 , 406, 407
Methyl Formate	O 1s	539.90	539.57	539.57	540.07	539.37	539.60	538.22	538.88	538.24	405 , 406, 407
Acetic Acid	O 1s	541.54	541.17	541.24	541.74	541.03	541.22	539.83	540.53	540.10	409
Acetic Acid	O 1s	539.63	539.32	539.32	539.80	539.12	539.36	537.97	538.62	538.31	409
Acetic Acid	C 1s	296.55	296.32	296.22	296.70	296.05	296.45	295.19	295.52	295.35	409
Acetic Acid	C 1s	292.75	292.44	292.46	292.84	292.33	292.73	291.50	292.12	291.55	409
Water	O 1s	541.08	540.73	540.96	541.41	540.74	540.89	539.54	540.38	539.7	407
Ozone	O 1s	548.87	548.59	548.67	549.30	548.41	548.73	546.98	547.60	546.44	410
Ozone	O 1s	543.48	543.21	543.25	543.77	543.04	543.36	541.73	542.40	541.75	410
Methane	C 1s	291.99	291.65	291.79	292.16	291.65	292.04	290.75	291.48	290.84	407
Nitrogen	N 1s	411.25	410.98	411.19	411.66	410.98	411.27	409.82	410.42	409.93	411
Ammonia	N 1s	406.85	406.50	406.70	407.16	406.51	406.76	405.41	406.25	405.52	405, 411, 406
Hydrogen Cyanide	N 1s	408.21	407.86	408.03	408.52	407.82	408.09	406.71	407.38	406.8	405, 411, 412
Hydrogen Cyanide	C 1s	294.59	294.32	294.47	294.88	294.31	294.62	293.36	293.84	293.5	405, 411, 412
Acetonitrile	N 1s	407.09	406.74	406.81	407.32	406.63	406.94	405.52	406.16	405.58	413
Acetonitrile	C 1s	293.88	293.55	293.62	294.00	293.48	293.85	292.61	293.26	292.88	413
Acetonitrile	C 1s	293.87	293.60	293.65	294.08	293.48	293.77	292.60	292.97	292.60	413
Glycine	O 1s	541.61	541.24	541.27	541.77	541.07	541.27	539.88	540.55	540.2	414
Glycine	O 1s	539.75	539.44	539.42	539.90	539.22	539.46	538.08	538.70	538.4	414
Glycine	N 1s	406.78	406.41	406.50	406.98	406.32	406.57	405.29	406.01	405.4	414
Glycine	C 1s	296.38	296.17	296.03	296.50	295.87	296.28	295.01	295.31	295.2	414
Glycine	C 1s	293.46	293.16	293.11	293.50	292.97	293.36	292.19	292.73	292.3	414
Pyridine	N 1s	406.24	405.84	405.83	406.35	405.64	405.90	404.63	405.23	404.82	415
Pyrrole	N 1s	407.54	407.14	407.19	407.70	406.99	407.21	405.96	406.59	406.18	415
Aniline	N 1s	406.63	406.23	406.25	406.74	406.07	406.32	405.04	405.71	405.31	415

Urea	O 1s	538.54	538.20	538.17	538.66	537.98	538.21	536.85	537.50	537.19	405
Urea	N 1s	407.41	407.07	407.12	407.60	406.94	407.20	405.88	406.56	406.09	405
Urea	C 1s	296.12	295.89	295.74	296.21	295.58	296.00	294.73	295.07	294.84	405
Methylamine	N 1s	406.47	406.10	406.24	406.72	406.05	406.28	405.00	405.75	405.17	405, 411, 406
Ethane	C 1s	291.88	291.54	291.61	291.99	291.46	291.83	290.63	291.28	290.71	407
Nitrobenzene	O 1s	540.42	540.05	539.86	540.40	539.67	539.96	538.50	539.07	538.63	405
Nitrobenzene	N 1s	413.44	413.12	412.92	413.56	412.71	413.10	411.57	411.99	411.6	407
Nitrobenzene	C 1s	293.46	293.13	292.97	293.42	292.83	293.18	292.07	292.42	292.08	405
Nitrobenzene	C 1s	292.58	292.23	292.09	292.52	291.95	292.32	291.17	291.59	291.13	405
Benzene	C 1s	291.75	291.38	291.30	291.72	291.15	291.48	290.38	290.83	290.38	416
Phenylacetylene	C 1s	292.39	292.01	291.89	292.32	291.73	292.02	291.01	291.41	290.88	417
Phenylacetylene	C 1s	291.84	291.45	291.32	291.76	291.18	291.52	290.41	290.84	290.55	417
Phenylacetylene	C 1s	291.84	291.45	291.32	291.76	291.18	291.52	290.41	290.84	290.16	417
Phenylacetylene	C 1s	291.85	291.46	291.32	291.75	291.18	291.52	290.42	290.84	289.75	417
Ethene	C 1s	292.25	291.90	291.95	292.36	291.79	292.13	290.93	291.50	290.82	407
Ethyne	C 1s	292.68	292.33	292.44	292.87	292.27	292.58	291.36	291.90	291.25	407
Carbon Monixide	O 1s	543.77	543.48	543.67	544.13	543.43	543.59	542.24	542.92	542.1	407
Carbon Monixide	C 1s	297.38	297.11	297.35	297.80	297.17	297.55	296.11	296.56	296.23	407
Carbon Dioxide	O 1s	542.68	542.39	542.52	543.01	542.30	542.53	541.08	541.81	541.32	411
Carbon Dioxide	C 1s	298.83	298.70	298.66	299.17	298.50	298.98	297.46	297.76	297.70	407
Tetrafluoromethane	F 1s	696.53	696.34	696.39	696.85	696.18	696.36	694.94	695.56	695.2	407
Tetrafluoromethane	C 1s	303.15	302.70	302.63	303.11	302.44	303.00	301.48	301.84	301.90	407
Fluoromethane	F 1s	693.93	693.66	693.82	694.26	693.58	693.68	692.37	693.07	692.4	418
Fluoromethane	C 1s	294.74	294.45	294.59	294.99	294.43	294.88	293.51	294.14	293.56	407
Trifluoromethane	F 1s	695.69	695.47	695.54	695.99	695.31	695.48	694.09	694.73	694.1	418
Trifluoromethane	C 1s	300.19	300.02	300.05	300.51	299.88	300.40	298.93	299.36	299.16	407
Oxygen	O 1s	546.02	545.75	545.92	546.38	545.69	545.93	544.34	545.39	544.2	407
Oxygen	O 1s	544.84	544.59	544.79	545.30	544.56	544.83	543.26	544.53	543.1	407

Table A.7: Ionization potential for the CORE65 test set for various DFAs, obtained using the ev*GW* method. Computational details are provided in sec. 8.1. Experimental data is taken from the references listed and corresponds to the same data used in ref. 29.

Name	State	BP86	PBE	TPSS	BH&HLYP	B3LYP	PBE0	TPSSh	LC-ωPBE	Exp.	Ref.
Methanol	O 1s	539.15	538.97	538.79	540.45	539.11	539.76	538.83	540.45	538.88	405 , 406, 407
Methanol	C 1s	291.84	291.97	292.60	293.90	292.45	292.84	293.02	293.58	292.3	407 , 405
Formaldehyde	O 1s	538.52	538.59	539.09	540.85	539.57	540.12	539.60	540.96	539.33	405 , 406, 407
Formaldehyde	C 1s	293.63	293.41	294.10	296.15	294.75	295.06	294.76	295.72	294.38	405
Dimethyl Ether	O 1s	538.34	538.29	538.39	539.95	538.47	539.28	538.63	540.01	538.36	405 , 406, 407
Dimethyl Ether	C 1s	291.28	291.39	292.24	293.68	292.31	292.70	292.33	293.40	292.17	408
Formic Acid	O 1s	540.27	540.36	540.22	542.18	540.56	541.42	540.49	542.05	540.69	409
Formic Acid	O 1s	538.13	539.15	538.27	540.40	538.88	539.76	539.04	540.56	539.02	409
Formic Acid	C 1s	294.85	294.82	295.11	297.51	295.79	296.20	295.81	296.93	295.75	409
Acetone	O 1s	537.60	537.73	537.57	539.42	537.94	538.75	537.76	539.61	537.73	405 , 406, 407
Acetone	C 1s	292.98	292.94	292.94	295.29	293.76	294.27	293.70	295.00	293.88	405
Acetone	C 1s	290.45	290.38	290.98	292.57	291.18	291.63	291.27	292.34	291.23	405
Methyl Formate	O 1s	539.58	539.75	539.56	541.39	539.95	540.54	539.73	541.38	539.64	405 , 406, 407
Methyl Formate	O 1s	537.78	537.91	538.01	540.00	538.50	539.23	538.60	540.14	538.24	405 , 406, 407
Acetic Acid	O 1s	539.46	539.55	539.65	541.66	540.05	540.88	539.82	541.52	540.10	409
Acetic Acid	O 1s	537.30	537.89	537.68	539.73	538.29	538.77	537.89	539.70	538.31	409
Acetic Acid	C 1s	294.18	294.41	294.53	297.04	295.40	295.76	295.33	296.57	295.35	409
Acetic Acid	C 1s	290.87	290.87	291.35	292.99	291.60	292.05	291.66	292.72	291.55	409
Water	O 1s	539.53	539.53	541.11	541.17	539.72	540.40	539.59	540.96	539.7	407
Ozone	O 1s	546.25	547.02	546.54	549.35	547.47	548.41	546.99	549.16	546.44	410
Ozone	O 1s	541.23	541.17	541.79	543.81	542.27	542.85	541.97	543.49	541.75	410
Methane	C 1s	290.05	290.09	290.66	292.14	290.91	291.30	291.09	292.01	290.84	407
Nitrogen	N 1s	408.99	410.00	409.58	411.52	409.43	410.33	410.32	411.76	409.93	411
Ammonia	N 1s	405.30	405.30	405.26	407.00	405.58	406.21	405.62	406.86	405.52	405, 411, 406
Hydrogen Cyanide	N 1s	406.33	406.45	406.53	408.36	406.99	407.22	407.25	408.50	406.8	405, 411, 412
Hydrogen Cyanide	C 1s	292.82	292.84	293.22	294.82	293.56	293.79	293.62	294.54	293.5	405, 411, 412
Acetonitrile	N 1s	404.99	405.14	405.35	407.25	406.16	405.98	405.97	407.41	405.58	413
Acetonitrile	C 1s	292.13	292.11	292.12	294.09	292.74	293.18	292.82	293.85	292.88	413
Acetonitrile	C 1s	291.73	291.86	292.19	294.10	293.04	292.98	292.71	293.56	292.60	413
Glycine	O 1s	539.24	539.55	539.26	541.72	540.05	540.88	540.09	541.51	540.2	414
Glycine	O 1s	537.48	537.79	537.55	539.85	538.42	539.23	538.22	539.30	538.4	414
Glycine	N 1s	405.22	405.42	405.26	406.94	405.34	406.09	405.34	406.72	405.4	414
Glycine	C 1s	294.15	294.07	294.44	296.88	295.14	295.57	295.04	296.38	295.2	414
Glycine	C 1s	291.35	291.47	291.79	293.73	292.29	292.76	292.21	293.44	292.3	414
Pyridine	N 1s	403.66	404.32	404.24	406.35	404.85	405.54	404.76	406.45	404.82	415
Pyrrole	N 1s	405.49	405.61	405.33	407.63	406.21	406.91	406.22	407.60	406.18	415
Aniline	N 1s	404.46	404.42	404.66	406.73	405.33	405.88	405.37	406.74	405.31	415

Urea	O 1s	536.26	536.56	536.64	538.61	537.12	537.74	537.12	538.87	537.19	405
Urea	N 1s	405.44	405.64	405.90	407.62	406.24	406.62	406.24	407.40	406.09	405
Urea	C 1s	293.74	293.70	294.15	296.62	294.88	295.31	294.98	296.11	294.84	405
Methylamine	N 1s	404.83	404.89	405.26	406.60	405.14	405.82	404.99	406.57	405.17	405, 411, 406
Ethane	C 1s	289.75	290.22	290.23	292.03	290.74	291.19	290.86	291.87	290.71	407
Nitrobenzene	O 1s	538.29	538.42	537.91	540.48	538.78	539.59	538.38	540.52	538.63	405
Nitrobenzene	N 1s	410.42	410.44	410.75	413.96	412.11	412.42	411.60	413.79	411.6	407
Nitrobenzene	C 1s	291.32	291.45	291.65	293.71	292.15	292.70	292.14	293.48	292.08	405
Nitrobenzene	C 1s	290.43	290.46	290.73	292.78	291.32	291.75	291.24	292.60	291.13	405
Benzene	C 1s	289.71	289.81	290.11	291.86	290.48	290.61	290.42	291.80	290.38	416
Phenylacetylene	C 1s	290.26	290.31	290.61	292.51	291.17	291.68	291.10	292.42	290.88	417
Phenylacetylene	C 1s	289.66	289.71	290.01	291.95	290.53	290.94	290.56	291.90	290.55	417
Phenylacetylene	C 1s	289.64	289.73	289.98	291.95	290.52	290.93	290.53	291.89	290.16	417
Phenylacetylene	C 1s	289.56	289.80	290.02	292.02	290.55	291.10	290.54	291.87	289.75	417
Ethene	C 1s	290.69	290.62	290.57	292.37	291.08	291.56	291.06	292.24	290.82	407
Ethyne	C 1s	290.56	291.04	291.09	292.80	291.81	291.61	291.67	292.84	291.25	407
Carbon Monixide	O 1s	542.36	542.39	541.89	543.81	542.89	543.98	542.64	544.09	542.1	407
Carbon Monixide	C 1s	295.54	295.52	295.95	297.66	296.01	296.52	296.20	297.14	296.23	407
Carbon Dioxide	O 1s	541.21	541.20	540.79	542.89	541.35	542.36	541.61	542.77	541.32	411
Carbon Dioxide	C 1s	296.55	296.54	296.95	299.55	297.70	298.03	297.21	298.79	297.70	407
Tetrafluoromethane	F 1s	694.11	694.85	694.65	696.81	695.03	695.88	695.03	696.71	695.2	407
Tetrafluoromethane	C 1s	300.32	300.28	300.88	303.66	301.82	302.09	301.49	302.72	301.90	407
Fluoromethane	F 1s	692.06	692.05	692.48	693.96	692.37	693.16	692.33	694.05	692.4	418
Fluoromethane	C 1s	292.62	292.72	293.30	295.04	293.67	294.05	293.77	294.72	293.56	407
Trifluoromethane	F 1s	693.88	693.98	693.53	695.88	694.31	694.87	694.39	695.80	694.1	418
Trifluoromethane	C 1s	297.85	297.84	298.40	300.88	299.18	299.49	299.01	300.19	299.16	407
Oxygen	O 1s	544.17	544.16	543.87	546.32	544.53	545.69	544.77	546.25	544.2	407
Oxygen	O 1s	542.90	542.86	542.75	545.14	543.68	544.36	543.56	545.01	543.1	407

Table A.8: Continuation of tab. A.4. Ionization potential for the CORE65 test set for various DFAs, obtained using the GW_0 method. Computational details are provided in sec. 8.1. Experimental data is taken from the references listed and corresponds to the same data used in ref. 29. LH07t-SVWN, LH12ct-SsirPW92, and LH14t-calPBE are abbreviated by LH07t, LH12ct, and LH14t.

Name	State	ωB97D-X	CAM-B3LYP	LH07t	LH12ct	LH14t	LH20t	LHJ14	mPSTS	Exp.	Ref.
Methanol	O 1s	540.27	539.84	540.09	540.63	539.89	540.11	538.64	539.40	538.88	405 , 406, 407
Methanol	C 1s	293.55	293.21	293.38	293.83	293.25	293.72	292.27	292.88	292.3	407 , 405
Formaldehyde	O 1s	541.43	540.35	540.45	541.06	540.28	540.58	539.05	540.01	539.33	405 , 406, 407
Formaldehyde	C 1s	295.73	295.42	295.64	296.10	295.49	295.93	294.31	295.10	294.38	405
Dimethyl Ether	O 1s	539.82	539.46	539.56	540.14	539.37	539.58	538.13	538.99	538.36	405 , 406, 407
Dimethyl Ether	C 1s	293.36	293.03	293.17	293.60	293.04	293.50	291.93	292.70	292.17	408
Formic Acid	O 1s	541.94	541.44	541.67	542.28	541.51	541.79	540.39	540.88	540.69	409
Formic Acid	O 1s	540.36	539.77	539.86	540.49	539.72	540.06	538.35	539.23	539.02	409
Formic Acid	C 1s	296.89	296.65	296.71	297.21	296.57	297.06	295.45	295.96	295.75	409
Acetone	O 1s	539.48	538.91	538.89	539.53	538.76	539.12	537.77	538.37	537.73	405 , 406, 407
Acetone	C 1s	294.87	294.53	294.58	295.08	294.41	294.80	293.38	293.96	293.88	405
Acetone	C 1s	292.26	291.92	292.01	292.43	291.89	292.32	290.94	291.56	291.23	405
Methyl Formate	O 1s	541.25	540.75	540.90	541.52	540.73	540.98	539.59	540.15	539.64	405 , 406, 407
Methyl Formate	O 1s	539.67	539.62	539.41	540.05	539.28	539.63	537.99	539.18	538.24	405 , 406, 407
Acetic Acid	O 1s	541.39	541.00	541.11	541.72	540.95	541.24	539.67	540.44	540.10	409
Acetic Acid	O 1s	539.64	539.18	539.16	539.79	539.03	539.38	537.88	538.61	538.31	409
Acetic Acid	C 1s	296.45	296.20	296.17	296.69	296.02	296.46	294.98	295.40	295.35	409
Acetic Acid	C 1s	292.66	292.33	292.42	292.83	292.30	292.74	291.27	292.00	291.55	409
Water	O 1s	540.97	540.52	540.87	541.40	540.68	540.91	540.05	540.23	539.7	407
Ozone	O 1s	548.48	548.98	548.53	549.29	548.32	548.75	546.69	547.65	546.44	410
Ozone	O 1s	543.34	543.47	543.33	543.75	545.95	543.39	542.19	542.10	541.75	410
Methane	C 1s	291.94	291.56	291.75	292.16	291.62	292.05	290.53	291.39	290.84	407
Nitrogen	N 1s	411.05	410.72	411.08	411.64	410.90	411.27	409.64	410.10	409.93	411
Ammonia	N 1s	406.77	406.34	406.63	407.15	406.46	406.77	404.91	406.11	405.52	405, 411, 406
Hydrogen Cyanide	N 1s	408.02	407.58	407.93	408.51	407.76	408.11	406.68	407.01	406.8	405, 411, 412
Hydrogen Cyanide	C 1s	294.47	294.17	294.41	294.87	294.26	294.64	293.26	293.62	293.5	405, 411, 412
Acetonitrile	N 1s	406.97	406.44	406.73	407.31	406.57	406.96	405.60	407.37	405.58	413
Acetonitrile	C 1s	293.79	293.45	293.58	294.00	293.45	293.86	292.32	293.16	292.88	413
Acetonitrile	C 1s	293.75	293.45	293.59	294.08	293.44	293.78	292.48	292.60	292.60	413
Glycine	O 1s	541.56	541.02	541.15	541.76	540.99	541.29	539.48	540.39	540.2	414
Glycine	O 1s	539.75	539.36	539.27	539.89	539.11	539.49	538.14	538.52	538.4	414
Glycine	N 1s	406.63	406.24	406.43	406.97	406.27	406.59	404.92	405.87	405.4	414
Glycine	C 1s	296.29	296.04	295.98	296.50	295.83	296.29	294.88	295.20	295.2	414
Glycine	C 1s	293.37	293.05	293.07	293.49	292.94	293.37	291.87	292.61	292.3	414
Pyridine	N 1s	406.17	405.75	405.74	406.34	405.59	405.92	404.41	405.16	404.82	415
Pyrrole	N 1s	407.54	407.12	407.10	407.69	406.94	407.24	405.60	406.50	406.18	415
Aniline	N 1s	406.49	406.10	406.17	406.74	406.02	406.34	404.82	405.57	405.31	415

Urea	O 1s	537.93	538.04	538.02	538.65	537.89	538.23	536.96	537.38	537.19	405
Urea	N 1s	407.25	406.88	407.05	407.59	406.89	407.22	405.55	406.33	406.09	405
Urea	C 1s	296.03	295.78	295.69	296.20	295.55	296.01	294.58	294.96	294.84	405
Methylamine	N 1s	406.40	405.93	406.18	406.71	406.00	406.29	404.55	405.61	405.17	405, 411, 406
Ethane	C 1s	291.80	291.44	291.57	291.99	291.43	291.84	290.16	291.18	290.71	407
Nitrobenzene	O 1s	540.31	539.89	540.08	540.38	539.50	539.99	538.39	538.90	538.63	405
Nitrobenzene	N 1s	413.27	412.96	412.84	413.55	412.66	413.12	411.15	411.71	411.6	407
Nitrobenzene	C 1s	293.39	293.02	292.91	293.41	292.79	293.20	291.88	292.35	292.08	405
Nitrobenzene	C 1s	292.52	292.13	292.01	292.51	291.91	292.33	291.03	291.49	291.13	405
Benzene	C 1s	291.76	291.30	291.24	291.71	291.11	291.49	290.21	290.60	290.38	416
Phenylacetylene	C 1s	292.30	291.93	291.83	292.32	291.70	292.04	290.92	291.38	290.88	417
Phenylacetylene	C 1s	291.83	291.38	291.26	291.76	291.14	291.54	290.24	290.69	290.55	417
Phenylacetylene	C 1s	291.83	291.38	291.26	291.76	291.14	291.54	290.24	290.67	290.16	417
Phenylacetylene	C 1s	291.77	291.43	291.25	291.75	291.14	291.53	290.34	290.81	289.75	417
Ethene	C 1s	292.08	291.92	291.89	292.35	291.75	292.15	290.61	291.45	290.82	407
Ethyne	C 1s	292.55	292.14	292.37	292.86	292.23	292.59	291.21	291.33	291.25	407
Carbon Monixide	O 1s	543.43	542.85	543.52	544.10	543.33	543.60	541.64	543.13	542.1	407
Carbon Monixide	C 1s	297.25	296.95	297.29	297.78	297.12	297.55	296.08	296.36	296.23	407
Carbon Dioxide	O 1s	542.36	541.96	542.39	543.00	542.22	542.55	540.86	541.17	541.32	411
Carbon Dioxide	C 1s	298.73	298.58	298.60	299.16	298.46	298.98	297.41	297.63	297.70	407
Tetrafluoromethane	F 1s	696.32	696.10	696.28	696.82	696.09	696.38	694.78	695.37	695.2	407
Tetrafluoromethane	C 1s	302.72	302.61	302.59	303.11	302.41	303.01	301.29	301.75	301.90	407
Fluoromethane	F 1s	693.81	693.38	693.70	694.23	693.49	693.69	692.52	692.88	692.4	418
Fluoromethane	C 1s	294.67	294.37	294.55	294.98	294.41	294.89	293.37	294.05	293.56	407
Trifluoromethane	F 1s	695.48	695.19	695.43	695.97	695.23	695.49	693.57	694.52	694.1	418
Trifluoromethane	C 1s	300.14	299.97	300.01	300.50	299.85	300.41	298.46	299.27	299.16	407
Oxygen	O 1s	545.75	546.19	546.10	546.32	544.95	545.97	543.80	545.84	544.2	407
Oxygen	O 1s	545.15	544.67	544.65	545.29	544.48	544.84	542.73	544.61	543.1	407

Table A.9: Ionization potential for the CORE65 test set for various DFAs, obtained using the ev*GW* method. Computational details are provided in sec. 8.1. Experimental data is taken from the references listed and corresponds to the same data used in ref. 29.

Name	State	BP86	PBE	TPSS	BH&HLYP	B3LYP	PBE0	TPSSh	LC-ωPBE	Exp.	Ref.
Methanol	O 1s	538.76	538.90	538.92	540.50	539.31	539.98	539.35	540.69	538.88	405, 406, 407
Methanol	C 1s	292.07	292.09	292.54	293.95	292.79	293.14	292.92	293.82	292.3	407, 405
Formaldehyde	O 1s	541.28	541.43	541.32	541.59	541.21	541.72	541.45	541.34	539.33	405, 406, 407
Formaldehyde	C 1s	295.73	295.75	296.02	296.71	296.05	296.28	296.21	296.11	294.38	405
Dimethyl Ether	O 1s	539.94	540.13	539.91	540.51	539.96	540.54	540.10	540.24	538.36	405, 406, 407
Dimethyl Ether	C 1s	293.13	293.19	293.51	294.13	293.46	293.71	293.69	293.61	292.17	408
Formic Acid	O 1s	542.29	542.44	542.36	542.83	542.32	542.85	542.53	542.51	540.69	409
Formic Acid	O 1s	540.60	540.74	540.67	541.09	540.63	541.13	540.84	540.80	539.02	409
Formic Acid	C 1s	296.58	296.58	296.86	298.00	297.12	297.33	297.14	297.25	295.75	409
Acetone	O 1s	539.54	539.69	539.66	540.00	539.55	540.07	539.81	539.78	537.73	405, 406, 407
Acetone	C 1s	294.61	294.66	294.81	295.71	294.97	295.29	295.04	295.21	293.88	405
Acetone	C 1s	292.20	292.27	292.59	293.00	292.43	292.72	292.74	292.57	291.23	405
Methyl Formate	O 1s	541.55	541.72	541.55	542.00	541.53	542.11	541.72	541.74	539.64	405, 406, 407
Methyl Formate	O 1s	540.12	540.27	540.21	540.64	540.16	540.68	540.38	540.34	538.24	405, 406, 407
Acetic Acid	O 1s	541.63	541.78	541.73	542.23	541.69	542.23	541.91	541.93	540.1	409
Acetic Acid	O 1s	539.82	539.96	539.92	540.34	539.86	540.37	540.08	540.08	538.31	409
Acetic Acid	C 1s	296.04	296.06	296.26	297.47	296.57	296.83	296.56	296.80	295.35	409
Acetic Acid	C 1s	292.62	292.68	293.02	293.45	292.87	293.16	293.18	292.99	291.55	409
Water	O 1s	541.25	541.39	541.38	541.81	541.32	541.76	541.53	541.48	539.7	407
Ozone	O 1s	548.61	548.75	548.66	550.16	549.03	549.65	549.03	549.54	546.44	410
Ozone	O 1s	543.61	543.72	543.75	544.72	543.90	544.37	544.01	544.00	541.75	410
Methane	C 1s	291.81	291.89	292.24	292.71	292.12	292.35	292.39	292.19	290.84	407
Nitrogen	N 1s	411.45	411.52	411.60	412.22	411.63	412.01	411.78	411.67	409.93	411
Ammonia	N 1s	406.79	406.93	407.05	407.59	406.98	407.40	407.23	407.12	405.52	405, 411, 406
Hydrogen Cyanide	N 1s	408.36	408.45	408.52	409.13	408.51	408.96	408.72	408.57	406.8	405, 411, 412
Hydrogen Cyanide	C 1s	294.57	294.59	294.79	295.45	294.84	295.09	294.97	294.85	293.5	405, 411, 412
Acetonitrile	N 1s	407.09	407.18	407.28	407.94	407.12	407.75	407.49	407.31	405.58	413
Acetonitrile	C 1s	293.74	293.79	294.13	294.61	293.88	294.31	294.30	294.02	292.88	413
Acetonitrile	C 1s	293.69	293.73	293.85	294.62	293.86	294.29	294.06	294.04	292.6	413
Glycine	O 1s	541.62	541.76	541.71	542.32	541.73	542.26	541.91	541.97	540.2	414
Glycine	O 1s	539.87	540.01	539.97	540.50	539.96	540.47	540.16	540.18	538.4	414
Glycine	N 1s	406.78	406.91	406.99	407.48	406.90	407.40	407.18	407.08	405.4	414
Glycine	C 1s	295.82	295.84	296.05	297.34	296.40	296.65	296.36	296.63	295.2	414
Glycine	C 1s	293.23	293.29	293.59	294.20	293.54	293.84	293.78	293.68	292.3	414
Pyridine	N 1s	406.07	406.22	406.18	406.88	406.18	406.75	406.40	406.43	404.82	415
Pyrrole	N 1s	407.24	407.39	407.37	408.16	407.43	408.01	407.62	407.68	406.18	415
Aniline	N 1s	406.27	406.41	406.46	407.20	406.46	407.00	406.69	406.80	405.31	415

Urea	O 1s	538.43	538.61	538.53	539.19	538.57	539.06	538.72	538.84	537.19	405
Urea	N 1s	407.15	407.31	407.36	408.11	407.39	407.86	407.57	407.63	406.09	405
Urea	C 1s	295.33	295.36	295.58	297.02	295.98	296.21	295.90	296.26	294.84	405
Methylamine	N 1s	406.33	406.49	406.53	407.15	406.51	406.99	406.72	406.72	405.17	405, 411, 406
Ethane	C 1s	291.63	291.73	292.00	292.58	291.94	292.23	292.18	292.09	290.71	407
Nitrobenzene	O 1s	540.32	540.46	540.39	541.11	540.26	540.81	540.36	540.71	538.63	405
Nitrobenzene	N 1s	412.64	412.77	412.75	414.46	413.06	413.65	412.96	413.76	411.6	407
Nitrobenzene	C 1s	293.13	293.20	293.36	294.19	293.30	293.67	293.40	293.61	292.08	405
Nitrobenzene	C 1s	292.33	292.39	292.59	293.28	292.45	292.80	292.60	292.72	291.13	405
Benzene	C 1s	291.27	291.34	291.53	292.32	291.58	291.95	291.76	291.85	290.38	416
Phenylacetylene	C 1s	291.81	291.89	292.03	292.95	292.15	292.56	292.29	292.50	290.88	417
Phenylacetylene	C 1s	291.25	291.33	291.52	292.41	291.61	292.00	291.78	291.97	290.55	417
Phenylacetylene	C 1s	291.25	291.32	291.52	292.41	291.61	292.00	291.78	291.97	290.16	417
Phenylacetylene	C 1s	291.28	291.35	291.55	292.42	291.63	292.02	291.80	291.98	289.75	417
Ethene	C 1s	292.07	292.12	292.38	292.97	292.33	292.64	292.56	292.43	290.82	407
Ethyne	C 1s	292.61	292.65	292.85	293.44	292.83	293.15	293.02	292.91	291.25	407
Carbon Monixide	O 1s	544.23	544.38	544.27	544.60	544.21	544.69	544.41	544.32	542.1	407
Carbon Monixide	C 1s	297.29	297.28	297.48	298.28	297.61	297.84	297.69	297.61	296.23	407
Carbon Dioxide	O 1s	542.98	543.12	543.09	543.54	542.87	543.37	543.28	543.08	541.32	411
Carbon Dioxide	C 1s	298.24	298.22	298.45	300.02	298.83	299.01	298.80	299.00	297.7	407
Tetrafluoromethane	F 1s	696.81	696.95	696.85	697.44	696.90	697.33	696.99	697.17	695.2	407
Tetrafluoromethane	C 1s	302.15	302.13	302.47	304.06	302.96	303.08	302.82	303.02	301.9	407
Fluoromethane	F 1s	694.32	694.46	694.26	694.63	694.21	694.68	694.35	694.51	692.4	418
Fluoromethane	C 1s	294.63	294.65	294.97	295.57	294.90	295.11	295.12	295.01	293.56	407
Trifluoromethane	F 1s	695.79	695.98	695.83	696.55	695.97	696.42	696.02	696.30	694.1	418
Trifluoromethane	C 1s	299.59	299.61	299.96	301.35	300.32	300.48	300.28	300.44	299.16	407
Oxygen	O 1s	546.31	546.41	546.42	547.18	546.51	546.94	546.63	546.59	544.2	407
Oxygen	O 1s	545.18	545.28	545.29	545.93	545.32	545.77	545.48	545.46	543.1	407

Table A.10: Continuation of tab. A.4. Ionization potential for the CORE65 test set for various DFAs, obtained using the ev*GW* method. Computational details are provided in sec. 8.1. Experimental data is taken from the references listed and corresponds to the same data used in ref. 29. LH07t-SVWN, LH12ct-SsirPW92, and LH14t-calPBE are abbreviated by LH07t, LH12ct, and LH14t.

Name	State	ωB97D-X	CAM-B3LYP	LH07t	LH12ct	LH14t	LH20t	LHJ14	mPSTS	Exp.	Ref.
Methanol	O 1s	540.43	540.07	540.22	540.68	540.01	540.14	538.86	539.61	538.88	405, 406, 407
Methanol	C 1s	293.70	293.42	293.52	293.88	293.38	293.76	292.53	293.13	292.3	407, 405
Formaldehyde	O 1s	541.36	541.26	541.97	542.20	541.71	541.57	540.79	541.64	539.33	405, 406, 407
Formaldehyde	C 1s	296.25	296.15	296.72	296.94	296.53	296.67	295.76	296.37	294.38	405
Dimethyl Ether	O 1s	540.20	540.09	540.61	540.88	540.39	540.23	539.39	540.21	538.36	405, 406, 407
Dimethyl Ether	C 1s	293.65	293.60	293.98	294.18	293.84	294.01	293.10	293.79	292.17	408
Formic Acid	O 1s	542.53	542.39	543.12	543.38	542.89	542.77	541.90	542.73	540.69	409
Formic Acid	O 1s	540.78	540.71	541.41	541.65	541.18	541.09	540.23	541.03	539.02	409
Formic Acid	C 1s	297.35	297.32	297.76	298.03	297.59	297.80	296.81	297.29	295.75	409
Acetone	O 1s	539.74	539.65	540.39	540.66	540.18	540.14	539.18	540.01	537.73	405, 406, 407
Acetone	C 1s	295.25	295.15	295.62	295.91	295.42	295.55	294.73	295.19	293.88	405
Acetone	C 1s	292.63	292.50	293.05	293.26	292.90	293.07	292.19	292.91	291.23	405
Methyl Formate	O 1s	541.76	541.60	542.34	542.61	542.10	541.95	541.12	541.91	539.64	405, 406, 407
Methyl Formate	O 1s	540.33	540.25	540.94	541.19	540.72	540.64	539.77	540.57	538.24	405, 406, 407
Acetic Acid	O 1s	541.92	541.79	542.53	542.80	542.30	542.22	541.28	542.11	540.1	409
Acetic Acid	O 1s	540.03	539.96	540.67	540.93	540.46	540.41	539.49	540.28	538.31	409
Acetic Acid	C 1s	296.84	296.80	297.20	297.50	297.02	297.20	296.30	296.70	295.35	409
Acetic Acid	C 1s	293.06	292.94	293.47	293.66	293.32	293.50	292.64	293.35	291.55	409
Water	O 1s	541.45	541.41	541.92	542.14	541.71	541.61	540.71	541.61	539.7	407
Ozone	O 1s	549.41	549.34	550.01	550.43	549.73	549.77	548.56	549.23	546.44	410
Ozone	O 1s	544.07	544.03	544.73	545.01	544.49	544.51	543.46	544.20	541.75	410
Methane	C 1s	292.27	292.20	292.54	292.72	292.41	292.58	291.64	292.45	290.84	407
Nitrogen	N 1s	411.81	411.72	412.42	412.68	412.20	412.22	411.27	411.95	409.93	411
Ammonia	N 1s	407.12	407.06	407.53	407.77	407.35	407.36	406.38	407.31	405.52	405, 411, 406
Hydrogen Cyanide	N 1s	408.71	408.58	409.30	409.58	409.07	409.09	408.08	408.92	406.8	405, 411, 412
Hydrogen Cyanide	C 1s	295.01	294.93	295.52	295.75	295.35	295.45	294.52	295.12	293.5	405, 411, 412
Acetonitrile	N 1s	407.33	407.31	408.05	408.35	407.86	407.92	406.88	407.70	405.58	413
Acetonitrile	C 1s	294.08	294.02	294.61	294.82	294.46	294.62	293.71	294.48	292.88	413
Acetonitrile	C 1s	294.07	294.06	294.65	294.91	294.47	294.55	293.71	294.20	292.6	413
Glycine	O 1s	541.97	541.84	542.54	542.82	542.32	542.26	541.29	542.11	540.2	414
Glycine	O 1s	540.14	540.08	540.76	541.02	540.55	540.51	539.56	540.35	538.4	414
Glycine	N 1s	407.11	406.96	407.62	407.90	407.42	407.44	406.53	407.37	405.4	414
Glycine	C 1s	296.68	296.64	297.01	297.31	296.83	297.03	296.10	296.50	295.2	414
Glycine	C 1s	293.76	293.65	294.11	294.32	293.95	294.13	293.29	293.94	292.3	414
Pyridine	N 1s	406.45	406.26	406.94	407.20	406.72	406.71	405.82	406.59	404.82	415
Pyrrole	N 1s	407.72	407.55	408.19	408.54	407.98	408.01	406.99	407.81	406.18	415
Aniline	N 1s	406.75	406.61	407.21	407.54	407.01	407.05	406.03	406.89	405.31	415

Urea	O 1s	538.72	538.76	539.50	539.75	538.99	538.94	538.34	539.14	537.19	405
Urea	N 1s	407.56	407.54	408.24	408.52	407.79	407.82	407.15	407.95	406.09	405
Urea	C 1s	296.26	296.29	296.67	296.96	296.29	296.50	295.79	296.21	294.84	405
Methylamine	N 1s	406.69	406.62	407.07	407.34	406.88	406.89	405.94	406.79	405.17	405, 411, 406
Ethane	C 1s	292.13	292.06	292.35	292.54	292.21	292.46	291.50	292.23	290.71	407
Nitrobenzene	O 1s	540.61	540.55	541.09	541.42	540.88	540.94	540.08	540.56	538.63	405
Nitrobenzene	N 1s	413.60	413.52	413.89	414.37	413.67	413.88	412.82	413.15	411.6	407
Nitrobenzene	C 1s	293.62	293.52	293.90	294.19	293.74	293.92	293.26	293.53	292.08	405
Nitrobenzene	C 1s	292.75	292.64	293.05	293.32	292.90	293.08	292.41	292.75	291.13	405
Benzene	C 1s	291.88	291.74	292.19	292.46	292.03	292.18	291.28	291.92	290.38	416
Phenylacetylene	C 1s	292.51	292.36	292.73	293.02	292.57	292.68	291.86	292.44	290.88	417
Phenylacetylene	C 1s	291.97	291.83	292.22	292.51	292.07	292.23	291.32	291.93	290.55	417
Phenylacetylene	C 1s	291.97	291.82	292.22	292.51	292.07	292.23	291.32	291.93	290.16	417
Phenylacetylene	C 1s	291.99	291.84	292.23	292.51	292.08	292.23	291.34	291.95	289.75	417
Ethene	C 1s	292.55	292.41	292.95	293.19	292.78	292.91	291.97	292.73	290.82	407
Ethyne	C 1s	293.04	292.91	293.48	293.72	293.30	293.39	292.47	293.18	291.25	407
Carbon Monixide	O 1s	544.34	544.27	544.97	545.18	544.71	544.56	543.74	544.58	542.1	407
Carbon Monixide	C 1s	297.82	297.73	298.36	298.60	298.16	298.29	297.30	297.85	296.23	407
Carbon Dioxide	O 1s	543.01	543.04	543.91	544.17	543.68	543.63	542.67	543.48	541.32	411
Carbon Dioxide	C 1s	299.07	299.17	299.65	299.99	299.49	299.76	298.62	298.96	297.7	407
Tetrafluoromethane	F 1s	696.95	697.10	697.69	697.90	697.46	697.33	696.51	697.15	695.2	407
Tetrafluoromethane	C 1s	303.09	303.24	303.54	303.84	303.35	303.67	302.62	302.95	301.9	407
Fluoromethane	F 1s	694.31	694.36	694.99	695.17	694.71	694.47	693.80	694.57	692.4	418
Fluoromethane	C 1s	295.05	295.02	295.50	295.68	295.32	295.48	294.64	295.31	293.56	407
Trifluoromethane	F 1s	696.07	696.18	696.59	696.79	696.37	696.24	695.40	696.05	694.1	418
Trifluoromethane	C 1s	300.49	300.57	300.81	301.08	300.64	300.93	299.88	300.32	299.16	407
Oxygen	O 1s	546.67	546.63	547.40	547.65	547.15	547.13	546.12	546.87	544.2	407
Oxygen	O 1s	545.48	545.44	546.23	546.53	545.98	545.98	544.95	545.89	543.1	407

A.5 Core-Excited States within *GW*-BSE

Table A.11: Core-excited states for selected transitions of small inorganic molecules using the *GW*-BSE method at the K, L_1 and $L_{2,3}$ edges for different *GW* approximations. The ground state reference is provided using the PBE0 [251] DFA. Further computational details are given in sec. 9.2. "H/L" indicates that the "scissor operator" was used, where aside from core levels only the highest occupied and lowest virtual states were explicitly optimized, while the remaining states were shifted accordingly. For "Valence" and additional ten virtual and occupied states were included. This number was slightly adjusted in order to not break degenerate states in an by case basis. Experimental values are taken from references indicated below. If not explicitly listed in the source material, the values are obtained obtained from reinterpretation of the experimental spectra listed in the reference.

		BSE(H/L)			BSE(Valence)				
Name	Transition	G_0W_0-1	GW_0	evGW	G_0W_0-1	GW_0	evGW	Exp.	Ref.
$SiCl_4$	Si $1s \rightarrow a_1$	1847.28	1847.03	1848.28	1847.38	1847.14	1848.59	1844.8	419
	Si $1s \rightarrow t_2$	1847.83	1847.59	1848.82	1847.92	1847.69	1849.14	1846	419
$FeCp_2$	Fe $1s \rightarrow e_{1g}$	7121.05	7126.56	7122.32	7120.86	7126.38	7122.77	7123	333
$TiCl_4$	Ti $1s \rightarrow t_2(, e)$	4970.65	4983.18	4986.57	4970.48	4982.32	4986.02	4969.15	420
$TiCl_3Cp$	Ti $1s \rightarrow d_{x^2-y^2,xy,z^2}$	4971.24	4964.93	4964.96	4970.94	4964.48	4966.11	4968.11	420
	Ti $1s \rightarrow d_{xz,yz}$	4972.78	4966.48	4966.50	4972.58	4966.10	4967.70	4969.5	420
$TiCl_2Cp_2$	Ti $1s \rightarrow d_{x^2-y^2}$	4971.87	4968.74	4973.35	4971.65	4969.10	4973.59	4967.28	420
	Ti $1s \rightarrow d_{xy,xz,yz,z^2}$	4973.25	4970.10	4974.73	4973.07	4970.49	4974.93	4968.7	420
$SiCl_4$	Si $2s \rightarrow t_2$	157.70	158.50	159.62	157.42	158.50	158.35	156.8	419
$PdCl_2$	Pd $2s \rightarrow 4d$	3622.05	3622.32	3620.05	3621.17	3622.04	3621.78	3610.9	421
$SiCl_4$	Si $2p_{3/2} \rightarrow 1$	103.31	103.22	104.00	103.22	103.15	104.07	104.25	419
	Si $2p_{1/2} \rightarrow 1'$	104.15	104.11	104.80	104.07	103.92	104.88	104.86	419
	Si $2p_{3/2} \rightarrow 2$	104.93	104.83	105.63	105.02	104.96	105.87	105.5	419
	Si $2p_{1/2} \rightarrow 2', 3'$	105.61	105.58	106.27	105.72	105.56	106.51	106.3	419
$FeCp_2$	Fe $2p_{3/2} \rightarrow e_{1g}$	709.83	710.37	710.40	709.67	710.33	710.60	709.5	422
	Fe $2p_{3/2} \rightarrow e_{2u}$	712.65	713.09	713.24	713.41	714.34	714.25	712.1	422
	Fe $2p_{1/2} \rightarrow e_{1g}$	722.08	721.74	722.48	721.99	721.85	722.59	721.9	422
	Fe $2p_{1/2} \rightarrow e_{2u}$	725.25	724.90	725.66	725.90	725.72	726.43	724.7	422
$TiCl_4$	Ti $2p_{3/2} \rightarrow 2e$	455.96	455.67	457.13	455.70	455.42	457.20	456.9	423
	Ti $2p_{3/2} \rightarrow 4t_2$	458.03	457.76	459.20	457.84	457.57	459.32	458.7	423
	Ti $2p_{1/2} \rightarrow 2e$	461.56	461.72	462.81	461.29	461.44	462.96	462.5	423
	Ti $2p_{1/2} \rightarrow 4t_2$	463.22	463.36	464.46	463.07	463.20	464.67	464.3	423
$TiCl_3Cp$	Ti $2p_{3/2} \rightarrow t_{2g}$-like	456.54	456.45	457.58	456.27	455.98	457.61	457	423
	Ti $2p_{3/2} \rightarrow e_g$-like	458.33	458.24	459.34	458.14	457.84	459.44	458.6	423
	Ti $2p_{1/2} \rightarrow t_{2g}$-like	461.95	461.98	463.06	461.68	461.52	463.10	462.7	423
	Ti $2p_{1/2} \rightarrow e_g$-like	463.67	463.68	464.78	463.51	463.31	464.89	464	423
$TiCl_2Cp_2$	Ti $2p_{3/2} \rightarrow a_1$	455.61	455.42	456.58	455.41	455.13	456.53	455.8	423
	Ti $2p_{3/2} \rightarrow b_1, a_2, b_2$	458.10	457.90	459.05	458.02	457.74	459.12	457.9	423
	Ti $2p_{1/2} \rightarrow a_1$	461.69	461.41	462.26	461.32	461.16	462.23	462	423
$PdCl_2$	Pd $2p_{3/2} \rightarrow 4d$	3174.36	3174.68	3175.92	3174.39	3174.63	3175.85	3172.5	421
	Pd $2p_{1/2} \rightarrow 4d$	3333.55	3333.17	3334.36	3333.53	3333.11	3334.31	3329.5	421
CrO_2Cl_2	Cr $2p_{3/2} \rightarrow 1$	578.24	577.80	579.10	578.37	577.67	579.15	577.44	424
	Cr $2p_{3/2} \rightarrow 2$	579.30	578.96	580.15	579.36	578.93	580.24	578.28	424
	Cr $2p_{3/2} \rightarrow 3$	580.62	580.22	581.46	580.87	580.44	581.72	579.28	424
	Cr $2p_{3/2} \rightarrow 1$	581.34	580.92	582.22	581.62	581.19	582.49	580.04	424
	Cr $2p_{1/2} \rightarrow 1$	587.57	587.40	588.11	586.80	586.36	587.20	587.19	424
$VOCl_3$	V $2p_{3/2} \rightarrow 1$	515.37	515.13	516.34	515.20	515.27	516.43	515.64	424
	V $2p_{3/2} \rightarrow 2$	516.92	516.68	517.88	517.02	516.84	518.22	517.05	424
	V $2p_{3/2} \rightarrow 3$	518.18	517.96	519.17	518.23	518.27	519.42	518.08	424
	V $2p_{1/2} \rightarrow 1$	521.99	522.03	523.25	521.78	521.97	523.30	523.18	424

Table A.12: Core-excited states for selected transitions of small inorganic molecules using the *GW*-cBSE method at the K, L_1 and $L_{2,3}$ edges for different *GW* approximations. The ground state reference is provided using the PBE0[251] DFA. Further computational details are given in sec. 9.2. "H/L" indicates that the "scissor operator" was used, where aside from core levels only the highest occupied and lowest virtual states were explicitly optimized, while the remaining states were shifted accordingly. For "Valence" and additional ten virtual and occupied states were included. This number was slightly adjusted in order to not break degenerate states in an by case basis. If not explicitly listed in the source material, the values are obtained obtained from reinterpretation of the experimental spectra listed in the reference.

		BSE(H/L)			BSE(valence)				
Name	Transition	G_0W_0-1	GW_0	evGW	G_0W_0-1	GW_0	evGW	Exp.	Ref.
$SiCl_4$	Si $1s \rightarrow a_1$	1847.78	1847.53	1848.79	1847.98	1848.23	1849.20	1844.8	419
	Si $1s \rightarrow t_2$	1848.30	1848.04	1849.32	1848.47	1848.23	1849.70	1846	419
$FeCp_2$	Fe $1s \rightarrow e_{1g}$	7121.48	7126.98	7122.80	7121.58	7127.06	7123.52	7123	333
$TiCl_4$	Ti $1s \rightarrow t_2(, e)$	4971.56	4984.11	4987.61	4971.73	4983.48	4987.27	4969.15	420
$TiCl_3Cp$	Ti $1s \rightarrow d_{x^2-y^2,xy,z^2}$	4972.17	4965.82	4965.93	4972.21	4965.67	4967.36	4968.11	420
	Ti $1s \rightarrow d_{xz,yz}$	4973.65	4967.28	4967.39	4973.74	4967.20	4968.85	4969.5	420
$TiCl_2Cp_2$	Ti $1s \rightarrow d_{x^2-y^2}$	4972.75	4969.56	4974.27	4972.73	4970.12	4974.72	4967.28	420
	Ti $1s \rightarrow d_{xy,xz,yz,z^2}$	4974.03	4970.86	4975.55	4974.05	4971.41	4975.95	4968.7	420
$SiCl_4$	Si $2s \rightarrow t_2$	158.12	158.89	160.03	157.90	158.99	158.84	156.8	419
$PdCl_2$	Pd $2s \rightarrow 4d$	3622.35	3622.60	3620.37	3621.48	3622.35	3622.11	3610.9	421
$SiCl_4$	Si $2p_{3/2} \rightarrow 1$	103.70	103.60	104.41	103.71	103.59	104.55	104.25	419
	Si $2p_{1/2} \rightarrow 1'$	104.52	104.47	105.20	104.52	104.35	105.34	104.86	419
	Si $2p_{3/2} \rightarrow 2$	105.35	105.24	106.05	105.23	105.36	106.30	105.5	419
	Si $2p_{1/2} \rightarrow 2', 3'$	106.05	106.01	106.72	106.27	106.08	107.05	106.3	419
$FeCp_2$	Fe $2p_{3/2} \rightarrow e_{1g}$	710.31	710.72	710.91	710.40	710.83	711.37	709.5	422
	Fe $2p_{3/2} \rightarrow e_{2u}$	712.74	713.24	713.35	713.69	714.61	714.52	712.1	422
	Fe $2p_{1/2} \rightarrow e_{1g}$	722.57	722.20	722.99	722.76	722.56	723.37	721.9	422
	Fe $2p_{1/2} \rightarrow e_{2u}$	725.41	725.05	725.85	726.18	725.98	726.73	724.7	422
$TiCl_4$	Ti $2p_{3/2} \rightarrow 2e$	457.08	456.74	458.32	457.13	456.75	458.64	456.9	423
	Ti $2p_{3/2} \rightarrow 4t_2$	458.94	458.69	460.25	459.10	458.75	460.59	458.7	423
	Ti $2p_{1/2} \rightarrow 2e$	462.66	462.77	463.99	462.68	462.76	464.39	462.5	423
	Ti $2p_{1/2} \rightarrow 4t_2$	464.19	464.26	465.50	464.32	464.35	465.93	464.3	423
$TiCl_3Cp$	Ti $2p_{3/2} \rightarrow t_{2g}$-like	457.51	457.37	458.57	456.55	456.22	457.71	457	423
	Ti $2p_{3/2} \rightarrow e_g$-like	459.23	459.09	460.28	459.03	458.69	460.15	458.6	423
	Ti $2p_{1/2} \rightarrow t_{2g}$-like	462.86	462.81	464.01	461.38	461.12	462.47	462.7	423
	Ti $2p_{1/2} \rightarrow e_g$-like	463.16	463.08	464.27	462.44	462.16	463.44	464	423
$TiCl_2Cp_2$	Ti $2p_{3/2} \rightarrow a_1$	456.54	456.29	457.54	456.55	456.22	457.70	455.8	423
	Ti $2p_{3/2} \rightarrow b_1, a_2, b_2$	458.91	458.66	459.89	459.02	458.69	460.14	457.9	423
	Ti $2p_{1/2} \rightarrow a_1$	461.73	461.49	462.69	461.39	461.11	462.48	462	423
$PdCl_2$	Pd $2p_{3/2} \rightarrow 4d$	3175.23	3175.46	3176.75	3175.21	3175.41	3176.72	3172.5	421
	Pd $2p_{1/2} \rightarrow 4d$	3334.38	3333.96	3335.23	3334.38	3333.93	3335.18	3329.5	421
CrO_2Cl_2	Cr $2p_{3/2} \rightarrow 1$	579.09	578.60	579.98	579.28	579.56	580.28	577.44	424
	Cr $2p_{3/2} \rightarrow 2$	580.09	579.68	580.96	580.24	579.72	581.14	578.28	424
	Cr $2p_{3/2} \rightarrow 3$	581.37	580.90	582.25	581.72	581.20	585.53	579.28	424
	Cr $2p_{3/2} \rightarrow 1$	582.12	581.64	582.98	582.48	582.05	583.37	580.04	424
	Cr $2p_{1/2} \rightarrow 1$	587.73	587.43	588.12	587.66	587.19	588.10	587.19	424
$VOCl_3$	V $2p_{3/2} \rightarrow 1$	516.30	516.01	517.32	516.42	516.36	517.64	515.64	424
	V $2p_{3/2} \rightarrow 2$	517.80	517.50	518.79	518.11	517.90	519.29	517.05	424
	V $2p_{3/2} \rightarrow 3$	518.97	518.72	520.01	519.31	519.25	520.47	518.08	424
	V $2p_{1/2} \rightarrow 1$	522.89	522.92	524.22	522.98	523.13	524.52	523.18	424

A.6 Statistical Data for Core-Excited States within *GW*-BSE for aligned spectra

Table A.13: Statistical data for the *GW*-BSE approach regarding CESs of molecules depicted in fig. 9.1 using different *GW* approaches. All values are in eV. See tab. 9.2 for further information.

BSE-GW	G_0W_0	GW_0 (H/L)	evGW	G_0W_0	GW_0 (H/L±10)	evGW
K, L_1+$L_{2,3}$						
MSE	0.41	0.40	0.40	0.60	0.65	0.58
MAD	0.41	0.40	0.40	0.60	0.65	0.58
MAPE	0.07	0.07	0.07	0.11	0.12	0.11
STD	0.47	0.39	0.38	0.58	0.63	0.57
Max.AD	2.19	1.49	1.44	2.14	2.29	2.44
$L_{2,3}$						
MSE	0.43	0.41	0.42	0.64	0.70	0.62
MAD	0.43	0.41	0.42	0.64	0.70	0.62
MAPE	0.08	0.08	0.08	0.13	0.14	0.13
STD	0.49	0.40	0.39	0.60	0.66	0.60
Max.AD	2.19	1.49	1.44	2.14	2.29	2.44

Table A.14: Statistical data for the *GW*-cBSE approach regarding CESs of molecules depicted in fig. 9.1 using different *GW* approaches. All values are in eV. See tab. 9.2 for further information.

cBSE-GW	G_0W_0	GW_0 (H/L)	evGW	G_0W_0	GW_0 (H/L±10)	evGW
K, L_1+$L_{2,3}$						
MSE	0.47	0.47	0.45	0.71	0.79	0.81
MAD	0.29	0.30	0.28	0.45	0.49	0.51
MAPE	0.09	0.09	0.09	0.14	0.15	0.16
STD	0.58	0.48	0.54	0.70	0.68	0.81
Max.AD	2.15	1.50	2.01	2.17	2.01	2.92
$L_{2,3}$						
MSE	0.49	0.50	0.47	0.77	0.83	0.88
MAD	0.36	0.37	0.35	0.56	0.61	0.64
MAPE	0.10	0.10	0.10	0.15	0.17	0.18
STD	0.61	0.49	0.56	0.72	0.70	0.83
Max.AD	2.15	1.50	2.01	2.17	2.01	2.92

List of Figures

4.1 The screened interaction of two quasiparticles. . . . 21
4.2 Schematic representation of Hedin's five equations. . . . 23
4.3 Schematic representation of different approaches in the context of the *GW* approximation. . . . 27
5.1 The analytic continuation of the self-energy in AC-*GW* . . . 33
5.2 Evaluation of the self-energy by using the contour deformation technique. . . . 35
5.3 The first part of the fsCD-*GW* algorithm. . . . 42
5.4 The second part of the fsCD-*GW* algorithm. . . . 43
5.5 The third part of the fsCD-*GW* algorithm. . . . 44
5.6 Errors of the quasiparticle energies for the lowest-lying 60 carbon $1s$ type orbitals of C_{60}. . . . 46
5.7 Optimized structures of coinage metal cations, $[dpfam_2Au_2M_2]^{2+}$. . . . 47
5.8 CPU timings for fsCD-*GW* and CD-*GW* for Cd clusters of varying sizes. . . . 49
6.1 Part one of the solution of the generalized linear system of equations required in damped response theory. . . . 58
6.2 Part two of the solution of the generalized linear system of equations required in damped response theory. . . . 59
6.3 Molar absorption coefficient as obtained using damped and linear response formulations for small Cd clusters. . . . 61
7.1 Simulated XAS spectrum for the Fe K-edge in $FeCp_2$. . . . 70
8.1 Comparison of various DFAs for the GW27 test set within the *GW* approximation. . . . 73
8.2 Comparison of various DFAs for the GW100 test set within the *GW* approximation. . . . 75
8.3 Comparison of various DFAs for the CORE65 test set within the *GW* approximation. . . . 77
9.1 Optimized geometries for the molecules in the test set used in the assessment for core excitations. . . . 81
10.1 Simulated and experimental XAS of lanthanum compounds. . . . 86
10.2 Simulated XAS of lanthanum compounds. Pre-edge peak. . . . 87
10.3 Non-relaxed difference densities of lanthanum compounds. . . . 88
A.1 CPU timings for fsCD-*GW* and CD-*GW* for Cd clusters of varying sizes using only six Gauss-Legendre quadrature points. . . . 91
A.2 Wall timings for fsCD-*GW* and CD-*GW* for Cd clusters of varying sizes. . . . 92

List of Tables

5.1 Quasiparticle energies using the standard and frequency-sampled contour defromation approach. 38
5.2 MSE, MAD and STD for thee coinage metal complexes 48
5.3 Selected CPU times for Cd clusters of varying sizes 50
6.1 The lowest two core-excited states at the carbon K-edge in CH_2CHF. 63
7.1 Gauge-dependent and -invariant isotropically-averaged oscillator strengths. 69
9.1 Comparison of different methods for the description of XAS for small molecules and atoms. 80
9.2 Statistical data for the *GW*-BSE approach for CESs. 83
9.3 Statistical data for the *GW* -cBSE approach for CESs. 83
A.1 Ionization potentials for the GW27 test set for various DFAs using G_0W_0 -1. 93
A.2 Ionization potentials for the GW27 test set for various DFAs using G_0W_0 -1 (continued). 94
A.3 Ionization potentials for the GW100 test set for various DFAs using G_0W_0 -1. 95
A.4 Ionization potentials for the GW100 test set for various DFAs using G_0W_0 -1 (continued). 98
A.5 Ionization potentials for the CORE65 test set for various DFAs using G_0W_0 -1. 101
A.6 Ionization potentials for the CORE65 test set for various DFAs using G_0W_0 -1 (continued). 103
A.7 Ionization potentials for the CORE65 test set for various DFAs using GW_0 105
A.8 Ionization potentials for the CORE65 test set for various DFAs using GW_0 (continued). 107
A.9 Ionization potentials for the CORE65 test set for various DFAs using evGW 109
A.10 Ionization potentials for the CORE65 test set for various DFAs using evGW (continued). 111
A.11 Core-excited states for selected transitions of small inorganic molecules using the *GW*-BSE method. 113
A.12 Core-excited states for selected transitions of small inorganic molecules using the *GW*-cBSE method. 114
A.13 Statistical data for the *GW*-BSE approach regarding CESs (aligned). 115
A.14 Statistical data for the *GW*-cBSE approach regarding CESs (aligned). 115

Acronyms and symbols

Acronyms

AAA	Adaptive Antoulas-Anderson (algorithm)
BSE	Bethe-Salpeter equation
CEBE	Core-electron binding energy
CES	Core-excited state
DFA	Density functional approximation
DFT	Density Functional Theory
DOS	Density of states
EA	Electron affinity
ECP	Effective core potential
ev*GW*	Eigenvalue-only self-consistent *GW* method
FWHM	Full width at half maximum
GPLHR	Generalized preconditioned locally harmonic residual
***GW*$_0$**	Partial-self-consistent *GW* method
***G*$_0$*W*$_0$**	Non-iterative *GW* method
HF	Hartree-Fock (theory)
IP	Ionization potential
KS − DFT	Kohn–Sham Density Functional Theory
LHF	Local hybrid functional
LMF	Local mixing function
MAPE	Mean absolute percentage error
MAD	Mean absolute deviation
Max.AD	Maximum absolute deviation
MSE	Mean signed error
NESC	Normalized elimination of the small component

NEXAFS	Near-edge X-ray absorption fine structure
PCC	Picture-change correction
qs*GW*	Quasiparticle self-consistent *GW* method
RPA	Random-phase approximation
RSH	Range-separated hybrid (functional)
sc*GW*	(Fully) self-consistent *GW* method
(m)SNSO	(Modified) screened nuclear spin–orbit
SOC	Spin-orbit coupling
STD	Standard deviation
SVD	Singular value decomposition
TDDFT	Time-Dependent Density Functional Theory
(HR−)XANES	(High-energy resolution) X-ray absorption near edge structure
XAS	X-ray absorption spectroscopy
XPS	X-ray photoelectron spectroscopy
X2C	Exact two-component (theory/decoupling)

Indices

$i, j, k, l, \ldots$	Occupied states
$a, b, c, d, \ldots$	Virtual states
$p, q, r, s, \ldots$	General indices
$P, Q, \ldots$	Auxiliary basis functions
$I, A, M, \ldots$	Many-electron states
α, β	Generalized Kramers- or spin-momenta

Permissions to Print

In this work selected sections, graphs and tables are presented, which have previously been used or adapted from previously published articles. The required permissions were obtained from the copyright owner. Specifically these are

- Sec. 9.1 tab. 9.1 contains material of an article published by Taylor Francis Group in Mol. Phys. on 23 May 2020, available online: https://wwww.tandfonline.com/10.1080/00268976.2020.1755064: Reproduced (adapted) with permission from *Quasirelativistic two-component core excitations and polarisabilities from a damped-response formulation of the Bethe–Salpeter equation*, Max Kehry, Christof Holzer, Yannick J. Franzke, W. Klopper, Mol. Phys. **118**, e1755064 (2020).
- Sec 8.1: Reproduced (adapted) with permission from *Assessing the Accuracy of Local Hybrid Density Functional Approximations for Molecular Response Properties*, Christof Holzer, Yannick J. Franzke, Max Kehry, J. Chem. Theory Comput. **17**, 2928–2947 (2021), Copyright 2021 The Authors. Published by American Chemical Society.

Bibliography

[1] P. Zimmermann, S. Peredkov, P. M. Abdala, S. DeBeer, M. Tromp, C. Müller, and J. A. van Bokhoven, Coord. Chem. Rev. **423**, 213466 (2020).

[2] N. M. Edelstein, P. G. Allen, J. J. Bucher, D. K. Shuh, C. D. Sofield, N. Kaltsoyannis, G. H. Maunder, M. R. Russo, and A. Sella, J. Am. Chem. Soc. **118**, 13115 (1996).

[3] A. Yaroslavtsev, A. Menushenkov, R. Chernikov, E. Clementyev, V. Lazukov, Y. Zubavichus, A. Veligzhanin, N. Efremova, A. Gribanov, and A. Kuchin, Z. Kristallogr. **225**, 482 (2010).

[4] H. Asakura, T. Shishido, K. Teramura, and T. Tanaka, Inorg. Chem. **53**, 6048 (2014).

[5] T. Pruessmann, P. Nagel, L. Simonelli, D. Batchelor, R. Gordon, B. Schimmelpfennig, M. Trumm, and T. Vitova, J. Synchrotron Radiat. **29**, 53 (2022).

[6] B. Schacherl, T. Prüssmann, K. Dardenne, K. Hardock, V. Krepper, J. Rothe, T. Vitova, and H. Geckeis, J. Synchrotron Rad. **29** (2022).

[7] W. Malzer, C. Schlesiger, and B. Kanngießer, Spectrochim. Acta B: At. Spectrosc. **177**, 106101 (2021).

[8] J. G. Moya-Cancino, A.-P. Honkanen, A. M. J. van der Eerden, H. Schaink, L. Folkertsma, M. Ghiasi, A. Longo, F. M. F. de Groot, F. Meirer, S. Huotari, and B. M. Weckhuysen, ChemCatChem **11**, 1039 (2019).

[9] A. Zimina, K. Dardenne, M. A. Denecke, D. E. Doronkin, E. Huttel, H. Lichtenberg, S. Mangold, T. Pruessmann, J. Rothe, T. Spangenberg, R. Steininger, T. Vitova, H. Geckeis, and J.-D. Grunwaldt, Rev. Sci. Instrum. **88**, 113113 (2017).

[10] S. Bernadotte, A. J. Atkins, and C. R. Jacob, J. Chem. Phys. **137**, 204106 (2012).

[11] N. H. List, J. Kauczor, T. Saue, H. J. A. Jensen, and P. Norman, J. Chem. Phys. **142**, 244111 (2015).

[12] M. Reiher, Wiley Interdiscip. Rev. Comput. **2**, 139 (2012).

[13] N. A. Besley and F. A. Asmuruf, Phys. Chem. Chem. Phys. **12**, 12024 (2010).

[14] N. A. Besley, Accounts of Chemical Research **53**, 1306 (2020).

[15] M. Stener, G. Fronzoni, and M. de Simone, Chem. Phys. Lett. **373**, 115 (2003).

[16] Y. Imamura, T. Otsuka, and H. Nakai, J. Comput. Chem. **28**, 2067 (2007).

[17] T. Fransson, I. E. Brumboiu, M. L. Vidal, P. Norman, S. Coriani, and A. Dreuw, J. Chem. Theory Comput. **17**, 1618 (2021).

[18] N. A. Besley, M. J. G. Peach, and D. J. Tozer, Phys. Chem. Chem. Phys. **11**, 10350 (2009).

[19] S. Coriani and H. Koch, J. Chem. Phys. **143**, 181103 (2015).

[20] J. Wenzel, M. Wormit, and A. Dreuw, J. Comput. Chem. **35**, 1900 (2014).

[21] P. Norman and A. Dreuw, Chem. Rev. **118**, 7208 (2018).

[22] D. Jacquemin, I. Duchemin, A. Blondel, and X. Blase, J. Chem. Theory Comput. **13**, 767 (2017).

[23] T. Rangel, S. M. Hamed, F. Bruneval, and J. B. Neaton, J. Chem. Phys. **146**, 194108 (2017).

[24] X. Gui, C. Holzer, and W. Klopper, J. Chem. Theory Comput. **14**, 2127 (2018).

[25] C. Holzer, *Die GW-Methode und Bethe-Salpeter-Gleichung in der Quantenchemie: Theorie und Anwendung*, Ph.D. thesis, Karlsruher Institut für Technologie (KIT), Germany (2019).

[26] X. Blase, I. Duchemin, D. Jacquemin, and P.-F. Loos, J. Phys. Chem. Lett. **11**, 7371 (2020).

[27] X. Blase, C. Attaccalite, and V. Olevano, Phys. Rev. B **83**, 115103 (2011).

[28] D. Golze, J. Wilhelm, M. J. van Setten, and P. Rinke, J. Chem. Theory Comput. **14**, 4856 (2018).

[29] D. Golze, L. Keller, and P. Rinke, J. Phys. Chem. Lett. **11**, 1840 (2020).

[30] "Modified developers version of TURBOMOLE V7.5.1 2021, a development of University of Karlsruhe and Forschungszentrum Karlsruhe GmbH, 1989-2007, TURBOMOLE GmbH, since 2007; available from `https://www.turbomole.org`." .

[31] R. Ahlrichs, M. Bär, M. Häser, H. Horn, and C. Kölmel, Chem. Phys. Lett. **162**, 165 (1989).

[32] F. Furche, R. Ahlrichs, C. Hättig, W. Klopper, M. Sierka, and F. Weigend, Wiley Interdiscip. Rev. Comput. Mol. Sci **4**, 91 (2014).

[33] S. G. Balasubramani, G. P. Chen, S. Coriani, M. Diedenhofen, M. S. Frank, Y. J. Franzke, F. Furche, R. Grotjahn, M. E. Harding, C. Hättig, A. Hellweg, B. Helmich-Paris, C. Holzer, U. Huniar, M. Kaupp, A. Marefat Khah, S. Karbalaei Khani, T. Müller, F. Mack, B. D. Nguyen, S. M. Parker, E. Perlt, D. Rappoport, K. Reiter, S. Roy, M. Rückert, G. Schmitz, M. Sierka, E. Tapavicza, D. P. Tew, C. van Wüllen, V. K. Voora, F. Weigend, A. Wodyński, and J. M. Yu, J. Chem. Phys. **152**, 184107 (2020).

[34] A. Einstein, Ann. Phys. **322**, 891 (1905).

[35] P. A. M. Dirac and R. H. Fowler, Proc. Math. Phys. Eng. **117**, 610 (1928).

[36] M. Krauss and W. J. Stevens, Annu. Rev. Phys. Chem. **35**, 357 (1984).

[37] A. Baldes, *Weiterentwicklung und Anwendung zweikomponentiger Hartree-Fock- und Dichtefunktionalmethoden*, Ph.D. thesis, Karlsruher Institut für Technologie (KIT), Germany (2012).

[38] J. A. Bearden and A. F. Burr, Rev. Mod. Phys. **39**, 125 (1967).

[39] W. Pauli, Z. Phys. **43**, 601 (1927).

[40] T. Saue, ChemPhysChem **12**, 3077 (2011).

[41] W. Liu, Mol. Phys. **108**, 1679 (2010).

[42] P. A. M. Dirac and R. H. Fowler, Proc. Math. Phys. Eng. **126**, 360 (1930).

[43] P. A. M. Dirac, Proc. Math. Phys. Eng. **133**, 60 (1931).

[44] M. Reiher and A. Wolf, *Relativistic Quantum Chemistry: The Fundamental Theory of Molecular Science* (Wiley-VCH, Weinheim, Germany, 2015).

[45] W. Liu, J. Chem. Phys. **152**, 180901 (2020).

[46] F. Jensen, *Introduction to computational chemistry* (John Wiley & Sons, Chichester, United Kingdom, 2017).

[47] L. L. Foldy and S. A. Wouthuysen, Phys. Rev. **78**, 29 (1950).

[48] J.-L. Heully, I. Lindgren, E. Lindroth, S. Lundqvist, and A.-M. Martensson-Pendrill, J. Phys. B **19**, 2799 (1986).

[49] W. Kutzelnigg, Chem. Phys. Recent Advances and Applications of Relativistic Quantum Chemistry, **395**, 16 (2012).

[50] K. G. Dyall, J. Chem. Phys. **106**, 9618 (1997).

[51] K. G. Dyall, J. Chem. Phys. **109**, 4201 (1998).

[52] K. G. Dyall and T. Enevoldsen, J. Chem. Phys. **111**, 10000 (1999).

[53] K. G. Dyall, J. Chem. Phys. **115**, 9136 (2001).

[54] W. Liu and D. Peng, J. Chem. Phys. **131**, 031104 (2009).

[55] D. Peng and M. Reiher, Theor. Chem. Acc. **131**, 1081 (2012).

[56] D. Peng, N. Middendorf, F. Weigend, and M. Reiher, J. Chem. Phys. **138**, 184105 (2013).

[57] N. Middendorf, *Entwicklung und Anwendung quantenchemischer Methoden mit relativistischen, entkoppelten Operatoren*, Ph.D. thesis, Karlsruher Institut für Technologie (KIT), Germany (2014).

[58] M. Iliaš and T. Saue, J. Chem. Phys. **126**, 064102 (2007).

[59] R. E. Stanton and S. Havriliak, J. Chem. Phys. **81**, 1910 (1984).

[60] D. Ferenc, P. Jeszenszki, and E. Mátyus, J. Chem. Phys. **156**, 084110 (2022).

[61] J. C. Boettger, Phys. Rev. B **62**, 7809 (2000).

[62] M. Filatov, W. Zou, and D. Cremer, J. Chem. Phys. **139**, 014106 (2013).

[63] W. Zou, M. Filatov, and D. Cremer, J. Chem. Phys. **142**, 214106 (2015).

[64] C. Chang, M. Pelissier, and P. Durand, Phys. Scr. **34**, 394 (1986).

[65] E. v. Lenthe, E. J. Baerends, and J. G. Snijders, J. Chem. Phys. **99**, 4597 (1993).

[66] S. Faas, J. G. Snijders, J. H. van Lenthe, E. van Lenthe, and E. J. Baerends, Chem. Phys. Lett. **246**, 632 (1995).

[67] E. van Lenthe, R. van Leeuwen, E. J. Baerends, and J. G. Snijders, Int. J. Quantum Chem. **57**, 281 (1996).

[68] M. Douglas and N. M. Kroll, Ann. Phys. (N. Y.) **82**, 89 (1974).

[69] B. A. Hess, Phys. Rev. A **33**, 3742 (1986).

[70] G. Jansen and B. A. Hess, Phys. Rev. A **39**, 6016 (1989).

[71] M. Reiher, Theor. Chem. Acc. **116**, 241 (2006).

[72] A. Wolf, M. Reiher, and B. A. Hess, J. Chem. Phys. **117**, 9215 (2002).

[73] C. van Wüllen, J. Chem. Phys. **120**, 7307 (2004).

[74] D. Peng and K. Hirao, J. Chem. Phys. **130**, 044102 (2009).

[75] M. Barysz, J. Chem. Phys. **114**, 9315 (2001).

[76] M. Barysz and A. J. Sadlej, J. Chem. Phys. **116**, 2696 (2002).

[77] B. Swirles and D. R. Hartree, Proc. R. Soc. A: Math. Phys. Eng. Sci. **152**, 625 (1935).

[78] G. Malli and J. Oreg, J. Chem. Phys. **63**, 830 (1975).

[79] A. Szabo and N. S. Ostlund, *Modern Quantum Chemistry: Introduction to Advanced Electronic Structure Theory* (Dover, New York, USA, 2012).

[80] T. Helgaker, P. Jorgensen, and J. Olsen, *Molecular Electronic-Structure Theory* (John Wiley & Sons, Chichester, United Kingdom, 2012).

[81] M. K. Armbruster, *Entwicklung und Implementierung zweikomponentiger Hartree-Fock- und Dichtefunktionalmethoden*, Ph.D. thesis, Karlsruher Institut für Technologie (KIT), Germany (2007).

[82] M. K. Armbruster, F. Weigend, C. v. Wüllen, and W. Klopper, Phys. Chem. Chem. Phys. **10**, 1748 (2008).

[83] J. Avery, *Creation and annihilation operators* (McGraw-Hill Companies, New York, USA, 1976).

[84] H. A. Kramers, Proc. Acad. Amst **33** (1930).

[85] E. Wigner, Nachr. Ges. Wiss. Gottingen, Math.-Phys. Kl. **1932**, 546 (1932).

[86] J. M. Kasper, A. J. Jenkins, S. Sun, and X. Li, J. Chem. Phys. **153**, 090903 (2020).

[87] P. Hafner, J. Phys. B **13**, 3297 (1980).

[88] A. Baldes and F. Weigend, Mol. Phys. **111**, 2617 (2013).

[89] P. Hohenberg and W. Kohn, Phys. Rev. **136**, B864 (1964).

[90] M. Levy, Proc. Natl. Acad. Sci. **76**, 6062 (1979).

[91] E. H. Lieb, Int. J. Quantum Chem. **24**, 243 (1983).

[92] W. Kohn and L. J. Sham, Phys. Rev. **140**, A1133 (1965).

[93] R. G. Parr and W. Yang, Annu. Rev. Phys. Chem. **46**, 701 (1995).

[94] R. G. Parr and Y. Weitao, *Density-Functional Theory of Atoms and Molecules*, International Series of Monographs on Chemistry (Oxford University Press, New York, USA, New York, 1995).

[95] W. Kohn, Rev. Mod. Phys. **71**, 1253 (1999).

[96] C. van Wüllen, in *Relativistic Methods for Chemists*, Challenges and Advances in Computational Chemistry and Physics, edited by M. Barysz and Y. Ishikawa (Springer, Dordrecht, Netherlands, 2010) pp. 191–214.

[97] E. Runge and E. K. U. Gross, Phys. Rev. Lett. **52**, 997 (1984).

[98] M. A. L. Marques, C. A. Ullrich, F. Nogueira, A. Rubio, K. Burke, and E. K. U. Gross, *Time-Dependent Density Functional Theory* (Springer Berlin, Heidelberg, Germany, 2006).

[99] R. van Leeuwen, Phys. Rev. Lett. **80**, 1280 (1998).

[100] R. Van Leeuwen, Int. J. Mod. Phys. B **15**, 1969 (2001).

[101] N. T. Maitra, R. van Leeuwen, and K. Burke, Phys. Rev. A **78**, 056501 (2008).

[102] G. Vignale, Phys. Rev. A **77**, 062511 (2008).

[103] M. Casida and M. Huix-Rotllant, Annu. Rev. Phys. Chem. **63**, 287 (2012).

[104] A. K. Rajagopal, Phys. Rev. A **50**, 3759 (1994).

[105] F. Furche, J. Chem. Phys. **114**, 5982 (2001).

[106] J. Gao, W. Liu, B. Song, and C. Liu, J. Chem. Phys. **121**, 6658 (2004).

[107] J. J. Goings, J. M. Kasper, F. Egidi, S. Sun, and X. Li, J. Chem. Phys. **145**, 104107 (2016).

[108] J. J. Goings, P. J. Lestrange, and X. Li, Wiley Interdiscip. Rev. Comput. Mol. Sci. **8**, e1341 (2018).

[109] A. L. Fetter and J. D. Walecka, *Quantum Theory of Many-Particle Systems* (Dover, New York, USA, 2012).

[110] E. K. U. Gross and W. Kohn, Phys. Rev. Lett. **55**, 2850 (1985).

[111] M. Petersilka, U. J. Gossmann, and E. K. U. Gross, Phys. Rev. Lett. **76**, 1212 (1996).

[112] T. Grabo, M. Petersilka, and E. K. U. Gross, Journal of Molecular Structure: THEOCHEM **501-502**, 353 (2000).

[113] Y. M. Niquet, M. Fuchs, and X. Gonze, Phys. Rev. A **68**, 032507 (2003).

[114] P. Norman, K. Ruud, and T. Saue, *Principles and Practices of Molecular Properties : Theory, Modeling, and Simulations*, Vol. First edition (John Wiley & Sons, Hoboken, USA, Hoboken, NJ, 2018).

[115] J. Olsen, H. J. A. Jensen, and P. Jørgensen, J. Comput. Phys. **74**, 265 (1988).

[116] M. Kühn, *Zweikomponentige Methoden im Rahmen der zeitabhängigen Dichtefunktionaltheorie-Theorie, Implementierung und Anwendung*, Ph.D. thesis, Karlsruher Institut für Technologie (KIT), Germany (2015).

[117] M. P. Heller, A. Serantes, M. Spaliński, V. Svensson, and B. Withers, Physical Review D **104**, 066002 (2021).

[118] D. Peng, W. Zou, and W. Liu, J. Chem. Phys. **123**, 144101 (2005).

[119] W. Liu and Y. Xiao, Chemical Society Reviews **47**, 4481 (2018).

[120] L. Konecny, M. Repisky, K. Ruud, and S. Komorovsky, J. Chem. Phys. **151**, 194112 (2019).

[121] F. Egidi, J. J. Goings, M. J. Frisch, and X. Li, J. Chem. Theory Comput. **12**, 3711 (2016).

[122] A. Zangwill and P. Soven, Phys. Rev. A **21**, 1561 (1980).

[123] E. K. U. Gross and W. Kohn, in *Advances in Quantum Chemistry*, Density Functional Theory of Many-Fermion Systems, Vol. 21, edited by P.-O. Löwdin (Academic Press, Cambridge, USA, 1990) pp. 255–291.

[124] C. Van Wüllen, J. Comput. Chem. **23**, 779 (2002).

[125] F. Wang and T. Ziegler, J. Chem. Phys. **121**, 12191 (2004).

[126] J. Gao, W. Zou, W. Liu, Y. Xiao, D. Peng, B. Song, and C. Liu, J. Chem. Phys. **123**, 054102 (2005).

[127] R. Bast, H. J. A. Jensen, and T. Saue, International Journal of Quantum Chemistry **109**, 2091 (2009).

[128] F. Egidi, S. Sun, J. J. Goings, G. Scalmani, M. J. Frisch, and X. Li, J. Chem. Theory Comput. **13**, 2591 (2017).

[129] M. E. Casida, in *Recent Advances in Density Functional Methods*, Recent Advances in Computational Chemistry, Vol. 1 (World Scientific Press, Singapore, 1995) pp. 155–192.

[130] C. Jamorski, M. E. Casida, and D. R. Salahub, J. Chem. Phys. **104**, 5134 (1996).

[131] R. Bauernschmitt and R. Ahlrichs, Chem. Phys. Lett. **256**, 454 (1996).

[132] R. Bauernschmitt, M. Häser, O. Treutler, and R. Ahlrichs, Chem. Phys. Lett. **264**, 573 (1997).

[133] R. Bauernschmitt, *Statische und dynamische Aspekte des Kohn-Sham-Formalismus: Stabilität, statischer Response, Anregungsenergien*, Ph.D. thesis, Karlsruher Institut für Technologie (KIT), Germany (1997).

[134] M. E. Casida, J. Mol. Struct. (THEOCHEM) **914**, 3 (2009).

[135] M. Kühn and F. Weigend, J. Chem. Phys. **142**, 034116 (2015).

[136] E. R. Davidson, J. Comput. Phys. **17**, 87 (1975).

[137] C. Holzer and W. Klopper, J. Chem. Phys. **150**, 204116 (2019).

[138] M. Kühn and F. Weigend, J. Chem. Theory Comput. **9**, 5341 (2013).

[139] R. B. Morgan, Linear Algebra and its Applications **154-156**, 289 (1991).

[140] E. Vecharynski, C. Yang, and F. Xue, arXiv:1506.06829 [math] (2015).

[141] R. Van Beeumen, D. B. Williams-Young, J. M. Kasper, C. Yang, E. G. Ng, and X. Li, J. Chem. Theory Comput. **13**, 4950 (2017).

[142] C. Huang and W. Liu, J. Comput. Chem. **40**, 1023 (2019).

[143] U. Ekström, P. Norman, V. Carravetta, and H. Ågren, Phys. Rev. Lett. **97**, 143001 (2006).

[144] K. Kristensen, J. Kauczor, T. Kjærgaard, and P. Jørgensen, J. Chem. Phys. **131**, 044112 (2009).

[145] P. Norman, D. M. Bishop, H. Jørgen Aa. Jensen, and J. Oddershede, J. Chem. Phys. **115**, 10323 (2001).

[146] P. Norman, D. M. Bishop, H. J. A. Jensen, and J. Oddershede, J. Chem. Phys. **123**, 194103 (2005).

[147] C. G. Sánchez, M. Stamenova, S. Sanvito, D. R. Bowler, A. P. Horsfield, and T. N. Todorov, J. Chem. Phys. **124**, 214708 (2006).

[148] J. Kauczor and P. Norman, J. Chem. Theory Comput. **10**, 2449 (2014).

[149] A. Devarajan, A. Gaenko, and J. Autschbach, J. Chem. Phys. **130**, 194102 (2009).

[150] M. Kehry, Y. J. Franzke, C. Holzer, and W. Klopper, Mol. Phys. **118**, e1755064 (2020).

[151] T. Lancaster and S. J. Blundell, *Quantum field theory for the gifted amateur* (Oxford University Press, New York, USA, 2014).

[152] L. Hedin, Phys. Rev. **139**, A796 (1965).

[153] V. M. Galitskii and A. B. Migdal, Sov. Phys. JETP **34** (1958).

[154] J. M. Luttinger and J. C. Ward, Phys. Rev. **118**, 1417 (1960).

[155] T. Koopmans, Physica **1**, 104 (1934).

[156] P. S. Bagus, Phys. Rev. **139**, A619 (1965).

[157] J. F. Janak, Phys. Rev. B **18**, 7165 (1978).

[158] R. W. Godby, M. Schlüter, and L. J. Sham, Phys. Rev. Lett. **56**, 2415 (1986).

[159] L. J. Sham and M. Schlüter, Phys. Rev. Lett. **51**, 1888 (1983).

[160] E. Rebolini, J. Toulouse, and A. Savin, arXiv:1304.1314 [cond-mat, physics:physics] (2013).

[161] M. Kühn and F. Weigend, J. Chem. Theory Comput. **11**, 969 (2015).

[162] L. Hedin, J. Condens. Matter Phys. **11**, R489 (1999).

[163] G. Strinati, Riv. Nuovo Cimento **11**, 1 (1988).

[164] J. Schwinger, Proc. Natl. Acad. Sci. **37**, 452 (1951).

[165] J. Schwinger, Proc. Natl. Acad. Sci. **37**, 455 (1951).

[166] G. Csanak, H. S. Taylor, and E. F. Varracchio, J. Chem. Phys. **61**, 263 (1974).

[167] A. J. Layzer, Phys. Rev. **129**, 897 (1963).

[168] G. Onida, L. Reining, and A. Rubio, Rev. Mod. Phys. **74**, 601 (2002).

[169] J. Hubbard and R. E. Peierls, Proc. R. Soc. A: Math. Phys. Eng. Sci. **240**, 539 (1957).

[170] J. C. Phillips, Phys. Rev. **123**, 420 (1961).

[171] F. Aryasetiawan and O. Gunnarsson, Reports on Progress in Physics **61**, 237 (1998).

[172] M. J. van Setten, F. Weigend, and F. Evers, J. Chem. Theory Comput. **9**, 232 (2013).

[173] A. L. Kutepov, Phys. Rev. B **95**, 195120 (2017).

[174] J. J. Quinn and R. A. Ferrell, Phys. Rev. **112**, 812 (1958).

[175] L. Hedin, Nucl. Instrum. **308**, 169 (1991).

[176] J. Lindhard, Dan. Vid. Selsk Mat.-Fys. Medd. **28**, 8 (1954).

[177] D. Pines and D. Bohm, Phys. Rev. **85**, 338 (1952).

[178] D. Bohm and D. Pines, Phys. Rev. **92**, 609 (1953).

[179] M. Gell-Mann and K. A. Brueckner, Phys. Rev. **106**, 364 (1957).

[180] P. Nozières and D. Pines, Phys. Rev. **111**, 442 (1958).

[181] F. Aryasetiawan and O. Gunnarsson, Phys. Rev. B **49**, 16214 (1994).

[182] M. Kühn, J. Chem. Theory Comput. **10**, 623 (2014).

[183] R. W. Godby, M. Schlüter, and L. J. Sham, Phys. Rev. B **37**, 10159 (1988).

[184] A. M. Lewis and T. C. Berkelbach, J. Chem. Theory Comput. **15**, 2925 (2019).

[185] E. L. Shirley, Phys. Rev. B **54**, 7758 (1996).

[186] R. Del Sole, L. Reining, and R. W. Godby, Phys. Rev. B **49**, 8024 (1994).

[187] A. Schindlmayr and R. W. Godby, Phys. Rev. Lett. **80**, 1702 (1998).

[188] W. Nelson, P. Bokes, P. Rinke, and R. W. Godby, Phys. Rev. A **75**, 032505 (2007).

[189] P. Romaniello, S. Guyot, and L. Reining, J. Chem. Phys. **131**, 154111 (2009).

[190] F. Aryasetiawan, R. Sakuma, and K. Karlsson, Phys. Rev. B **85**, 035106 (2012).

[191] J. Wetherell, M. J. P. Hodgson, and R. W. Godby, Phys. Rev. B **97**, 121102 (2018).

[192] Y. Wang, P. Rinke, and X. Ren, J. Chem. Theory Comput. **17**, 5140 (2021).

[193] B. Holm and U. von Barth, Phys. Rev. B **57**, 2108 (1998).

[194] A. Stan, N. E. Dahlen, and R. v. Leeuwen, Europhys. Lett. **76**, 298 (2006).

[195] F. Caruso, P. Rinke, X. Ren, M. Scheffler, and A. Rubio, Phys. Rev. B **86**, 081102 (2012).

[196] P. Koval, D. Foerster, and D. Sánchez-Portal, Phys. Rev. B **89**, 155417 (2014).

[197] M. S. Hybertsen and S. G. Louie, Phys. Rev. Lett. **55**, 1418 (1985).

[198] M. S. Hybertsen and S. G. Louie, Phys. Rev. B **34**, 5390 (1986).

[199] M. Giantomassi, M. Stankovski, R. Shaltaf, M. Grüning, F. Bruneval, P. Rinke, and G.-M. Rignanese, Phys. Status Solidi B **248**, 275 (2011).

[200] F. Hüser, T. Olsen, and K. S. Thygesen, Phys. Rev. B **87**, 235132 (2013).

[201] A. Rasmussen, T. Deilmann, and K. S. Thygesen, Npj Comput. Mater. **7**, 1 (2021).

[202] E. Monino and P.-F. Loos, arXiv:2202.11589 [cond-mat, physics:nucl-th, physics:physics] (2022).

[203] J. S. Zhou, J. J. Kas, L. Sponza, I. Reshetnyak, M. Guzzo, C. Giorgetti, M. Gatti, F. Sottile, J. J. Rehr, and L. Reining, J. Chem. Phys. **143**, 184109 (2015).

[204] D. Golze, M. Dvorak, and P. Rinke, Front. Chem. **7** (2019).

[205] N. Pueyo Bellafont, P. S. Bagus, and F. Illas, J. Chem. Phys. **142**, 214102 (2015).

[206] C. Holzer, Y. J. Franzke, and M. Kehry, J. Chem. Theory Comput. **17**, 2928 (2021).

[207] U. von Barth and B. Holm, Phys. Rev. B **54**, 8411 (1996).

[208] P. García-González and R. W. Godby, Phys. Rev. B **63**, 075112 (2001).

[209] A. Stan, N. E. Dahlen, and R. van Leeuwen, J. Chem. Phys. **130**, 114105 (2009).

[210] C. Rostgaard, K. W. Jacobsen, and K. S. Thygesen, Phys. Rev. B **81**, 085103 (2010).

[211] S. V. Faleev, M. van Schilfgaarde, and T. Kotani, Phys. Rev. Lett. **93**, 126406 (2004).

[212] M. van Schilfgaarde, T. Kotani, and S. Faleev, Phys. Rev. Lett. **96**, 226402 (2006).

[213] T. Kotani, M. v. Schilfgaarde, S. V. Faleev, and A. Chantis, J. Condens. Matter Phys. **19**, 365236 (2007).

[214] F. Kaplan, *Quasiparticle self-consistent GW-approximation for molecules: calculation of single-particle excitation energies for molecules*, Ph.D. thesis, Karlsruher Institut für Technologie (KIT), Germany (2015).

[215] F. Kaplan, M. E. Harding, C. Seiler, F. Weigend, F. Evers, and M. J. van Setten, J. Chem. Theory Comput. **12**, 2528 (2016).

[216] M. Shishkin and G. Kresse, Phys. Rev. B **75**, 235102 (2007).

[217] N. Marom, F. Caruso, X. Ren, O. T. Hofmann, T. Körzdörfer, J. R. Chelikowsky, A. Rubio, M. Scheffler, and P. Rinke, Phys. Rev. B **86**, 245127 (2012).

[218] L. Keller, V. Blum, P. Rinke, and D. Golze, J. Chem. Phys. **153**, 114110 (2020).

[219] M. K. Armbruster, W. Klopper, and F. Weigend, Phys. Chem. Chem. Phys. **8**, 4862 (2006).

[220] F. Weigend and A. Baldes, J. Chem. Phys. **133**, 174102 (2010).

[221] P. Pollak and F. Weigend, J. Chem. Theory Comput. **13**, 3696 (2017).

[222] Y. J. Franzke, L. Spiske, P. Pollak, and F. Weigend, J. Chem. Theory Comput. **16**, 5658 (2020).

[223] K. Eichkorn, O. Treutler, H. Öhm, M. Häser, and R. Ahlrichs, Chem. Phys. Lett. **240**, 283 (1995).

[224] F. Weigend, M. Häser, H. Patzelt, and R. Ahlrichs, Chem. Phys. Lett. **294**, 143 (1998).

[225] F. Weigend, Phys. Chem. Chem. Phys. **4**, 4285 (2002).

[226] F. Neese, J. Comput. Chem. **24**, 1740 (2003).

[227] F. Weigend, M. Kattannek, and R. Ahlrichs, J. Chem. Phys. **130**, 164106 (2009).

[228] H. N. Rojas, R. W. Godby, and R. J. Needs, Phys. Rev. Lett. **74**, 1827 (1995).

[229] M. M. Rieger, L. Steinbeck, I. D. White, H. N. Rojas, and R. W. Godby, Comput. Phys. Commun. **117**, 211 (1999).

[230] S. Lebègue, B. Arnaud, M. Alouani, and P. E. Bloechl, Phys. Rev. B **67**, 155208 (2003).

[231] S.-H. Ke, Phys. Rev. B **84**, 205415 (2011).

[232] J. Wilhelm, M. Del Ben, and J. Hutter, J. Chem. Theory Comput. **12**, 3623 (2016).

[233] P. Liu, M. Kaltak, J. Klimeš, and G. Kresse, Phys. Rev. B **94**, 165109 (2016).

[234] J. Wilhelm, D. Golze, L. Talirz, J. Hutter, and C. A. Pignedoli, J. Phys. Chem. Lett. **9**, 306 (2018).

[235] B. I. Lundqvist, Phys. Konden. Mater. **7**, 117 (1968).

[236] M. Govoni and G. Galli, J. Chem. Theory Comput. **11**, 2680 (2015).

[237] T. Zhu and G. K.-L. Chan, J. Chem. Theory Comput. **17**, 727 (2021).

[238] H. Eshuis, J. Yarkony, and F. Furche, J. Chem. Phys. **132**, 234114 (2010).

[239] F. Liu, L. Lin, D. Vigil-Fowler, J. Lischner, A. F. Kemper, S. Sharifzadeh, F. H. da Jornada, J. Deslippe, C. Yang, J. B. Neaton, and S. G. Louie, J. Comput. Phys. **286**, 1 (2015).

[240] M. J. van Setten, F. Caruso, S. Sharifzadeh, X. Ren, M. Scheffler, F. Liu, J. Lischner, L. Lin, J. R. Deslippe, S. G. Louie, C. Yang, F. Weigend, J. B. Neaton, F. Evers, and P. Rinke, J. Chem. Theory Comput. **11**, 5665 (2015).

[241] X. Ren, P. Rinke, V. Blum, J. Wieferink, A. Tkatchenko, A. Sanfilippo, K. Reuter, and M. Scheffler, New J. Phys. **14**, 053020 (2012).

[242] G. Baym and N. D. Mermin, Journal of Mathematical Physics **2**, 232 (1961).

[243] H. J. Vidberg and J. W. Serene, J. Low Temp. Phys. **29**, 179 (1977).

[244] E. T. Whittaker and G. N. Watson, *A course of modern analysis: an introduction to the general theory of infinite processes and of analytic functions; with an account of the principal transcendental functions* (Cambridge University Press, Cambridge, USA, 1958).

[245] J. Schött, I. L. M. Locht, E. Lundin, O. Grånäs, O. Eriksson, and I. Di Marco, Phys. Rev. B **93**, 075104 (2016).

[246] I. Duchemin and X. Blase, J. Chem. Theory Comput. **16**, 1742 (2020).

[247] I. Duchemin and X. Blase, J. Chem. Theory Comput. **17**, 2383 (2021).

[248] M. Froissart, Les rencontres physiciens-mathématiciens de Strasbourg -RCP25 **9**, 1 (1969).

[249] P. Gonnet, S. Güttel, and L. N. Trefethen, SIAM Rev. **55**, 101 (2013).

[250] M. Barysz, in *Practical Aspects of Computational Chemistry IV*, edited by J. Leszczynski and M. K. Shukla (Springer, Boston, USA, 2016) pp. 1–24.

[251] C. Adamo and V. Barone, J. Chem. Phys. **110**, 6158 (1999).

[252] O. Treutler and R. Ahlrichs, J. Chem. Phys. **102**, 346 (1995).

[253] O. Treutler, *Entwicklung und Anwendung von Dichtefunktionalmethoden*, Ph.D. thesis, Karlsruher Institut für Technologie (KIT), Germany (1995).

[254] Y. J. Franzke, R. Treß, T. M. Pazdera, and F. Weigend, Phys. Chem. Chem. Phys. **21**, 16658 (2019).

[255] M. E. Harding and Y. J. Franzke, "Optimized auxiliary basis sets for relativistic all-electron post-Hartree–Fock and Kohn–Sham calculations," In preparation.

[256] A. C. Antoulas and B. D. Q. Anderson, IMA J. Math. Control. Inf. **3**, 61 (1986).

[257] Y. Nakatsukasa, O. Sète, and L. N. Trefethen, SIAM J. Sci. Comput. **40**, A1494 (2018).

[258] J.-P. Berrut and L. N. Trefethen, SIAM Rev. **46**, 501 (2004).

[259] S.-I. Filip, Y. Nakatsukasa, L. N. Trefethen, and B. Beckermann, SIAM J. Sci. Comput. **40**, A2427 (2018).

[260] M. Fiedler, Linear Algebra Appl. **58**, 75 (1984).

[261] R. M. Corless, in *In Laureano GonzalezVega and Tomas Recio, Eds., Proceedings EACA* (2004) pp. 317–322.

[262] G. Klein, *Applications of Linear Barycentric Rational Interpolation*, Ph.D. thesis, Université de Fribourg, Switzerland (2012).

[263] E. Anderson, Z. Bai, C. Bischof, S. Blackford, J. Demmel, J. Dongarra, J. Du Croz, A. Greenbaum, S. Hammarling, A. McKenney, and D. Sorensen, *LAPACK Users' Guide*, 3rd ed. (Society for Industrial and Applied Mathematics, Philadelphia, USA, 1999).

[264] M. Dahlen, E. H. Hollesen, M. Kehry, M. T. Gamer, S. Lebedkin, D. Schooss, M. M. Kappes, W. Klopper, and P. W. Roesky, Angew. Chem. **60**, 23365 (2021).

[265] S. Kohaut and M. Springborg, Phys. Chem. Chem. Phys. **18**, 28524 (2016).

[266] F. Weigend and R. Ahlrichs, Phys. Chem. Chem. Phys. **7**, 3297 (2005).

[267] F. Weigend, Phys. Chem. Chem. Phys. **8**, 1057 (2006).

[268] M. Dahlen, M. Kehry, S. Lebedkin, M. M. Kappes, W. Klopper, and P. W. Roesky, Dalton Trans. **50**, 13412 (2021).

[269] K. A. Peterson and C. Puzzarini, Theor. Chem. Acc. **114**, 283 (2005).

[270] A. Klamt and G. Schüürmann, J. Chem. Soc., Perkin Trans. 2 , 799 (1993).

[271] A. Schäfer, A. Klamt, D. Sattel, J. C. W. Lohrenz, and F. Eckert, Phys. Chem. Chem. Phys. **2**, 2187 (2000).

[272] D. Peng and M. Reiher, J. Chem. Phys. **136**, 244108 (2012).

[273] Y. J. Franzke, N. Middendorf, and F. Weigend, J. Chem. Phys. **148**, 104110 (2018).

[274] E. E. Salpeter and H. A. Bethe, Phys. Rev. **84**, 1232 (1951).

[275] A. Dreuw and M. Head-Gordon, Chem. Rev. **105**, 4009 (2005).

[276] F. Neese, Coord. Chem. Rev. **253**, 526 (2009).

[277] I. Duchemin, T. Deutsch, and X. Blase, Phys. Rev. Lett. **109**, 167801 (2012).

[278] D. Jacquemin, I. Duchemin, and X. Blase, J. Phys. Chem. Lett. **8**, 1524 (2017).

[279] X. Gui, *Theoretical Description of Excited States and Optical Properties of Transition Metal Complexes in the Framework of the Bethe–Salpeter Equation*, Ph.D. thesis, Karlsruher Institut für Technologie (KIT), Germany (2021).

[280] C. Holzer and W. Klopper, J. Chem. Phys. **149**, 101101 (2018).

[281] V. Olevano, J. Toulouse, and P. Schuck, J. Chem. Phys. **150**, 084112 (2019).

[282] P.-F. Loos and X. Blase, J. Chem. Phys. **153**, 114120 (2020).

[283] S. J. Bintrim and T. C. Berkelbach, J. Chem. Phys. **156**, 044114 (2022).

[284] C. Holzer, A. M. Teale, F. Hampe, S. Stopkowicz, T. Helgaker, and W. Klopper, J. Chem. Phys. **150**, 214112 (2019).

[285] C. Holzer, A. Pausch, and W. Klopper, Front. Chem. **9**, 746162 (2021).

[286] Y. J. Franzke, C. Holzer, and F. Mack, J. Chem. Theory Comput. **18**, 1030 (2022).

[287] K. Krause and W. Klopper, J. Comput. Chem. **38**, 383 (2017).

[288] Y. J. Franzke, *Calculation of NMR parameters in a modern relativistic density functional framework : theory, implementation, and application*, Ph.D. thesis, Karlsruher Institut für Technologie (KIT), Germany (2021).

[289] L. S. Cederbaum, W. Domcke, and J. Schirmer, Phys. Rev. A **22**, 206 (1980).

[290] A. Barth and L. S. Cederbaum, Phys. Rev. A **23**, 1038 (1981).

[291] K. Lopata, B. E. Van Kuiken, M. Khalil, and N. Govind, J. Chem. Theory Comput. **8**, 3284 (2012).

[292] X. Leng, F. Jin, M. Wei, and Y. Ma, Wiley Interdiscip. Rev. Comput. Mol. Sci. WIRES COMPUT MOL SCI **6**, 532 (2016).

[293] M. Guzzo, G. Lani, F. Sottile, P. Romaniello, M. Gatti, J. J. Kas, J. J. Rehr, M. G. Silly, F. Sirotti, and L. Reining, Phys. Rev. Lett. **107**, 166401 (2011).

[294] F. Bruneval, S. M. Hamed, and J. B. Neaton, J. Chem. Phys. **142**, 244101 (2015).

[295] G. L. G. Sleijpen and H. A. Van der Vorst, SIAM Rev. **42**, 267 (2000).

[296] C. C. Paige, B. N. Parlett, and H. A. van der Vorst, Numer Linear Algebra Appl. **2**, 115 (1995).

[297] D. Zuev, E. Vecharynski, C. Yang, N. Orms, and A. I. Krylov, J. Comput. Chem. **36**, 273 (2015).

[298] E. Vecharynski, C. Yang, and F. Xue, SIAM J. Sci. Comput. **38**, A500 (2016).

[299] M. L. Vidal, X. Feng, E. Epifanovsky, A. I. Krylov, and S. Coriani, J. Chem. Theory Comput. **15**, 3117 (2019).

[300] M. M. Müller, N. Perdana, C. Rockstuhl, and C. Holzer, J. Chem. Phys. **156**, 094103 (2022).

[301] B. Zerulla, M. Krstić, D. Beutel, C. Holzer, C. Wöll, C. Rockstuhl, and I. Fernandez-Corbaton, Adv. Mater. Interfaces **n/a**, 2200350 (2022).

[302] L. Bučinský, S. Biskupič, and D. Jayatilaka, J. Chem. Phys. **133**, 174125 (2010).

[303] J. Autschbach, D. Peng, and M. Reiher, J. Chem. Theory Comput. **8**, 4239 (2012).

[304] Y. Ikabata and H. Nakai, Phys. Chem. Chem. Phys. **23**, 15458 (2021).

[305] S. M. Parker, D. Rappoport, and F. Furche, J. Chem. Theory Comput. **14**, 807 (2018).

[306] M. Hochstenbach and Y. Notay, GAMM-Mitteilungen **29**, 368 (2006).

[307] P. J. Lestrange, F. Egidi, and X. Li, J. Chem. Phys. **143**, 234103 (2015).

[308] J. Wenzel and A. Dreuw, J. Chem. Theory Comput. **12**, 1314 (2016).

[309] A. Barth and J. Schirmer, J. Phys. B **18**, 867 (1985).

[310] J. Wenzel, A. Holzer, M. Wormit, and A. Dreuw, J. Chem. Phys. **142**, 214104 (2015).

[311] J. Liu, D. Matthews, S. Coriani, and L. Cheng, J. Chem. Theory Comput. **15**, 1642 (2019).

[312] D. A. Matthews, Mol. Phys. **118**, e1771448 (2020).

[313] R. McLaren, S. A. C. Clark, I. Ishii, and A. P. Hitchcock, Phys. Rev. A **36**, 1683 (1987).

[314] D. H. Kobe, Am. J. Phys. **50**, 128 (1982).

[315] M. Gell-Mann, Nuovo Cim. **4**, 848 (1956).

[316] D. P. Craig and T. Thirunamachandran, *Molecular Quantum Electrodynamics: An Introduction to Radiation-molecule Interactions* (Dover, New York, USA, 1998).

[317] P. W. Atkins and R. S. Friedman, *Molecular Quantum Mechanics* (Oxford University Press, Oxford, United Kingdom, 2011).

[318] J. D. Jackson and L. B. Okun, Rev. Mod. Phys. **73**, 663 (2001).

[319] T. Helgaker, S. Coriani, P. Jørgensen, K. Kristensen, J. Olsen, and K. Ruud, Chem. Rev. **112**, 543 (2012).

[320] N. H. List, T. R. L. Melin, M. van Horn, and T. Saue, J. Chem. Phys. **152**, 184110 (2020).

[321] C. Cohen-Tannoudji, B. Diu, and F. Laloë, *Band 2 Quantenmechanik* (De Gruyter, Berlin, Germany, 2019).

[322] P. A. M. Dirac and N. H. D. Bohr, Proc. Math. Phys. Eng. **114**, 243 (1927).

[323] F. Ding, W. Liang, C. T. Chapman, C. M. Isborn, and X. Li, J. Chem. Phys. **135**, 164101 (2011).

[324] S. Luber and M. Reiher, Chem. Phys. Accurate determination of molecular spectra and structure, **346**, 212 (2008).

[325] S. DeBeer George, T. Petrenko, and F. Neese, Inorganica Chim. Acta **361**, 965 (2008).

[326] S. DeBeer George, T. Petrenko, and F. Neese, J. Phys. Chem. A **112**, 12936 (2008).

[327] L. N. Vidal, F. Egidi, V. Barone, and C. Cappelli, J. Chem. Phys. **142**, 174101 (2015).

[328] L. K. Sørensen, M. Guo, R. Lindh, and M. Lundberg, Mol. Phys. **115**, 174 (2017).

[329] N. H. List, T. Saue, and P. Norman, Mol. Phys. **115**, 63 (2017).

[330] L. K. Sørensen, E. Kieri, S. Srivastav, M. Lundberg, and R. Lindh, Phys. Rev. A **99**, 013419 (2019).

[331] B. Supriadi, T. Prihandono, V. Rizqiyah, Z. R. Ridlo, N. Faroh, and S. Andika, J. Phys. Conf. Ser. **1211**, 012051 (2019).

[332] L. Visscher and K. G. Dyall, At. Data Nucl. Data Tables **67**, 207 (1997).

[333] I. Ismail, R. Guillemin, T. Marchenko, O. Travnikova, J. M. Ablett, J.-P. Rueff, M.-N. Piancastelli, M. Simon, and L. Journel, Rev. Sci. Instrum. **89**, 063107 (2018).

[334] J. W. Knight, X. Wang, L. Gallandi, O. Dolgounitcheva, X. Ren, J. V. Ortiz, P. Rinke, T. Körzdörfer, and N. Marom, J. Chem. Theory Comput. **12**, 615 (2016).

[335] M. Govoni and G. Galli, J. Chem. Theory Comput. **14**, 1895 (2018).

[336] M. J. van Setten, R. Costa, F. Viñes, and F. Illas, J. Chem. Theory Comput. **14**, 877 (2018).

[337] J. Jaramillo, G. E. Scuseria, and M. Ernzerhof, J. Chem. Phys. **118**, 1068 (2003).

[338] J. P. Perdew, V. N. Staroverov, J. Tao, and G. E. Scuseria, Phys. Rev. A **78**, 052513 (2008).

[339] C. A. Jiménez-Hoyos, B. G. Janesko, G. E. Scuseria, V. N. Staroverov, and J. P. Perdew, Mol. Phys. **107**, 1077 (2009).

[340] F. Liu, E. Proynov, J.-G. Yu, T. R. Furlani, and J. Kong, J. Chem. Phys. **137**, 114104 (2012).

[341] A. V. Arbuznikov and M. Kaupp, Chem. Phys. Lett. **440**, 160 (2007).

[342] E. R. Johnson, J. Chem. Phys. **141**, 124120 (2014).

[343] T. M. Maier, A. V. Arbuznikov, and M. Kaupp, Wiley Interdiscip. Rev. Comput. Mol. Sci. **9**, e1378 (2019).

[344] K. Krause, M. E. Harding, and W. Klopper, Mol. Phys. **113**, 1952 (2015).

[345] D. Golze, "NOMAD," (2020), dataset "CORE65 benchmark set". 2020; https://dx.doi.org/10.17172/NOMAD/2020.02.14-1.

[346] A. Schäfer, C. Huber, and R. Ahlrichs, J. Chem. Phys. **100**, 5829 (1994).

[347] J. P. Perdew, Phys. Rev. B **33**, 8822 (1986).

[348] A. D. Becke, Phys. Rev. A **38**, 3098 (1988).

[349] J. P. Perdew, K. Burke, and M. Ernzerhof, Phys. Rev. Lett. **77**, 3865 (1996).

[350] J. Tao, J. P. Perdew, V. N. Staroverov, and G. E. Scuseria, Phys. Rev. Lett. **91**, 146401 (2003).

[351] C. Lee, W. Yang, and R. G. Parr, Phys. Rev. B **37**, 785 (1988).

[352] A. D. Becke, J. Chem. Phys. **98**, 1372 (1993).

[353] P. J. Stephens, F. J. Devlin, C. F. Chabalowski, and M. J. Frisch, J. Phys. Chem. **98**, 11623 (1994).

[354] S. Lehtola, C. Steigemann, M. J. T. Oliveira, and M. A. L. Marques, SoftwareX **7**, 1 (2018).

[355] M. A. L. Marques, M. J. T. Oliveira, and T. Burnus, Comput. Phys. Commun. **183**, 2272 (2012).

[356] O. A. Vydrov and G. E. Scuseria, J. Chem. Phys. **125**, 234109 (2006).

[357] J.-D. Chai and M. Head-Gordon, Phys. Chem. Chem. Phys. **10**, 6615 (2008).

[358] T. Yanai, D. P. Tew, and N. C. Handy, Chem. Phys. Lett. **393**, 51 (2004).

[359] H. Bahmann, A. Rodenberg, A. V. Arbuznikov, and M. Kaupp, J. Chem. Phys. **126**, 011103 (2007).

[360] A. V. Arbuznikov and M. Kaupp, J. Chem. Phys. **136**, 014111 (2012).

[361] A. V. Arbuznikov and M. Kaupp, J. Chem. Phys. **141**, 204101 (2014).

[362] M. Haasler, T. M. Maier, R. Grotjahn, S. Gückel, A. V. Arbuznikov, and M. Kaupp, J. Chem. Theory Comput. **16**, 5645 (2020).

[363] S. V. Kruppa, C. Groß, X. Gui, F. Bäppler, B. Kwasigroch, Y. Sun, R. Diller, W. Klopper, G. Niedner-Schatteburg, C. Riehn, and W. R. Thiel, Eur. J. Chem. **25**, 11269 (2019).

[364] H. E. Wagner, P. Di Martino-Fumo, P. Boden, M. Zimmer, W. Klopper, F. Breher, and M. Gerhards, Eur. J. Chem. **26**, 10743 (2020).

[365] M. Grupe, P. Boden, P. Di Martino-Fumo, X. Gui, C. Bruschi, R. Israil, M. Schmitt, M. Nieger, M. Gerhards, W. Klopper, C. Riehn, C. Bizzarri, and R. Diller, Eur. J. Chem. **27**, 15252 (2021).

[366] S. Inanlou, R. Cortés-Mejía, A. Deniz Özdemir, S. Höfener, W. Klopper, W. Wenzel, W. Xie, and M. Elstner, Phys. Chem. Chem. Phys. **24**, 4576 (2022).

[367] F. Krätschmer, X. Gui, M. T. Gamer, W. Klopper, and P. W. Roesky, Dalton Trans. **51**, 5471 (2022).

[368] A. Marini, G. Onida, and R. Del Sole, Phys. Rev. Lett. **88**, 016403 (2001).

[369] F. Bruneval and M. A. L. Marques, J. Chem. Theory Comput. **9**, 324 (2013).

[370] F. Bruneval, N. Dattani, and M. J. van Setten, Front. Chem. **9**, 749779 (2021).

[371] C. Faber, P. Boulanger, C. Attaccalite, I. Duchemin, and X. Blase, Philosophical Transactions of the Royal Society A: Mathematical, Physical and Engineering Sciences **372**, 20130271 (2014).

[372] Y. Yao, D. Golze, P. Rinke, V. Blum, and Y. Kanai, J. Chem. Theory Comput. **18**, 1569 (2022).

[373] J. Cole, Z. Henderson, A. G. Thomas, C. L. Compeán-González, A. J. Greer, C. Hardacre, F. Venturini, W. Q. Garzon, P. Ferrer, D. C. Grinter, G. Held, and K. L. Syres, J. Phys. Chem. C **125**, 22778 (2021).

[374] O. Takahashi and L. G. M. Pettersson, J. Chem. Phys. **121**, 10339 (2004).

[375] S. Coriani, O. Christiansen, T. Fransson, and P. Norman, Phys. Rev. A **85**, 022507 (2012).

[376] J. J. Rehr, F. D. Vila, J. J. Kas, N. Y. Hirshberg, K. Kowalski, and B. Peng, J. Chem. Phys. **152**, 174113 (2020).

[377] R. Faber and S. Coriani, Phys. Chem. Chem. Phys. **22**, 2642 (2020).

[378] R. Faber and S. Coriani, J. Chem. Theory Comput. **15**, 520 (2019).

[379] R. H. Myhre, S. Coriani, and H. Koch, J. Chem. Theory Comput. **12**, 2633 (2016).

[380] B. Peng, P. J. Lestrange, J. J. Goings, M. Caricato, and X. Li, J. Chem. Theory Comput. **11**, 4146 (2015).

[381] N. A. Besley, Chem. Phys. Lett. **542**, 42 (2012).

[382] M. L. Vidal, P. Pokhilko, A. I. Krylov, and S. Coriani, J. Phys. Chem. Lett. **11**, 8314 (2020).

[383] K. Kaufmann, W. Baumeister, and M. Jungen, J. Phys. B: At. Mol. Opt. Phys. **22**, 2223 (1989).

[384] T. F. Stetina, J. M. Kasper, and X. Li, J. Chem. Phys. **150**, 234103 (2019).

[385] R. Bechmann and R. F. S. Hearmon, *Elastic, piezoelectric, piezooptic and electrooptic constants of crystals* (Springer, Berlin, Germany, 1966).

[386] A. R. Hoy and P. R. Bunker, J. Mol. Spectrosc. **74**, 1 (1979).

[387] D.-W. Chen, K. Narahari Rao, and R. S. McDowell, J. Mol. Spectrosc. **61**, 71 (1976).

[388] T. H. Dunning, J. Chem. Phys. **90**, 1007 (1989).

[389] R. A. Kendall, T. H. Dunning, and R. J. Harrison, J. Chem. Phys. **96**, 6796 (1992).

[390] D. E. Woon and T. H. Dunning, J. Chem. Phys. **103**, 4572 (1995).

[391] F. Weigend, A. Köhn, and C. Hättig, J. Chem. Phys. **116**, 3175 (2002).

[392] T. Noro, M. Sekiya, and T. Koga, Theor. Chem. Acc. **131**, 1124 (2012).

[393] T. M. Maier, H. Bahmann, A. V. Arbuznikov, and M. Kaupp, J. Chem. Phys. **144**, 074106 (2016).

[394] M. Coreno, L. Avaldi, R. Camilloni, K. C. Prince, M. de Simone, J. Karvonen, R. Colle, and S. Simonucci, Phys. Rev. A **59**, 2494 (1999).

[395] J. Schirmer, A. B. Trofimov, K. J. Randall, J. Feldhaus, A. M. Bradshaw, Y. Ma, C. T. Chen, and F. Sette, Phys. Rev. A **47**, 1136 (1993).

[396] Y. Ma, C. T. Chen, G. Meigs, K. Randall, and F. Sette, Phys. Rev. A **44**, 1848 (1991).

[397] R. Püttner, I. Dominguez, T. J. Morgan, C. Cisneros, R. F. Fink, E. Rotenberg, T. Warwick, M. Domke, G. Kaindl, and A. S. Schlachter, Phys. Rev. A **59**, 3415 (1999).

[398] O.-P. Sairanen, A. Kivimäki, E. Nõmmiste, H. Aksela, and S. Aksela, Phys. Rev. A **54**, 2834 (1996).

[399] D. Jacquemin, I. Duchemin, and X. Blase, Mol. Phys. **114**, 957 (2016).

[400] J. M. Kasper, P. J. Lestrange, T. F. Stetina, and X. Li, J. Chem. Theory Comput. **14**, 1998 (2018).

[401] M. W. Löble, J. M. Keith, A. B. Altman, S. C. E. Stieber, E. R. Batista, K. S. Boland, S. D. Conradson, D. L. Clark, J. Lezama Pacheco, S. A. Kozimor, R. L. Martin, S. G. Minasian, A. C. Olson, B. L. Scott, D. K. Shuh, T. Tyliszczak, M. P. Wilkerson, and R. A. Zehnder, J. Am. Chem. Soc. **137**, 2506 (2015).

[402] S. G. Minasian, E. R. Batista, C. H. Booth, D. L. Clark, J. M. Keith, S. A. Kozimor, W. W. Lukens, R. L. Martin, D. K. Shuh, S. C. E. Stieber, T. Tylisczcak, and X.-d. Wen, J. Am. Chem. Soc. **139**, 18052 (2017).

[403] T. Vitova, P. W. Roesky, and S. Dehnen, Commun. Chem. **5**, 1 (2022).

[404] B. Weinert, F. Weigend, and S. Dehnen, Eur. J. Chem. **18**, 13589 (2012).

[405] A. A. Bakke, H.-W. Chen, and W. L. Jolly, J. Electron Spectrosc. Relat. Phenom. **20**, 333 (1980).

[406] B. E. Mills, R. L. Martin, and D. A. Shirley, J. Am. Chem. Soc. **98**, 2380 (1976).

[407] K. Siegbahn, C. Nordling, G. Johansson, J. Hedman, P. Hedén, K. Hamrin, U. Gelius, T. Bergmark, L. Werme, R. Manne, *et al.*, Co., Amsterdam (1969).

[408] J. E. Drake, C. Riddle, H. E. Henderson, and B. Glavinčevski, Can. J. Chem **55**, 2957 (1977).

[409] A. Naves de Brito, N. Correia, S. Svensson, and H. Ågren, J. Chem. Phys. **95**, 2965 (1991).

[410] A. Mocellin, K. Wiesner, S. L. Sorensen, C. Miron, K. L. Guen, D. Céolin, M. Simon, P. Morin, A. B. Machado, O. Björneholm, and A. N. de Brito, Chem. Phys. Lett. **435**, 214 (2007).

[411] T. D. Thomas and R. W. Shaw, J. Electron Spectrosc. Relat. Phenom. The International Journal on Theoretical and Experimental Aspects of Electron Spectroscopy, **5**, 1081 (1974).

[412] W. L. Jolly, P. Finn, R. K. Pearson, and J. M. Hollander, Inorg. Chem. **10**, 378 (1971).

[413] A. Naves de Brito, S. Svensson, H. Ågren, and J. Delhalle, J. Electron Spectrosc. Relat. Phenom. **63**, 239 (1993).

[414] O. Plekan, V. Feyer, R. Richter, M. Coreno, M. de Simone, K. C. Prince, and V. Carravetta, J. Phys. Chem. A **111**, 10998 (2007).

[415] R. G. Cavell and D. A. Allison, J. Am. Chem. Soc. **99**, 4203 (1977).

[416] V. Myrseth, K. J. Børve, and T. D. Thomas, J. Org. Chem. Res. **72**, 5715 (2007).

[417] V. Carravetta, G. Iucci, A. Ferri, M. V. Russo, S. Stranges, M. de Simone, and G. Polzonetti, Chem. Phys. **264**, 175 (2001).

[418] T. D. Thomas, J. Am. Chem. Soc. **92**, 4184 (1970).

[419] J. D. Bozek, K. H. Tan, G. M. Bancroft, and J. S. Tse, Chem. Phys. Lett. **138**, 33 (1987).

[420] S. DeBeer George, P. Brant, and E. I. Solomon, J. Am. Chem. Soc. **127**, 667 (2005).

[421] T. K. Sham, Phys. Rev. B **31**, 1903 (1985).

[422] K. Godehusen, T. Richter, P. Zimmermann, and P. Wernet, J. Phys. Chem. A **121**, 66 (2017).

[423] A. Wen and A. Hitchcock, Can. J. Chem **71**, 1632 (1993).

[424] G. Fronzoni, M. Stener, P. Decleva, M. d. Simone, M. Coreno, P. Franceschi, C. Furlani, and K. C. Prince, J. Phys. Chem. A **113**, 2914 (2009)

Acknowledgments

Throughout my studies at the KIT, many people have supported me in various ways. Here, I would like to take a second to name some of them, even though many more have contributed in many shapes or forms, be it through scientific discussions or more mundane topics.

First of all, as is tradition, I would like to thank my supervisor Professor Wim Klopper, who gave me the opportunity to study interesting fields during my stay at his group. Although highly critical, these discussions were often helpful and motivating. Thank you especially for the opportunities provided.

I would like to especially name two people here, Dr. Christof Holzer and Dr. Yannick J. Franzke, who were always ready for a discussion regarding the depths of (quasi-)relativistic methods, many-body perturbation theory, and many other things. They were great co-workers and I am thankful for their critics and comments, and for proofreading the drafts of this work. Yannick, Christof, thank you very much for your time and support.

Next, I would like to thank apl. Professor Florian Weigend for accepting being a co-referee, as well as helpful discussions, especially regarding programming in the `TURBOMOLE` environment. Thank you.

I would also like to thank the people from the Theoretical Chemistry Group for the nice atmosphere, including, but not limited to, Dr. Nils Schieschke, Rodrigo Cortés Mejia, Ansgar Pausch, Florian Rehak, and many others. Thank you.

I am grateful for the financial support provided in the context of the transregional collaborative research center SFB/TRR88 “Cooperative Effects in Homo and Heterometallic Complexes (3MET)”, funded by the Deutsche Forschungsgemeinschaft (DFG).

Further thanks go towards all other people I had the opportunity to work with, and hope to continue to do so in the near future. Thank your for the interesting topics provided.

Finally, I thank my family and friends, who supported me throughout everything. I thank my partner, Victoria Le, not only for the time during this thesis and the relentless proof reading, but for the last couple of years. Thank you!